

Improved Modeling and Optimization of Spiral Blast Freezers

By

Eric Alar

A dissertation submitted in partial fulfillment of

the requirements for the degree of

Doctor of Philosophy

(Mechanical Engineering)

at the

UNIVERSITY OF WISCONSIN-MADISON

2025

Date of final oral examination: 01/14/2025

The dissertation is approved by the following members of the Final Oral Committee:

Douglas Reindl, Professor, Mechanical Engineering

Gregory Nellis, Professor, Mechanical Engineering

Richard Hartel, Professor, Food Science

Allison Mahvi, Assistant Professor, Mechanical Engineering

Krishnan Suresh, Professor, Mechanical Engineering

Acknowledgements

Doug Reindl was my advisor for this work. His immense practical understanding of industrial refrigeration systems combined with technical engineering expertise was invaluable (as was his patience). Greg Nellis helped with much of the modeling and deriving the blast effect calculations – he is brilliant and was a pleasure to work with. Tyler Young did a great job advancing our CFD work and has a bright future ahead of him as an engineer. Erik Pagenkopf managed the wind tunnel experiments and did much of the data collection. I thank all of these gentlemen for all of the help and I am infinitely grateful.

Table of Contents

1	Introduction	1
1.1	Motivations for Improving Low-Temperature Freezing Systems	1
1.2	Research Gaps and Necessity	6
1.3	Statement of Research	20
2	Methodology.....	21
2.1	One-Dimensional Conduction Model	21
2.2	Food Product Thermal Model.....	29
2.3	Performance Factors	35
2.4	Identifying Ideal Velocity Profiles.....	41
2.5	CFD Setup and Assumptions	44
2.6	Modeling Validation: Phantom I	49
2.7	Phantom II.....	59
2.8	Uncertainty analysis.....	65
3	Results	68
3.1	CFD as a Tool for Assessing Blast Freezer Air Flow	69
3.2	Thermal Model Results.....	79
3.3	Monte Carlo Simulation Results	104
3.4	Optimization Results.....	108
3.5	Cyclical Variation.....	110

3.6	Optimization Techniques on an Overall System.....	111
3.7	Phantom I Field Testing.....	115
3.8	Phantom Wind Tunnel Results	126
3.9	Phantom I Field-testing Results.....	142
4	Conclusions and Recommendations.....	150
4.1	Results and Implications.....	151
4.2	Limitations and Challenges.....	153
4.3	Future Research Ideas.....	155
5	References	157
6	Appendix	161

Table 1: Nomenclature of variables, along with a description, typical value (if applicable), and units (Choi & Okos, 1986).

Nomenclature	Description	Typical Value (if Applicable)	Units
A	Overall surface area	0.2	m ²
α	Thermal diffusivity		m ² /s
c	Specific heat		J/kg-K
Δt	Time step		s
Δy	Node spacing		m
dU/dt	Change in internal energy vs time		W
ϵ	Emissivity of aluminum	0.1	
F	F term in Levy's model	0.704	
G	G term in Levy's model	0.659	
h	Local heat transfer coefficient between the surface and surrounding air	31.9	W/m ² -K
\bar{h}	Average heat transfer coefficient	31.9	W/m ² -K
K	Constant factor		

		$\sqrt{2}$	
k	Thermal conductivity	0.02616	W/m-K
k_{air}	Thermal conductivity of air	0.023	W/m-K
k_c	Thermal conductivity of carbohydrates	0.187	W/m-K
k_f	Thermal conductivity of fat	0.184	W/m-K
k_I	Thermal conductivity (Parallel model)	0.216	W/m-K
k_{ice}	Thermal conductivity of ice	2.292	W/m-K
k_{II}	Thermal conductivity (Levy's model)	0.687	W/m-K
k_{IV}	Thermal conductivity (EMT theory)	0.387	W/m-K
L	Thickness of the product	0.016	m
L or L_{char}	Characteristic length (distance from leading edge of plate)	0.153	m
L_w	Latent heat of fusion of water	333.6	J/g
mA	milliamp transmitter output	4.3	mA
μ	Air viscosity	0.01839	centipoise
M_j	Molecular weight of solids (estimate)	50000	g/mol
mV	milliVolts produced by heat flux sensor	2	mV
M_w	Molecular weight of water	18.02	g/mol
N	Number of nodes		
v	Air velocity measured by anemometer	5	m/s
Nu	Nusselt number	186	-
Nu_0	Nusselt number at zero-degree angle	207	-
Nu_{rr}	Nusselt number reduction ratio	0.9	-
\dot{q}_{conv}	Convection term		W
\dot{q}_{flux}	Heat flux measured by sensor	1500	W/m ²
\dot{q}_{LS}	Conduction term, lower surface		W
\dot{q}_{rad}	Radiation correction factor	23	W/m ²
\dot{q}_{US}	Conduction term, upper surface		W
ρ	Density	1.189	kg/m ³
Re	Reynolds number	49,250	-
R_{rad}	Radiation thermal resistance	7.8	K/W
S	Corrected heat flux sensor calibration coefficient in milliVolts	0.0013	mV-m ² /W
S_{calib}	Heat flux sensor calibration coefficient in microVolts	1.27	μ V-m ² /W
σ	Stefan-Boltzmann constant	5.67×10^{-8}	W/m ² -K ⁴

T	Temperature	-10	°C (or K)
t	Time		s
T_0	Initial temperature vector	311	K
T_∞	Temperature of air inside spiral	286	K
$T_{if,K}$	Initial freezing temperature	237.1	K
T_{ini}	Initial temperature	311	K
T_s	Surface temperature of plate at the heat flux sensor	308	K
U	Internal energy		J
V_{air}	Volume fraction of air	0.541	
V_c	Volume fraction of carbohydrates	0.491	
V_{fat}	Volume fraction of fat	0.039	
V_{ice}	Volume fraction of ice	0.424	
$Void_f$	Void fraction	0.541	
V_w	Volume fraction of water	0.047	
x_{bw}	“Bound water” (estimate)	0.035	
x_j	All solids other than water/ice and fat	0.625	
x_{tw}	Mass fraction of total water	0.346	

Abstract

The global food industry relies heavily on spiral air blast freezers for frozen food production, a process that is both energy-intensive and environmentally impactful. This dissertation focuses on advancing the modeling and optimization of spiral air blast freezers to improve energy efficiency, reduce environmental impact, and enhance system performance. Despite their widespread use, significant research gaps remain including better modeling techniques, process understanding, and experimental validation.

This research addresses these challenges by developing advanced computational and experimental techniques to evaluate and enhance freezer performance. Key contributions include the development of a one-dimensional thermal model incorporating temperature-dependent properties, the use of computational fluid dynamics (CFD) to establish velocity-dependent heat transfer coefficients, and the introduction of

optimization techniques to improve airflow management. Experimental validations were conducted using custom pseudo products in operational spiral freezers, providing benchmarks and ensuring model accuracy.

Findings demonstrate the potential for significant energy savings and improved freezer modeling and performance through optimized airflow designs and the integration of practical engineering strategies. This work lays the foundation for spiral blast freezers that are not only more efficient but also aligned with global sustainability goals, offering actionable insights for researchers and industry professionals.

1 Introduction

The global food industry relies heavily on refrigeration systems for frozen food production, making it a significant consumer of energy and contributor to greenhouse gas emissions. Spiral air blast freezers, central to these processes, are among the most energy-intensive components due to their reliance on high-velocity airflow and ultra-low temperatures. This energy demand underscores the need for optimization to improve efficiency, reduce environmental impact, and enhance overall system performance.

1.1 Motivations for Improving Low-Temperature Freezing Systems

Spiral air blast freezers, although integral to food production, are energy-intensive, and prone to inefficiencies that may create bottlenecks, escalate costs, and increase waste. Despite their importance, advancements in the technology have been slow to develop, with many systems relying on excessive refrigeration and fan power instead of optimized designs. Research has been limited by oversimplified models and inadequate validation, leaving gaps in understanding airflow and heat transfer dynamics. This research addresses these challenges by proposing advanced thermal modeling techniques, detailed CFD modeling, and practical optimization techniques.

1.1.1 Energy Intensity Concentration

The global primary energy consumption reached approximately 634 EJ/year (601 quads/year) in 2022, with fossil fuels comprising 89% of the energy mix (EIA, 2022). The food and beverage sector contributes approximately 30% of global energy consumption and over 20% of greenhouse gas emissions (FAO, 2011). Figure 1 shows these statistics in greater detail.

	2018	2019	2020	2021	2022
World					
Consumption (quad Btu)	565.002	567.714	542.272	569.813	600.598
Coal (quad Btu)	167.041	166.301	161.033	168.981	194.021
Natural gas (quad Btu)	143.541	146.172	143.887	149.669	148.69
Petroleum and other liquids (quad Btu)	198.268	196.806	178.456	189.705	194.759
Nuclear, renewables, and other (quad Btu)	57.489	59.785	60.065	62.794	64.44
Nuclear (quad Btu)	26.778	27.879	26.931	27.745	26.877
Renewables and other (quad Btu)	30.71	31.907	33.134	35.049	37.563

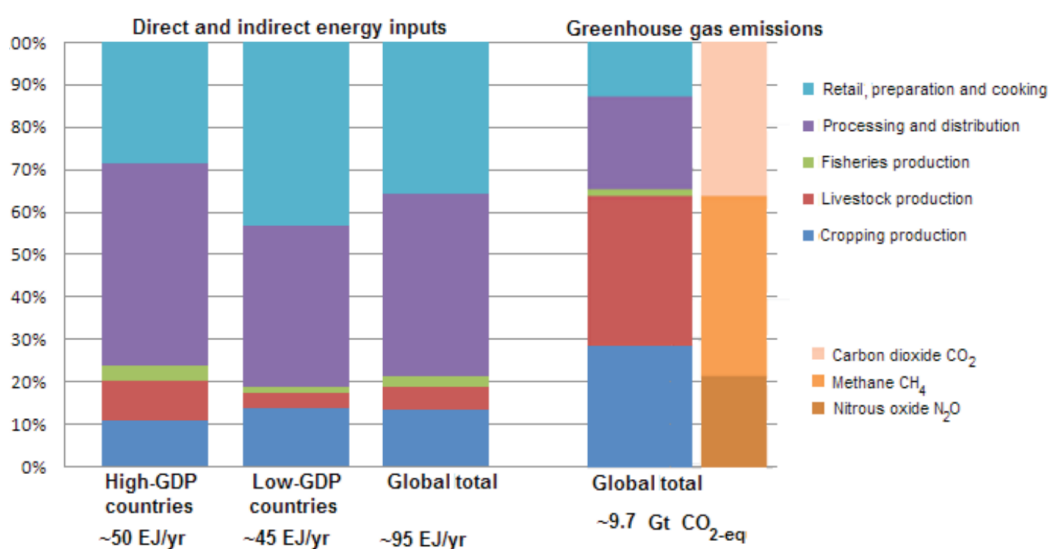


Figure 1: The upper figure shows total global energy consumption by source (EIA, 2022) and the lower figure shows the energy consumed and total CO₂ emitted by the food sector in 2011 (FAO, 2011).

Within the food industry, globally, "Processing and Distribution" is the most energy-intensive segment, accounting for about 42% of the sector's energy use. An additional 35% is consumed by "Retail, Preparation, and Cooking," bringing the combined energy demand of the food sector to 95 EJ/year (90 quads/year), which is shown at the bottom of Figure 1. Although food processing and distribution facilities, which are heavily reliant on refrigeration, are fewer in number compared to retail and preparation operations, they exhibit significantly higher energy intensity. This highlights the potential for impactful energy reductions through efficiency improvements in processing facilities. This research focuses on spiral air blast freezing, the dominant technology used in the production of frozen foods

(ASHRAE, 2018). Spiral freezers are widely used in large-scale processing facilities for nonparticulate food products due to their compact design and superior performance (ASHRAE, 2014); however, the high energy intensity of air blast freezing systems presents a critical opportunity for strategic optimization, enabling meaningful reductions in energy consumption.

1.1.2 Food Production Bottleneck

In contrast to traditional static freezing methods, most dynamic air blast freezing systems incorporate well into plants using continuous conveyors that move food products through a processing plant. The latter stages in the production of frozen foodstuffs is a step in the continuous process that involves the actual freezing of the food product. Dynamic freezing systems integrate into continuous production systems by utilizing a conveyor that can move products to be frozen through a refrigerated enclosure where high-velocity air is used to rapidly freeze food products – an air blast freezer. One configuration of a continuous freezer is the spiral air blast freezer illustrated in Figure 2. Spiral blast freezers use a helical conveyor belt arrangement within a refrigerated enclosure to permit a sufficient dwell time within the freezer to achieve product freezing while simultaneously limiting the overall footprint of the freezing system itself. A key advantage of using a dynamic freezing system in continuous process systems is the ability to seamlessly integrate the freezer with upstream and downstream processes, enabling continuous product flow and high throughput.

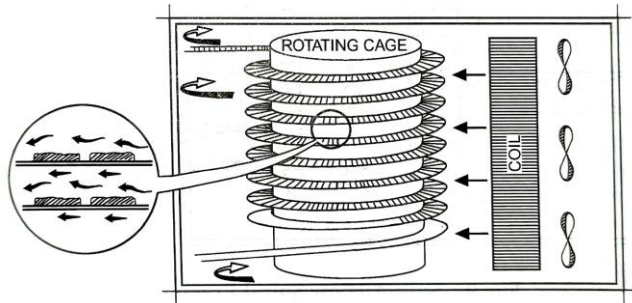


Figure 2: A horizontal airflow spiral freezer (ASHRAE, 2018).

Although spiral blast freezers integrate well into continuous flow food production processes, they quickly become a production bottleneck when the freezer is performing poorly, as explained by Kolbe and Kramer (2007). For example, inadequate freezing capacity or uneven airflow can lead to insufficiently frozen products, which might require the products to be discarded or reprocessed, resulting in potentially large amounts of waste, degraded food quality, or food safety concerns. Similarly, downtime or poor maintenance of the freezing system can halt an entire production line, significantly reducing throughput and increasing operational costs.

1.1.3 Substantial Capital Investment

Dynamic freezing systems represent a significant capital expenditure in food production. To meet stringent sanitation, corrosion, and safety standards, freezer enclosures and components (such as valves) are primarily constructed from stainless steel, driving up initial costs. Most air blast freezers use evaporators in a direct-refrigerant arrangement to remove heat from the product and ammonia (R717) is the principal refrigerant used in food processing facilities. Although ammonia has a number of desirable characteristics that include low refrigerant costs, no ozone depletion potential, and no global warming potential, it is classified by ASHRAE 34 (2024) as having higher toxic and mild flammability resulting in a safety group classification of B2L. Ammonia is corrosive to copper, but it is not reactive to carbon or stainless steel. Since stainless steel is easier to maintain than carbon steel from external corrosion, it is the most common piping material used within spiral blast freezers. Although commodity prices are highly

dynamic, at the time of writing, the material cost of stainless-steel piping is approximately 3x that of carbon steel (Metallica Metals, 2024). Freezers incur additional costs due to other mechanical components, including large electric motors to drive the conveying system and fans for rapid air circulation within the freezer. Maintaining ultra-low temperatures also requires high operational costs; for example, lowering refrigeration temperatures by 10°F (-12°C) can increase utility bills by 15% (ASHRAE, 2018). For corporations, these systems are a long-term substantial capital investment integral to production, affecting throughput, product quality, and reliability, making overall lifetime efficiency critical to managing costs and ensuring a maximum return on investment.

1.1.4 Stagnation in Technology

Since its inception in the early part of the 20th century, blast freezing has contributed to the economic growth of multiple countries (Dempsey and Bansal, 2012). This process not only allows for the rapid freezing of food but also facilitates the global distribution of frozen goods. However, air blast freezing has experienced minimal technological innovation in recent decades. While early technology produced quickly frozen food with ample throughput, modern systems have not kept pace as they often neglect optimal airflow management and rely on excess refrigeration capacity and “brute-force” fan power. Field evaluations conducted as a part of this project and a review of current product literature from manufacturers of dynamic freezing systems reveal that many spiral freezers lack internal baffling for efficiently directing airflow internally, leading to reduced energy efficiency and suboptimal freezing performance. Additionally, freezer design companies are often reluctant to deviate from existing designs due to liability concerns, fearing (for good reason) that changes from legacy designs might result in systems failing to meet performance specifications for customers, resulting in legal consequences. With rising energy costs and growing environmental concerns, the need for advancements in spiral freezer design is increasingly important.

1.2 Research Gaps and Necessity

Despite the critical role of spiral air blast freezers in food production, significant gaps remain in understanding and optimizing their performance. Previous studies have often relied on oversimplified models, such as uniform airflow that leads to constant heat transfer coefficients, which fail to capture the complex dynamics within these systems. Furthermore, technological advancements in freezer design have stagnated, with many systems relying on excessive energy use rather than targeted optimizations. This research identifies key opportunities for improvement, including enhancing airflow management, developing more accurate predictive models for heat transfer and product freezing, and validating these models through experimental data. Addressing these gaps will provide actionable strategies for improving freezer efficiency, reducing energy consumption, and advancing the sustainability of food production systems.

1.2.1 Improvement Potential

The global push for sustainability, driven by ambitious initiatives like the Paris Agreement, aims to limit global warming to 1.5°C by the end of the 21st century through zero-carbon goals and a 70% reduction in emissions by participating countries (UNFCCC, 2024). In the United States, the federal government has advanced its own ambitious net-zero policies under the Council on Environmental Quality (CEQ, 2024), reflecting a broader trend toward stricter emissions regulations and carbon pricing. These measures incentivize companies in various ways to adopt more sustainable practices, avoid financial disincentives, and align with international initiatives like the European Union's Green Deal (European Commission, 2024).

For food companies operating large low-temperature freezing systems, embracing strategies that can improve the thermal and energy performance of their freezing systems can offer substantial financial benefits. Enhanced freezing system efficiency allows businesses to produce more food with the same

equipment. Improved energy efficiency reduces operational costs by lowering unit electricity consumption. Lower electricity consumption contributes to improvements in carbon footprint; thereby, helping companies achieve sustainability goals without compromising profitability. Furthermore, energy sustainable policies can improve the reputation of a name brand, leading to investor and talent attraction.

1.2.2 Previous Applications of CFD

The initial analysis of blast freezers conducted in the present research focused on performance improvement by considering the spatial geometry within the freezing system and airflow experienced locally at the food product boundary as it moved through the freezing system. The application of Computational Fluid Dynamics (CFD), as a tool to help understand air flow patterns within a given freezing system, was utilized to evaluate proposed internal spiral freezer modifications that seek to efficiently increase air flow across the food product being frozen. Although there has been limited use of CFD on blast freezers in the past, the existing research seeks to address certain limitations and gaps that hinder a comprehensive understanding of the energy flows within a spiral freezing system. For instance, Guiqiang (2014) attempted to apply CFD to a blast freezer in order to predict the freezing behavior of simulated pork in polythene packaging; however, his model lacked crucial details such as disclosing the number of nodes used and demonstrating mesh-independency which raises questions about the validity results and conclusions. Additionally, the paper did not provide detailed CFD flow streamlines or visualizations, which are vital for comprehending fluid behavior and validating the model. The only plot in the paper that showed CFD results was a 2-D contour flow field of velocity but even that plot lacked detail. The local velocity experienced by the product as a function of simulation time inside the freezer was not provided. The paper assumed the heat transfer coefficient experienced by the product was constant during the freezing process, but relative to even the basic flow field described, this would be impossible. Additionally, the paper neglected any localized natural convection effects in the analysis,

simply stating it can be ignored since air speeds across the product are between 0.5 m/s and 5 m/s, in a sweeping statement. This is an unnecessary oversimplification to the problem, and potentially leads to incorrect analyses, because it ignores the variance of the velocity of air across products being conveyed through the freezer at different instances during their dwell time in the freezer. These velocities can be potentially less than 0.5 m/s (below the stated threshold). Lastly, the heat transfer coefficient was never field-verified. The only attempt to validate the CFD model relied on comparing the pulldown temperatures of the product (at various locations inside the food) during the freezing process. There was no mention of fan curves used, implying that the fan could deliver infinite air flow rate at a perfect, prescribed velocity. A real fan curve would produce a velocity that was a function of the pressure drop of the system. To conclude, this paper lacked a solid CFD foundation to support realistic conclusions on the performance of an existing blast freezer or evaluations of proposed modifications to an existing blast freezer.

Okita (2013) attempted to utilize CFD in evaluating a blast freezer with the computational domain shown in Figure 3. The modeled space appears to be a 2.5 x 2.5 x 2.7 meter enclosure based on a rough approximation of dimensions shown, though never explicitly stated. The number of elements used to discretize the computational domain ranged from 122,000 to 608,000 which is quite small by today's standards for appropriately resolving air flows within the computational domain. The size of mesh elements is not explicitly listed in the paper and no evidence of mesh refinement is provided. Based on geometries of the products and diagrams, computational elements appear to range from 30-50 mm. A Courant number of 3 was chosen by the author as an upper limit. Although this might be sufficient for large open spaces where velocity is not significantly changing, in areas near the blast freezer's fans and in other areas where the product is being conveyed, the air velocity will be changing much more quickly. This means that the Courant number should be limited to less than unity so air velocity does not "skip" elements. An approach to address this limitation would be the addition of inflation layers, but they were

not used in Okita's modeling. Moreover, this paper lacks essential discussions on critical aspects such as wall treatments (e.g., y^+), fan curves, and other pertinent details that can significantly influence simulation accuracy.

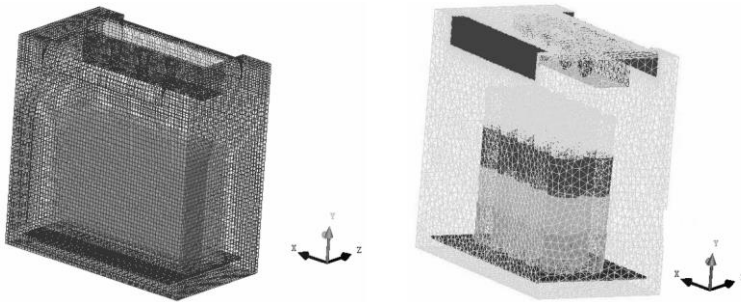


Figure 3: A simplified geometry of an air blast freezer is shown from Okita (2013).

Another limitation in both the Okita and Guiqiang models was their assumption that the air velocity across the product was perfectly horizontal inside of the blast freezer which is not evidenced by field observations of air blast freezers considered in the present research effort. Presumably, this assumption was made to make the process of resolving the heat transfer coefficient across the product relatively straightforward.

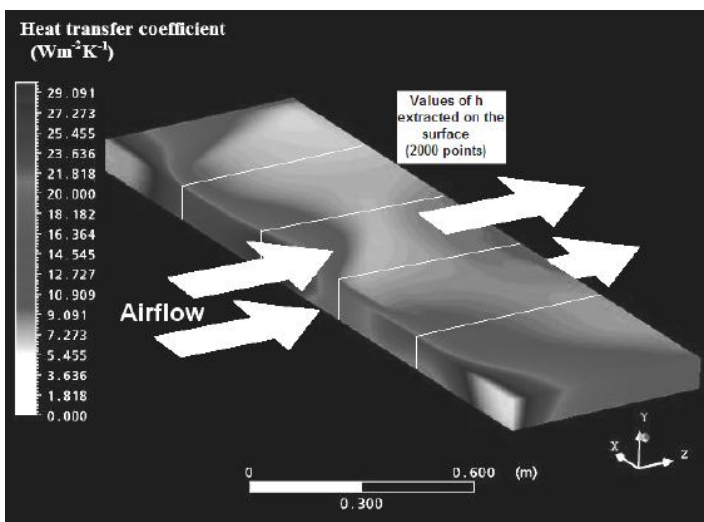


Figure 4: CFD to determine heat transfer coefficient across a product (Okita 2013).

Figure 4 shows heat transfer coefficients being predicted in Okita's work. Although the top of the plate is flat, the edge has thickness to it. This blunted edge has some effects on the heat transfer coefficient as flow develops over the plate. Airflow is shown to be perfectly horizontal. The drawback is that the velocity field within a real blast freezer is virtually never perfectly horizontal, never at steady state, and never without turbulence (e.g., eddies) in all three spatial dimensions.

The work of Khenien (2019) represents a significant advancement in the field of CFD studies on blast freezers. This paper discusses important factors such as wall treatments and the importance of y^+ in CFD simulations. The spiral height studied was 6 meters (~20 ft) tall and consisted of 15 tiers – but no other dimensions of the modeled freezer were given. Based on figures in the paper, the refrigerated enclosure appears to be approximately 12 x 10 x 10 m (H) (~39 x 33 x 33 ft). Khenien used a Reynolds Averaged Navier Stokes (RANS) approach to account for turbulent behavior to further enhance the performance of the freezer modeling. One noteworthy improvement over the previously mentioned papers is the substantial increase in the number of elements Khenien used in the CFD simulation which ranged from 10 million to 70 million elements. This higher resolution enabled a more detailed and precise representation of the flow behavior and thermal characteristics inside a blast freezer. Cornish pasty was the product considered, which had a “D” shaped aspect ratio. Certain aspects of the Khenien study can be further improved. For example, the oversimplification of the overall blast freezer model into two rectangular boxes and a cylinder, while perhaps convenient from a computational standpoint, does not fully capture the complexities of a spiral blast freezer. This geometry is illustrated in Figure 5.

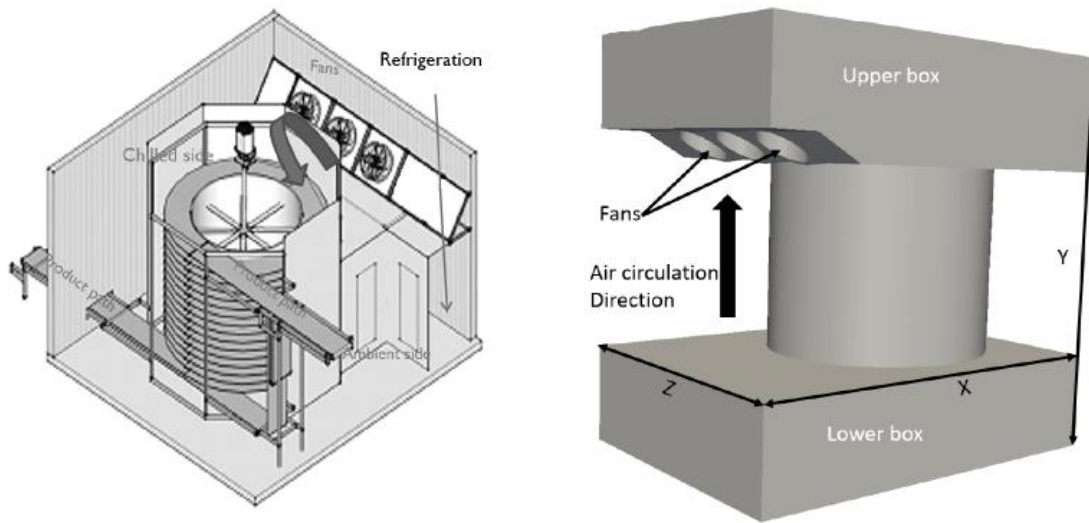


Figure 5: A drawing of a blast freezer is shown on the left, with its re-created, simplified version on the right from Khenian (2019).

This figure from Khenian appears to show that multiple important elements from the actual spiral freezer design such as baffling, refrigerant coils, and metal structures are absent from the CFD model. The spiral belt and its frame were not modeled – products were simply added to the model in circular tiers to represent the spiral belt. Evaporator coils were not modeled – they were omitted and treated as just mass flow boundaries. Additionally, the absence of information regarding the use of fan curves raises questions about the accuracy of the representation of airflow patterns and its distribution within the freezer. A constant inlet velocity of 12 m/s was used for the fan discharge condition rather than a fan curve that would provide “feedback” to decrease volumetric air flow rates based on pressure drop across the computational domain. No inflation layers were mentioned in the larger CFD model, which would introduce errors in specific areas within the computational domain where velocity is changing quickly (such as fan outlets, walls, coils, etc.). These factors limit the potential for CFD to be used as a tool in predicting the performance of spiral air blast freezers. Collectively, the prior work in this area underscores the need for a comprehensive and detailed study.

1.2.3 Predicting Air-side Heat Transfer

Past research has attempted to estimate the external heat transfer coefficient on food products being conveyed through a dynamic blast freezer using currently available convection correlations along with calculated (or inferred) air velocity. Introduced as Figure 2 from ASHRAE earlier in this chapter suggests that the spiral blast freezer is producing “horizontal airflow” in its most ideal condition. Leinhard (2020) provides valuable and up-to-date correlations for laminar, transitional, and turbulent flow over a flat plate subject to such horizontal airflow. These correlations enable the prediction of Nusselt number (and subsequently heat transfer coefficients) based on velocity, film temperature, and some indication of the turbulence present in the system. Some of these correlations are shown graphically in Figure 6; however, it is essential to highlight that these correlations are believed to be applicable only to “flat plates” with horizontal air flow. A “flat plate” in this context would have a thin vertical leading edge, and it would be shaped in such a way, like an airfoil, to prevent flow separation off the surface of the plate, so that air would not be disturbed as it traveled along the upper surface of the plate. While Leinhard's work is salient, there exists a notable gap in available information regarding the behavior of a flat plate when air flow across the plate is not uniformly horizontal but approaching the product at a specific non-zero angle. The uncertainty in predicting freezing rates using CFD-predicted velocities and existing forced convection recipes on a food product in operation is unknown.

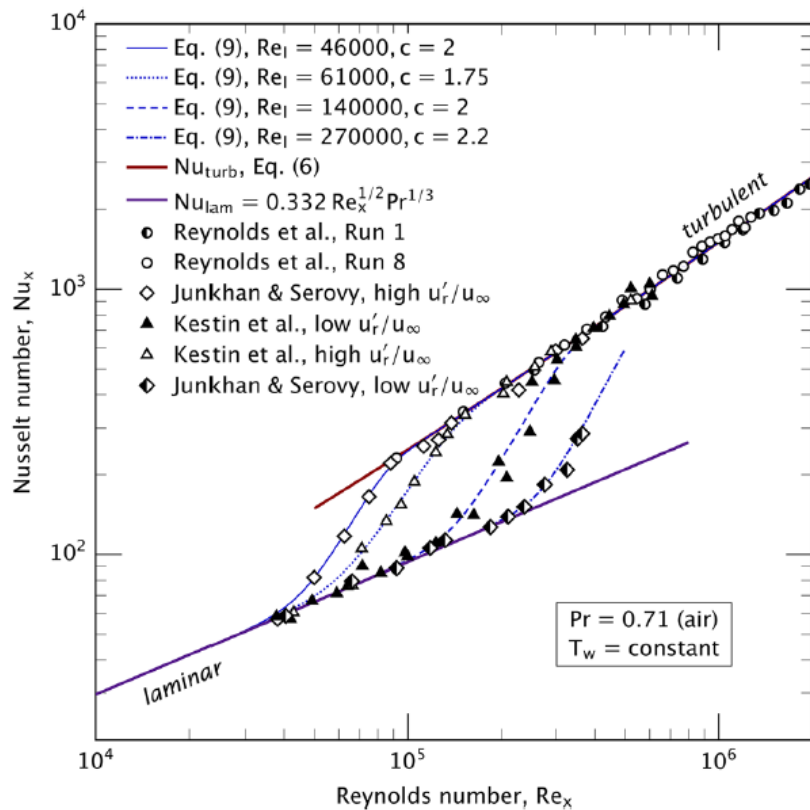


Figure 6: Convection correlation that combines the flat plate effects taken from various other investigators (Leinhard 2020).

A persistent difficulty is simply measuring heat transfer coefficient in an actual food production environment (or anywhere). To address this challenge, Amarante (2005) offered techniques for using heat flux sensors to measure external heat transfer coefficients. Amarante's team calibrated their heat flux sensors at various horizontal air speeds ranging from 0 to 7 m/s as shown in Figure 7. They accomplished this by calculating heat transfer coefficient using heat flux sensors and applying a correction factor to match a simulated numerical model of the same setup. However, this method is simply fitting measured data to a model; therefore, expectedly to produce strong agreement between measured and simulated data. Improving these experimental methods, while also using Leinhard's correlations, could lead to a better understanding of the external heat transfer coefficient experienced by a product in a spiral freezer.

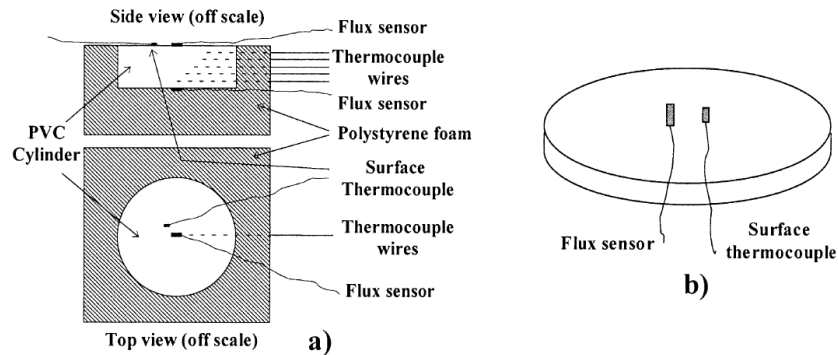


Figure 7: Heat flux sensors shown mounted to PVC in an experiment to measure heat transfer coefficient by Amarante (2003).

Although perfectly horizontal airflow has been assumed in spiral blast freezers, this simplifying assumption is likely not reflective of the actual air flow across products being conveyed through a dynamic freezing system. It is unknown what effect the angle of air flow over the product has on the heat transfer coefficient that product is experiencing during its dwell time in a freezing system. This assumption could lead to increased (or reduced) heat transfer coefficient that could have a substantial effect on predicting freezer performance. If the angle and uniformity of airflow across the product are controllable variables, this knowledge or understanding would be valuable to design engineers and researchers.

After using CFD to establish the velocity field inside a spiral freezer, resulting velocity can be linked to the product in its location while traveling through the freezing system. Knowing the velocity across the product in the spiral allows estimates of the external heat transfer coefficient to be developed as an input to a more detailed thermal model of the food product itself. The product model can then be used to predict the temperature throughout the product as a function of time. Such a thermal model requires characterizing thermal properties of the foodstuff. Prior research efforts have focused on methods that can more accurately estimate the thermal properties of the food products (Cleland, 2019, Gulati, 2013). These

studies use the composition of a food product such as the quantity of fat, protein, water, and air void fraction to predict the initial freezing transition temperature of the product as well as other properties including a mass-weighted effective density, thermal conductivity, specific heat, and ice fraction. Cleland (2019) incorporated the research of many others (notably Gulati, 2013, Choi & Okos, 1986, and Carson, 2017) into a comprehensive method that can be used to predict the thermal properties of the following classes of foods:

- Class I: Unfrozen, non-porous foods (e.g., slab of meat)
- Class II: Frozen, non-porous foods (e.g., frozen chicken)
- Class III: Unfrozen, porous foods (e.g., bread)
- Class IV: Frozen, porous foods (e.g., frozen pizza crust)

Cleland and Gulati's studies offer comparatively simple yet valuable approaches for estimating food thermal properties; however, they do acknowledge the presence of an inherent 10-20% or greater margin of error that exists when attempting to model the food due to unavoidable complexities in food microstructure. Cleland (2019) demonstrated the derived thermal properties through his model, that revealed mathematical discontinuities in volumetric heat capacity, enthalpy, thermal conductivity, and density curves posing challenges for numerical finite difference methods. It is reasonable to assume that these curves really exhibit smoother behavior, reflecting the intricacies involved in accurately representing thermal properties of food. An example of a set of discontinuous generic food thermal property curves are shown in Figure 8.

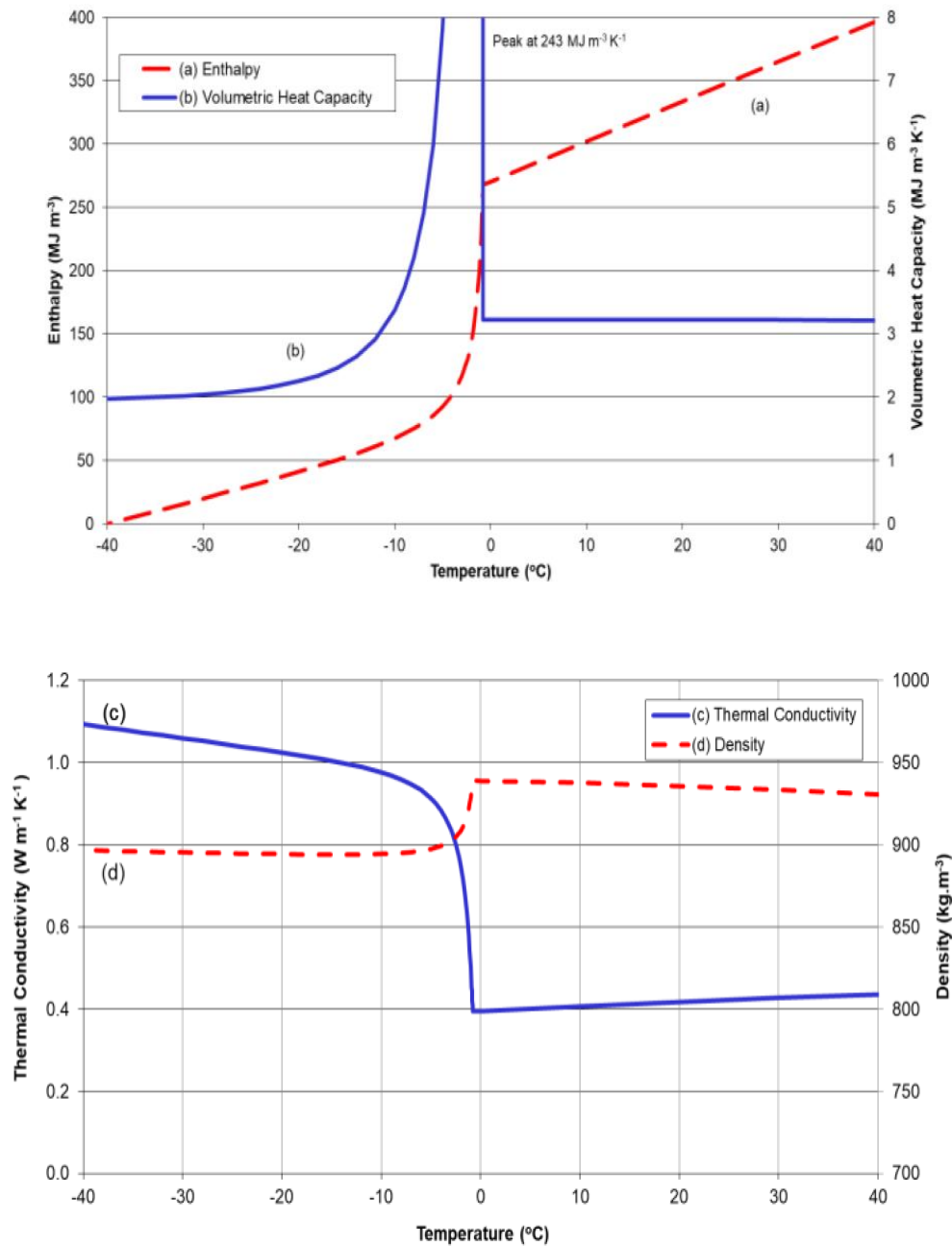


Figure 8: Thermal properties as a function of temperature for an example product (Cleland, 2019).

A reason the thermal properties exhibit discontinuous behavior is likely because an infinitesimal element size is being considered. But each element of the food product throughout its modeled volume would be approaching this discontinuity at a different time during a typical freezing process because

temperature is never uniform throughout the product. A numerical model would have to have a time step of infinitesimal size and nearly infinite nodes to sufficiently capture these discontinuities, which would be computationally prohibitive, if not impossible. If the time step sizes are chosen to be finite and reasonably large, then such sharp behaviors in density and heat capacity lead to significant energy and mass loss errors from the model. To realistically model a food product using established numerical methods while accounting for all mass and energy, modifications to these thermal properties are required to eliminate the discontinuous nature of the curves. No known work has considered addressing these limitations in food freezing processes, including food freezing within a dynamic blast freezer.

Researchers have made significant strides in developing product models that use food properties to predict the temperature response during the freezing process, resulting in several archetypal "freezing curves." For instance, Cleland (1987) and Huan (2003) have successfully incorporated temperature-dependent food properties into their numerical models to accurately forecast the temperature response of food in blast freezing operations (see Figure 9 from Huan). However, it is worth noting that these models typically do not encompass detailed considerations of the freezer's velocity and resultant heat transfer coefficient throughout the freezing process – considerations addressed in the present work.

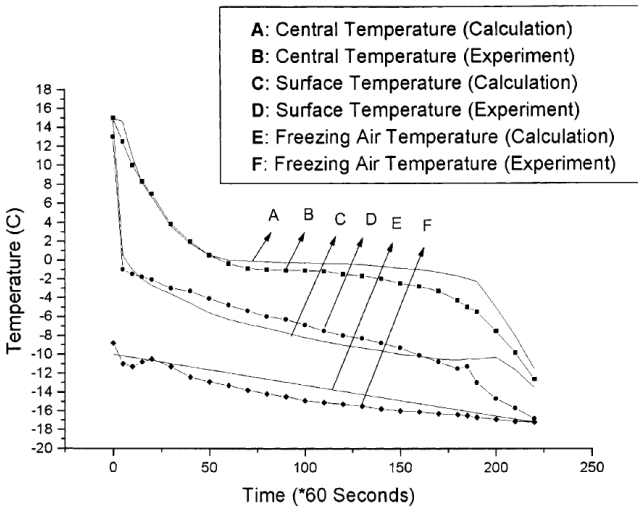


Figure 9: A typical freezing curve exhibited by a modeled food product in a “quick freezer” (Huan, 2003).

The freezing curves shown from Huan’s model exhibit peculiar behaviors that are unexplained by the author. For example, in Figure 9, the calculated center temperature is warmer than the experimentally measured center temperature during the freezing region, yet the calculated surface temperature is cooler than the experimentally measured temperature. This suggests errors in thermal properties or Biot number are not fully accounted for. Further, at around the Time = 175(*60) second mark, the surface of the experimental product abruptly drops in temperature and crosses over the calculated surface temperature. Such a distinctive behavior should perhaps have been captured by the model.

Furthermore, while these past studies have yielded interesting results, similar to the CFD review, a crucial aspect that remains to be addressed is the model validation through real-world field measurements in actual blast freezers. Such validation studies are essential to ascertain the reliability and accuracy of the predictions generated by these numerical models when compared to practical real-world operating scenarios. Incorporating velocity and heat transfer coefficient data, along with anchoring the CFD models with real field measurements, is needed to enhance the precision and practicality of the freezing process

predictions. In other words, the measured field data that a product in a freezer experiences should match the behavior that the models predict.

1.2.4 Enlisting Practical Optimization

Over the past few decades, research in optimization methods has experienced a surge in advancement, presenting effective solutions for minimizing or maximizing a wide variety of objective functions under both linear and nonlinear constraints. Past research by others (including Bendsøe in 1988) laid the groundwork for integrating optimization into Computer-Aided Engineering (CAE) practices, opening up new possibilities for the application of these techniques for design optimization. In the present day, the availability of commercial software like MATLAB with versatile and powerful functions such as `fminsearchcon` written by D'Errico (2022) simplified the conversion of constrained problems into straightforward programmable optimization routines. Moreover, the advancements in optimization via CAE are not limited to proprietary software. Free and open-source alternatives like Python's SciPy (SciPy, 2023) offer similar optimization capabilities, enabling researchers and practitioners to harness the latest developments and incredible potential in optimization into their work with minimal financial constraints. While not yet discussed in the context of blast freezer research, there are numerous aspects within this research that can benefit by application of these advancements. A premise of the current research effort is that the utilization of optimization techniques, in conjunction with CAE tools, can help enhance freezer design, improve thermal and energy efficiency, and optimize the overall performance of spiral blast freezers.

1.3 Statement of Research

The key challenge in optimizing spiral freezers is achieving greater efficiency while ensuring that production throughput remains uncompromised (if not augmented), requiring strategies that balance operational improvements with the demands of high-volume processing. Current systems often rely on lower air temperatures and higher air velocities to improve freezing rates but, taken at face value, these strategies significantly increase energy usage and operational costs. To address this challenge, it is essential to develop modeling and experimental techniques that allow determination of existing spiral freezer performance, along with actionable performance improvement strategies. The following list of objectives have been set forth for the present research efforts to address a number of the limitations noted above in past work and achieve significant performance improvements in low temperature blast freezing systems.

Objectives:

1. Develop a food simulation model incorporating temperature-dependent thermal properties to accurately represent the freezing process that can be rapidly solved using modern computational tools.
2. Quantify the impact of air velocity profiles on freezing performance and energy efficiency.
3. Use CFD and in situ data to establish velocity-dependent heat transfer coefficients, accounting for spatial and temporal variations in airflow.
4. Propose optimized air-side designs, including the use of baffles, to improve airflow management and enhance system efficiency.
5. Develop a pseudo product that can be used in an actual spiral freezer to validate the thermal model and CFD, and to benchmark different freezers against one another.
6. Establish correlations that show the effect of velocity magnitude and angle over the product has on the external heat transfer coefficient.

7. Introduce engineering strategies (i.e., best practices) that should be targeted, and others that should be avoided, in the design and operation of spiral blast freezers.

2 Methodology

The methodology for this research encompasses the development and analysis of numerical models to simulate the freezing process in air blast spiral freezers. This includes the derivation of governing equations for heat transfer, numerical solution techniques, and the use of experimental and computational methods to validate and optimize the models. The primary focus is on understanding and improving the thermal performance of products frozen within these systems by exploring dynamic airflow and temperature conditions, enabling actionable insights for process enhancement and energy efficiency.

2.1 One-Dimensional Conduction Model

A one-dimensional (1-D) conduction model was developed to simulate the freezing process of various food products, accounting for critical factors such as conduction within the product and convection at its surfaces. This model serves as the foundation for evaluating heat transfer dynamics in spiral freezers. Simplifications, such as neglecting radiation and tactfully using temperature-dependent material properties, ensure computational efficiency while preserving accuracy. A method to validate the numerical model's results against experimental data is introduced, offering a robust solution for understanding and optimizing freezing performance in industrial settings.

2.1.1 *Derivation of Ordinary Differential Equations*

Food products being frozen in an air blast spiral freezer typically enter at a uniform temperature well above their intended final temperature and the products themselves could either be packaged or unpackaged. For example, a bread or dough product might exit its upstream process such as a proofer or

par-baker at a temperature of 38°C (100°F). The warm product would then enter the spiral freezer and be exposed to an environment with extremely low air temperatures and high air velocity intended to quickly remove heat from the product by increased forced convection heat transfer with the freezer air. Removing heat from the core of the product relies on conduction causing the center temperature of the product to gradually decrease and, eventually, equilibrate with the temperature inside the freezer if the dwell time within the freezer is sufficiently long. Oftentimes, process facilities will establish and monitor exit criteria such as a center temperature of the product exiting the freezer reaching -10°C (10°F) or lower. Production process operators may have the ability to vary the belt speed (dwell time), fan speed, evaporator coil defrost, refrigeration saturation temperature, and product volume (load) in response to product temperatures above (or below) the established criteria.

An unsteady 1-D numerical conduction model of the freezing process of a planar food product (dough) was derived using the boundary conditions and control volumes shown in Figure 10. This model experiences convection on both the upper and lower surfaces, and conduction in the interior. Radiation is neglected in this analysis for two reasons. First, the focus of the present research effort was on comparing the relative effect of baffling changes within the spiral freezer. As such, the effects of radiation would have mostly “canceled out” between modeling iterations. Second, the heat transfer due to radiation was calculated using measured data in a real spiral freezer and found to be responsible for only 2% of the overall heat transfer between the product and freezer environment based on an experimental pseudo product (which will be introduced later). Therefore, radiation effects are neglected in this 1-D model.

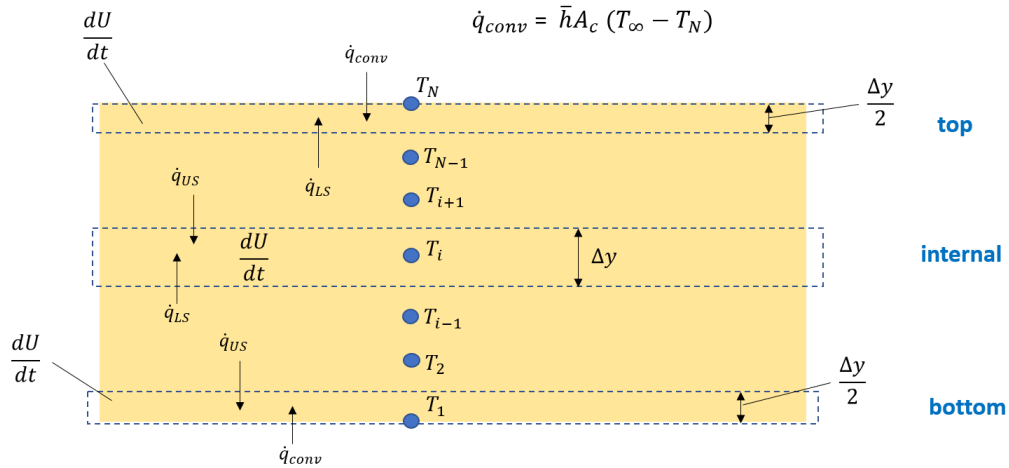


Figure 10: 1-D numerical thermal model of the dough product.

An energy balance on the bottom surface of the modeled product shown in Figure 10 at the first node T_1 , which has a convection term on the bottom and a conduction term on the top of the node, produces Equation 1:

$$\frac{dU_1}{dt} = \dot{q}_{US} + \dot{q}_{conv} \quad (1)$$

The internal nodes, shown in Figure 10, experience only conduction between adjacent nodes on the boundary surfaces above and below between the given node, i , as shown by Equation 2:

$$\frac{dU_i}{dt} = \dot{q}_{US} + \dot{q}_{LS} \quad (2)$$

The top surface node, N , of the model is similar to Eq. 1, except the conduction is now on the node's lower surface and convection is on the top:

$$\frac{dU_N}{dt} = \dot{q}_{LS} + \dot{q}_{conv} \quad (3)$$

Substituting relevant dimensions and properties into Equation 1 from Figure 10 produces the following differential equation for the bottom node 1:

$$\frac{dT_1}{dt} = \frac{2 k_{T_1, T_2}}{\Delta y^2 \rho c_1} (T_2 - T_1) + \frac{2 \bar{h}(T_\infty - T_1)}{\Delta y \rho c_1} \quad (4)$$

The internal nodes are slightly different, because the nodes are double the size of the end nodes, and they have two conduction terms instead of a conduction and convection term. This is shown in Figure 10. Substituting terms from Figure 10 into Eq. 2 produces the following for internal node i :

$$\frac{dT_i}{dt} = \frac{k_{T_{i+1}, T_i}}{\Delta y^2 \rho c_i} (T_{i+1} - T_i) + \frac{k_{T_{i-1}, T_i}}{\Delta y^2 \rho c_i} (T_{i-1} - T_i) \quad (5)$$

Finally, the upper node, N , is determined by substituting in properties and dimensions from Figure 10 into Eq. 3, which produces the following:

$$\frac{dT_N}{dt} = \frac{2 k_{T_{N-1}, T_N}}{\Delta y^2 \rho c_N} (T_{N-1} - T_N) + \frac{2 \bar{h}(T_\infty - T_N)}{\Delta y \rho c_N} \quad (6)$$

The Δy term is variable and represents the spacing between nodes and is determined based on the overall thickness of the product, L , and the number of nodes used in the model, N . This is shown in Eq. 7:

$$\Delta y = \frac{L}{N - 1} \quad (7)$$

In the differential equations Eq. 4-6, the average surface heat transfer coefficient, \bar{h} , is dependent on the air's velocity, temperature, and thermal properties over the product. Within the dynamic freezing system, this surface heat transfer coefficient will be dependent on time (position within the freezer), and varies continuously, as shown in a simplified manner by Equation 8.

$$\bar{h} = f(t) \quad (8)$$

The actual velocity and resulting heat transfer coefficient (HTC) for a product within a spiral is not known a priori. As noted in Chapter 1, several past researchers have simply assigned or assumed a value of the HTC to estimate product freezing time. CFD could be used to determine the heat transfer coefficient, however, in a computational domain as large as a spiral freezer, the energy equation required to be solved would be computationally unfeasible with sufficient resolution, since the product is moving, it is constantly being exposed to new geometry within the spiral freezer that influences the velocity of air. Also, in CFD, assumptions such as constant heat flux or constant temperatures are typically made to calculate a heat transfer coefficient, making this an educated guess at best. A different method was developed in this research and will be presented in Chapter 3. As a first step to exercise the 1-D model, a nominal heat transfer coefficient of h_{orig} , of 25 W/m²-K was found to make the 1-D thermal model match the actual measured thermal performance (i.e., belt speed and exiting product temperature) of an actual spiral freezer evaluated as part of this project. This value of heat transfer coefficient corresponds to an air velocity of $vel_{orig} = 5$ m/s and spot anemometer measurements inside of the actual spiral freezer corroborated this velocity magnitude. The baseline heat transfer coefficient h_{new} is subsequently scaled using local velocity vel_{new} values predicted by the CFD model using the relationship shown in Eq. (9). This scaling relationship is based on typical turbulent external flow correlations (such as Dittus-Boelter) that calculate the Nusselt number as a function of $Re^{0.8}$ (Winterton 1998). The major takeaway is that heat transfer coefficient scales with velocity but with diminishing returns to the 4/5 power.

$$h_{new} = \frac{Vel_{new}^{0.8}}{Vel_{orig}^{0.8}} h_{orig} \quad (9)$$

2.1.2 ODE113 Solver in MATLAB

The differential equations Eq. 4-6 can be solved using a variety of numerical techniques and, initially, analytical finite difference methods were used to validate the equation set. Although functional, the

analytical methods with constant time-steps were found to be quite slow therefore alternative integration techniques were explored, including ODE45 and ODE113 in MATLAB. An example of the function call that solves system of differential equations using ODE113 is shown in Equation 10 (Nellis & Klein, 2009).

$$[time, T] = ODE113 \left(\left\{ \frac{dT}{dt} \right\}, \Delta t, T_0 \right) \quad (10)$$

ODE113 is a numerical solver for ordinary differential equations (ODEs) that uses a variable time step and is ideal for problems that have long, smooth dynamics where high accuracy is required. ODE45 was also evaluated but underperformed compared to ODE113 once simulations became increasingly complex, such as when heat transfer coefficients as a function of time from field measurements and temperatures were supplied to the equation set as boundary conditions. Both ODE solvers have a variable time step, and therefore a convergence study with a fixed timestep is not easily possible. Spatial resolution was evaluated in Section 2.1.3. However, the relative tolerance of the function was varied to confirm converged solutions. This is shown in Figure 11. Note that the error here is defined as the deviation of the center temperature of the simulated food product upon exiting the freezer after the ODE is solved compared to the converged result with the lowest relative tolerance of 10^{-6} .

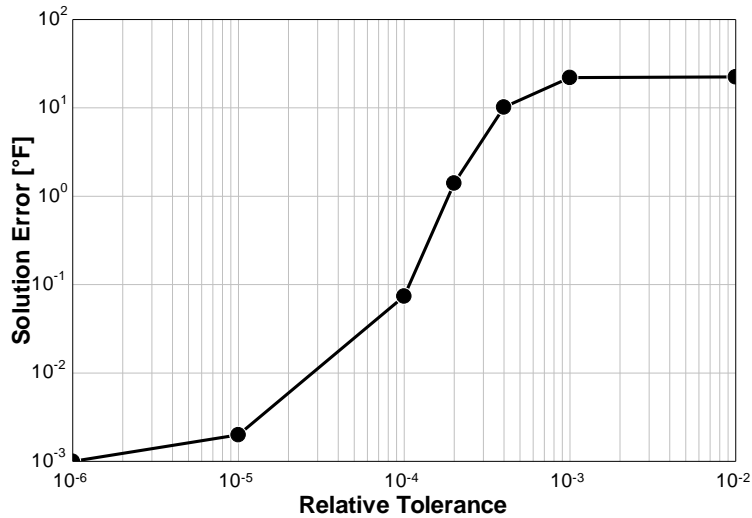


Figure 11: Error in the temperature solution as a function of the relative tolerance used in the ODE113 solver.

In Eq. 10, T is a vector or matrix of temperatures that is a function of *time*, dT/dt is a vector of the differential temperature terms derived from Eq. 4-6, Δt is the time step (which is variable), and T_0 is the initial temperature vector, which in this case is the temperature that the product enters the spiral freezer. Table 1 shows the nomenclature used in the 1-D thermal model, along with brief descriptions of the variables and their units.

This numerical technique allows the thermal conductivity and specific heat capacity of the product to be expressed as functions of temperature and the heat transfer coefficient to vary as a function of time based on the local velocity of air across the product as it is conveyed through the spiral freezer. It must be noted that an energy balance was performed on this time-dependent model that ensured that the total heat transfer between each node throughout the entire simulation was equivalent to the overall available heat capacity of the product model. In other words, no energy “was lost” in the simulation.

2.1.3 Vectorization in MATLAB

To solve the system of ODEs efficiently, the model was implemented in MATLAB with vectorization. This approach eliminates computational overhead associated with “for” loops, optimizing performance for the large-scale simulations discussed later in Section 2.4.2. MATLAB, as a commercial software, is uniquely powerful in solving matrices and vectors quickly using highly optimized low level math processes, parallelization, and batch processing techniques. MATLAB’s name comes from “MATrix LABORatory,” as it was designed for this exact purpose.

Although temperature-dependent food thermal properties will be introduced in Section 2.2.1, a convergence study on the vectorized ODE food model introduced earlier in Section 2.1.1 was conducted, shown in Figure 12, to determine the number of nodes required to ensure numerical stability and accuracy. The error here was defined as the time required for the center of the product to meet freezing requirements compared to the time required at the maximum node count of 180.

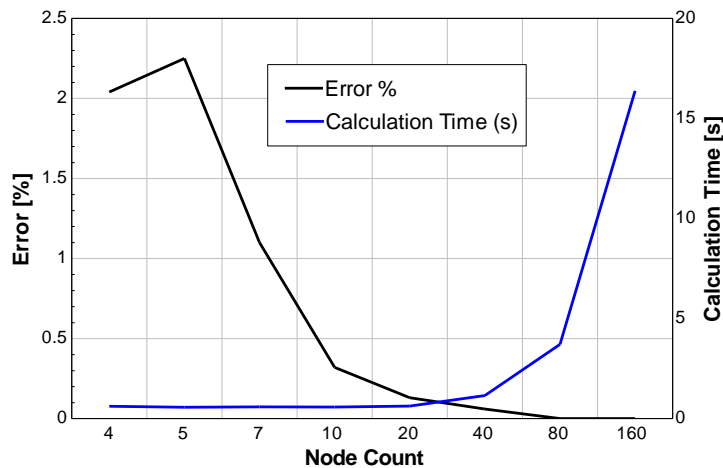


Figure 12: Modeling error and calculation time as a function of node count.

The results indicate that 20 to 40 nodes provide an optimal balance between computational efficiency and solution precision. Typically, 40 or 80 nodes were used whether speed was desired for large model calculation ensembles or optimal accuracy was required for single model use cases. However, this discretization is likely dependent on the

dough product's thermal properties and the geometry of the 1-D plane. Studies should be completed for other modeled food types and geometries.

2.1.4 Symmetry Model

The 1-D thermal model assumes symmetrical convection boundaries for most cases, treating the product's upper and lower surfaces equivalently. This assumption simplifies computations without sacrificing substantial accuracy for standard geometries like slabs. For cases with asymmetrical airflow, the model was adjusted by incorporating distinct heat transfer coefficients and contact resistances for each surface based on experimental data or other methods. Establishing the proper contact resistance between a product and the conveyor belt while it is being exposed to high velocity air is so inherently complex that usually the symmetrical model was preferred. However, a study was performed that field-measured the performance between different belt materials in a spiral freezer that will be presented in Chapter 3.

2.2 Food Product Thermal Model

2.2.1 Temperature Dependent Properties

The 1-D thermal model of the food product was developed to predict the product's freezing thermal behavior given the temperature the product experiences during its dwell time in the blast freezer. The first food product modeled was two varieties of a flat dough product (pizza crust). Beginning with the product's mass composition of fat, carbohydrates, water, and the known weight and volume of the individual product unit, a detailed one-dimensional thermal model was constructed based on the methods presented by Cleland (2019), which is an amalgamation of methods by other researchers. The product in this research had a diameter of 0.29 m, thickness of 16 mm, overall mass of 0.57 kg, 35% mass fraction of water, 62% carbohydrates, and 3% fat. The estimated void fraction of the dough at the entry to the

freezing system was 54%. Using the methods of Cleland (2019) the temperature-dependent thermal conductivity for the dough product is shown in Figure 13 (left). The thermal conductivity tends to decrease as the temperature decreases with the exception of a near step-change increase near the freezing point of water.

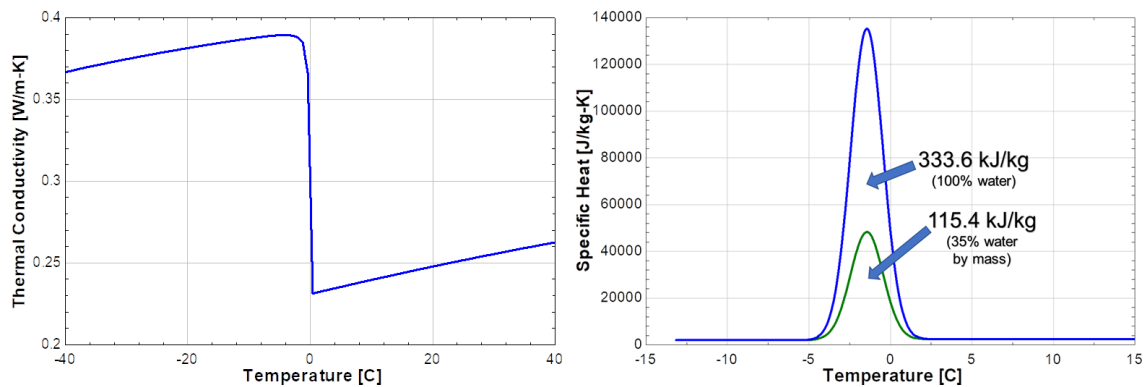


Figure 13: Thermal conductivity as a function of temperature for the product using methods from Cleland (2019) is shown on the left. Specific heat as a function of temperature is shown on the right.

The product's temperature-dependent specific heat shown in Figure 13 (right) was initially modeled using methods presented in Cleland (2019); however, this approach produced a step change in specific heat capacity that was not tolerated well by the numerical techniques used to solve the system of differential equations. The behavior associated with the freezing process was modified to represent the temperature-dependent heat capacity by the continuous function shown in Figure 13 (right). When this function is integrated, the result is equal to the latent heat of fusion of water based on its mass fraction within the product in addition to the change in sensible heat capacity of the food. The difference between this and the original step change is that the step change requires an infinitesimally small time step to capture the abrupt change in the specific heat capacity, in addition to many nodes. Since every node in the discretized food product is at a different temperature during the transient cooling/freezing process, this small time step would be required at many different temporal instances in a numerical simulation, which makes it difficult to program and unnecessarily slow. The continuous Gaussian distribution shown in

Figure 13 and given by Equation 11 allows a larger time step, where accuracy is retained as the product passes through this freezing region and the overall cooling process is sufficiently captured with no discernable loss in accuracy. Another reason this equation was used to model the specific heat is for performance, as it allows very rapid calculations of food properties, which is conducive to running many simulations quickly. Equation 11 provides the specific heat, c (J/kg), as a function of temperature, T (K); the parameter μ is the mean freezing temperature (273 K), and σ is the standard deviation which can be adjusted, but for the preliminary analysis reported here is set to 1 K.

$$c = \frac{1}{\sigma\sqrt{2\pi}} e^{\left(\frac{-1}{2}\left(\frac{T-\mu}{\sigma}\right)^2\right)} 113100 \left[\frac{J}{kg}\right] + 2460 \left[\frac{J}{kg}\right] \quad (11)$$

The initial freezing temperature was determined based on the freezing point depression theory, or Raoult's Law (Cleland, 2019, Boonsupthip, 2007). Initial freezing temperature is critical to enable computing the ice fraction as a function of time during the process. Ice fraction is used in deriving additional thermal properties, which will be explained in more detail shortly. In addition, some properties, such as thermal conductivity, can vary significantly with the product's freezing period as already noted above. Indeed, this is the point where many of the properties produce discontinuous curves shown in Figure 13. The calculation for initial freezing temperature, $T_{if,K}$, is given by Equation 12 using techniques from Cleland (2019). Table 1 identifies the nomenclature used here and typical values.

$$\frac{1}{T_{if,K}} = \frac{1}{273.15} - \frac{R}{M_w - L_w} \ln \left(\frac{\frac{x_{tw} - x_{bw}}{M_w}}{\frac{x_{tw} - x_{bw}}{M_w} - \frac{x_j}{M_j}} \right) \quad (12)$$

Subsequent properties use the initial freezing temperature and the real time continuously decreasing product temperature to calculate an ice fraction (shown in Eq. 13) that is used to derive properties within the transition region between liquid and solid water content. The initial freezing temperature is used in calculating an ice fraction, which is zero above this temperature, then increases as the temperature of the

product decreases. The ice fraction is limited by the original proportion of water in the food. The calculation of ice fraction, x_{ice} , was shown by Miles (1997), Chen (1985), and Cleland (2019) for foods with low concentrations of solutes; this calculation is given by Equation 13:

$$x_{ice} = (x_{tw} - x_{bw}) \left(1 - \frac{T_{if}}{T}\right) \quad (13)$$

Using the calculated fraction of ice, water, carbohydrates, and fat, thermal conductivity is calculated using the Effective Medium Theory (EMT) because it is a Class IV (i.e., frozen, porous) food according to Carson (2016). Recall the classes of food discussed previously in Section 1.1.4. This conductivity calculation is given by Equation 14:

$$k_{IV} = (3Void_f - 1)k_{air} + (3(1 - V_{air}) - 1)k_{II} + \frac{\sqrt{((3V_{air} - 1)k_{air} + (3(1 - V_{air}) - 1)k_{II})^2 + 8k_{II}k_{air}}}{4} \quad (14)$$

The conductivity k_{IV} shown in Eq. 14 is a function of k_{II} , which must be determined using Levy's model (Levy, 1981). Levy's model combines the individual constituents of the food product, including ice and water, as if they were dispersed uniformly within the food model according to a well-known Maxwell-Eucken model (Cleland, 2019). For many homogeneous foods, this appears to be an adequate assumption. The calculation for Levy's conductivity is begun in Eq. 15.

$$k_{II} = k_{ice} \left(\frac{2 k_{ice} + k_l - 2(k_{ice} - k_l) F}{2 k_{ice} + k_l + (k_{ice} - k_l) F} \right) \quad (15)$$

Levy's model has two additional terms, F and G . F is determined by Equation 16:

$$F = \frac{\frac{2}{G} - 1 + 2(1 - V_{ice}) - \left(\sqrt{\left(\frac{2}{G} - 1 + 2(1 - V_{ice}) \right)^2 - 8 \left(\frac{1 - V_{ice}}{G} \right)} \right)}{2} \quad (16)$$

G is shown in Equation 17:

$$G = \frac{(k_{ice} - k_I)^2}{(k_{ice} - k_I)^2 + k_{ice} \left(\frac{k_I}{2}\right)} \quad (17)$$

Lastly, k_{II} (from Equation 15) and G are both functions of k_I , a conductivity term that is calculated using the Parallel model shown by Carson (2016). The calculation for k_I is shown in Equation 18:

$$k_I = \frac{k_w V_w + k_f V_{fat} + k_c V_c}{1 - V_{ice}} \quad (18)$$

In this research, the temperature of the freezing product varies as a function of time; therefore, few of the properties shown above are truly constant during the product's dwell time in the spiral freezer. Equations 11-18 establish temperature-dependent functions for thermal properties of the product that are called by the algorithm to solve the system of equations for the 1-D finite difference product thermal model. Table 1 at the beginning of Chapter 1 shows the values of the variables and a description of the nomenclature used for the frozen dough product at $T = -10^\circ\text{C}$ (14°F).

A constant density of 533.8 kg/m^3 (33.32 lbm/ft^3) was used, which was calculated directly from the measured mass and volume of the specific dough product. This calculated density agreed closely with a composite temperature-dependent model constructed using methods from Cleland (2019). The density calculated using the composite method was also discontinuous, and this adversely affected numerical stability because it led to a loss of mass discovered by running an energy balance verification on the numerical model. Also, the discontinuous temperature-dependent density showed little change throughout the operating range; therefore, a constant value was safely assumed. Additionally, using constant density allowed for faster computational performance, allowing many simulations in a smaller amount of time.

2.2.2 *Selectable Food Types*

To better understand the thermal behavior of different products with different geometries and the implications of these attributes in the freezing process, other numerical food product models were developed. One of these models focused on a one-dimensional (1-D) spherical geometry, representing common food items such as chicken drumsticks and wings. The 1-D spherical model complements the existing 1-D plane wall model, providing insights into how geometry influences heat transfer during freezing. The 1-D spherical model was designed using a node-based approach, where the geometry was discretized into concentric rings surrounding a central node. Each ring represented a successive layer of the sphere, with its temperature governed by the heat conduction equation and boundary conditions applied to the outermost layer. The numerical method solved the transient heat conduction equations iteratively, tracking temperature changes at each node over time.

Temperature-dependent thermal properties were incorporated, allowing the model to account for variations in conductivity and heat capacity as the product cooled. The spherical model was systematically compared to the previously developed 1-D plane wall model to assess the influence of geometry on cooling curves and temperature variations. This comparison was useful in identifying geometry-specific thermal behaviors that could be leveraged to optimize freezing strategies. Understanding these differences allows for the strategic exploitation of distinct cooling patterns, such as those observed in "crust freezing," where only the product's surface freezes while the core remains unfrozen. Insights from these geometry-dependent behaviors also open opportunities for implementing energy-saving strategies tailored to specific product geometries.

In addition to geometry variations, additional food thermal property models were developed, including one that simulates chicken breast meat. This model, activated through a configurable flag in the MATLAB ODE code, accounts for the significantly different fat, carbohydrates, and moisture content of

chicken compared to other products such as pizza dough. These compositional differences produced distinct cooling behaviors under identical conditions that will be further elaborated upon in Chapter 3.

2.3 Performance Factors

2.3.1 Optimization for Belt Speed

The conveyor belt speed within a dynamic freezing system is a critical parameter in balancing freezing time and energy efficiency while being held to a constraint metric such as a required product exit temperature. CFD-predicted velocity is used as an input to the product thermal model to estimate the transient temperature response of the product as it progresses through the spiral and for evaluating overall freezing time and temperature. A lower than desired freezing temperature allows the speed of the spiral belt to be increased, which in turn increases product throughput while achieving target temperature. Figure 14 illustrates this behavior. If the desired output temperature of the product is -12°C (10°F), increasing the belt speed will result in products leaving the freezer in a warmer state. Slowing the belt down will result in the product exiting cooler and more closely approaching the freezer temperature.

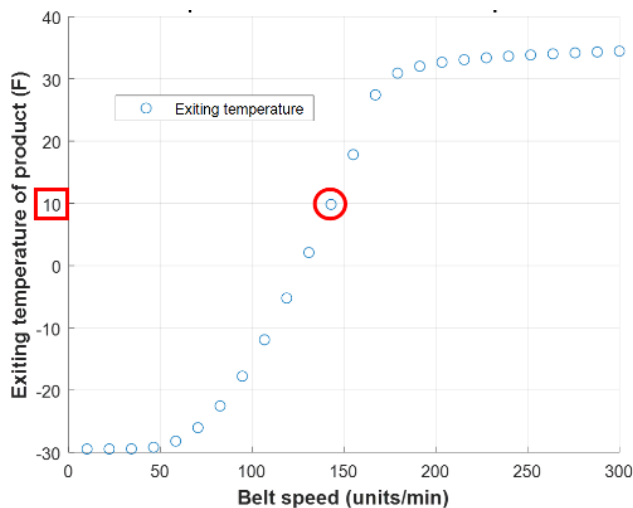


Figure 14: The exiting temperature of the product as a function of belt speed.

Figure 14 shows that decreasing the belt speed to 50 units/min or slower results in the exiting temperature of the product approaching the -30°F air supply temperature. If the belt speed is increased above 150 units/min (in this specific case), the exiting temperature of the product corresponds to the initial freezing point of the product (approximately 32°F). In between these two extremes, the exiting temperature of the product can be quite sensitive to the belt speed, as the water contained in the product is mostly in a single-phase state.

The belt speed in a spiral freezing system is used as an independent variable that can be adjusted; the manufacturing plant changes this belt speed using a variable speed drive to maximize the throughput of the blast freezer while still achieving the desired temperature of the product exiting. The MATLAB optimization function `fminsearchcon`, a minimization routine that allows constraints, was used to automate this process of choosing the maximum belt speed that causes the product to leave in a completely frozen state (D'Errico 2022, Suresh 2021).

In this way, a given velocity profile can be imposed on the 1-D model which then automatically adjusts the belt speed as an independent variable to minimize the temperature difference between the maximum (center) temperature in the product and the desired leaving temperature of the product (i.e., the temperature considered to be completely frozen). Once “favorable” air velocity profiles over the product are better understood, modifications to the air flow patterns within a spiral freezer can be pursued to improve freezing performance of the system.

2.3.2 Air Velocity Over Product

Air velocity over the product is a critical factor influencing the performance of spiral freezers, as it directly impacts the heat transfer coefficient, which governs the rate of heat removal from the product. Key characteristics such as velocity magnitude, direction, and temporal variations play vital roles in determining freezing efficiency, uniformity, and energy consumption. Higher air velocities enhance heat

transfer, leading to faster freezing times that can preserve product quality by minimizing the size of ice crystal formations and maintaining desirable texture. However, the primary energy required to generate increased air velocities grows cubically, creating a need to balance freezing efficiency against rising operational costs. Beyond a certain point, the marginal benefits of higher air velocity are outweighed by the additional energy expenditure, necessitating careful optimization for each application. In addition, freezing systems operate with an upper constraint on air velocity to avoid dislodging product from the conveyor belt that can lead to belt jams or other product (e.g. pizza topping) losses leading to diminished production yields.

The direction of airflow also significantly affects freezing performance. As products move through the spiral freezer on the conveyor belt, they encounter airflow from multiple directions due to the freezer's geometry, including the center drum of the spiral, support structures, and internal baffles. Well-directed airflow ensures the product experiences uniform exposure to cold air, reducing temperature gradients and minimizing uneven freezing. Conversely, misdirected airflow can lead to inefficiencies such as short-circuiting, where cold air bypasses the product, or dead zones, areas with low airflow velocity that result in inconsistent freezing and decreased refrigeration system performance.

Temporal variations in air velocity further influence freezing dynamics. Products experience fluctuations in airflow intensity depending on their position relative to fans and bulk airflow distribution patterns. For instance, products nearer to fans may experience higher velocities than those farther downstream. The interaction between the product's trajectory and the spatial distribution of coldest air significantly impacts freezing performance. Timing and location of exposure to peak velocities and temperatures can create localized enhancement or degradation in heat transfer. This dynamic interaction was systematically studied and will be discussed in Chapter 3 with surprising conclusions.

2.3.3 *Air Temperature Over Product*

Maintaining consistent air temperature is essential for achieving uniform freezing in spiral freezers. Spatial temperature gradients can be minimized through optimized airflow strategies and high air exchange rates, but reducing the average air temperature to accelerate freezing often increases energy consumption, as refrigeration systems must work harder to maintain lower suction pressures. This necessitates a balance between operational efficiency and cost. In practice, air temperatures in spiral freezers typically range from -40°C (-40°F) to -20°C (4°F), depending on the product type and desired freezing time. However, achieving uniform low temperatures throughout the freezer is challenging due to factors such as equipment design, airflow patterns, and variable product loading. These factors can create spatial temperature variations that lead to uneven freezing and require robust airflow control and temperature monitoring systems to address.

Operational dynamics introduce additional complexities to maintaining uniform air temperatures. Sequential defrosting of evaporator coils, where individual coils are heated and isolated with dampers, can create localized hotspots, disrupting temperature consistency. The "chimney effect," wherein warm air rises rapidly within the freezer, exacerbates vertical temperature stratification, further complicating uniform freezing. Moreover, the entry zone of the spiral freezer often exhibits localized higher temperatures and increased humidity due to infiltration of plant air into the freezing system and product loading, which can disrupt freezing efficiency and product uniformity. Addressing these challenges requires a comprehensive, holistic approach to airflow management and temperature regulation to maintain desired thermal conditions throughout the freezer.

The temperature difference between the product's surface and the surrounding air (ΔT) is the driving force for convective heat transfer. As the product cools, ΔT decreases, reducing the rate of heat removal from the product. Strategies such as increasing air velocity near the freezer exit could counteract this

effect, though it remains uncertain whether this strategy is more effective than pursuing velocity increases at the freezer's entrance, where ΔT is initially highest; this was studied and is addressed in Chapter 3. Maintaining consistent ΔT across each product being conveyed through a freezing system is crucial for consistent freezing and process output, reducing variability in freezing times and avoiding issues such as partial or over-freezing, which can compromise product quality. In production environments, sample products are typically periodically tested throughout operating shifts upon exiting the freezer to ensure their internal temperatures meet specified ranges. A low variance in this temperature data is essential for optimal freezer performance and product quality.

Lower air temperatures result in faster freezing by increasing ΔT , preserving product quality by minimizing ice crystal growth and maintaining desirable texture and appearance, which is explained in more detail by Kolbe and Kramer (2007) and Wu (et al., 2021). Additionally, products frozen more rapidly lose less intercellular moisture upon thawing, further enhancing quality. Conversely, slower freezing caused by a smaller ΔT leads to larger ice crystal formation, which negatively impacts structural integrity, causing soggy and significant water loss upon thawing. Optimizing air temperature is therefore critical to balancing freezing performance, energy efficiency, and product quality.

2.3.4 Belt Material

The 1-D thermal model used in this research assumes the same heat transfer coefficient on both the top and bottom surfaces of the product, a simplification that streamlines the analysis while maintaining sufficient accuracy for most applications. In practice, however, the bottom of the food product rests on the conveyor belt, introducing additional thermal resistance factors influenced by the belt material, the open area of the belt, the airflow around the belt and within its cavities, and the type of product being frozen. Modeling this complex thermal resistance network would require numerous assumptions, many of them nearly arbitrary, making the analysis unnecessarily cumbersome and potentially less reliable.

Additionally, the majority of this research is comparative in nature, rendering the influence of belt material inconsequential, because it does not change between iterations, and altering it in practice would involve substantial logistical challenges. Instead of attempting to model all of the complex thermal interactions of the product on the belt, a heat flux sensor was employed in the experimental setup that will be described in Section 2.6. This sensor was mounted on the underside of a simulated product to directly measure the heat flow through the bottom surface. These measurements were then compared to the heat transfer occurring on the top surface, driven exclusively by forced convection.

The material of the conveyor belt in a spiral blast freezer has an influence on both heat transfer and product quality. The two most common materials for conveyor belts in low temperature dynamic freezing systems are stainless steel and food grade plastic. Stainless steel belts, known for their comparatively higher thermal conductivity, facilitate rapid and efficient heat transfer between the product and the freezing environment. This leads to faster freezing times and improved cooling efficiency, which are advantageous in high-throughput industrial settings. However, the open weave design of stainless steel belts, while enhancing airflow, can create surface imprints on softer unpackaged products like dough due to increased contact pressure. These imprints may compromise the aesthetic appeal of certain products, making stainless steel less suitable for applications where visual presentation on the bottom side of a product is critical. Additionally, stainless steel belts are generally significantly more expensive than their plastic counterparts, increasing initial capital and replacement costs.

Plastic conveyor belts on the other hand have lower thermal conductivity, which slows heat transfer and extends freezing times. Despite this limitation, their smoother and less open surface minimizes surface imprints on soft or delicate products, preserving their appearance and structural integrity. Plastic belts are also lighter than stainless steel, which reduces drive belt motor power, maintenance requirements, and operational downtime. Moreover, they are easier to remove and replace in large

sections, a valuable advantage in cases of operational issues, such as if a belt slips or is damaged during production. While plastic belts may lack the thermal efficiency of stainless steel, their ability to handle products without deformation makes them ideal for applications where surface quality takes precedence over rapid freezing. One other consideration is that plastic belts are flammable, with melted remains that are more difficult to clean up in the event of a fire, as compared to stainless steel belts. The selection of belt material ultimately depends on the specific requirements of the application, balancing heat transfer performance, aesthetic product preservation, and cost considerations.

The measurements on various belts in this research including stainless steel belts and plastic (Blue Acetal Intralox 2600 series) were conducted in an operational spiral freezer to provide practical insights into the comparative performance of the two materials. The findings from this analysis will offer a data-driven basis for evaluating the trade-offs between these conveyor belt materials and will be further detailed in Chapter 3.

2.4 Identifying Ideal Velocity Profiles

As noted in Section 2.3.2 the velocity of air over the product has a direct influence on the external heat transfer coefficient thermally coupling the freezer environment to the process of heat removal from product. It has also been noted that the velocity field throughout a dynamic freezing system is varied and field measurements on different freezing systems show quite a range of velocity fields. The underlying question that needs to be answered is *what is a desirable velocity field to maximize freezing performance while balancing power demands for fan operation?* Increased fan power to achieve higher velocities brings a direct increase in the power to operate the fans (cubic relationship) and that increased fan power leads to an increased parasitic thermal load within the freezing system. In the sections that follow, an analysis of the effects of time-varying velocity profiles during the freezing process is conducted. Velocity

profiles that optimize overall freezing performance are identified and serve as landmarks for designers of freezing systems to target to improve the performance of both existing freezing systems in operation and planning for next generation of freezing systems. Unfortunately, optimizing the performance of a dynamic freezing system does not rely solely on single air velocity but on time-varying velocities over the product as well as other environmental factors such as air temperature.

Monte Carlo simulations are used as a means of exploring the solution space in search for optimal performance. To ensure the simulations are robust, randomization is used as a strategy to minimize the likelihood of becoming “stuck” in regions with local minima.

2.4.1 Randomization

Randomization was a critical component of this research, enabling the effective use of computational resources to explore a broad range of not only potential solutions but solutions that support optimal operation. Randomized initial values were incorporated into optimization algorithms to avoid convergence to local minima and improve solution robustness. This approach was particularly crucial for determining optimal airflow profiles and belt speeds within models constrained by non-linear dynamics. By introducing randomness into initial parameter guesses, such as time-varying air velocity profiles, the methodology minimized the risk of overlooking global maxima and ensured a comprehensive search of the solution space. Additionally, randomized adjustments in airflow configurations allowed for systematic evaluation of diverse scenarios without bias from predefined assumptions, providing valuable insights into configurations that enhance performance.

The MATLAB ODE code, described in Section 2.1.1, was engineered with exceptional robustness, capable of handling significant variations in input parameters without system failures and crashes. This resilience was vital for automating the testing of thousands of permutations, enabling the algorithms to efficiently navigate diverse parameter sets without manual intervention. This automated approach

increased productivity by more than 100 times, eliminating the need for labor-intensive manual iteration and significantly accelerated the exploration of parameter spaces. Randomization not only facilitated this computational efficiency, but also yielded insights that would have been unattainable through deterministic methods, ultimately contributing to the development of more effective and reliable optimization strategies.

2.4.2 Monte Carlo Simulations

Monte Carlo simulations were employed, both explicitly and implicitly, to explore variability in freezer performance and optimize operational parameters. Historically, transient simulations of food models as intricate as the one detailed in Section 2.1.1 would have required significantly more computational time; however, advancements in computational efficiency and power allowed the simulations in this research, even with a larger 1-D product model node count of 80, to be completed within seconds. Monte Carlo techniques were utilized to generate extensive datasets of potential air velocity profiles within the spiral freezer. These profiles were evaluated to identify those delivering the highest performance, with shared traits among the top-performing profiles analyzed and subsequently targeted as initial conditions for subsequent optimization algorithms, which further refined them. The results of the Monte Carlo simulations were visualized using Pareto fronts, which displayed the limits of performance and helped catalog velocity features that were advantageous to optimal spiral freezer performance.

Other Monte Carlo simulations incorporated variations in air velocity, belt speed, and temperature to generate a complete range of the solution space showing the tradeoffs and limits of these factors. The resulting Pareto fronts not only highlighted optimal solutions but also provided actionable insights into areas where performance improvements could be achieved and operational adjustments made. This approach ensured a data-driven basis for optimizing freezer operations.

2.4.3 Optimization

Optimization techniques play a pivotal role in enhancing the modeling and performance of blast freezers by systematically refining critical parameters to achieve objectives such as reduced freezing times and improved energy efficiency. Even fundamental field adjustments, such as changing the belt speed to achieve a target product temperature, can be considered a basic form of optimization. As described in detail in Section 2.3.1, optimization was initially employed to determine the belt speed required to achieve a specified center temperature for the food product. Additionally, optimization was employed to refine polynomial curves that were used to represent time-varying velocity profiles, with the aim of maximizing belt speed, and thus product throughput, within specified constraints. These constraints typically included upper and lower velocity bounds and an average velocity limit for the entire profile. This approach inherently penalized profiles with extremely large velocity peaks, as such peaks consume a disproportionate share of the average velocity allowance and exhibit diminishing returns in heat transfer efficiency, as demonstrated in Equation 9.

Programmatic optimization methods were utilized to refine both belt speeds and airflow profiles. By iteratively adjusting these parameters, the model identified configurations that optimized freezing performance while balancing rapid freezing with energy conservation. This systematic approach enabled the development of efficient, data-driven solutions to improve freezer throughput and operational effectiveness. The results of this will be shown in Section 2.4.

2.5 CFD Setup and Assumptions

2.5.1 Simplifications

The dynamic freezing systems used in food production facilities today are quite large, on the order of 283 m³ (10,000 ft³) or more of internal volume. In addition, blast freezing systems have a number of internal physical elements at considerably smaller length scales such as belt openings that are on the order

of tens of millimeters or the spaces between finned surfaces on evaporator coils on the order of millimeters. The excessively large computational domain couple with small feature details creates a challenge in creating a three-dimensional mesh that can be solved in a reasonable time.

These realities require simplifications in computational fluid dynamics (CFD) to effectively and efficiently model the complex geometry while properly capturing the airflow dynamics. To capture the essential physics of airflow and heat transfer without excessive computational demands, several key simplifications were employed in the CFD models developed. The evaporator coils and spiral conveyor belt, which have intricate geometries, were modeled as porous media. This approach eliminated the need for fine mesh resolution to detail every physical feature, such as the flow passages within the coils or belt. Instead, the hydraulic resistance of these components was approximated and calibrated using empirical data from actual operating spiral freezing systems, allowing for an accurate representation of bulk airflow with a significantly reduced computational load.

A global grid size was selected to balance accuracy and computational efficiency. Areas of particular interest, such as regions near fans or product surfaces, were refined with smaller mesh sizes and inflation layers to ensure critical details were resolved without requiring a uniformly fine grid throughout the computational domain representing the freezer. This hierarchical meshing approach minimized computational costs while preserving accuracy in areas with quickly changing airflow. Mesh convergence studies were performed to validate that as the mesh was refined more, the CFD solution converged. One such study is shown in Figure 15, where the starting mesh size is reduced from 0.4 m (16") to less than 0.05 m (2"). The velocity modeled at the refrigeration coils and along the spiral freezer clearly converge to stable conditions as this mesh size is reduced, indicating that the CFD model is stable. Simulations also assumed steady-state or time-averaged airflow conditions, simplifying transient airflow behavior. While

these dynamic changes are important, they were either excluded or addressed separately in smaller-scale studies to prioritize the assessment of long-term freezer operational performance.

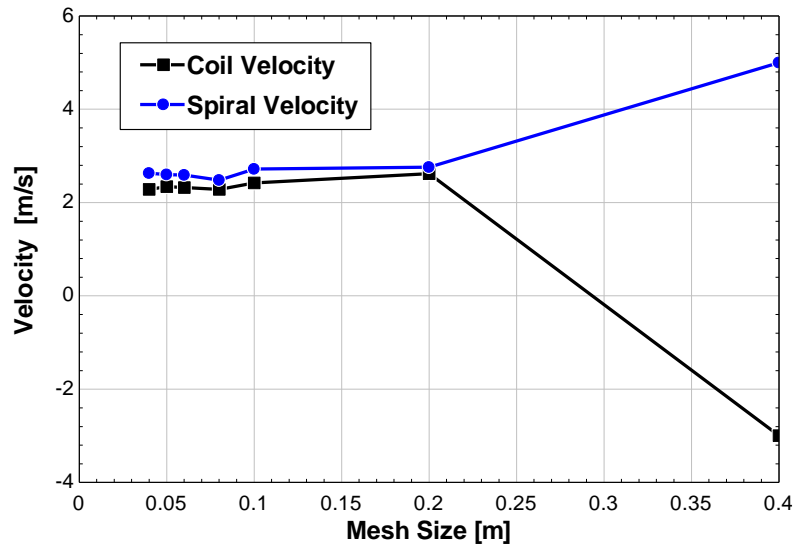


Figure 15: Mesh study done in ANSYS Fluent to test convergence of CFD model.

To model the airflow generated by the fans, detailed mechanics of the fan blades themselves were bypassed by incorporating fan performance curves directly as boundary conditions. This ensured realistic airflow rates and pressure drops without needing to simulate the internal mechanics of the fans. The fan curves were taken directly from the fan manufacturer’s product literature using the serial numbers of actual fans deployed in a real operating spiral freezer.

Advanced wall treatments were utilized in the CFD modeling to refine the mesh at critical areas, including physical structures near fans, walls, and other object surfaces such as baffles, ensuring accurate capture of boundary layer effects. The y^+ value, a dimensionless parameter representing the distance of the first computational cell from the wall normalized by local flow conditions, was carefully considered in mesh refinement and defining inflation layers. This parameter is important for the accuracy and validity of wall-bounded flow simulations, particularly in scenarios involving significant turbulence, such as

airflow studies within spiral freezers. Striking a balance between computational cost and simulation accuracy was sought. For large-scale systems like spiral freezers, maintaining y^+ less than one with a highly refined mesh was determined to be computationally prohibitive. Instead, a practical approach was adopted, employing coarser meshes with wall functions to achieve moderate y^+ values, generally below 300, while ensuring the chosen turbulence model and flow regime supported this approximation. Through iterative mesh refinement during CFD testing, it was found that significant improvements in airflow dynamics within the spiral freezer could be observed without the need for exhaustive refinement of wall treatments. This approach enabled efficient yet reliable simulations, capturing essential airflow behaviors while maintaining manageable computational demands.

These simplifications allowed the CFD models to effectively capture airflow patterns and velocity distributions within the spiral freezer without overwhelming computational resources. While trade-offs in detail were necessary, validation against experimental data and surrogate models ensured that the simulations remained both accurate and reliable for engineering analysis.

2.5.2 *Porous Media*

In the CFD model of the spiral freezer, porous media were used to represent the conveyor belts and evaporator coils, simplifying their intricate geometries while capturing their effects on bulk airflow. This approach avoided the need for a fine mesh to resolve the physical details of each coil or belt opening, significantly reducing computational demand. To accurately replicate the airflow dynamics, anisotropic flow resistances were assigned to the porous media parameters, reflecting the directional dependence of airflow through these components. Specifically, the resistance in the vertical direction was modeled to be higher than in the lateral directions, mimicking the natural tendency of air to flow more easily along the horizontal plane due to the tiers in the spiral freezer belt and passages in evaporator coils. The parameters for these resistances were calibrated and tuned using empirical data, ensuring that the porous media

accurately represented the hydraulic behavior and contributed to realistic airflow simulations in the freezer environment.

2.5.3 Point Cloud Analysis

A “point cloud” was developed in the CFD modeling of the spiral to capture discrete velocity vectors along the path trajectory of food products as they moved on the conveyor through the freezing system. The points in the cloud were carefully aligned with the actual path taken by food products in the modeled spiral freezer, which was based on physical data from an actual spiral freezing system, as shown in Figure 16. The point cloud consisted of 3,200 discrete points, each corresponding to a specific location on the conveyor belt path. It enabled the generation of a high-resolution dataset that included the air velocity magnitude and its x, y, and z components at each point of the cloud. By accurately representing the conditions encountered by food products, the point cloud provided a robust dataset that could be directly compared to experimental measurements from operational spiral freezers.

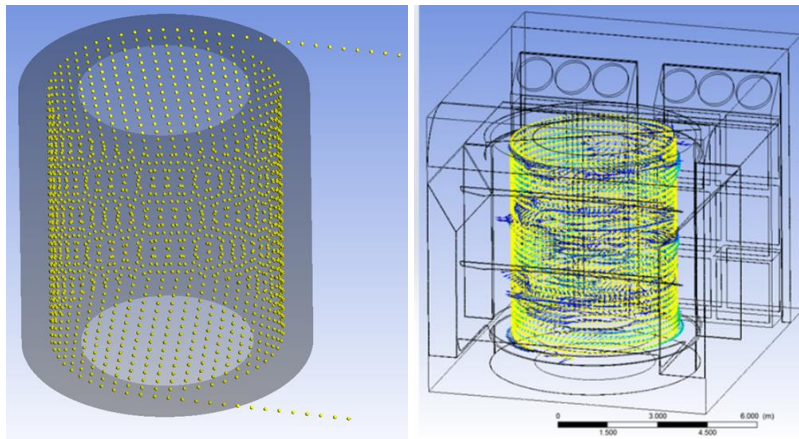


Figure 16: The point cloud used in the CFD model to track the velocity along the path a product follows in a spiral freezer.

This detailed comparison of velocity and temperature profiles derived from the point cloud against field measurements validated the CFD simulations and confirmed their accuracy and reliability. Multiple examples of the point cloud’s utility will be shown in Chapter 3.

2.6 Modeling Validation: Phantom I

To validate the thermal models and CFD predictions developed in this research, a surrogate device known as Phantom I was designed and constructed. Phantom I was engineered to replicate the physical geometry of a food product within a spiral blast freezer, providing a controlled and measurable platform for assessing in situ heat transfer dynamics and airflow interactions. This device served as a critical tool for bridging the gap between theoretical models and real-world freezer performance, enabling direct measurement of key parameters such as ambient temperature, product surface temperature, and heat flux. The following subsections detail the mechanical design and instrumentation of Phantom I, emphasizing its role in experimental validation and performance benchmarking.

2.6.1 *Mechanical Design*

A geometrically-similar surrogate device was designed to collect data on the thermal environment within a spiral blast freezer. Referred to as “Phantom I”, this instrument was engineered to accurately measure surface heat transfer coefficients and temperatures that would be experienced by actual food products being conveyed through the blast freezer. The instrument measures surface heat fluxes and temperatures on both the upper and lower surfaces while being robust enough to withstand the operational environment of an industrial freezer. Constructed from T6061-T651 aluminum, this high-conductivity metal was chosen to ensure minimal temperature gradients within the instrument as well as being durable and able to maintain its structural integrity while being conveyed side-by-side with actual products in an operational industrial spiral freezer. The Phantom I is a circular flat plate having a diameter of 11.5 inches (29 cm) and overall thickness of 5/8 inches (1.6 cm) replicating the geometry of the dough product (pizza crusts) being processed in the first freezer utilized in this project. The Phantom is comprised of two equally sized aluminum plates machined to a thickness of 5/16 inches (0.8 cm). The split plate design is needed to incorporate a heat source in the center of the surrogate product. The heat source enabled the

Phantom to maintain a measurable temperature difference between the plate's exposed surface and the local thermal environment within the spiral freezer so a non-zero heat flux would be assured throughout its movement through the freezing system. A mechanical drawing of the Phantom I is provided in Figure 17.

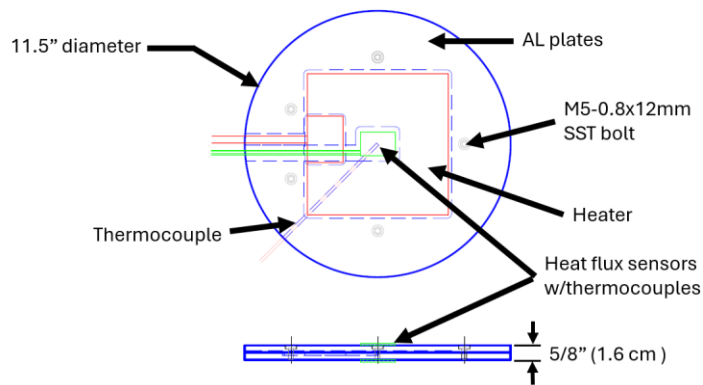


Figure 17: Mechanical drawing of the Phantom I.

The electric resistance heater sits within a machined groove between the two aluminum plates with the machined depth of the channel configured to maintain an intentional interference fit, ensuring it was compressed for optimal thermal contact. Gennel brand G107 thermal paste with a thermal conductivity of 3.17 W/m-K was applied between the heater and the plates to fill any surface irregularities and minimize contact resistance. To measure heat flux, and subsequently calculate heat transfer coefficients, a heat flux sensor was mounted on the top surface of the Phantom using HPFIX brand 30mm wide high-conductivity adhesive with a thermal conductivity of 1.5 W/m-K and 0.2 mm thickness. Another heat flux sensor was positioned in a slight recessed cavity on the bottom of the Phantom, coincident with the bottom aluminum plate to capture heat flux data on the lower surface. The recess in the bottom of the plate was necessary so the plate would lie flat on the belt. Figure 18 shows critical Phantom components.

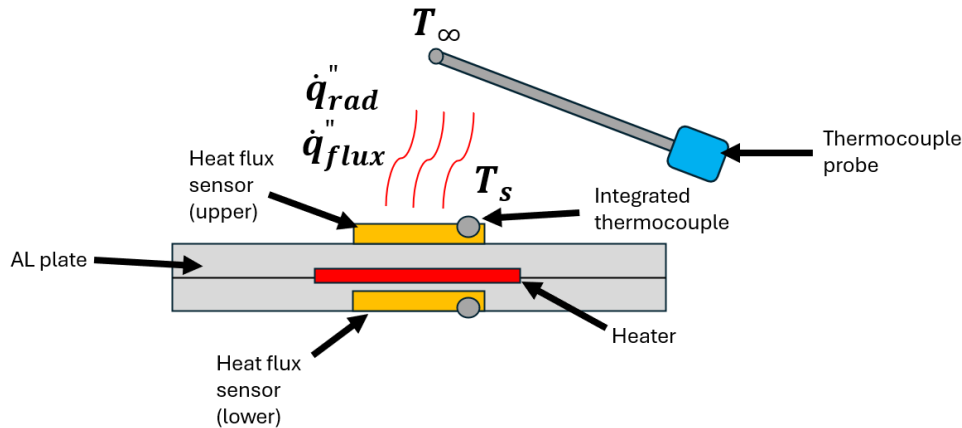


Figure 18: The Phantom I.

Several Type-T thermocouples were installed on the Phantom to monitor temperatures at critical locations, including at the top surface coincident with the heat flux sensor, at the bottom surface coincident with this heat flux sensor, within an internal cavity adjacent to the heating element, and one that captured the local air temperature within the spiral freezer. These thermocouples provided real-time data on temperature differences, enabling precise calculations of heat transfer rates. The Phantom I was also designed for structural durability, ensuring it could endure mechanical stresses typical of spiral freezer environments such as abrupt belt transitions. Compact and portable, it was designed to be easily integrated into the product path alongside actual food items. Figure 19 shows a photo of the Phantom I, with its instrumentation tote on the left and the aluminum pseudo-product on the right.

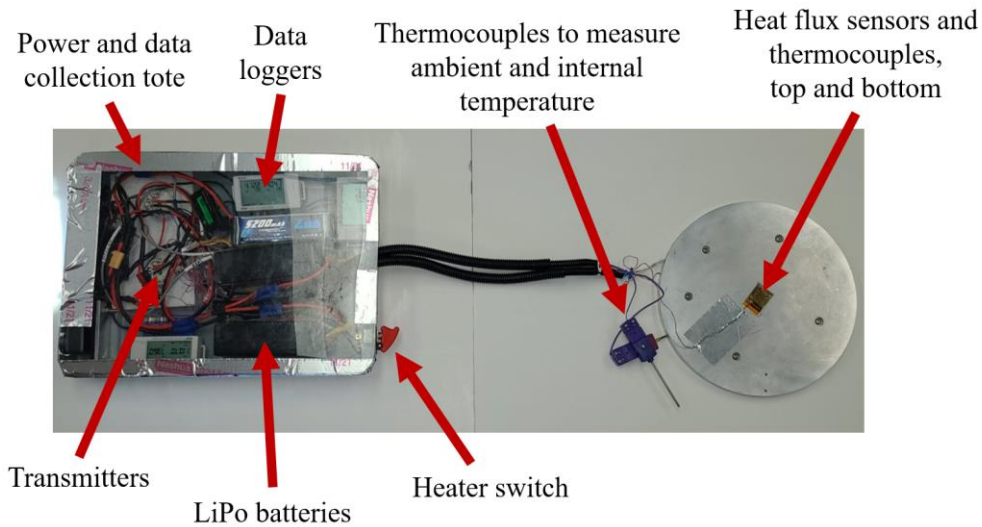


Figure 19: The Phantom I, a portable device designed to measure heat transfer coefficient and temperature inside spiral freezers.

2.6.2 Electrical Circuitry

The electrical circuitry of Phantom I was designed to enable precise measurement of the data being collected in the harsh conditions of a spiral freezer. Figure 20 shows a simplified version of the wiring diagram. The largest electrical load was the electric resistance heater already introduced in Section 2.6.1 embedded within the aluminum plates. Power to the heating element is supplied to the heater by Lithium polymer (LiPo) batteries and was indirectly measured using voltage across a calibrated shunt resistor that corresponded to amperage through the heater circuit. Furthermore, the red switch shown in Figure 19 allowed the heater power to be turned off while the batteries kept the data acquisition system continuously active, allowing a “power saving mode” when the Phantom was on standby before and after the Phantom was inside a spiral freezer. All of the major components of the Phantom are listed in

Table 2 at the end of this section.

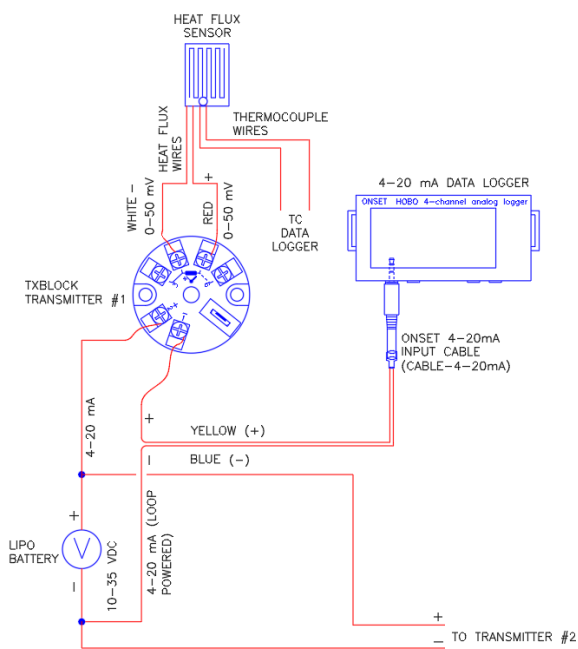


Figure 20: Phantom wiring diagram.

The heat flux sensors employed in Phantom I were FluxTeq PHFS-01 models, selected for their high accuracy and NIST traceability, shown in Figure 20. These sensors have a measurement range of ± 150 kW/m² and capable of reliably operating in temperatures ranging from -50°C (-58°F) to 120°C (248°F). The sensors output a millivolt signal proportional to the instantaneous heat flux through the sensor which is equal to the heat flux at the coincident surface of the aluminum plate. The output signals from the heat flux sensors were converted to a 4-20 mA signal using loop-powered TxBlock-USB transmitters, which ensured data fidelity during logging. The transmitters were designed to operate within a broad power range (10-35 V DC), allowing them to handle potential voltage drops from battery power sources in the low-temperature environment.

Data from the heat flux sensors, heater current, and thermocouples were recorded using Hobo data loggers, providing precise, time-stamped measurements throughout the freezer cycle. These loggers enabled detailed post-process analysis, including the calculation of surface heat transfer coefficients, and the application of thermal correction factors to account for radiation effects. The entire electrical system

was powered by a compact and reliable battery pack capable of sustaining operation in extreme low-temperature conditions, ensuring uninterrupted functionality throughout the Phantom's journey in the spiral freezer. This robust electrical circuitry was integral to Phantom I's ability to deliver reliable and actionable data under demanding operational conditions.

Table 2: The mechanical and electrical details of the Phantom I.

Category	Component	Description	Specifications
Apparatus	Aluminum plate	Two T6061- T651 circular aluminum plates resembling a generic blunted "flat plate" mated into one overall plate with M6 bolts	11.5" diameter, overall thickness: 1.6 cm (5/8"), grooved to accept heater element with interference fit
Apparatus	Heater	Silicone rubber coated heater embedded in the aluminum plate	23 cm x 23 cm (9" x 9"), 403W at 24V DC
Apparatus	Thermal adhesive (CPU tape)	Used to affix heat flux sensors to the top of the aluminum plate	Width: 30mm x 30mm, 0.2mm thick, thermal conductivity: 1.5 W/m-K
Apparatus	Thermal paste	Applied to minimize contact resistance due to dimensional variation in heater surfaces and aluminum plates	Thermal conductivity: 3.17 W/m-K
Instrumentation/sensors	Batteries	Two 4S Lipo batteries	4S, 14.8V, 5200 mAh per battery
Instrumentation/sensors	Heat flux sensors, FluxTeq model PHFS-01	NIST traceable sensors used to measure heat flux affixed to the aluminum plates, 380-micron thick thermopile coated in Kapton (polyimide)	Measurement range: ± 150 kW/m ² , accuracy: $\pm 2.5\%$ reading, -50 to 120°C operating temperature
Instrumentation/sensors	TxBLOCK-USB loop-powered temperature transmitters	Converts mV signal from heat flux sensors to a 4-20 mA signal for better data fidelity, programmable using USB	Range: 0-50 mV (scales to 4-20 mA), power supply: 10-35 V DC, accuracy: $\pm 0.1\%$, operating temperature: -40 to 85°C
Instrumentation/sensors	HOBO® UX120-006M 4-channel analog data loggers	Used to read the 4-20 mA signals from each heat flux sensor	Accuracy: ± 0.001 mA $\pm 0.2\%$ of reading
Instrumentation/sensors	HOBO® UX120-014M 4-channel thermocouple data loggers	Used to directly measure the Type-T thermocouple signals	Accuracy: $\pm 0.6^\circ\text{C} \pm$ thermocouple probe accuracy
Instrumentation/sensors	Type-T thermocouples	Used to measure temperature at the heat flux sensor and the ambient environment	Accuracy: $\pm 1^\circ\text{C}$ (2°C is used in calculations accounting for data logger, conservatively)

The sensitive electrical components were placed in a polypropylene tote and sealed with aluminum tape around a polycarbonate top plate. The tote was iteratively reduced in size throughout successive plant visits to fit the entrance of multiple spiral freezers. The final height of the Phantom was 2 inches, as shown in Figure 21.



Figure 21: The profile of the Phantom equipment tote.

2.6.3 Action Camera

An action camera integrated into the Phantom I was a vital tool for visually supplementing the thermal and airflow data collected by the sensors. A photo of the front of the Phantom that shows this camera (along with an LED light bar) is shown in Figure 22. The main purpose of the camera is that it allowed a global time to be recorded at the beginning of each run, which enabled more accurate synchronization of the Phantom data with the point cloud from the CFD analysis introduced in Section 2.5.3. The precise position of the Phantom could be determined down to the second inside the freezers using internal structures within the freezer as landmarks. In some freezers, there were belt stoppages for a period of time that influenced measured data. With the video footage, this could easily be clipped out of the data.

The camera also captured insights into operational dynamics and potential issues that are not discernible from sensor data alone. The camera documented critical moments, such as the Phantom's transitions between different conveyor belt systems, where mechanical stresses, abrupt bursts of airflow,

or mechanical obstruction could affect the freezer performance. The camera identified disruptions such as blockages or "jam-ups" caused by product congestion, as shown in Figure 23. The camera also provided visual evidence of frost accumulation on internal structural supports, where frost build-up could impede airflow and reduce heat transfer efficiency.



Figure 22: The front of the Phantom I with the action camera on the right.



Figure 23: Leftover remains of a product jam-up are shown on the left.

Figure 24 shows a screenshot of the Phantom entering a spiral freezer that had a substantial amount of frost buildup on structures within the spiral freezer. In this particular example, an unexpected use-case for the equipment tote was discovered: snowplow. The action camera observed unexpected unsanitary conditions by capturing footage of the freezer interior, which showed potential food particle buildup that missed routine deep-cleaning operations. The visual documentation provided by the camera proved invaluable for this research and provided a new perspective to what product sees inside freezers that has not been shown in any other known published works.



Figure 24: Frost buildup in a freezer captured by the Phantom’s camera on board the snowplow.

2.6.4 *Phantom equations*

The millivolt signal produced by the heat flux sensors is converted to a 4-20 mA signal using loop-powered transmitters. The 4-20 mA signal, commonly used in industrial controls, showed higher data fidelity using the portable loggers employed for collection when compared to attempts to directly measure and amplify the mV signal. Also, small battery-powered portable devices that can measure 4-20 mA signals are readily available but small mV signal measuring devices are typically constrained to thermocouple signals. Dedicated devices for measuring generic mV signals are often physically large and need to be plugged in. Portability is a consideration here based on the subsequent planned use of this instrument in an actual dynamic air blast freezing system.

The signal transmitters used in this experiment are versatile in that they can utilize a relatively broad power supply ranging from 10-35 V DC with no loss in accuracy, which is especially critical because they are often powered with an external battery that experiences a voltage decrease during operation in a freezer as the battery discharges in the harsh low ambient temperature environment. Thermocouple data loggers were used to directly measure the Type-T thermocouple signals. All the data loggers shared the same time stamp during initialization so that collected data could be synchronized to the nearest second, and synchronized to the action camera introduced in Section 2.6.3.

The equation to convert 4-20 mA milliAmps to 0-50 milliVolt is shown:

$$mV = \left(\frac{mA - 4}{16} \right) 50 \quad (19)$$

The calibration method by the heat flux sensor manufacturer produces an equation that is a function of the calibration sensitivity S_{calib} and the surface temperature T_s for each sensor. This sensitivity varied from 0.00125 to 0.00134 mV/(W/m²) for all the flux sensors used. Equation 20 produces the overall sensitivity coefficient S :

$$S = (0.00334 T_s + 0.917) S_{calib} \quad (20)$$

A correction factor (\dot{q}_{rad}'') was applied to remove radiation from the measured surface heat flux, isolating the heat transfer that is due to convection. The radiation correction resistance term (R_{rad}) is calculated in Equation 21, taken from Nellis and Klein (2009):

$$R_{rad} = \frac{1}{A\varepsilon\sigma(T_s^2 + T_\infty^2)(T_s + T_\infty)} \quad (21)$$

where A is the overall surface area of the plate, ε is the estimated emissivity of aluminum, and σ is the Stefan-Boltzmann constant of 5.67×10^{-8} W/m²-K⁴. A handheld infrared thermometer was used to

measure the emissivity of the aluminum which was found to be approximately 0.1. Equation 22 shows the application of this radiation resistance in deriving a simple radiation correction factor \dot{q}_{rad}'' :

$$\dot{q}_{rad}'' = \frac{T_s - T_\infty}{R_{rad} A} \quad (22)$$

The heat flux \dot{q}_{flux}'' for each sensor in W/m² is then calculated using Equation 23, with \dot{q}_{meas}'' shown as the uncorrected measured heat flux and the radiation correction factor \dot{q}_{rad}'' subtracted:

$$\dot{q}_{flux}'' = \dot{q}_{meas}'' - \dot{q}_{rad}'' \quad (23)$$

The last step is to use Newton's law of cooling to calculate the local heat transfer coefficient shown in Equation 24:

$$h = \frac{\dot{q}_{flux}''}{T_s - T_\infty} \quad (24)$$

Table 1 at the beginning of Chapter 1 shows a summary of the variables and their descriptions from Equations 19-24, along with typical values for each as a reference.

2.7 Phantom II

The Phantom II was developed to examine how airflow angle impacts the measured heat transfer coefficient, a key parameter in freezing processes. While previous studies assumed horizontal airflow over a flat plate, real-world spiral freezers feature multidirectional airflow due to fan currents, conveyor geometry, and product placement. These deviations raised questions about the accuracy of traditional convection correlations.

To address this, Phantom II's square geometry was designed to better represent the flat plate configuration used in convection studies. Granted, the edge of the Phantom II is blunted, therefore it more

resembles the theoretical studies shown in Section 1.2.2. This setup allows controlled testing of angular airflow variations, providing insights into real-world heat transfer dynamics.

2.7.1 Horizontal Flow Assumptions

The Phantom II was developed to address uncertainties surrounding the impact of airflow “impingement” angle on the surface-measured heat transfer coefficient, a critical parameter in the freezing process. Existing literature and previous experiments with the round Phantom I are based on the assumption of predominantly horizontal airflow across a flat plate. However, in real-world spiral freezers, airflow is often multidirectional due to the complex interplay of fan-generated air currents, conveyor belt geometry, physical structures within the spiral, and product placement. Airflow impacts the product surface at a certain velocity magnitude and angular direction. The discrepancy observed between theoretical models and operational conditions raised questions about the validity of only using horizontal airflow assumptions to model heat transfer accurately. The goal of Phantom II was to create a platform for exploring how angular deviations in airflow affect convective heat transfer once this angle is added experimentally.

2.7.2 Phantom II Design

The design of the Phantom II represents a change from its predecessor, featuring square aluminum plates instead of round ones. The details and dimensions are shown in Figure 25. This modification was implemented to better replicate the geometric conditions of flat plate heat transfer as described in theoretical and empirical studies. However, the edges of the plate are blunt, rather than thin, which makes it more like a food product than an infinitesimally-thin plate. Three heat flux sensors were along the length of developing flow on the top side to ascertain differences in heat transfer coefficient depending on the length measurements were taken from the leading edge. The initial version of the Phantom II had three heat flux sensors on its bottom as well, but were removed in later stages once it was placed in actual

operating spiral freezers. Constructed from high thermal conductivity T6061-T651 aluminum, the Phantom II retains the robust thermal and mechanical properties required to endure experimental conditions, including controlled airflow exceeding 10 m/s (2000 feet/min) in wind tunnels. Its design also includes an embedded heater, and thermocouples at strategic locations, providing high-resolution measurements of heat transfer and temperature gradients across the plate's surface. Most of the equipment, including the sensors, are the same as Phantom I, and the data acquisition and equations required to obtain heat transfer coefficient are the same as those presented in Section 2.6.4.

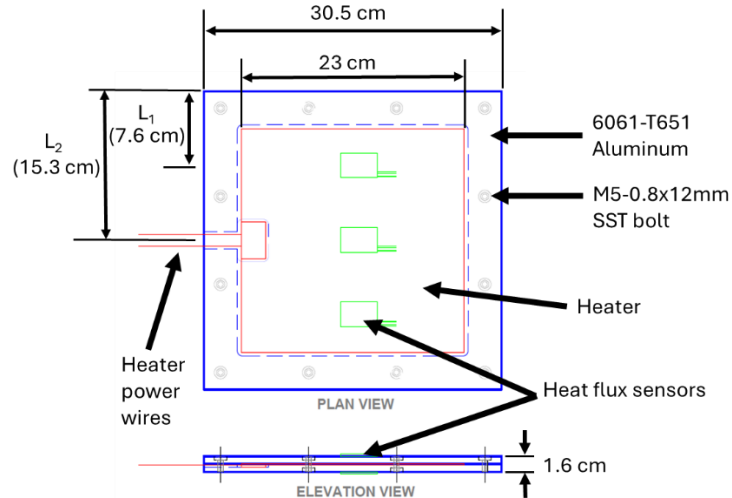


Figure 25: The Phantom II design.

2.7.3 Wind Tunnel Experimental Setup

To investigate the effects of airflow angle on heat transfer, an adjustable testing frame was constructed from welded galvanized steel Unistrut, with a fixture to securely hold the Phantom II by its edges using stainless steel hardware. The prototype version of this apparatus is shown in Figure 26, using the round Phantom I for initial tests.

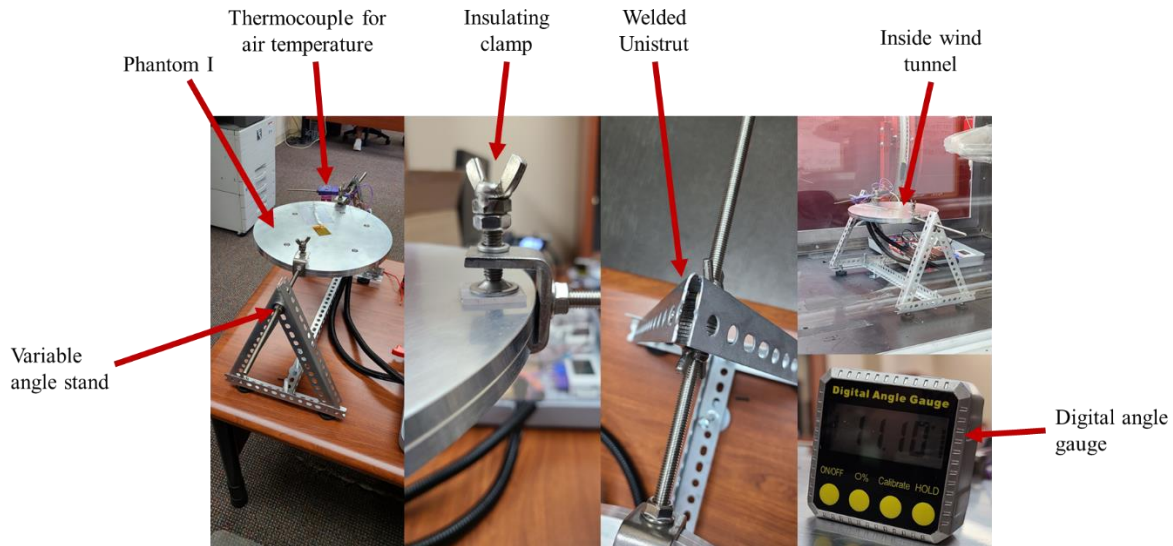


Figure 26: The Phantom wind tunnel angle testing stand.

The Phantom II setup within a wind tunnel was designed to allow precise control of both airflow angle and velocity relative to the Phantom's surface, with airflow through the wind tunnel's test section generated by a variable frequency-driven fan. Air velocity and temperature were monitored and recorded at one-second intervals for subsequent post-processing. The square geometry of Phantom II ensured uniform exposure to airflow across its surface, enabling detailed analysis of angular variations. This controlled experimental environment provided critical insights into the influence of airflow direction on convective heat transfer, addressing gaps between theoretical models and the complex dynamics encountered in operational spiral freezers that will be presented in Chapter 3.

2.7.4 *Velocity at an Angle Initial Experiment*

Initial experiments with the Phantom II were conducted to measure the leeward and downwind surface heat transfer coefficients under varying airflow angles, offering a preliminary understanding of if and how angular deviations impact convective heat transfer. By systematically adjusting the airflow angle by tilting the Phantom within the wind tunnel, detailed data were captured, as shown in Figure 27, which

presents the average heat transfer coefficient recorded by all three sensors on the top side of the plate. The results revealed that non-horizontal airflow introduced substantial variations in heat transfer, underscoring the limitations of the traditional uniform horizontal airflow assumption commonly used in freezer modeling. These findings provided valuable new insights into the influence of airflow direction on thermal performance, offering a more nuanced understanding relevant to freezer applications.

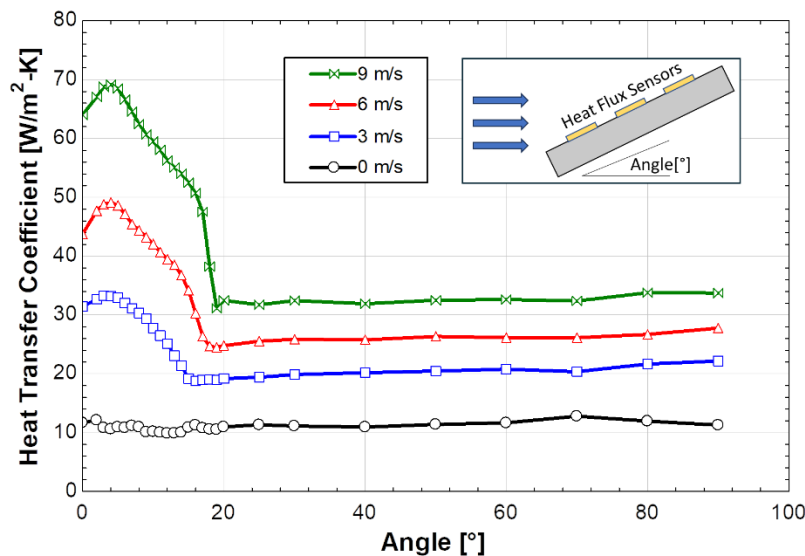


Figure 27: Initial wind tunnel tests showing heat transfer coefficient as a function of angle.

2.7.5 Dimensionless Results

Dimensionless Nusselt number and Reynolds numbers were calculated using the heat transfer coefficient data from the wind tunnel. The Nusselt number is derived using the heat transfer coefficient, characteristic length L , and the thermal conductivity k of air over the plate, shown in Equation 25. The temperature used in determining thermal conductivity is the film temperature, the average temperature of the surface of the plate, and the air inside the wind tunnel. The characteristic length is the distance from the leading edge of the plate of the heat flux sensor being considered along the direction of air flow, shown in Figure 25 as L_1 , L_2 , etc.

$$Nu = \frac{h L}{k} \quad (25)$$

Depending on the analysis, either the average heat transfer coefficient of all three sensors or the center sensors on a given plate side was used. In the final analysis using the Phantom II in an actual spiral freezer, presented in Chapter 3, only the center heat flux sensor was used due to it being in the center of the plate as the plate traveled circularly within an operating spiral freezer. In other words, its characteristic length was more constant than the sensors near the edges, making it a more reliable indicator of heat transfer coefficient over the surface.

A Testo 405i hot wire anemometer (accuracy ± 0.55 m/s) was used to simultaneously measure the velocity of the air inside of the wind tunnel during testing to calculate Reynolds number. The calculation for this is shown in Equation 26, where ρ is air density, v is air velocity measured by the anemometer, L is the characteristic length, and μ is the dynamic viscosity.

$$Re = \frac{\rho v L}{\mu} \quad (26)$$

A term was developed in this research that compared the measured Nusselt number at a prescribed angle to the same Nusselt number at zero impingement angle (Nu_0), named the Nusselt number reduction ratio, or Nu_{rr} , shown in Equation 27:

$$Nu_{rr} = \frac{Nu}{Nu_0} \quad (27)$$

The Nu_{rr} shown in Equation 27 allows the findings of this research from this specific setup of heat flux sensors, temperature sensors, and physical apparatus, to be separated and used with any other method of determining Nusselt number for a given geometry, scaling it using a known angle of impingement. Much more actionable detail is devoted to this in Chapter 3. Table 1 shows a description and typical value of all of the terms introduced for the Phantom II.

2.8 Uncertainty analysis

An uncertainty analysis was performed on the system to obtain an estimate of overall expected measurement accuracy for the surface heat transfer coefficient. Major contributors including thermocouples, heat flux sensors, milliamp transmitters, and the hot wire anemometer were considered and their individual uncertainties, derived from manufacturer literature or calibration data, were then propagated through to the overall uncertainty in the calculated surface heat transfer coefficient. The required properties of air (viscosity, density, and thermal conductivity) were estimated using data reported by Lemon (2004). The result, shown in Table 1, is a heat transfer coefficient uncertainty of 14%. The Nusselt number, derived in Section 2.7.5 from the heat transfer coefficient as shown in Equation 25, has a calculated uncertainty of 14.5%. The Reynolds number (determined using the hot wire anemometer instead of the heat flux sensor), has an uncertainty of 13.1%. The purpose of these calculations is to show the relative influences of major components of the measurement to drive insights into the utility of heat flux sensors and motivate similar future efforts. Table 4 and Table 5 show more detail from each of the three cases, showing individual sensor contributions on Nusselt number and Reynolds number from Table 3.

Table 3: Overall uncertainty analysis on measurements, devices, properties, and calculated values.

Measurements and devices	Symbol	Typical value	Units	Accuracy/ uncertainty
Ambient temperature	T_∞	286	K	± 2 K
Flux surface temperature	T_s	308	K	± 2 K
Milliamp transmitter	mA	4.3	mA	± 0.01 mA

Flux sensitivity coefficient	S_{calib}	1.27	$\mu\text{V}/(\text{W}/\text{m}^2)$	$\pm 2.5\%$
Hot wire anemometer	U_{inf}	5.0	m/s	± 0.55 m/s

Properties

Viscosity	μ	0.01839	centipoise	5.0%
Density	ρ	1.189	kg/m^3	5.0%
Thermal conductivity	k	0.02616	W/m-K	3.0%

Calculated uncertainty

% Uncertainty

Heat transfer coefficient	\bar{h}	31.9	W/m ² -K	4.5 W/m ² -K	14.1
Nusselt number	Nu	186	-	27	14.5
Reynolds number	Re	49250	-	6450	13.1

Table 4 shows the detailed view of the Nusselt number uncertainty, showing the individual contributions from the component sensors. The ambient temperature and flux surface temperature measurements make up a combined 88% of the overall uncertainty. This is because the temperature sensors have greater listed relative inaccuracy than the heat flux sensors. Since Nu is largely a function of the heat transfer coefficient, as shown in Equation 25, the uncertainty in h would be nearly identical in magnitude to the uncertainty in Nu in this instance, therefore an uncertainty analysis on h will not be shown but can be assumed to be around the same uncertainty as that of Nu (14.5%). The uncertainty in the characteristic length is ignored in this analysis because an accurate measurement of length is much easier to make than the other measurements.

Table 4: Detail of Nusselt number uncertainty contributions.

Nu = 186 ± 27 (14.5%)		Typical Value	Units	Uncertainty	% of Uncertainty
Thermal conductivity	k	0.03	W/m-K	±3.0%	4.3
Milliamp transmitter	mA	4.3	mA	±0.01 mA	5.1
Flux sensitivity coefficient	S_{calib}	1.27	μV/(W/m ²)	±2.5%	2.8
Ambient temperature	T_{∞}	286	K	±2 K	38.2
Flux surface temperature	T_s	308	K	±2 K	49.7

The uncertainty in Reynolds number, previously defined in Equation 26, is shown in Table 5. 71% of the error in Reynolds number is attributed to the hot wire anemometer velocity measurement.

Table 5: Detail of Reynolds number uncertainty.

Re = 49251 ± 6454 (13.1%)		Typical Value	Units	Uncertainty	% of Uncertainty
Viscosity	μ	0.02	centipoise	±5.0%	14.6
Density	ρ	1.19	kg/m ³	±5.0%	14.6
Ambient temperature	T_{∞}	286	°K	±2 °K	0.2
Flux surface temperature	T_s	308	°K	±2 °K	0.2
Hot wire anemometer	U_{inf}	5.0	m/s	±0.55 m/s	70.5

The analysis revealed that uncertainties in less dominant factors, such as the heat flux sensors and milliamp transmitters, contributed proportionally less to the overall error. Although this does not make them any less important to the experiment, it just motivates experiments to perhaps prioritize improvements in temperature and velocity measurement instrumentation and methods before moving onto others. By breaking down individual contributions to uncertainty, the analysis delivers valuable guidance for optimizing sensor selection and system design in subsequent investigations.

3 Results

This section presents a comprehensive analysis of the research findings, starting with the application of CFD to predict airflow within a spiral freezing system with a goal of using the CFD results iteratively to optimize freezer thermal performance. Altering air flow within the freezer relies on addressing interior areas with high losses or redirecting air flow using baffling to improve air flow patterns local to the food products being conveyed through the enclosure. The detailed CFD velocity profiling is input to the 1-D product thermal model to assess overall freezing performance reflected in a metric of the maximum belt speed (i.e. product throughput) to achieve a defined product core temperature. Because the food product model accommodates different food geometries and food properties, the approach is flexible in its ability to further expand in application to a wide variety of products. Monte Carlo simulations and optimization studies are used as tools to provide insights into improving freezing system performance, with Pareto fronts illustrating trade-offs between key operational parameters such as fan velocity and air temperature, and throughput. Results from the thermal model demonstrate how product temperature evolves with dwell time, the impact of belt speed on freezing rates, and the influence of airflow timing, termed the “blast effect.” Field-testing of the Phantom I in a food processing facility provided confidence in the heat transfer predictions and CFD model accuracy, while wind tunnel experiments with the Phantom II further

investigated the effects of air velocity, airflow angle, and Nusselt number relationships. Finally, field benchmarking of five spiral freezers across different food processing plants and types of products provided a comparative analysis of system performance using experimental and modeled results.

3.1 CFD as a Tool for Assessing Blast Freezer Air Flow

This section summarizes the use of computational fluid dynamics (CFD) to analyze and optimize airflow within a spiral freezer through the addition of physical structures referred to as “baffling” within the spiral. The modeled spiral freezer, based on an actual large-scale spiral freezing system operating in Plant 1, revealed inefficiencies such as regions of bypassing airflow and dead zones within the spiral that resulted in reduced air velocity over food product leading to poor freezing performance. Iterative CFD analyses tested various baffling configurations to direct airflow more effectively within the spiral freezing system. Implementing the proposed physical modifications resulted in predictions of increased velocity delivered to the product by 40% compared to the as-found freezer serving as the baseline.

3.1.1 *CFD Description*

The CFD software used was ANSYS Fluent, Release 19.3, 2019 (Workbench Environment). The modeling considered a real, operating spiral freezer as part of a broader research study that investigated six (6) different freezing systems in five (5) food production plants. The spiral freezer from Plant 1, shown in a CAD drawing in Figure 28, had dimensions of 30 feet wide by 35 feet long and 30 feet high with a resulting footprint of 1,050 ft² and volume of 31,500 ft³. Within the freezer was the spiral conveyor, six evaporator coils (two vertically stacked rows of three side-by-side coils), six fans, and various other components including spiral belt support structure, drive motor, and structural members. The CFD study incorporated the modeling techniques discussed in Section 2.5 to ensure the CFD mesh balanced computational efficiency with accuracy. The model limited the 3-D tetrahedral element sizes to a maximum of 10 to 12.5 centimeters per edge. Inflation layers were utilized for improved near-wall mesh

resolution, with a first layer thickness of 7.5 mm, a minimum of 10 growth layers, and a growth rate of approximately 1.3. A sphere of influence was applied near the fans, refining the element size to 0.5 cm within a 200 cm radius. This mesh setup resulted in a node count that ranged from 5.3 to 8.6 million and 12.6 to 21 million elements. The resulting y^+ values achieved at the walls fell within a range from 30 to 200, ensuring compatibility with the turbulence model's enhanced wall treatment. Additional details and methodologies related to this CFD work are extensively documented in Tyler Young's M.S. thesis, which was completed in collaboration with the author in 2023 (Young, 2023).

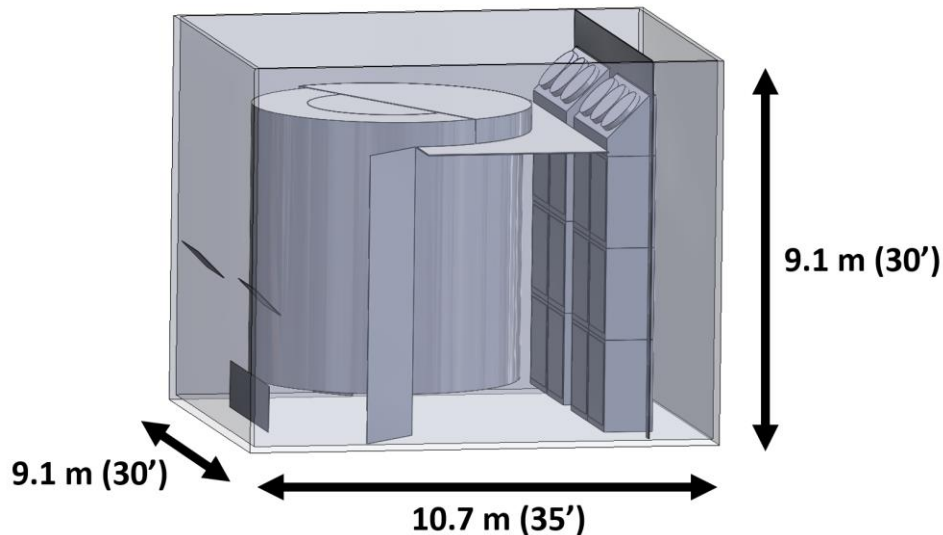


Figure 28: 3-D model of an actual spiral freezer from Plant 1 modeled in CFD.

The airflow was simulated using the two-equation k -epsilon realizable turbulence model with enhanced wall treatment, which is suitable for capturing complex interactions between the freezer geometry and airflow patterns. The manufacturer's fan curve for the Airfoil Impellers fan model U2-33Y-6-42PM was obtained and implemented in the CFD model to relate the developed volumetric air flow developed to vary with the external pressure drop of that air as it flowed from the fan discharge, through the spiral enclosure, evaporator coils, and back to the fan inlet. This detail was intended to accurately

capture realistic fan operation within the CFD model. Air transport properties were derived using a temperature of -28°F (-33.3°C) at standard atmospheric pressure (14.696 psi) which were consistent with the actual thermal conditions encountered during operation of the spiral freezer.

The point cloud introduced in Section 2.5.3 was integrated into the study to extract three-dimensional velocity data along the product's path from the CFD model, producing a 3200-point vector of velocity in the x, y, and z directions. A visual representation of the helical point cloud is shown in Figure 29 (right) along with streamlines throughout the entire computational domain (left) from one of the CFD baffling iterations.

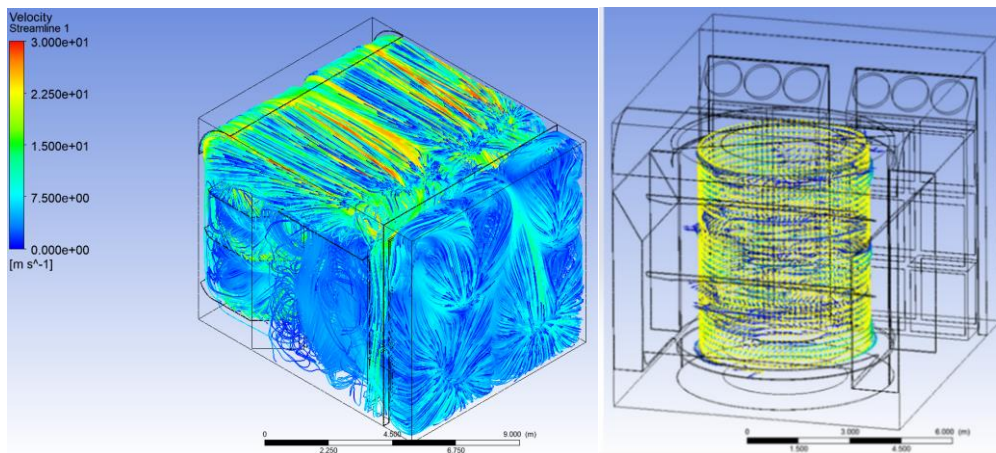


Figure 29: CFD streamlines (left) and the point cloud (right) that tracks velocity as a function of position.

This study built upon previous CFD work in spiral freezers by incorporating enhanced mesh refinement, wall treatment effects, and more internal structural details. These improvements addressed unnecessary simplifications present in the prior studies referenced in Section 1.2.2, providing a more accurate representation of airflow behavior within the spiral freezer. This comprehensive approach lays the groundwork for CFD to be used as a tool for modeling air flow within large-scale spiral freezers into the future.

3.1.2 Velocity from Point Cloud

The existing spiral air blast freezing system from Plant 1 processing a flat par (partially) baked dough product (pizza crust) serves as the reference for this work. A 2-D drawing of this freezer is shown in Figure 30 along with an illustration of the general pattern of air flow within the spiral using arrows scaled in size to reflect the relative air velocity. In this freezing system, the dough product enters near the top of the spiral (denoted by the box labeled “Inlet”) and leaves near the bottom (at the location labeled as “Outlet”).

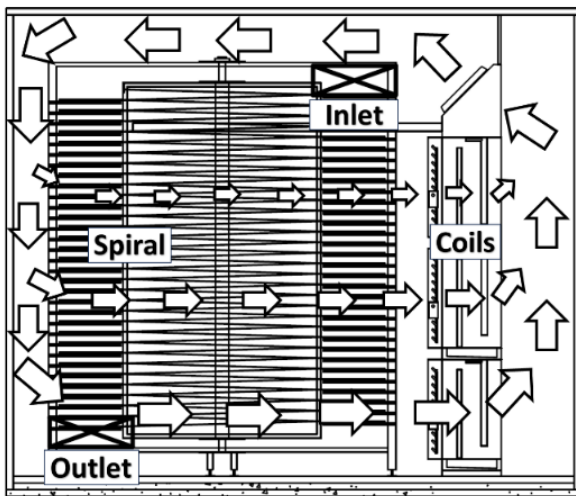


Figure 30: Spiral freezer from Plant 1.

Figure 31 (left) shows the CFD-predicted quasi-steady air velocity magnitude (total of x, y, and z components) experienced by the product along its trajectory through the spiral during its dwell time, as captured by the point cloud. The food product experiences comparatively low air velocities in the first half of its dwell time (corresponding to the upper half of the spiral from time 0 to approximately 850 seconds) while the product experiences higher air velocities during the latter part of its dwell time (corresponding to the lower half of the spiral from time 850 to 1700 seconds). Figure 31 (right) shows the

corresponding heat transfer coefficient over the product as it moves through the spiral as-calculated using the Dittus-Boelter velocity^{0.8} relationship introduced in Section 2.1.1.

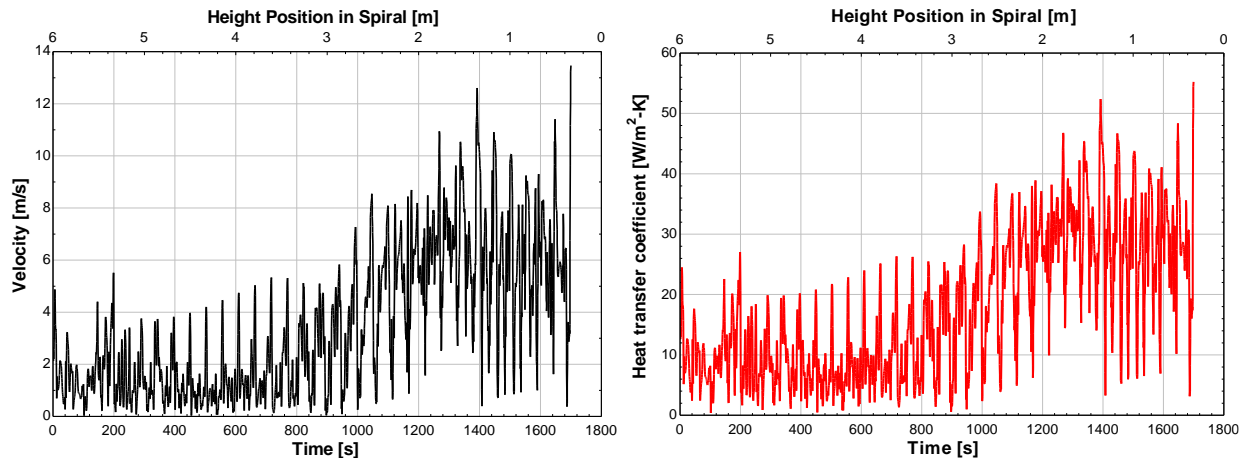


Figure 31: The local air velocity (left) experienced by a product as it travels through a spiral belt freezer and the predicted heat transfer coefficient (right).

As the product is conveyed through the spiral, it experiences an oscillating velocity due to the product’s flow path moving closer to and then farther away from the areas of locally high velocity adjacent to the fans within the freezing system. This cyclic velocity profile with each rotation around the spiral is a characteristic pattern that was confirmed through field measurements taken in several operating spiral freezing systems during the course of the present research effort. Figure 32 shows velocity streamlines at a vertical cross section midway up the spiral. It clearly shows low velocity on the left (furthest away from the fans) and peak velocities at the apex of the spiral where the air flow speeds up due to the narrowing path posed by the spiral nearing the sidewall of the freezer. The product experiences a second “dead zone” at the right-side of the spiral which is near the entrance to the evaporator coils. This image is intended to further explain the cyclical variation in velocity observed in the point cloud trends. Although the air velocity in some localized areas appears to be exceeding 10 m/s, the dead zone appears to experience nearly zero airflow. This runs contrary to claims put forth in existing literature, as discussed in Section 1.2.2. The existence of these pronounced dead zones in spiral freezers was confirmed in the field using Phantom 1, which will be discussed further in Section 3.7.1. Surprisingly, this cyclical

variation in airflow has not been reported or discussed in any other known studies of spiral blast freezers.

Its effect on performance will be assessed in Section 3.5.

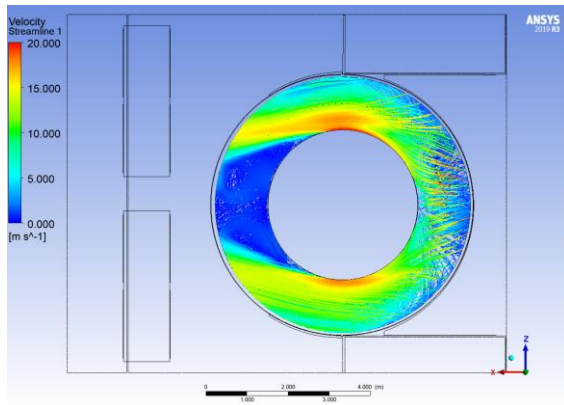
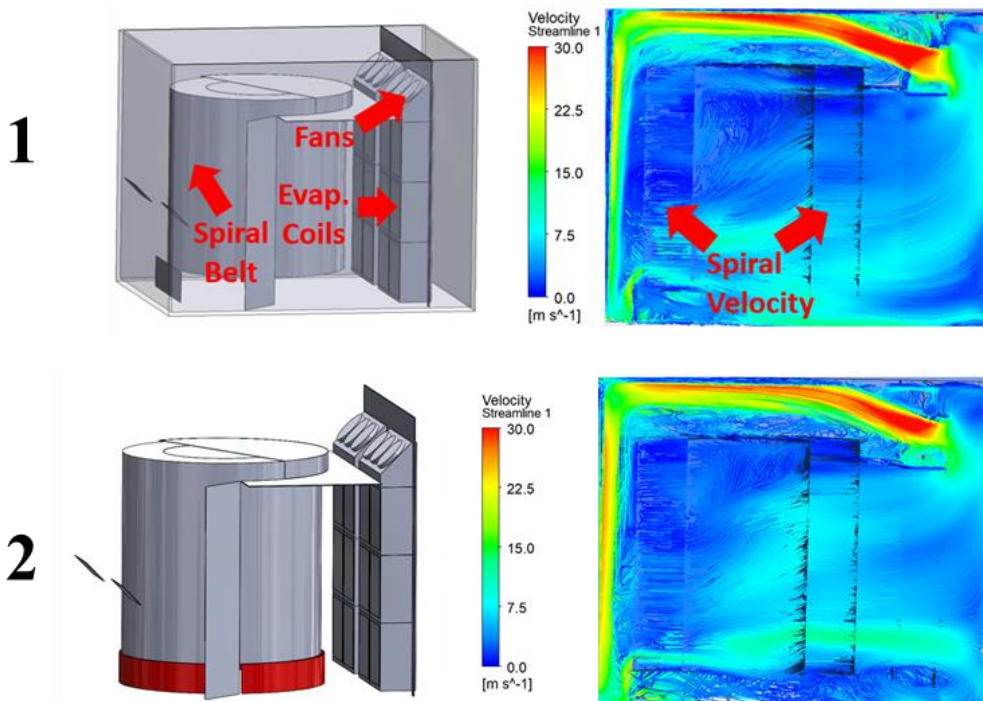


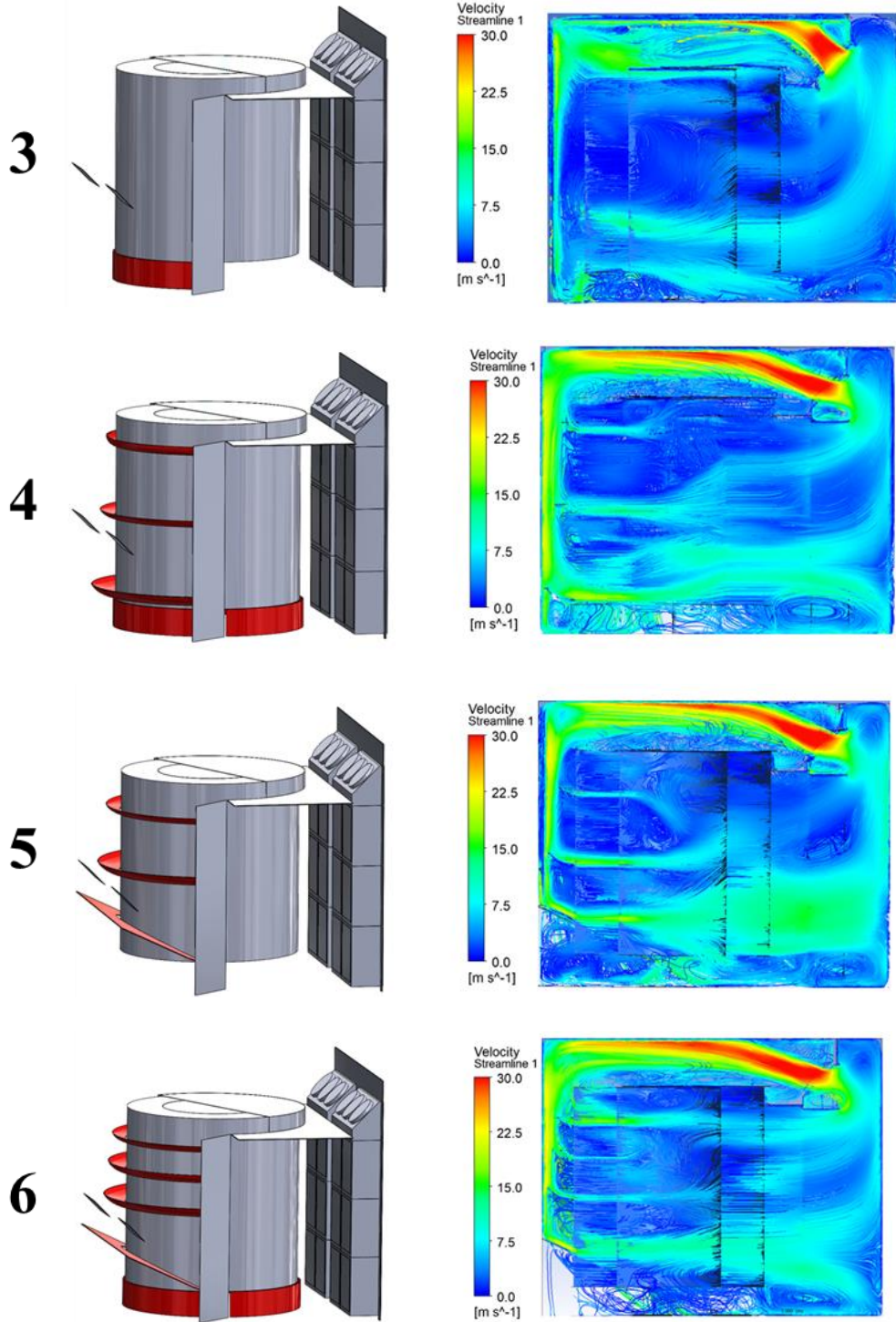
Figure 32: Plan view of air flow observed around the spiral cross section.

Multiple initial baffling modifications were incorporated into the CFD model in an attempt to improve air flow patterns within the spiral with a focus on those areas where the spiral belt traverse the product. A summary of the conditions and baffling modifications attempted are shown in Table 6 with the physical changes noted in red within **Figure 33**. The Spiral Velocity shown in Table 6 is the average velocity magnitude throughout the entire point cloud. The relative performance of the changes is defined as the change in spiral velocity experienced by the product compared with the spiral velocity of the original CFD model. The cases are shown in the first column, and the corresponding physical baffling and CFD details of these changes are shown in Figure 33. As can be seen, only two or three changes significantly increased the performance with option 7 yielding an impressive 42% improvement in air velocity over the base case. The baffles that were effective tended to work individually or in concert with one another.

Table 6: Summary of CFD baffling iterations.

Case	Condition/Baffling Added	Spiral Velocity (ft/min)	Relative Performance
1	Existing spiral freezer	827 (4.2 m/s)	1.00
2	Both skirts at the base of the spiral	785 (4.0 m/s)	0.95
3	Skirt at the base of the spiral only on the side opposite the evaporator coils	846 (4.3 m/s)	1.02
4	Curved baffles (x3) to re-direct air flow through the spiral at distributed vertical locations and both skirts at spiral base	854 (4.3 m/s)	1.03
5	Bottom plate	882 (4.5 m/s)	1.07
6	Curved baffles (x3), bottom plate, skirts	907 (4.6 m/s)	1.10
7	All baffles, plus cubes, center drum	1,174 (6.0 m/s)	1.42





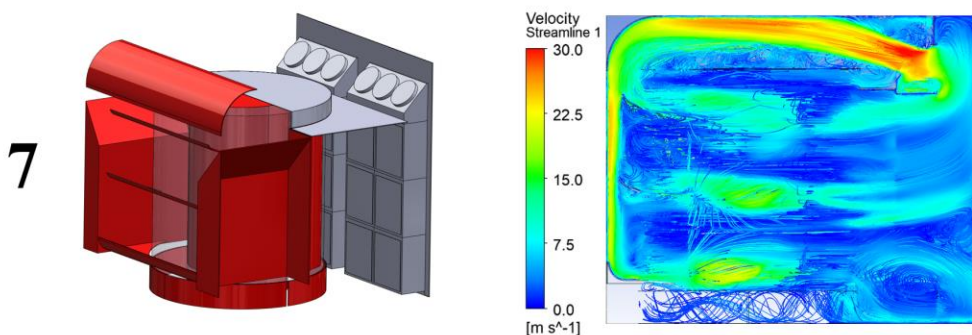


Figure 33: Physical baffling added to spiral freezer and the results of the CFD.

Case 1 is the unmodified existing spiral freezer. The fans discharge air at about a 45 degree angle at the top of the spiral. The high velocity air traverses across the top of the spiral between the ceiling and the top row of the spiral belt where it reaches the opposite side wall and makes a 90 degree turn down the back wall. This abrupt 90 degree turn results in a non-recoverable pressure drop and only a small region of air flow maintains high velocity as it flows from ceiling to floor on the opposite (back) wall. Because there is no structure to direct air to flow through the spiral belt, the air impinges on the floor where it must make another 90 degree turn to flow away from the back wall through the lower tiers of the spiral belt back across the evaporator coils and to a plenum returning air to the fan inlets.

Proposed modification to the base case begins with Case 2 shown in Figure 33. In Case 2, “skirt baffles” that wrapped around the base of the spiral circumferentially were added with the goal of preventing the higher velocity air reaching the bottom of the freezer enclosure from bypassing the belt through an open portion created by the last level of the spiral and the enclosure floor. These skirt baffles actually *reduced* the velocity performance by 5%. The “full skirt” tended to hurt performance because once air entered this skirted area (through the core of the spiral), it could not easily leave, creating a flow disruption. Case 3, with only one skirt baffle on 180° of the opposite side of the room as the coils, experienced a very small 2% improvement in airflow. Case 4 added curved, tiered baffles to the exterior of the spiral that were designed to “peel off” a portion of the main bulk air flow path that moves down the

back wall of the freezer. There appeared to be little benefit in these baffles, even though visually, based on the prior CFD results, they appeared promising. Case 5 introduced a bottom plate baffle that blocked air from being able to enter under the spiral. This is the first significant performance improvement, which showed a 7% increase in spiral velocity over the baseline. The next iteration, Case 6, included all three tiered curved baffles, the flat bottom plate, and the full skirt – these modifications resulted in a 10% improvement in air velocity. A number of small-scale “sub-studies” were conducted separately to better inform the research as to more specific modifications that could be pursued to more significantly improve air flow. Although not reported here, these sub-studies pointed to baffling arrangements that would more aggressively direct or “force” air flow **through the spiral horizontally**. Case 7 implemented a few specific baffles intended to achieve this objective including: 1) a structure called a “drum baffle” that fills the center or core of the spiral belt, 2) two “cube baffles” near the back walls on either side of the room that prevent air from bypassing between the apex of the spiral and the freezer’s sidewalls and 3) the bottom plate previously introduced. The result was an increase in velocity delivered over the product by 42% as shown in Table 6. From further small-scale sub-studies, it was demonstrated that the upper tiered baffles, the skirt, and the corner baffle shown in Case 7 were not significant factors that contributed to this performance increase. The majority of the performance increase was due to the drum, cubes, and bottom plate baffle that forced air through the spiral.

Because each spiral freezer manufacturer has their own unique designs, the results of this particular application of interior modifications are not universally applicable; however, these findings do underscore the importance of pursuing designs that direct air flow through the levels of the spiral belt conveying product. The present research also underscores how the iterative CFD process can be used as a tool to study various baffling modifications to the spiral freezer to determine which arrangements can significantly enhance air velocity experienced by the product versus modifications that have minimal positive effect. While some modifications that might initially appear self-evident, such as the full skirt

baffle, disrupted airflow and reduced performance, others, like the bottom plate, were non-obvious and marked a clear improvement by preventing air from bypassing under the spiral.

Any open area within the freezer enclosure where air can bypass the spiral belt results in a “short circuit” of air flow with, potentially, significant freezer performance degradation. Another important consideration is that regions of air flow with very high velocity peaks can result in aerodynamically dislocating food products and toppings depending on the product, which can lead to substantial product loss and production costs when dislodged product results in a belt malfunction (jam). In cases where a single spiral runs a range of food products with some products more susceptible to high air velocity while other products are less susceptible to high air velocity, variable speed drives on fans can be used to manage air velocity and maintain maximum freezer performance. The variability of velocity is important and will be discussed in Section 3.3. Young (2023) significantly evolved upon the CFD work shown, focusing on it exclusively, and developed new strategies, including using the same equipment (fans, coils, etc.) in different layouts to produce even larger increases in performance than with just using baffles. Some of these layouts used fewer fans, yet retained the same number of evaporator coils, with better overall performance, creating promising new conceptual designs for the next generation of spiral air blast freezers (Young, 2023).

3.2 Thermal Model Results

This chapter presents the outcomes of the thermal model developed to simulate product temperature dynamics within a spiral freezer. Key findings include the modeling of product temperature as a function of dwell time while exposed to a highly dynamic air velocity and air temperature environment which coupled to impact the product’s thermal boundary conditions. The impact of belt speed on achieving target product temperatures is analyzed, emphasizing the relationship between throughput and freezing efficiency. Additionally, the “blast effect,” which explores the macro timing of high-velocity airflow

exposure during the product's dwell time within the freezer, is introduced to evaluate its influence on overall freezing performance. The model's adaptability is demonstrated through simulations of various food types and geometries, providing insights into the interplay between product-specific thermal properties and freezing conditions.

3.2.1 Product Temperature as a Function of Dwell Time

The velocity profile generated by the CFD model, previously presented in Figure 31, was applied to the 1-D thermal model introduced in Section 2.1 to produce a freezing curve of the product as a function of dwell time within a spiral freezer, shown in Figure 34. One key observation from this graph is that the surface temperatures of the product are more responsive to ambient velocity variations than the center. This heightened sensitivity is due to the surfaces being on the thermal boundaries of the model, where direct exposure to convective heat transfer occurs. In contrast, the interior layers of the food product being less thermally coupled to the freezer's environment and governed primarily by conduction within the product, resulting in a more attenuated response to velocity fluctuations.

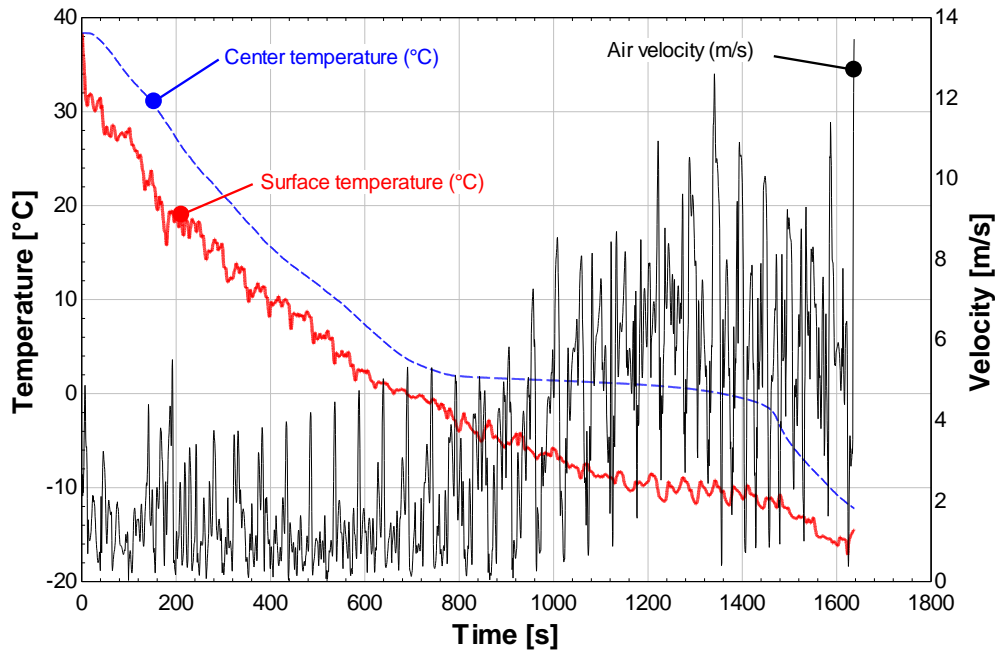


Figure 34: Temperature of a dough product as a function of dwell time (base case).

Additionally, the freezing curve exhibits a temperature plateau near 0°C (32°F) during a portion of the freezing process as expected due to the effects of the enthalpy of fusion, as water content within the product transitions from liquid to solid phase. This phase change absorbs significant energy, temporarily delaying further cooling. These results align with established thermal behavior of food products undergoing freezing and provide insight into the interplay between convective and conductive heat transfer mechanisms within the product during its dwell time in the spiral freezer.

3.2.2 Belt Speed and Time

Previously introduced in Chapter 2, the belt speed in a spiral freezing system is an adjustable parameter by production personnel typically controlled by a variable speed drive, allowing manufacturing facilities to maximize the throughput of the freezer while ensuring the product exits at the desired terminal product temperature (usually a defined core temperature or temperature range). To automate the determination of the required belt speed to achieve this, the MATLAB optimization function `fminsearchcon`, a minimization routine accommodating constraints by D'Errico (2022), was employed.

This approach allowed determination of the maximum belt speed at which the product exits in a fully frozen state, using function implementation and techniques shown by Suresh (2021). By imposing a given time-dependent velocity profile on the 1-D product thermal model, belt speed is treated as an independent variable optimized to minimize the temperature difference between the product's maximum internal (center) temperature and the desired fully frozen temperature. This methodology not only determined the fastest belt speed that delivered target temperature, but also enabled the identification of new favorable velocity profiles to further inform airflow modifications that would be desirable to enhance freezer performance.

3.2.3 Blast Effect Introduction

As illustrated in Figure 35 (left), the reference air velocity profile derived from the CFD model indicates that the product experiences a significantly higher velocity at end of its dwell period corresponding the lower portion of the spiral freezer (near the product outfeed) compared to the upper portion (near the infeed). This bias reflects the physical design of the spiral freezer, specifically, its air-side, and prompted an initial study to determine whether this arrangement was advantageous for freezing performance.

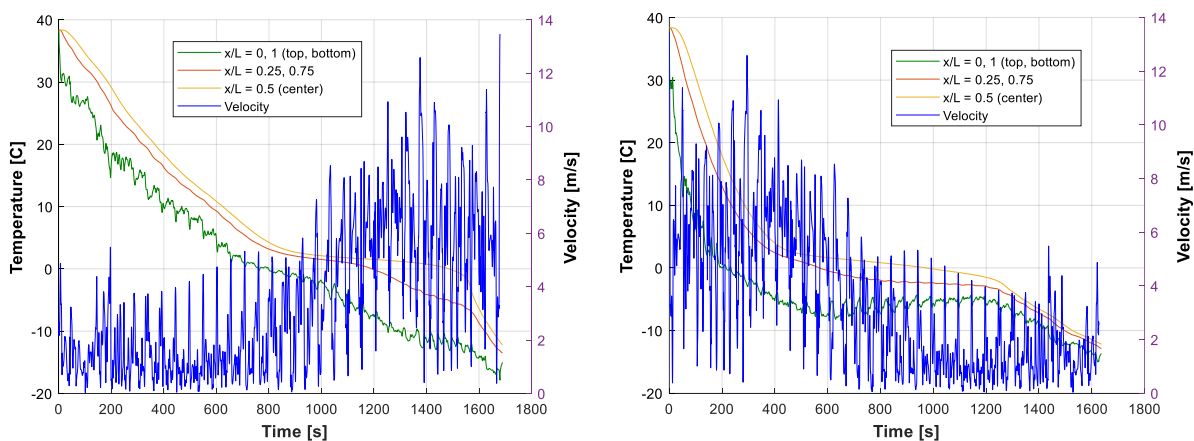


Figure 35: Base case velocity profile (left) and the reverse velocity profile (right) for comparison.

A comparative was conducted by simply “mirroring” the base case reference velocity distribution. In this analysis, the product experiences a higher air velocity at the infeed and lower velocity at the outfeed. Surprisingly, the results of shifting the higher air velocity to the infeed led to over a 3% increase in belt speed while all other characteristics remained the same as shown in Figure 35 (right). This improvement demonstrates that directing higher air velocity across the product earlier in the freezing process dwell time may enhance overall performance, aligning with the objectives of rapid freezing in terms of food quality and reduced moisture loss. Early freezing prevents excessive moisture loss by sealing water content in the product's outer layers as they freeze more quickly (Wu et al., 2021). The dough product used in this study exhibited negligible moisture loss (<1%), verified through gravimetric analysis; therefore, product moisture retention was not considered to be a significant factor in subsequent thermal analyses. However, the finding that relatively simple adjustments to airflow distribution can yield significant improvements in product throughput underscores the importance of optimizing blast freezer conditions. To further explore this observed effect, the simplified heat transfer model shown in Figure 36 was developed to illustrate the comparative impact of “blasting early” (higher air velocity over the product at the start of the freezing dwell time) versus “blasting late” (higher air velocity over the product latter in the freezing dwell time). The results confirm the behavior observed in mirroring the air velocity profile discussed above, prioritizing higher air velocity early in the freezing process, improves freezing times.

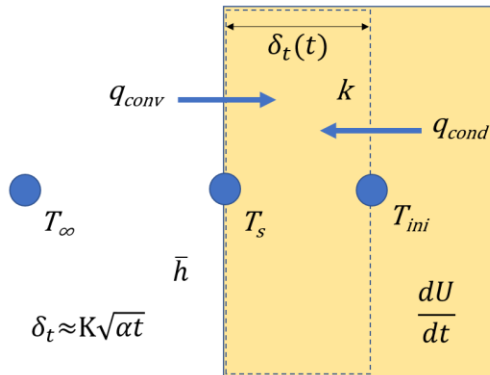


Figure 36: A semi-infinite 1-D plane wall model with convection, conduction, time-varying thermal penetration depth, and an energy generation term dU/dt .

Using the behavior of thermal diffusivity in a plane wall, concepts from Nellis and Klein (2009), Figure 36 can be approximately described by Equation 28, where T_s is solved for implicitly. The descriptions of variables used in this simple model were shown in Table 1 at the beginning of Chapter 1.

$$h A_c (T_\infty - T_s) \approx k A_c \left(\frac{T_s - T_{ini}}{K \sqrt{\alpha t}} \right) \quad (28)$$

Next, the change in internal energy with respect to time, dU/dt , of the entire wall can be defined as:

$$\frac{dU}{dt} = h A_c (T_\infty - T_s) \quad (29)$$

Where α is the thermal diffusivity represented in Equation 30:

$$\alpha = \frac{k}{\rho c} \quad (30)$$

The integral of Equation 29, with respect to time, is the overall energy (Q in Figure 37) that is transferred in this plane wall model. The only unknowns in this simplified case are the constant K and the temperature of the product, T_s . Arbitrary unit values (i.e., 1) are selected for the thermal properties, and K is set to $\sqrt{2}$ to satisfy initial conditions. Time, t , is varied, and the heat transfer coefficient is doubled (or halved) midway through the transient analysis to simulate “blasting late” vs “blasting early,” and the results are shown in Figure 37. The “do nothing” (i.e., constant) case is simply the average of the two heat

transfer coefficients used. In this example, $h = 0.25 \text{ W/m}^2\text{-K}$ is used for the low, $0.5 \text{ W/m}^2\text{-K}$ as the high heat transfer coefficient, and $0.325 \text{ W/m}^2\text{-K}$ is used in the do nothing (i.e., constant) case.

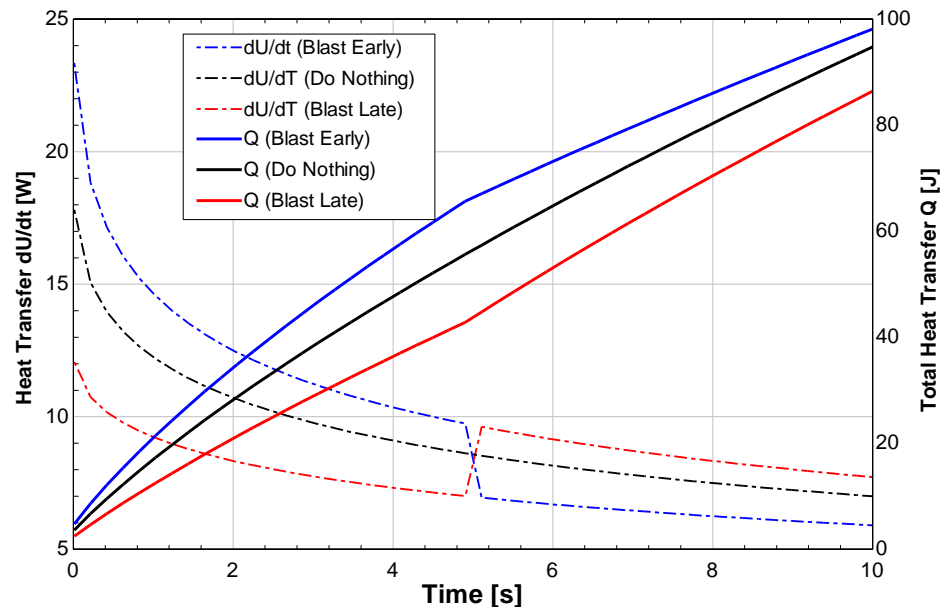


Figure 37: The “blast effect” is shown.

The “blast early” effect, or simply “blast effect” occurs because the initially higher heat transfer coefficient leverages the large ΔT between the surface of the product and the cold temperature inside of the freezer that occurs early in the product’s dwell time within the freezer. This high heat transfer coefficient early leads to a higher dU/dt (Q) or overall heat removal from the product. The area under the dU/dt curves in Figure 37 is the total heat transferred from the product (in Joules), as shown on the right y-axis. In this simple example, the blasting-early case has around a 10% greater area under the dU/dt curve, or 10% greater heat transfer relative to blasting late. Therefore, it can be advantageous to increase velocity over the product early in the freezing process, confirming the observations of the mirrored velocity profile shown in Figure 35. Surprisingly, blasting early is even slightly better than having a constant average velocity over the product (~3% greater heat transfer). Note, this blast early advantage appears only applicable in a specific range of Biot numbers ($(h_{\text{avg}}L)/k$) between 0 and ~30, which will be investigated more thoroughly in the next section.

3.2.4 Blast Effect Dimensionless Model

A more detailed dimensionless model was created to show and explore the blast effect using techniques from Meyers (1998) and Nellis & Klein (2009). The variables shown here are introduced in Table 1. Consider a plane wall shown in Figure 38 of thickness $2L$ that experiences convection along both edges.

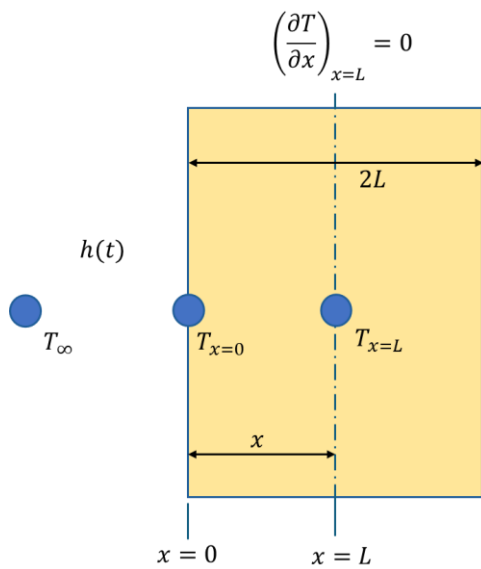


Figure 38: A symmetrical plane wall of length $2L$.

Taking advantage of the symmetry of the problem, the computational domain is $0 < x < L$; where $x = 0$ corresponds to the surface experiencing convection and $x = L$ corresponds to the centerline. Assuming constant properties, the governing differential equation for the problem is:

$$\alpha \frac{\partial^2 T}{\partial x^2} = \frac{\partial T}{\partial t} \quad (31)$$

The material is assumed to be initially at a uniform temperature:

$$T_{t=0} = T_{ini} \quad (32)$$

The boundary condition at $x = L$ is:

$$\left(\frac{\partial T}{\partial x}\right)_{x=L} = 0 \quad (33)$$

The boundary condition at $x = 0$ is:

$$h(t)(T_{\infty} - T_{x=0}) = -k \left(\frac{\partial T}{\partial x}\right)_{x=0} \quad (34)$$

where the heat transfer coefficient, h , is a function of time:

$$h(t) = \begin{cases} h_{avg} + \Delta h & \text{for } 0 < t < t_{switch} \\ h_{avg} - \Delta h & \text{for } t_{switch} < t \end{cases} \quad (35)$$

where h_{avg} is the average heat transfer coefficient and Δh is the change relative to that average (a positive value of Δh indicates a blast first or early situation while a negative value indicates a blast last or late situation).

The following dimensionless parameters are defined:

$$\theta = \frac{T - T_{ini}}{T_{\infty} - T_{ini}} \quad (36)$$

$$\tilde{t} = \frac{t\alpha}{L^2} \quad (37)$$

$$\tilde{x} = \frac{x}{L} \quad (38)$$

$$Bi = \frac{h_{avg}L}{k} \quad (39)$$

$$\beta = \frac{\Delta h}{h_{avg}} \quad (40)$$

Substituting Eqs. (36) through (40) into Eqs. (31) through (35) provides the dimensionless form of the problem:

$$\frac{\partial^2 \theta}{\partial \tilde{x}^2} = \frac{\partial \theta}{\partial \tilde{t}} \quad (41)$$

$$\theta_{\tilde{t}=0} = 0 \quad (42)$$

$$\left(\frac{\partial \theta}{\partial \tilde{x}}\right)_{\tilde{x}=1} = 0 \quad (43)$$

$$Bi(1 \pm \alpha)(1 - \theta_{\tilde{x}=0}) = -\left(\frac{\partial \theta}{\partial \tilde{x}}\right)_{\tilde{x}=0} \quad (44)$$

where the positive value in Eq. 44 is applied if $\tilde{t} < \tilde{t}_{switch}$ and the negative value is applied afterwards. The objective of the problem is to predict the time required (t_f) for the center temperature to reach some specified value, T_f . Therefore, the outcome of the problem is the dimensionless time required ($\tilde{t}_f = t_f \alpha / L^2$) for the dimensionless center temperature to reach a specified value ($\theta_f = (T_f - T_{ini}) / (T_\infty - T_{ini})$). This process is complicated by the requirement that the switch time for the altered heat transfer coefficient be half of the freezing time ($\tilde{t}_{switch} = \tilde{t}_f / 2$, corresponding to a product experiencing elevated and reduced heat transfer coefficient each 50% of the time). It will be necessary to iteratively adjust \tilde{t}_{switch} during a simulation. The numerical implementation follows.

The computational domain is discretized according to:

$$\tilde{x}_i = \frac{(i-1)}{(M-1)} \text{ for } i = 1..M \quad (45)$$

where M is the number of nodes. The distance between adjacent nodes is then:

$$\Delta\tilde{x}_i = \frac{1}{(M-1)} \quad (46)$$

The state equation corresponding to each of the internal nodes comes from Eq. 41:

$$\frac{\partial\theta_i}{\partial\tilde{t}} = \frac{(\theta_{i+1} + \theta_{i-1} - 2\theta_i)}{\Delta\tilde{x}^2} \text{ for } i = 2..(M-1) \quad (47)$$

The state equation for node 1 is:

$$\frac{\partial\theta_1}{\partial\tilde{t}} = \frac{2Bi}{\Delta\tilde{x}}(1 \pm \beta)(1 - \theta_1) + \frac{2}{\Delta\tilde{x}^2}(\theta_2 - \theta_1) \quad (48)$$

and for node M is:

$$\frac{\partial\theta_M}{\partial\tilde{t}} = \frac{2}{\Delta\tilde{x}^2}(\theta_{M-1} - \theta_M) \quad (49)$$

The state equations were simulated through time using MATLAB's `ode45` function with an event function implemented that terminated the simulation when $\theta_M = \theta_f$ which corresponds to \tilde{t}_f . A successive substitution method was used to adjust the value of \tilde{t}_{switch} until it is equal to $\tilde{t}_f/2$. The result is a numerical model capable of predicting dimensionless freezing time as a function of three parameters: the Biot number (Bi), the relative amplitude of the heat transfer coefficient change (β), and the dimensionless freezing temperature (θ_f).

We are interested in how the freezing time changes by implementing a blast early ($\beta > 0$) or blast late ($\beta < 0$) type of process. Therefore, the fractional change in freezing time is defined relative to the constant heat transfer coefficient ($\beta = 0$) case.

$$fr = \frac{\tilde{t}_{f,\beta} - \tilde{t}_{f,\beta=0}}{\tilde{t}_{f,\beta=0}} \quad (50)$$

Note that $fr > 0$ corresponds to an undesirable increase in freezing time while $fr < 0$ indicates that the freezing time has been reduced (which is desirable). Figure 39 through Figure 41 illustrate fr in the parameter space of b and Bi for $qf = 0.25, 0.5,$ and $0.75,$ respectively. A log10 of Biot of -1 corresponds to 0.1 while 2 corresponds to 100.

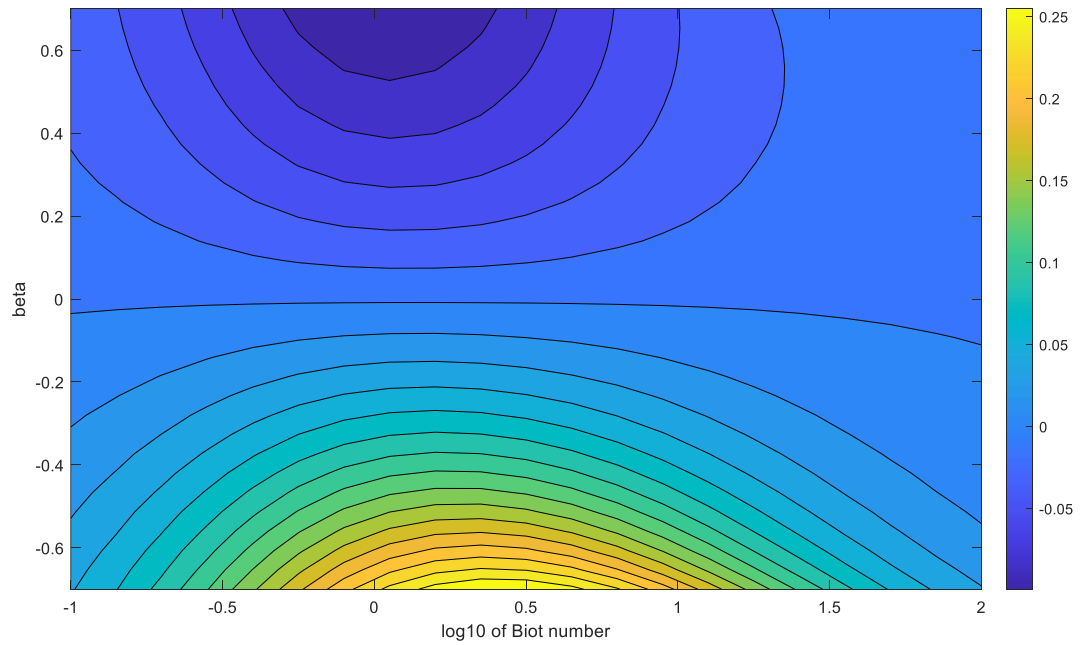


Figure 39: Fractional reduction in freezing time as a function of the log base 10 of the Biot number and the value of the blast freezing parameter for $\theta_f = 0.25$.

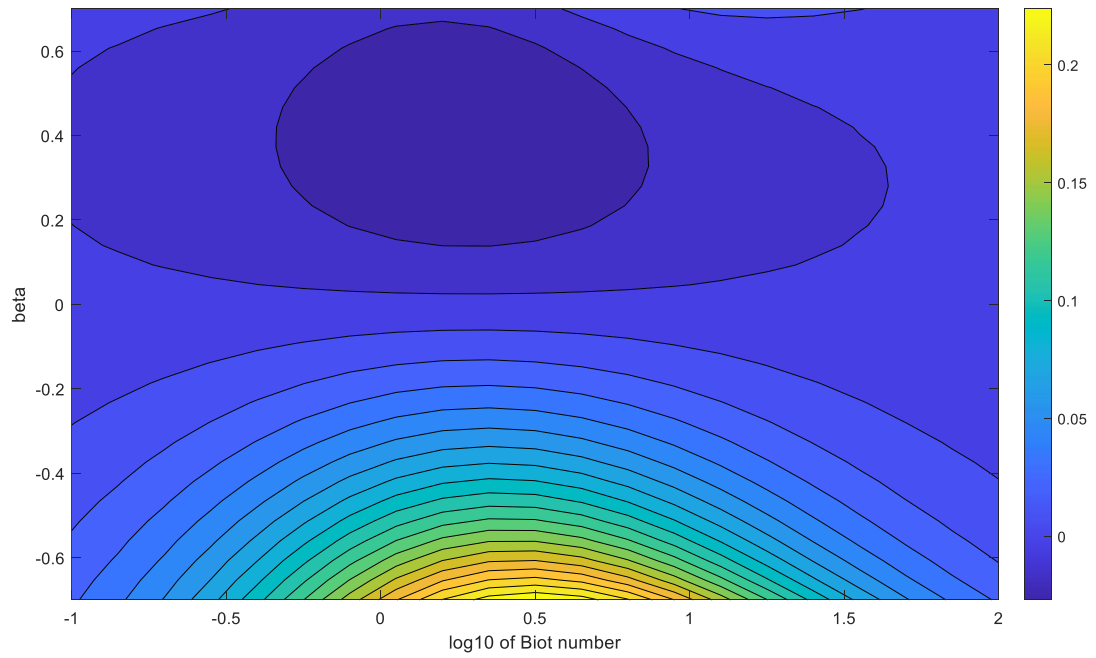


Figure 40: Fractional reduction in freezing time as a function of the log base 10 of the Biot number and the value of the blast freezing parameter for $\theta_f = 0.5$.

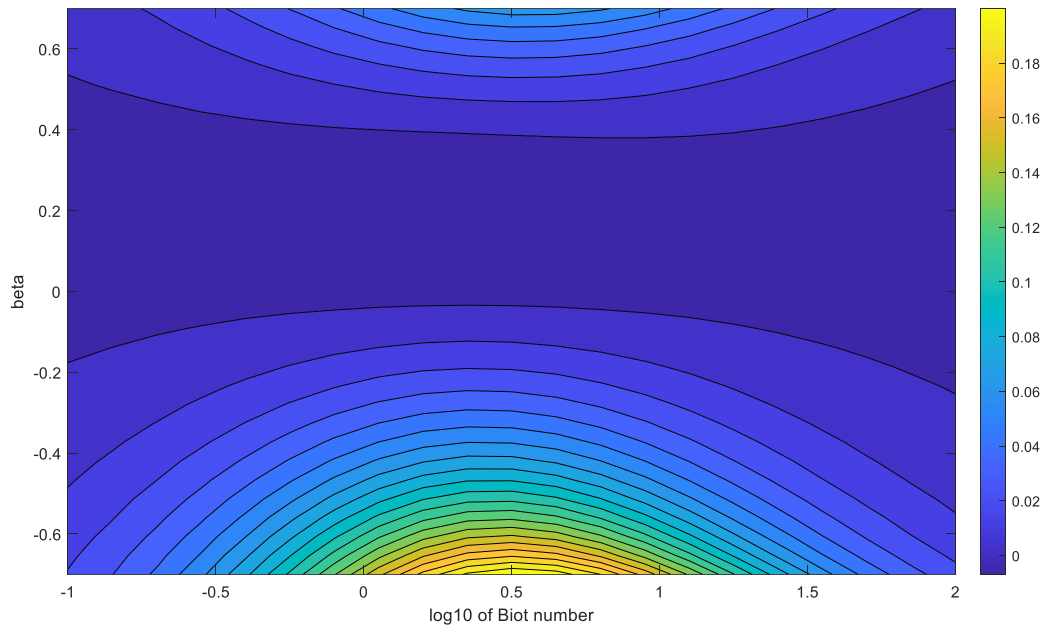


Figure 41: Fractional reduction in freezing time as a function of the log base 10 of the Biot number and the value of the blast freezing parameter for $\theta_f = 0.75$.

Figure 39 through Figure 41 show that **under all conditions the blast early approach is better than the blast late approach** (i.e., it is better to be on the $\beta > 0$ side of the graph). The dark blue area near the top of Figure 39, where $fr < 0$, is where the blast early effect shows better performance in freezing and can achieve nearly a 10% reduction in freezing time compared to even a constant heat transfer coefficient under certain conditions. Remarkably, compared to the blast late case, **for some values of β and Bi , there is a 30% improvement in freezing time if blast early is implemented**. For example, in Figure 39 ($\theta_f = 0.25$), at a $\beta = 0.7$, and \log_{10} of Bi of 0, $fr = -0.10$. At $\beta = -0.7$, \log_{10} of Bi of 0, $fr = 0.2$. The difference in these freezing reductions is 0.30, or 30%.

The significance of the blast effect is diminished as θ_f is increased (corresponding to requiring that the center temperature approach the ambient temperature more closely). The importance and benefit of blasting earlier is therefore more pronounced for blast freezers using a lower temperature air stream with

product exit temperatures that are not approaching the air temperature which is the case for the vast majority of dynamic freezing systems in operation today.

Notice that the impact of the blast freezing process approaches zero at both high and low values of Bi . At high values of Bi , the resistance to heat transfer is almost entirely internal due to conduction and the surface temperature is very close to T_∞ throughout the process and less affected by variations in the surface heat transfer coefficient. At low values of Bi , the resistance to heat transfer is almost entirely due to convection and the lumped capacitance approximation becomes justified. It is less obvious why fr should approach zero in this low Bi regime.

As Bi approaches zero we can develop a lumped capacitance model; an energy balance on the material (all of the material since internal temperature gradients can be ignored) provides:

$$h(t)(T_\infty - T) = \rho c L \frac{dT}{dt} \quad (51)$$

with the initial condition:

$$T_{t=0} = T_{ini} \quad (52)$$

We can nondimensionalize Eq. 51 by defining the same dimensionless temperature:

$$\theta = \frac{T - T_{ini}}{T_\infty - T_{ini}} \quad (53)$$

and a dimensionless time that is normalized using the lumped capacitance time constant

$$\hat{t} = \frac{th_{avg}}{\rho c L} \quad (54)$$

Substituting Eqs. 53 and 54 into Eqs. 51 and 52 provides:

$$(1 \pm \beta)(1 - \theta) = \frac{d\theta}{d\hat{t}} \quad (55)$$

with

$$\theta_{\hat{t}=0} = 0 \quad (56)$$

For the first half of the process ($0 < \hat{t} < \hat{t}_f/2$) the positive value is used in Eq. 55 while the negative value is used for the last half ($\hat{t}_f/2 < \hat{t} < \hat{t}_f$). Therefore, Eq. 55 can be written as:

$$(1 + \beta)(1 - \theta) = \frac{d\theta}{d\hat{t}} \text{ for } 0 < \hat{t} < \frac{\hat{t}_f}{2} \quad (57)$$

Separating Eq. 57 and integrating leads to:

$$(1 + \beta) \int_0^{\hat{t}_f/2} d\hat{t} = \int_0^{\theta_{\hat{t}=\hat{t}_f/2}} \frac{d\theta}{(1 - \theta)} \quad (58)$$

which leads to:

$$(1 + \beta) \frac{\hat{t}_f}{2} = -\ln(1 - \theta_{\hat{t}=\hat{t}_f/2}) \quad (59)$$

Solving for $\theta_{\hat{t}=\hat{t}_f/2}$ provides:

$$\theta_{\hat{t}=\hat{t}_f/2} = 1 - \exp\left[-(1 + \beta) \frac{\hat{t}_f}{2}\right] \quad (60)$$

For the second half of the process Eq. 55 can be written as:

$$(1 - \beta)(1 - \theta) = \frac{d\theta}{d\hat{t}} \text{ for } \frac{\hat{t}_f}{2} < \hat{t} < \hat{t}_f \quad (61)$$

Separating and integrating Eq. 61 leads to:

$$(1 - \beta) \int_{\hat{t}_f/2}^{\hat{t}_f} d\hat{t} = \int_{1 - \exp\left[-(1 + \beta) \frac{\hat{t}_f}{2}\right]}^{\theta_f} \frac{d\theta}{(1 - \theta)} \quad (62)$$

or:

$$(1 - \beta) \frac{\hat{t}_f}{2} = -\ln\left[\frac{1 - \theta_f}{\exp\left[-(1 + \beta) \frac{\hat{t}_f}{2}\right]}\right] \quad (63)$$

Solving Eq. 63 provides:

$$\exp\left[-(1 - \beta) \frac{\hat{t}_f}{2}\right] \exp\left[-(1 + \beta) \frac{\hat{t}_f}{2}\right] = 1 - \theta_f \quad (64)$$

or:

$$\theta_f = 1 - \exp\left[-(1 - \beta)\frac{\hat{t}_f}{2} - (1 + \beta)\frac{\hat{t}_f}{2}\right] \quad (65)$$

Simplifying provides:

$$\theta_f = 1 - \exp[-\hat{t}_f] \quad (66)$$

and therefore the freezing time does not depend on β for cases where Bi is approaching zero.

The development of the dimensionless model for the blast effect highlights the intricate interplay between heat transfer dynamics and freezing performance under varying surface heat transfer coefficient conditions. By leveraging a systematic numerical approach, the model effectively predicted the impact of key parameters, namely, the Biot number, the relative amplitude of heat transfer coefficient changes, and the dimensionless freezing temperature, on the dimensionless freezing time. Results indicate that implementing a "blast early" strategy ($\beta > 0$) consistently reduced freezing time compared to both the "blast late" strategy ($\beta < 0$) and the constant ("do nothing") heat transfer coefficient scenario ($\beta = 0$), with reductions up to 30% in certain parameter spaces.

Importantly, the benefits of the blast early approach diminish as θ_f increases, reflecting reduced sensitivity when the center temperature more closely approached ambient conditions. The model also revealed diminishing effects at both high and low Biot numbers. At high Bi values, the dominance of conduction minimizes the influence of convection variations, while at low Bi , the lumped capacitance approximation explains the negligible impact of varying heat transfer coefficients. The lumped capacitance analysis confirmed that freezing time is independent of β in this regime.

These insights highlight the importance of the awareness of the blast effect in designing freezing processes that involve an interaction of moving food products and high air velocity such as in spiral blast freezers. Practically, it is much better to blast food early with higher air velocity than blast late. It will be

shown in Chapter 3.3 using Monte Carlo simulations with a dough product that it is essentially as beneficial to have a relatively constant airflow in a spiral freezer. However, blasting product with higher velocity air later in the cooling process can be detrimental given the airflow path and the specific thermal properties of the food (including dough). The dimensionless blast effect model provides a foundation for further exploration of heat transfer dynamics in freezing applications and the pursuit of air flow arrangements that preferentially deliver higher air velocity across the product early in its dwell time within the freezer. To the author's knowledge, this phenomenon has never been described in any other known research in food engineering or heat transfer.

3.2.5 Selectable Food Types and Geometries

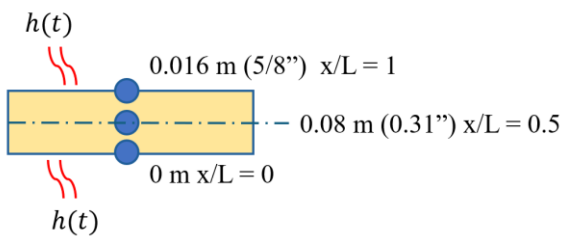
In the previously established 1-D plane wall model introduced in Section 2.1.1, heat transfer was modeled as occurring in a linear direction, resulting in relatively uniform temperature reductions across the thickness of the product slab. To further investigate the model's behavior, the food type was changed from dough to modeled chicken breast, allowing for the examination of how the slab model responds to significantly different thermal properties, including thermal conductivity, heat capacity (influenced by water content), and density.

This comparative analysis aimed to evaluate the impact of these differing thermal properties on the freezing process. A detailed derivation of the chicken breast's thermal properties can be found in the Appendix, while Table 7 summarizes the three primary thermal properties, comparatively, for dough and chicken. The "Effect" column in Table 7, discussed later in this section, quantifies the influence of these property changes. The "Chicken/Dough" ratio highlights the relative difference between the thermal properties of chicken breast and dough, serving as a basis for understanding the distinct thermal responses of these two materials in the freezing model.

Table 7: Thermal properties of dough and chicken breast compared.

Properties at 300K						
	Symbol	Units	Dough	Chicken breast	Chicken/dough	Effect
Thermal conductivity	k	W/m-K	0.2531	0.5398	2.13	1.07x
Heat capacity	c	J/kg-K	2097	3490	1.66	0.468x
Density	ρ	kg/m ³	533.8	1150	2.15	0.462x

For comparative purposes, a simplified version of the standard plane model of pizza crust is shown in Figure 42, which is 5/8" thick and experiences convection on its upper and lower surfaces. Its upper surface can be defined as $x/L = 1$, lower surface defined as $x/L = 0$, and center point as $x/L = 0.5$. Recall that the temperature at this center point is what is being controlled by the model (by adjusting belt speed). The actual model had 40 nodes – only 3 are shown in the figure for simplification.

**Figure 42:** 1-D plane model shown with highlighted locations corresponding to Figure 43.

In Figure 43, (a) and (b) show the dough slab experiencing the baseline velocity profile from Plant 1, and (c) and (d) show the same geometry changed to a slab of chicken instead of dough.

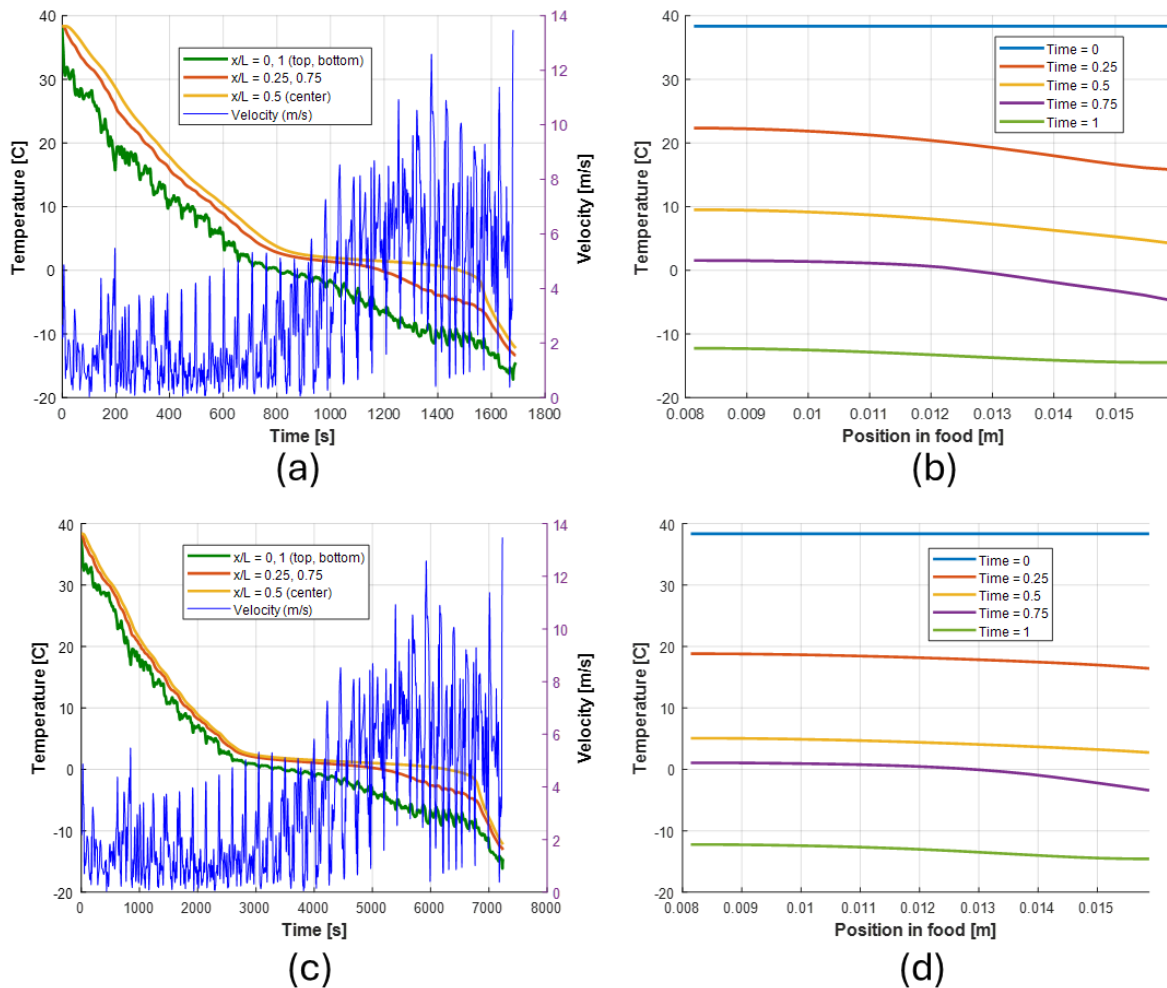


Figure 43: The original dough slab is shown in (a) and (b) and the same slab geometry changed to chicken breast is shown in (c) and (d).

If the constraint of achieving a product center temperature of 10°F (-12.2°C) upon exiting the freezer was enforced, the change to chicken resulted in a significant reduction in belt speed from 141.7 to 32.9 products per minute, or 23% of the dough's belt speed. In other words, the dough product could be processed 4.3 times faster than chicken. The temperature profiles shown in (b) and (d) in Figure 43 illustrate the product temperatures at various positions along the slab as a function of five dimensionless dwell times. These graphs reveal that chicken exhibits a flatter temperature profile at each dwell time compared to dough, likely due to its longer dwell time, which allows for greater conduction-driven heat

transfer within the product. The substantially lower belt speed for chicken can be partially attributed to its higher water content, which leads to a higher heat capacity. In this study, chicken was modeled with a total water content of 77%, compared to only 35% for the dough, further explaining the increased thermal load and slower processing speed for chicken.

A sensitivity study was conducted to isolate the effects of individual thermal properties by standardizing all other properties and varying only one at a time. The results, summarized in the “Effect” column of Table 7, provide insights into the influence of each property. For instance, the thermal conductivity of chicken breast meat was found to be 2.13 times that of dough, which intuitively suggests enhanced heat transfer within the chicken. However, this increase in thermal conductivity translated to only a 7% improvement in belt speed for chicken. This relatively modest effect is likely due to the surface heat transfer coefficient acting as the limiting factor in the freezing process, rather than internal conduction within the food itself.

In the next phase of the sensitivity study, only the heat capacity of the dough model was adjusted to match that of chicken, while other properties remained constant. Chicken’s heat capacity is 1.66 times greater than that of dough, which intuitively suggests that it would require more time to freeze, resulting in a slower belt speed. The analysis confirmed this, with the belt speed reducing to 66.3 products per minute compared to the original 141.7, or 46.8% of the speed achieved with dough. This means that the belt speed for dough is approximately 2.1 times faster than chicken when only heat capacity is considered, indicating that heat capacity has a slightly greater than 1:1 effect on belt speed.

Lastly, the density of the dough model was adjusted to match that of chicken while heat capacity and other properties were kept unchanged. Chicken’s density is 2.15 times greater than that of dough, which would be expected to increase freezing time and slow belt speed. The resulting belt speed dropped to

46.2% of the dough speed, or approximately 2.2 times slower than dough. This finding shows that density has a nearly exact 1:1 effect on belt speed, highlighting its proportional influence on the freezing process.

The subsequent study focused on developing and analyzing a spherical food model to account for the geometric variations found in products like chicken drumsticks, chicken wings, meat chunks, or other items with thicker profiles and potentially different volume-to-surface area ratios compared to the previously studied dough slab. The 1-D conduction model was re-derived in spherical coordinates to reflect the radial symmetry of such food items. This approach allowed for a more accurate representation of the heat transfer process in products with significant curvature.

A product diameter of 2.5 inches was selected as the baseline for the study. To simulate the conduction process within the spherical geometry, a vector of radial nodes, $r(i)$, was defined according to the following equation (with the other variables previously introduced in Table 1):

$$r(i) = \left(\frac{(i-1)L}{N-1} \right) \quad (67)$$

The center node is unique since it only experiences conduction in one direction and is derived:

$$\frac{dT_1}{dt} = \frac{4\pi k_{T_1, T_2} \left(r_1 + \frac{\Delta r}{2} \right)^2 (T_2 - T_1)}{\Delta r \rho_1 c_1 \left(\frac{4\pi}{3} \left(\frac{\Delta r}{2} \right)^3 \right)} \quad (68)$$

The second node, which is also unique in a spherical model, is shown:

$$\frac{dT_2}{dt} = \frac{4\pi k_{T_1, T_2} \left(r_1 + \frac{\Delta r}{2} \right)^2 \frac{(T_2 - T_1)}{\Delta r} + \frac{4\pi k_{T_3, T_2} (T_3 - T_2)}{\left(\left(\frac{1}{r_2} + \frac{1}{r_3} \right) \right)}{\rho_2 c_2 \left(\frac{4\pi}{3} \left(\left(r_2 + \frac{\Delta y}{2} \right)^3 - \left(r_2 - \frac{\Delta y}{2} \right)^3 \right) \right)} \quad (69)$$

The internal nodes are shown next:

$$\frac{dT_i}{dt} = \frac{4\pi k_{T_{i-1}, T_i} \left(\frac{T_{i-1} - T_i}{\frac{1}{r_{i-1}} - \frac{1}{r_i}} \right) + 4\pi k_{T_{i+1}, T_i} \left(\frac{T_{i+1} - T_i}{\frac{1}{r_i} - \frac{1}{r_{i+1}}} \right)}{\rho_i c_i \left(\frac{4\pi}{3} \left(\left(r_i + \frac{\Delta y}{2} \right)^3 - \left(r_i - \frac{\Delta y}{2} \right)^3 \right) \right)} \quad (70)$$

Lastly, the outer shell of the sphere which experiences forced convection is shown:

$$\frac{dT_N}{dt} = \frac{4\pi k_{T_{N-1}, T_N} \left(\frac{T_{N-1} - T_N}{\frac{1}{r_{N-1}} - \frac{1}{r_N}} \right) + h4\pi D^2 (T_\infty - T_N)}{\rho_N c_N \left(\frac{4\pi}{3} \left((r_N)^3 - \left(r_{N-1} + \frac{\Delta y}{2} \right)^3 \right) \right)} \quad (71)$$

A representation of the spherical model is shown in Figure 44. The actual model had 80 nodes, but only 3 nodes are highlighted in the figure. The radius is 1.25" and the outer shell can be described as $x/R = 1$, with its center point $x/R = 0$, and a point halfway between these two defined as $x/R = 0.5$. Note that in the spherical case, the temperature being controlled is still the center temperature, which is $x/R = 0$, and this is slightly different than the temperature being controlled in the plane model ($x/L = 0.5$). The center of the sphere is necessarily the highest temperature because convection is assumed to be uniform across the entire surface area of the sphere and the food is considered homogeneous.

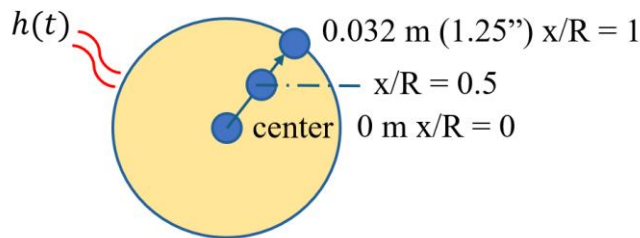


Figure 44: Spherical model of food in radial coordinates with nodes shown in specific locations.

The initial study using the spherical geometry retained all thermal properties of dough while transitioning to the newly derived spherical conduction model. This analysis, illustrated in Figure 45, revealed a belt speed increase to 184.5 products per minute, representing a 1.3x improvement compared to the plane geometry. The increase is likely attributable to the greater surface area provided by the spherical product, enhancing heat transfer. However, practical considerations such as packing limitations, which could restrict airflow and cooling efficiency, were not accounted for in this analysis. Additionally, the use of dough as the modeled product, while useful for consistency, may not fully represent realistic scenarios for spherical food items.

The most significant finding from this study was the temperature profile within the spherical product as a function of time in the freezer. While the outer surface of the food rapidly reached extremely cold temperatures (approaching -35°C), the core required significantly more time to reach the target temperature of -10°C . This pronounced temperature gradient highlights the challenges associated with freezing products with larger volume-to-surface area ratios, emphasizing the importance of considering geometry in optimizing freezing processes.

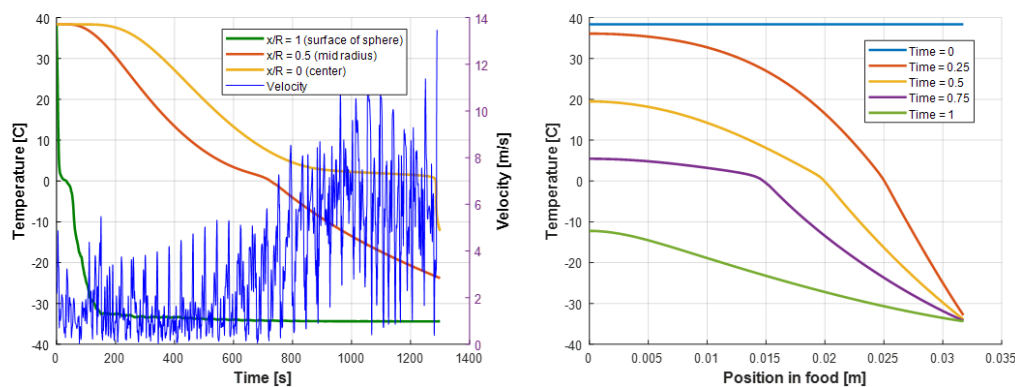


Figure 45: Using dough properties but with a spherical 1-D conduction model.

The last study used both the spherical geometry and changed the food properties to that of chicken breast meat instead of dough. This is shown in Figure 46. The result of this is the belt speed is 58.7, or 41.4% that of the plane model with dough. Recall that maintaining the 1-D plane geometry and switching to chicken resulted in a belt speed of 23% of the original. Therefore, some of that belt speed was recouped by switching to a more spherical product.

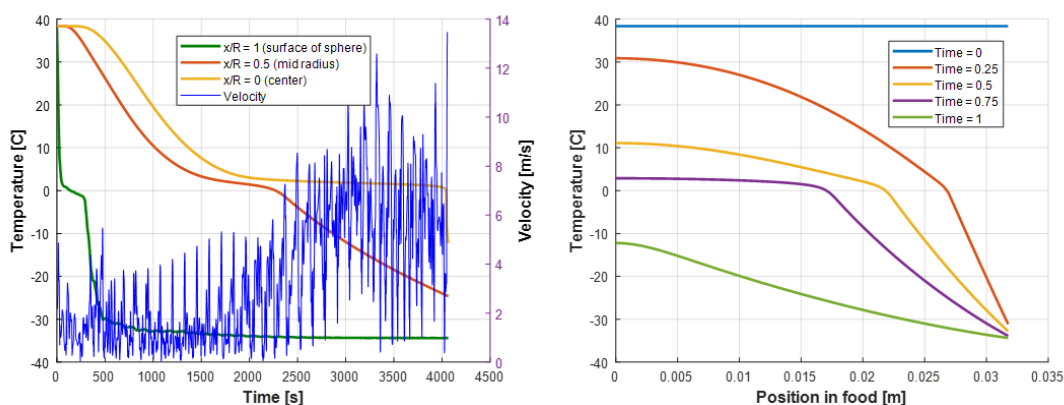


Figure 46: Spherical food model with chicken properties.

Although not studied here, the diameter of the product would undoubtedly have a large influence on these results. One major drawback of the features of the spherical temperature profile shown in Figure 45 and Figure 46 is the extremely cold surface temperature of the product that is reached and then maintained for nearly the entire cooling period. For a product like meat, this could result in quality degradation. However, meat (including chicken and beef) sealed packaging adds significant thermal resistance, complicating this problem – but likely reducing the negative effect as well. Since packaging was not a focal point in the present effort, it was not explicitly studied. Additionally, many chicken and meat products are purposely only “crust frozen” to preserve moisture while qualifying as “fresh” not previously frozen product, and then they are purposely sent to slower, static freezer systems where they slowly equilibrate to a target temperature. The center temperature of meat is often not targeted in a spiral blast freezer in the way that it is with pizza crust. In this regard, a spiral freezer such as the one shown in

Figure 46 accomplishes crust freezing extremely quickly and therefore this belt speed might be able capable of being substantially faster than what is shown with the correct loading and belt speed.

The study of selectable food types and geometries provides insights into how product properties and shapes influence freezing performance in spiral freezers. By comparing the thermal properties of dough and chicken breast, the analysis highlights how factors such as conductivity, heat capacity, and density affect belt speed and freezing efficiency. Sensitivity studies demonstrate the varying impact of individual thermal properties, with heat capacity and density showing the most pronounced effects on belt speed. Transitioning from a planar to a spherical geometry revealed differences in freezing dynamics, including faster belt speeds for spherical products due to increased surface area but also challenges such as extreme surface temperatures that could lead to quality degradation. While the spherical model offers valuable insights, practical considerations such as packaging and industry-specific freezing goals, like crust freezing for chicken, suggest that further studies are needed to fully understand and optimize the interplay between geometry, material properties, and freezing strategies in dynamic systems.

3.3 Monte Carlo Simulation Results

Before introducing results of the Monte Carlo simulations, a limiting case was analyzed that considered a constant velocity throughout the spiral where the magnitude of the constant velocity was allowed to vary from 0.5 m/s and up to 10 m/s. The resulting production throughput for this constant velocity case and the scaled as-found velocity profiles from Figure 35 that lead to the same time average velocity case are compared in Figure 47. Interestingly, the constant velocity profile yielded the best performance compared to the existing and reversed velocity profiles. The motivating question was: *is there a realistic velocity profile that can meet or exceed the performance of this ideal constant velocity case?*

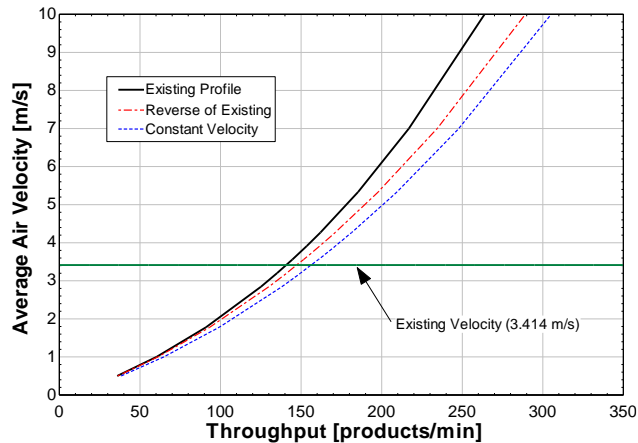


Figure 47: Air velocity as a function of the product throughput (i.e., belt speed) of various velocity schemas.

The Monte Carlo analysis was conducted using 1000s of different randomly generated five-point polynomial velocity profiles using MATLAB's Piecewise Cubic Hermite Interpolating Polynomial (PCHIP) function. A B-spline was also attempted, but the optimization algorithm was more stable using PCHIP. An example of how the algorithm worked is shown in Figure 48 for a five-point case.

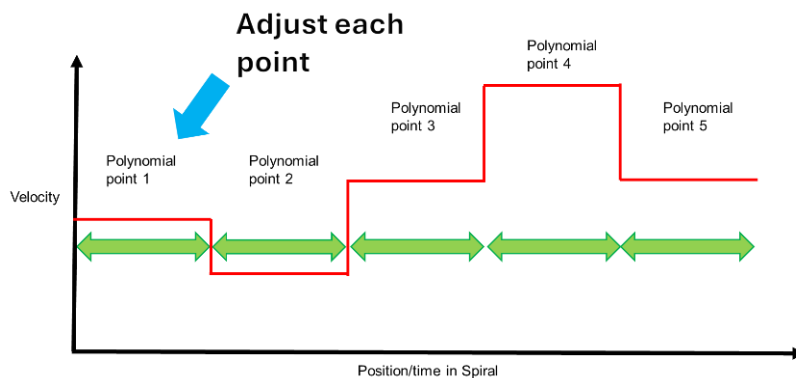


Figure 48: The randomized polynomial generator.

A few examples of the result of the random generator are shown in Figure 49. Multiple constraints were added, including individual limits on each point that kept velocity between 0.1 m/s and 12 m/s, and

later a constraint that was activated by a flag in the code that fixed the average of the entire polynomial to a specified value.

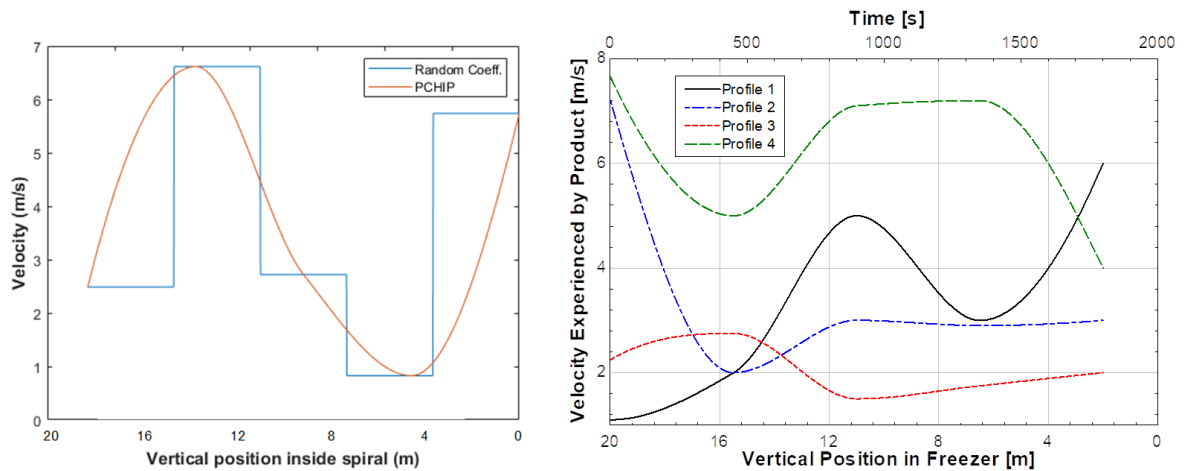


Figure 49: Examples of random velocity profile polynomials generated by the MATLAB algorithm.

3.3.1 Pareto fronts

Throughout this analysis, the air temperature was held constant at -30°F (-34.4°C). Thousands of random velocity profiles were generated across a spectrum of velocity magnitudes to create a Pareto front of the feasible operating domain as shown in Figure 50. What emerges from the analysis are a large number of suboptimal performing velocity profiles appearing above a sharper edge of optimal cases. This sharp edge represents the Pareto front of the best possible performing velocity profiles to achieve a given throughput. Points on the edge of the Pareto graph are top performers that deliver better performance, while points above the leading edge are lower performing.

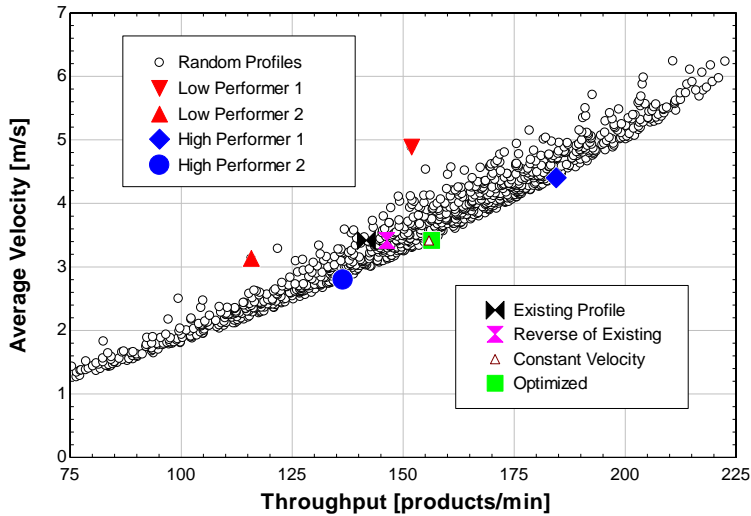


Figure 50: The results of a 1000-point Monte Carlo simulation are shown as a Pareto front along with selected profiles.

Included in Figure 50 are symbols that correspond to various, interesting velocity profiles; these include the two profiles analyzed previously and shown in Figure 35, two suboptimal velocity profiles, and two high performing velocity profiles. Figure 51 compares the two highlighted poor performing velocity profiles (on the left) where both exhibit low velocity over the product early in the dwell time, followed by a high peak of velocity in the latter half of the product's dwell time. The two high performing velocity profiles (right) show much higher air velocity over the product early in the dwell time and have a relatively constant velocity throughout the entire dwell time. High velocity peaks are penalized because of the less than linear impact that velocity has on the resulting heat transfer coefficient, as shown in Equation 9.

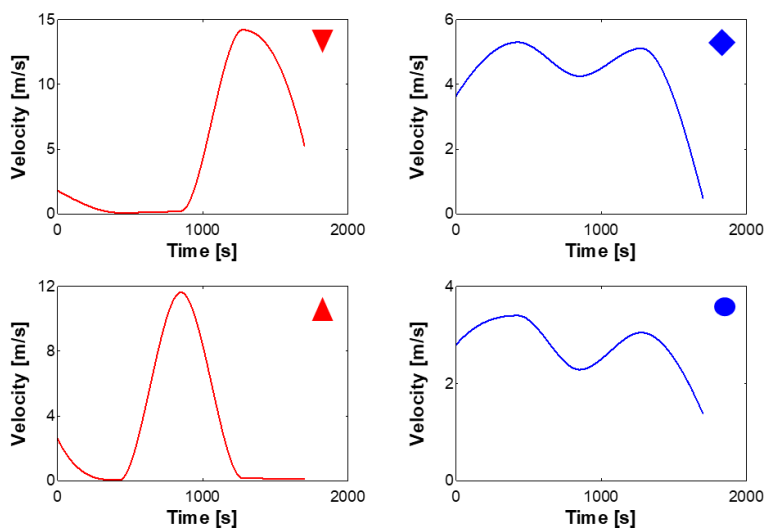


Figure 51: Low (left) and high (right) performing velocity profiles from Figure 50.

3.4 Optimization Results

Figure 50 showed an optimized velocity profile denoted as a square. To determine this condition, a velocity profile near the Pareto front was selected. **The best performing velocity profile produced a 26% higher throughput than the lowest performer at the same average velocity.** Next, an additional optimization algorithm was written that varied the five base points of the polynomial that made up the selected best performing velocity profile while maximizing the throughput to achieve the global optimum profile to determine if any further improvement could be obtained.

The optimal velocity profile, as determined from the Monte Carlo randomization and the further optimization refinement, is shown in Figure 52. The optimized velocity profile produced 156.4 products/min, which is a 10.4% improvement over the existing base case velocity profile which netted 141.7 products/min. For reference, the constant average velocity case (i.e., a straight horizontal line of 3.414 m/s), resulted in a 10.0% improvement over the base case – very close to the best non-constant velocity profile evaluated. Therefore, the characteristics of higher performing profiles in a spiral freezer

will have higher velocity early in the dwell time, but it is nearly equally beneficial to provide a relatively constant air velocity throughout the dwell time. The worst performing velocity profiles have relatively high periods (i.e., peaks) of velocity late and low velocity early in the freezing process, and can result in performance reductions greater than 10%. This type of temporal velocity profile should be avoided. This result agrees with the blast effect phenomenon described in Section 3.2.3.

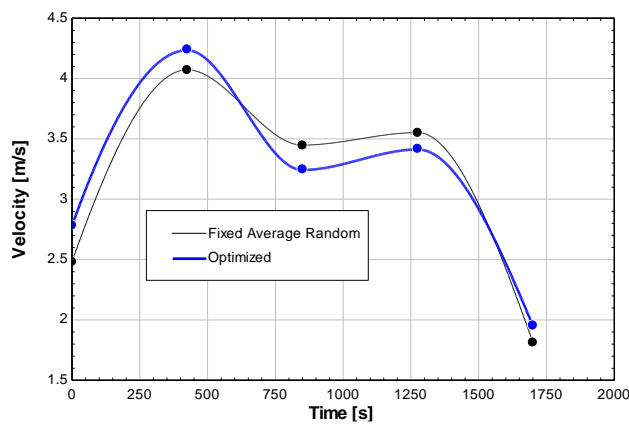


Figure 52: The optimized velocity profile is shown.

The optimum velocity profile scaled to different average velocities continues along the Pareto front, implying that an effective air flow design will perform well at many different velocity magnitudes, as shown in Figure 53.

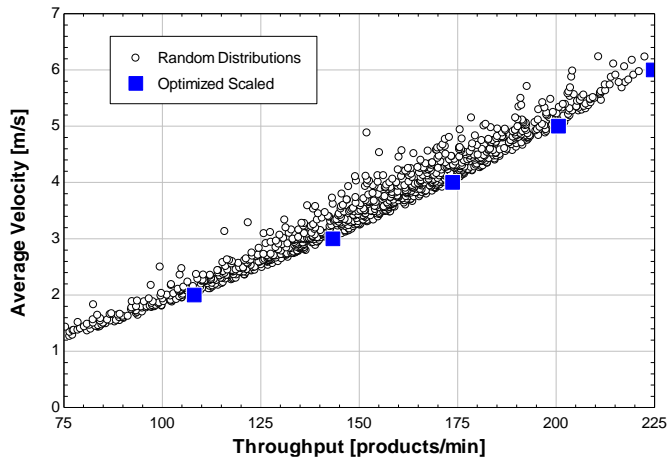


Figure 53: The optimized velocity profile is shown scaled along the Pareto front.

3.5 Cyclical Variation

The previous analysis was focused on a time-varying velocity profile with a relatively low frequency of velocity variation (i.e., relatively large time periods between velocity variations which is consistent with five points defining the velocity distribution). The actual velocity data from Figure 35 shows that there is a substantial higher frequency component in the temporal velocity fluctuations due to the product traveling in the helical path of the spiral where it experiences large velocity changes during each revolution of the spiral conveyor belt. There are as many oscillations in air velocity across the product as there are number of tiers of the spiral (typically over 30). This effect was introduced when explaining the CFD results in Section 3.1.2. Often the fluctuations in air velocity within the spiral are quite large relative to the mean velocity. The velocity profiles used in the Monte Carlo analysis and the resulting optimal profiles found are much smoother, which raises the question of their validity in an actual freezing system that unavoidably contains higher frequency velocity oscillations. To more clearly understand the effect of higher frequency velocity variation on freezing performance, a large amplitude sinusoidal oscillation was added to the optimum profile identified in the optimization analysis which corresponded to the tier-to-tier frequency of Plant 1. Figure 54 (left) shows the product temperature response for the smooth, ideal velocity case from Figure 52 while Figure 54 (right) shows the product temperature response for the same

average velocity but with the high frequency component added. The impact to product temperature for the high frequency oscillation is minimal except at the surface of the product. The belt speed optimizing algorithm determined that the dwell time with the smooth profile was 1% less than the case with the oscillations, which alternatively means less than 1% faster belt speed (i.e., product throughput) for the smooth case relative to the oscillating case. In other words, the higher frequency oscillations in air velocity experienced by the product as it travels around the helical spiral do not have a substantial effect on overall freezing system performance; rather, the velocity variation over a much longer time scale is more important.

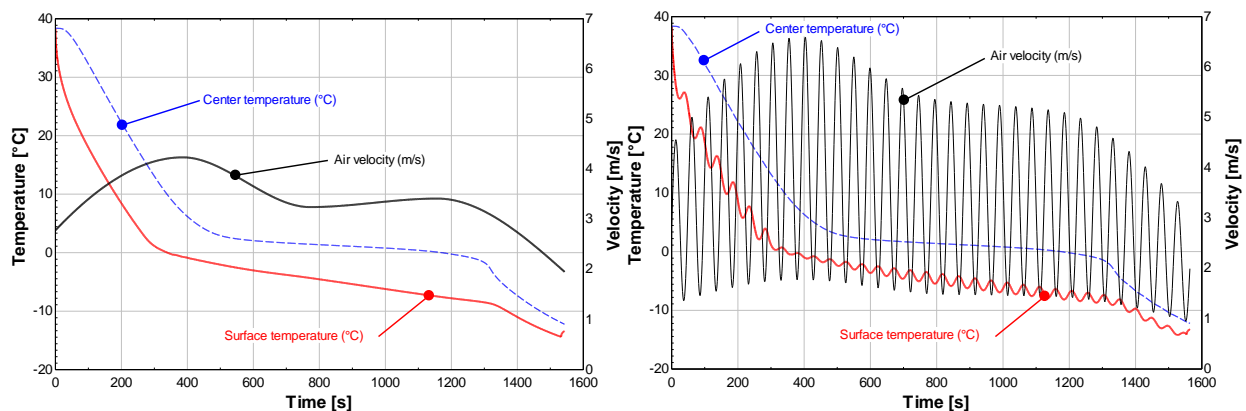


Figure 54: The left figure shows a smooth optimal velocity profile and the associated product temperature. A large, high frequency oscillation is added to the velocity in the right figure.

3.6 Optimization Techniques on an Overall System

An energy model of a spiral freezer within a food production plant was developed to account for key thermal loads, variable compressor efficiency as a function of suction pressure and condensing temperature, fan power scaling with the cube of airflow (CFM), and variable product throughput. Table 8 provides a summary of the thermal loads and their respective contributions to the model under operating conditions of approximately 144 products per minute, a condensing temperature of 35°C (95°F), and a

freezer temperature of -34.5°C (-30.1°F). This load analysis is based on the foundational work of Tyler Young (2023), with modifications to incorporate the flexibility of variable load capabilities.

Table 8: General energy balance.

General energy balance/load calculations		
Source	kW	%
Heat leak through floor	1.1	0.2
Infiltration (air changes)	58.7	10.9
Fan motor heat	18.6	3.5
Fan energy	121.7	22.6
Product load	332.3	61.8
Transmission through walls	5.3	1.0
Total:	537.7	

As illustrated in Table 8, the primary contributors to the energy balance of the system are the product load and fan energy. To accurately represent the refrigerant-side dynamics, a variable efficiency two-stage refrigeration system model was developed, as depicted in Figure 55. This model transitioned between single-stage and two-stage operation at a specified evaporator temperature, and this trajectory is denoted by the green line in the figure. This approach ensures that the system consistently operates at optimal efficiency based on the prevailing conditions.

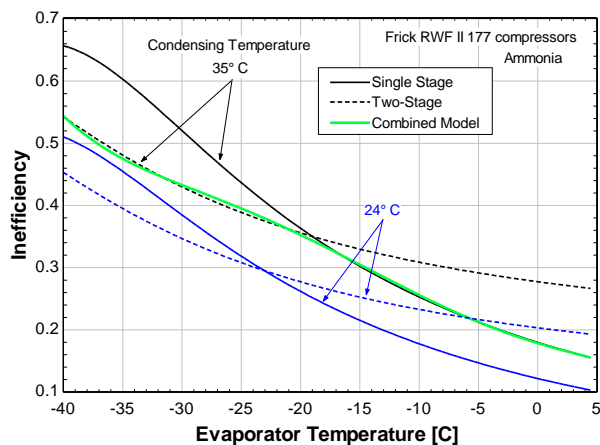


Figure 55: Inefficiency of single and two-stage ammonia refrigeration systems as a function of evaporator temperature.

In Figure 55, inefficiency is represented by the amount of electrical energy required to deliver the necessary cooling capacity. As the evaporator temperature decreases, inefficiency increases, indicating a proportional decline in system efficiency and more energy consumption per unit of cooling. The compressor modeled in this analysis is a Frick RWF II 177 ammonia compressor, with its performance parameters derived using Frick's Coolware software (Frick, 2023).

Hundreds of combinations of conditions were evaluated using the thermal model, leveraging the Monte Carlo simulation techniques from Section 3.3. These simulations incorporated variations in air velocity within the spiral freezer, air delivery temperature, and resultant product throughput. Assuming evaporator capacity is not a limiting factor, the results are presented in Figure 56. The left panel illustrates that achieving maximum throughput requires maintaining the freezer temperature (i.e., evaporator temperature) as low as possible, with air velocity having the most significant impact on throughput beyond a threshold evaporator temperature. The right panel of Figure 56 indicates that the energy cost per hour of facility operation remains relatively stable when lowering the evaporator temperature; however, increasing fan speed to deliver higher air velocities significantly raises energy costs. This highlights the importance of optimizing baffling to improve air delivery to the products without increasing fan power.

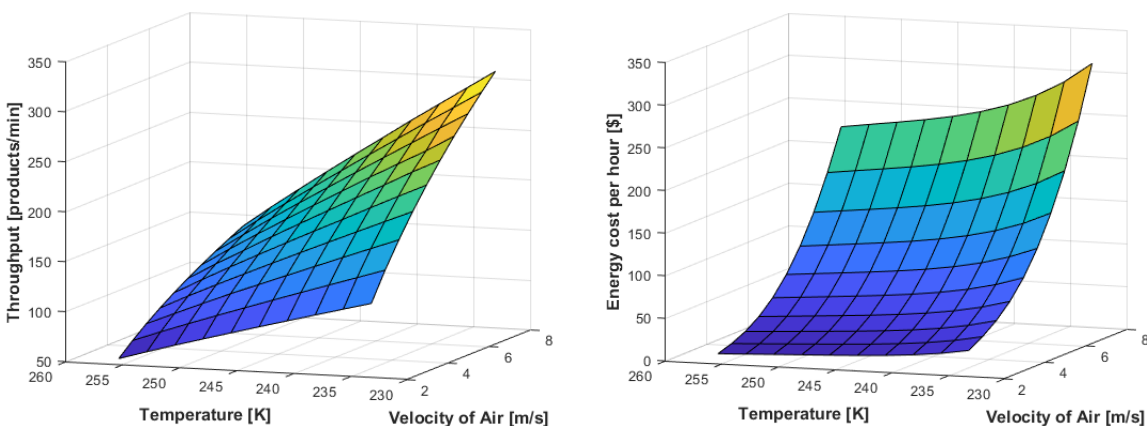


Figure 56: The results of an energy analysis on a spiral blast freezer showing the operating envelope subject to common constraints.

Optimizing the overall energy performance of a spiral freezer requires balancing multiple factors, including air velocity, evaporator temperature, and system efficiency. While maintaining a lower evaporator temperature can significantly enhance product throughput, the feasibility of implementing such changes is constrained by the interconnected nature of refrigeration systems in food production plants. Since spiral freezers often share a common refrigerant supply at a plant-level suction pressure, reducing the evaporator temperature for a single freezer would often necessitate a plant-wide adjustment of suction pressure which may not be practical for a wide range of facilities without significant capital investment. This adjustment would incur additional energy costs across the facility, magnifying the financial implications of such a change. Conversely, controlling air velocity within an individual spiral freezer is a more practical and probably more cost-effective solution, as it can be independently managed using variable frequency drives (VFDs) on fans (assuming the fans have this capability).

The analysis demonstrated that air velocity has the largest impact on throughput beyond a certain evaporator temperature, but increasing fan speed also raises energy consumption exponentially due to the cubic relationship between fan power and air velocity. This reinforces the need for improved airflow management, such as baffling strategies, to enhance air delivery without relying on increased fan power.

Ultimately, while lowering evaporator temperature offers performance gains, its broader implications on plant operations and costs make air velocity optimization within individual freezers an enticing strategy for enhancing efficiency.

3.7 Phantom I Field Testing

Thus far, the analyses and findings presented in Chapter 3 have been primarily theoretical. The development and deployment of a heat transfer instrument, the Phantom I, were pivotal in validating key aspects of this work. Certain results, such as the significant cyclical variations in velocity within a spiral freezer, appeared to contradict established literature, underscoring the need for anchoring the theoretical analysis with empirical verification. Additionally, the “velocity profiles” predicted by the CFD simulations for Plant 1 were untested hypotheses requiring experimental substantiation. The “blast effect,” which highlighted the critical importance of product flow and airflow direction within a spiral freezer, especially when there was an airflow imbalance, was never mentioned in any other study to the author’s knowledge. The Phantom I was required as a crucial tool to bridge the gap between the theoretical predictions of this research and real-world observations. Placing a device within an actual operating spiral freezer in a food processing facility to verify the accuracy of the model predictions would provide significant validation and strengthen the credibility of these new findings.

3.7.1 *Measured HTC Compared to Model*

The Phantom I was prepared for deployment on-site at Plant 1 in a controlled environment maintained at approximately 50°F. Once fully prepared, the Phantom’s core heater was activated, and the aluminum pseudo food product was allowed to reach a temperature of around 100°F (reflecting the typical product temperature at the infeed to the spiral freezer) before being carefully placed inside the operational spiral freezer. The results from Phantom I’s inaugural field deployment, with no data scaling, filtering, or

adjustments, are presented in Figure 57 along with the predicted heat transfer coefficient using velocities from the CFD model.

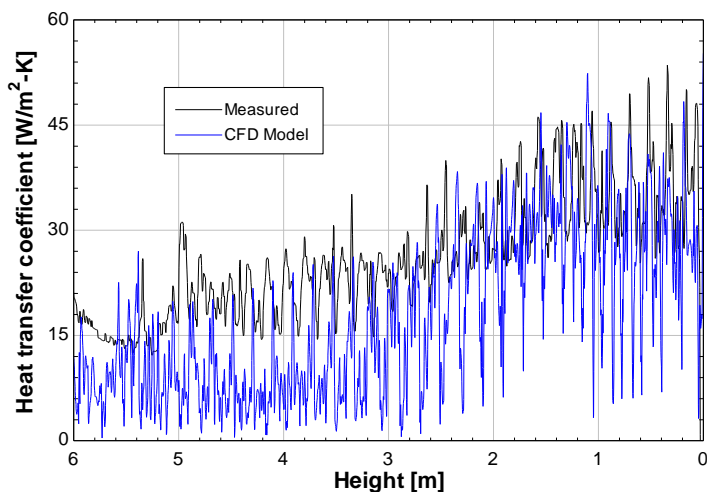


Figure 57: The results of measured heat transfer coefficient and calculated heat transfer coefficient in a spiral freezer.

The results show that the heat transfer coefficients predicted by the CFD modeling align qualitatively and generally with the actual measurements. Notably, this represents the first known measurement of heat transfer coefficients conducted throughout a low temperature spiral freezing system using a dimensionally similar surrogate product, marking an advancement in the field. The results are highly repeatable, with many different runs in the same spiral freezer, operating at identical conditions, appearing very similar to one another. The Phantom I was used in six (6) freezing systems across five (5) different food processing facilities, and this comparative analysis will be shown in Chapter 3.9, but the agreement between the model and one of the other plants is shown in Figure 58, underscoring the reproducibility of the data.

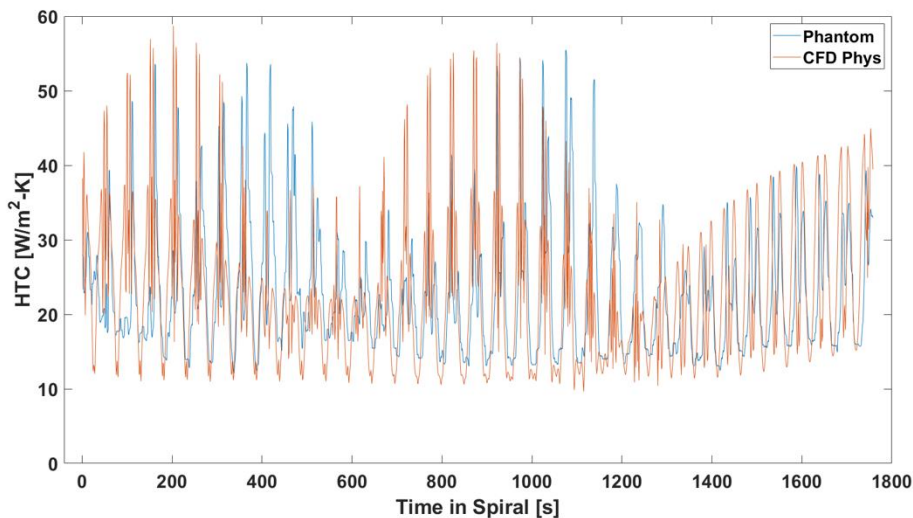


Figure 58: The Phantom I measured data compared to the CFD model.

As Figure 58 shows, there is strong agreement between the Phantom I's measured heat transfer coefficient and that predicted by the CFD velocity converted to heat transfer coefficient by equations shown in Chapter 2.

3.7.2 Uncertainty and Error Bars

An accuracy study (in addition to the one shown in Chapter 2.8) was conducted on measured data from a spiral freezer at a different plant utilizing the pseudo-product. This uncertainty analysis, incorporating a 5% error in heat flux (as specified in the heat flux sensor product literature) and a conservative estimate of a 3°F error in thermocouple measurements, yielded the results shown in Figure 59. Although the heat transfer coefficient varies significantly depending on the Phantom's position within the spiral, due to its proximity to and distance from the fans, the measured values fall within a calculated uncertainty range of 6 to 8%, consistent with uncertainty methods outlined in ASME PTC 19.1 (ASME, 2013).

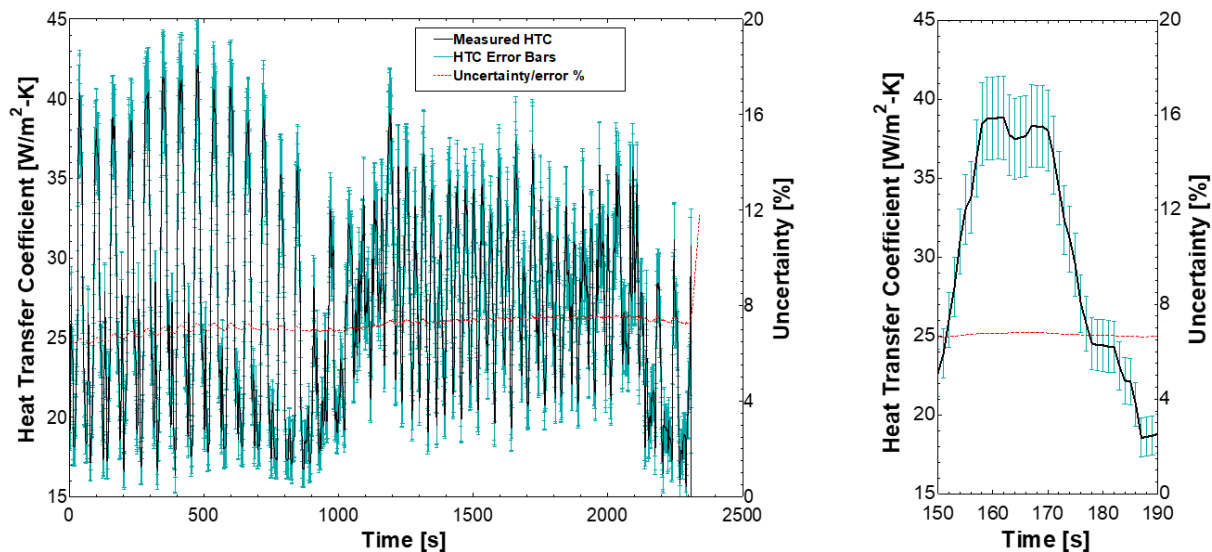


Figure 59: Uncertainty analysis on the phantom product in a spiral freezer from a plant is shown on the left. The right view is a magnified version of the graph showing a typical peak and a trough taken from the data.

As illustrated in Figure 59, including error bars for the Phantom data in every graph would provide minimal additional insight due to the behavior of the data. However, an 8% uncertainty can be assumed for all Phantom data presented subsequently in this work.

3.7.3 Energy Calculations from Phantom I

The Phantom serves as a valuable tool for estimating the heat transfer provided by a spiral freezer to a product. The electrical power supplied to the Phantom is primarily dissipated through convection within the spiral freezer, while the Phantom simultaneously undergoes a global temperature decrease, but then stabilizes with a maintained ΔT . These combined effects represent the net energy removal from the Phantom, offering a practical measurement for benchmarking the performance of air blast freezing systems across different food processing facilities. Figure 60 presents the results from two separate runs of the Phantom within an operational spiral freezer.

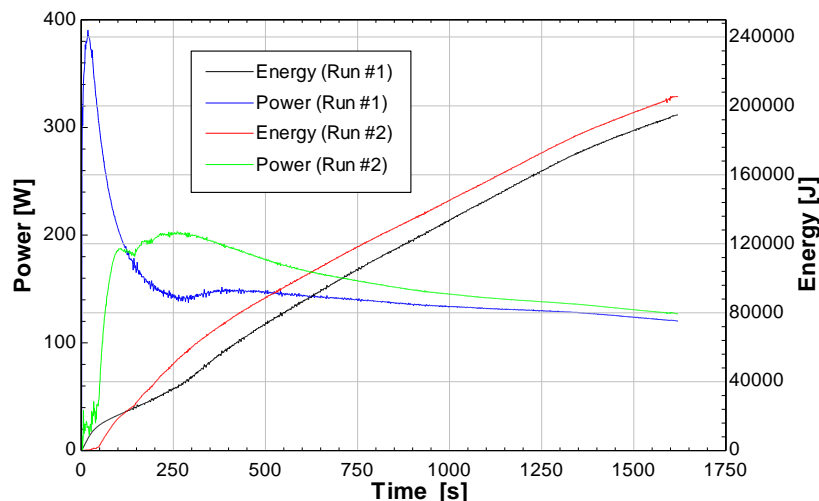


Figure 60: Comparing the power in watts (i.e., electrical and thermal) that the phantom is consuming and also the integral of this (i.e., the total overall energy transfer experienced by the product).

Figure 60 illustrates that after a few minutes, the thermal energy removed from the Phantom stabilizes at approximately 120 W in both Runs #1 and #2. These runs were conducted in the same spiral freezer under comparable operating conditions, including similar product loading configurations, targeted air temperatures, and belt speeds. The total energy removed, measured in joules, is primarily influenced by the dwell time. For a dwell time of approximately 1700 seconds, the Phantom experiences a net energy removal of around 200 kJ in both cases.

It is important to note that the Phantom has a constant supply of electrical energy, introducing an internal energy generation term that causes its temperature to remain elevated within the spiral freezer. This internal energy generation prevents direct comparison of the results shown in Figure 60 with actual food products. However, the Phantom's temperature response over time suggests that the heat removal for

food products may be of a similar magnitude. The temperature of the Phantom does decrease within the spiral freezer from Plant 1 from around 100°F (38°C) to 30°F (-1°C).

A method that can be used to use the Phantom data to compare different freezers is to integrate the measured heat transfer coefficient (h), along with the temperature difference (ΔT) between the surface of the Phantom (T_s) and measured temperature inside the freezer (T_∞), shown in the following equation:

$$\text{int}(HTC\Delta T) = \int_{t=0}^{t=\text{dwell}} h(T_s - T_\infty) dt \quad (72)$$

It was determined that if the surface temperature T_s was held constant, the result of this more closely matches energy balances from the MATLAB model. If $T_s = 30^\circ\text{F}$ (-1.1°C) is used, an example of this integrated heat transfer coefficient is shown in Figure 61.

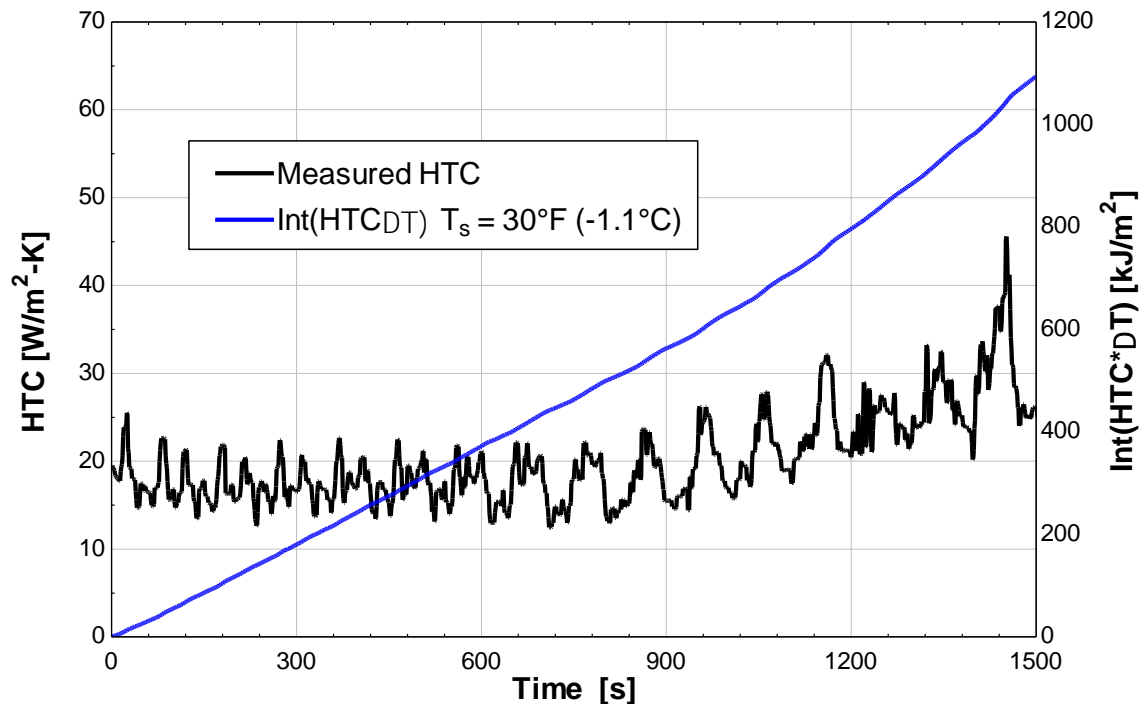


Figure 61: The heat transfer coefficient measured by the Phantom; then multiplied by ΔT and integrated as a function of time in a spiral freezer.

The total integrated heat transfer coefficient shown in Figure 61 is 1093 kJ/m². This can be used to compare the relative performance of spiral freezers. Other metrics that have been used are the time-

averaged heat transfer coefficient \bar{h} (in this case 20.2 W/m²-K), along with the time-averaged temperature T_∞ (-35.1°F /-37.3°C). The last metric used is a simpler version of Equation 72 and is simply the average heat transfer coefficient (\bar{h}) multiplied by the average ΔT :

$$\bar{h}\Delta T = \bar{h}(T_s - T_\infty) \quad (73)$$

If T_s of 30°F (-1.1°C) is used, Eq. 73 produces a $\bar{h}\Delta T$ of 729 W/m² in this example. These metrics will be used to compare 5 plants in Section 3.9 in more detail.

3.7.4 *Phantom Data Versus MATLAB Model*

Data collected from the Phantom, including temperatures and the measured heat transfer coefficient, were integrated into the 1-D heat transfer model. For this analysis, the thermal properties of aluminum, such as density, thermal conductivity, and heat capacity, were used in place of food properties. The resulting comparison between the modeled and actual temperatures is shown in Figure 62. All three Phantom runs in the figure are from the same spiral freezer from Plant 1 with close to the same operating conditions.

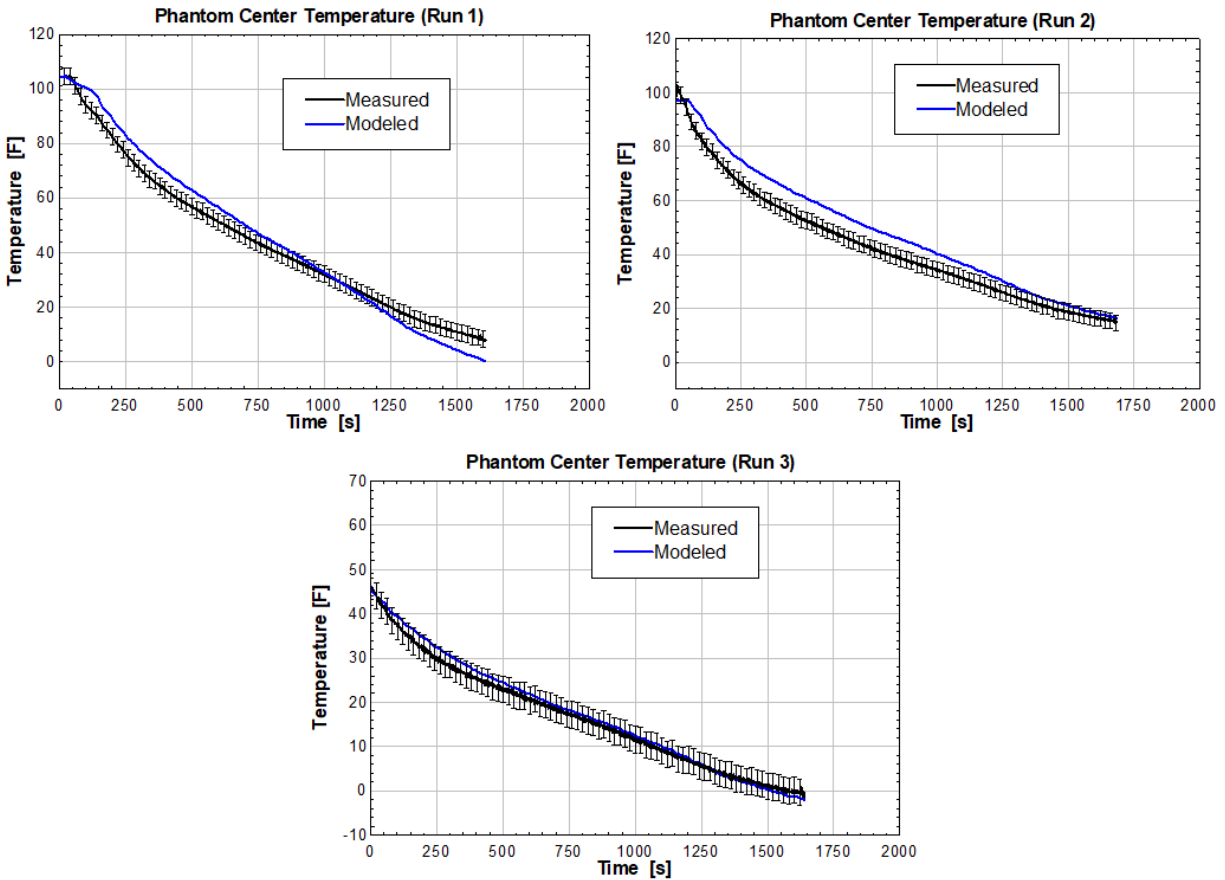


Figure 62: Comparing the phantom modeled temperature to the actual temperature.

The 1-D model demonstrated strong agreement with the temperatures observed during the Phantom's operation inside the wind tunnel discussed in the next section, providing validation for this modeling approach. Variations among the three runs can be attributed to differences in experimental setup. Run 1 was conducted with the spiral belt fully loaded with product, while Run 2 was the same spiral only partially-loaded with product. In Run 3, the Phantom was cooler due to residual thermal effects from a previous run through the spiral and short turnaround time for a second run. Additionally, discrepancies in the temperature profiles could result from the Phantom's positioning relative to other products on the spiral belt. Airflow disruptions caused by neighboring products may have also influenced the heat transfer experienced by the Phantom, introducing potential measurement variability.

3.7.5 *Belt material*

The Phantom I is equipped with a recessed heat flux sensor on its bottom side intended to gather data in order to evaluate heat transfer differences between stainless steel and plastic belts in spiral blast freezers. As introduced in Section 2.3.4, numerous factors influence the heat transfer occurring between a product's bottom surface and the belt, including the belt's open area, material thermal conductivity, air velocity around and through the belt, and contact conditions. Modeling this intricate process requires substantial assumptions, making this evaluation highly complex and impractical. Furthermore, variations in belt design, operational conditions, and freezer configurations across plants complicate direct comparisons of absolute heat transfer values.

Instead, a comparative metric—the ratio of heat transfer from the bottom of the Phantom to that from the top—was used to evaluate a known plastic belt (Blue Acetal Intralox 2600 series) and a stainless steel belt. This approach eliminated the need to account for plant-specific variations and focused on relative performance under similar operating conditions. Figure 63 illustrates this ratio for two plants: one with a plastic belt and the other with a stainless steel belt in their spiral freezers.

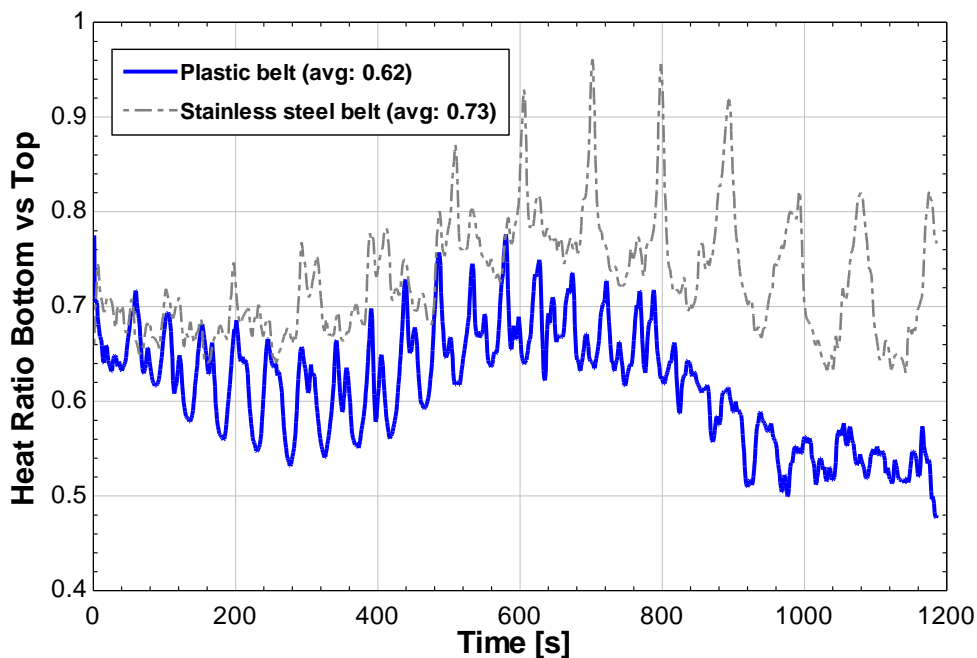


Figure 63: The ratio of heat through the bottom of the Phantom versus the top for different belt materials.

The results in Figure 63 show that the stainless steel belt consistently facilitates greater heat transfer through the bottom of the Phantom compared to the plastic belt throughout the 20-minute observation period. On average, **the stainless steel belt achieved 7% more heat transfer than the plastic belt**. This difference highlights the impact of belt material on thermal performance, with stainless steel's superior thermal conductivity contributing to greater heat transfer. These findings underscore the importance of considering belt material in the design and operation of spiral freezers, particularly for applications where rapid and uniform freezing is critical. Other pros and cons of each belt material were discussed in Section 2.3.4.

3.7.6 Coil Defrost

Coil defrosting is a critical operational function in spiral blast freezers, designed to remove ice buildup from evaporator coils while maintaining the necessary temperature within the freezer space. During a defrost cycle, the targeted coil is typically heated using refrigerant hot gas that can have refrigerant supply

temperatures on the order of 100°F (38°C). To isolate the defrosting coil and minimize its impact on the freezer when defrosting during production, today's spiral freezers utilize dampers on one or both sides of the evaporator coil to "close off airflow" through the coil and reduce parasitic heat load to the spiral. In some freezer designs, the specific fan associated with the defrosting coil is also turned off in attempts to block air flow through the defrosting evaporator. Despite these measures, a defrost cycle can release substantial heat and moisture back into the spiral freezer, potentially impacting the thermal environment. Most of the melted ice from the defrosting coil drains into a heated drain pan and is removed from the system via a gravity drain tube; however, residual heat and moisture may still influence the internal air temperature and product conditions. Therefore, defrost sequence control and operation are critical to sustaining high spiral freezer performance during production periods.

Due to the limited number of temperature sensors typically installed in a spiral freezer, accurately measuring the impact of a defrost cycle on the overall temperature distribution within the freezer space and its effect on the product is challenging. The Phantom, equipped with precise measurement capabilities, offers a unique advantage in capturing the temperature effects of a defrost cycle as experienced by the actual product. As shown in Figure 64, the Phantom's air thermocouple recorded the temperature variations during a defrost event, with time stamps provided by the freezer's programmable logic controller (PLC). While the timing of defrost cycles is usually well-documented, their thermal impact on the product inside the spiral freezer often remains unknown (or denied).

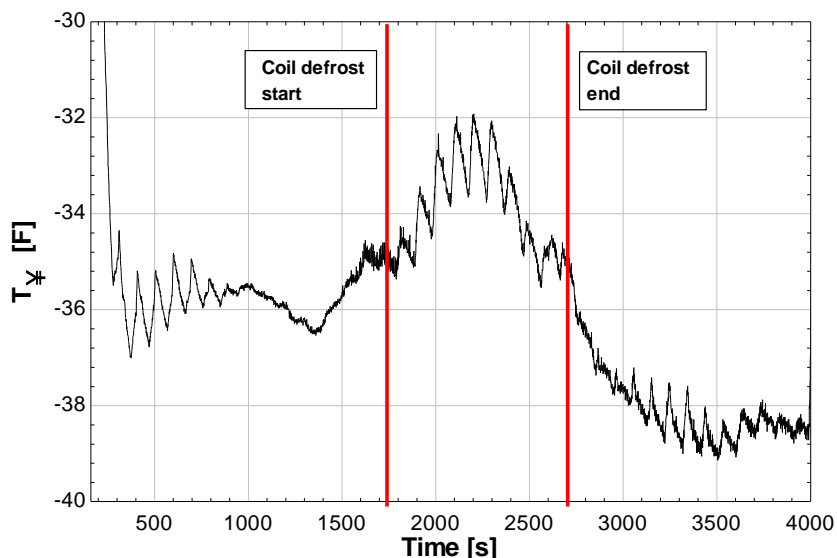


Figure 64: A defrost cycle captured by the Phantom's air thermocouple.

In this specific instance, the defrost cycle lasted approximately 20 minutes and resulted in a measurable temperature rise of at least 3°F (1.7°C). In other cases, temperature increases as large as 7°F (3.9°C) have been observed using the Phantom. These measurements highlight the potential variability in thermal impact caused by defrosting and underscore the importance of understanding these effects to ensure consistent product quality and optimal freezer performance. The ability of the Phantom to quantify these variations provides valuable insights that can inform operational adjustments and improve overall freezer efficiency. It is also noteworthy that the freezer's air temperature after the defrost was substantially below the air temperature prior to defrost reflecting the enhanced evaporator capacity following the removal of accumulated frost on the coil.

3.8 Phantom Wind Tunnel Results

As noted in Section 2.7, Phantom II was built to better understand the effects of directional airflow over a flat plate as opposed to uniform and parallel flow assumed in many of the heat transfer correlation for flat plates. Figure 65 shows the experimental setup of the Phantom II used in the wind tunnel, highlighting the top three heat flux sensors, bottom three heat flux sensors, the center of each of these sets

of three sensors, the angle of air impingement as defined in this study, the direction of airflow, and the bottom of the wind tunnel for reference (not to scale).

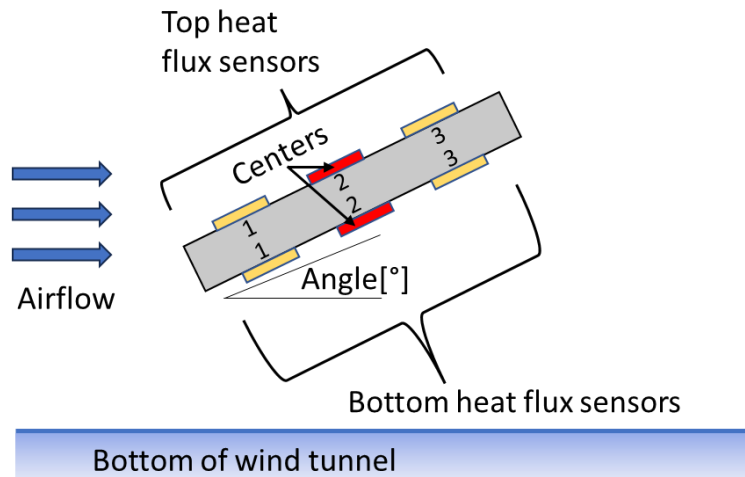


Figure 65: The top heat flux sensors, the bottom heat flux sensors, and the center of each set of sensors, along with the impingement angle of the Phantom II in the wind tunnel.

The air velocity within the wind tunnel used to gather data from Phantom II was varied between 1 and 9 m/s, and the flat plate was pitched at angles ranging from 0° to 90° relative to the airflow direction, as illustrated in Figure 66. The heat transfer coefficient on the top (leeward) surface of the plate exhibited an initial increase in magnitude as the pitch angle increased up to approximately 5° , followed by a decline as the angle continued to rise. These findings represent the average of the three measured heat transfer coefficients on the top of the plate. The initial increase is attributed to flow separation effects occurring at the leading rectangular face of the flat plate, which result from its finite thickness and blunt leading edge which differs from a traditional flat plate that has a thin or knife-like leading edge.

At a pitch angle of approximately 20° , the heat transfer coefficient stabilized and became nearly independent of the pitch angle, remaining at a reduced magnitude compared to the lower angles of attack. This "dead zone" indicates a regime where the influence of angle on the heat transfer coefficient diminishes, and air velocity emerges as the dominant factor affecting overall heat transfer performance.

This behavior underscores the complex interplay between pitch angle, flow separation, and velocity in determining the heat transfer characteristics of the flat plate.

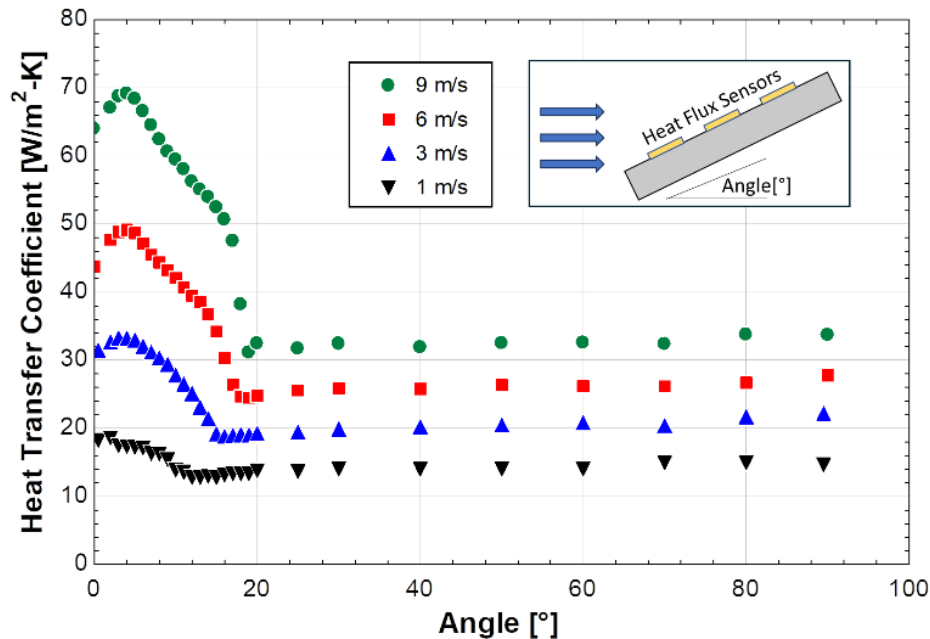


Figure 66: Heat transfer coefficient of a flat blunt object at various angles and velocities.

3.8.1 3-D Data Results

A total of 20,000 data points were collected in the wind tunnel across a range of pitch angles from 0° to 90° and Reynolds numbers between 0 and 90,000. Based on observations from Figure 66, which revealed that critical changes in the top surface's heat transfer coefficient predominantly occur at angles below 20° , testing efforts were concentrated on collecting data in this region. Conversely, as Figure 66 demonstrated, beyond a 20° angle of air impingement, the heat transfer coefficient exhibited minimal variation with angle at a constant Reynolds number. Consequently, less sampling was conducted in this range, as the heat transfer coefficient in this region was largely influenced by Reynolds number alone. The targeted data collection strategy and the resulting distribution of sampled data points are illustrated in Figure 67.

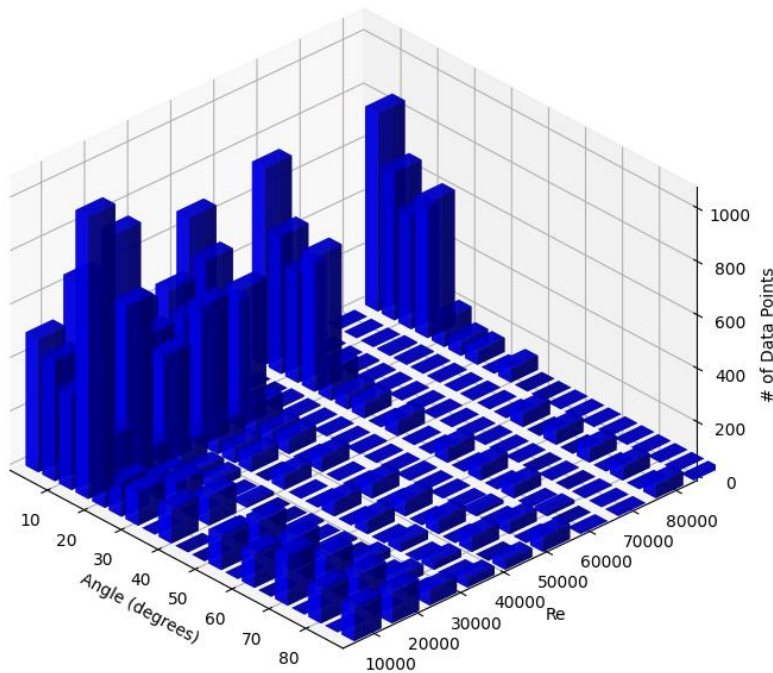


Figure 67: Map of the testing domain of angle range and Reynolds number.

A 3-D representation of the Nusselt number (Nu) as a function of angle and Reynolds number (Re) was generated and is shown in Figure 68. The influence of angle on the Nusselt number becomes more pronounced with increasing Re , as evidenced by the broadening ridge on the graph with larger angles. While the slight increase in Nusselt number on the top side of the plate between 0° and 5° , observed in Figure 66, is present, it is less significant on this absolute scale when viewed within the context of the larger dataset. Beyond 20° , Nu on the top side becomes consistently flat, indicating a reduced sensitivity to angle of impingement. However, even within this flat region, the Nu remains strongly dependent on Re , highlighting the dominant role of velocity in determining heat transfer performance at higher angles. The bottom side of the plate sees a Nu maximum at around 28° and generally much higher magnitude than the top side of the plate.

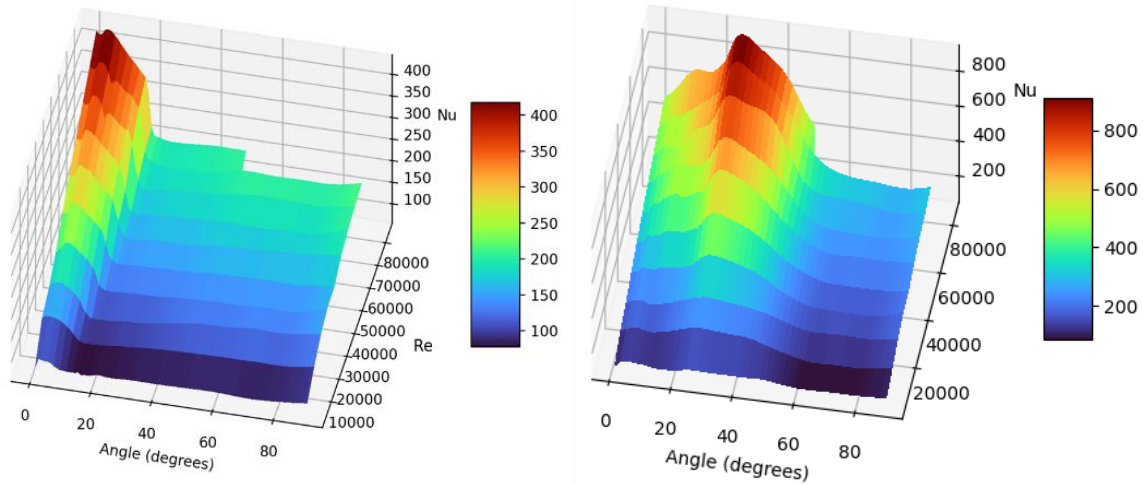


Figure 68: Nusselt number as a function of angle and Reynolds number for the top (left) and the bottom (right).

3.8.2 Heat Transfer Coefficient

Re numbers based on the average of all three sensors between 5,000 and 90,000 were achieved in the wind tunnel and the average of the three top heat transfer coefficients was recorded at various angles of attack shown in Figure 69.

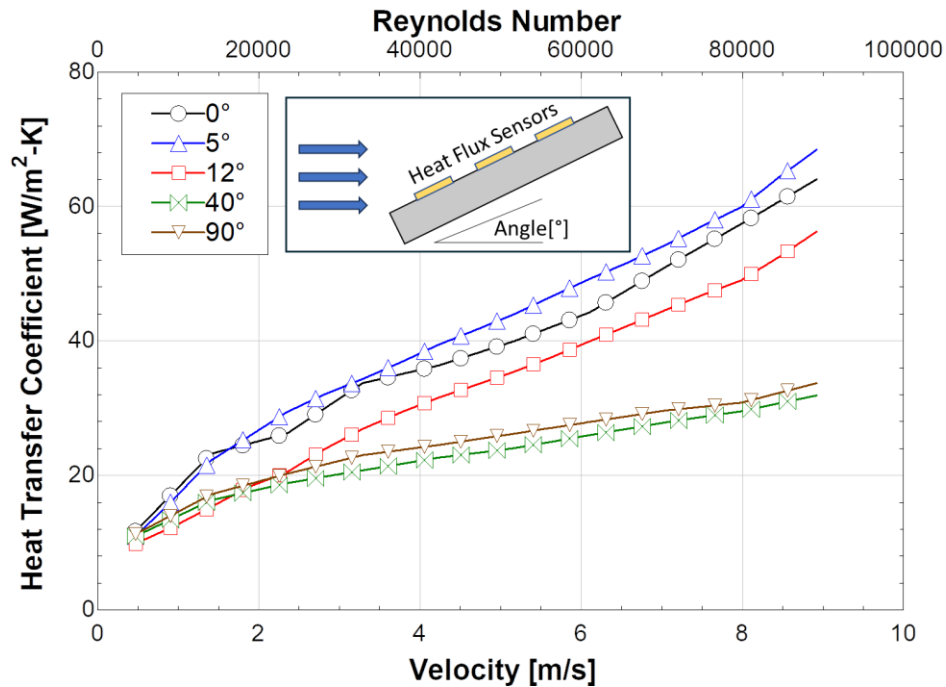


Figure 69: Average of the three heat transfer coefficients on top of the plate as it is pitched into the wind source as a function of velocity/Reynolds number at various angles.

Beyond a narrow likely laminar region, the heat transfer coefficient exhibits an almost linear scaling with Re for data collected at each angle. At low Re , angles between 12° and 90° produced similar heat transfer coefficients, while angles between 40° and 90° showed diminished heat transfer coefficients above a Re of approximately 20,000, aligning with the observations in Figure 66. Below a Re of approximately 15,000, the effect of angle on heat transfer coefficient was relatively minor. However, for Re values exceeding 15,000, the influence of angle became significantly more pronounced. Notably, at Re values greater than 20,000, the 5° angle consistently produced the highest overall heat transfer coefficient compared to other angles, suggesting a potential optimal configuration for heat transfer with this "blunted flat plate" geometry.

Figure 70 presents the heat transfer coefficient as measured exclusively by the top and bottom center heat flux sensors. The top center sensor, being less affected by flow separation at the edges of the blunt

plate, does not exhibit an optimal heat transfer coefficient at intermediate angles. Instead, it shows a maximum heat transfer coefficient at 0° , followed by a sharp decline up to approximately 20° . Beyond this angle, the heat transfer coefficient enters the same "dead zone" observed in Figure 66, where further changes in angle have little to no effect. Figure 70 (right) shows the measured heat transfer coefficient of the center bottom of the plate as the plate is pitched into the wind stream. Interestingly, the bottom sensor measures a much higher heat transfer coefficient than the forward sensor as was also shown in Figure 68. There appears to be a maximum reached around 28° . This increased heat transfer coefficient is probably due to airflow eddies created by separating air flowing around the plate increasing turbulent intensity at the backside surface of the plate and rapidly removing thermal energy, but more studies would have to be done on the backside to determine the reason for this effect.

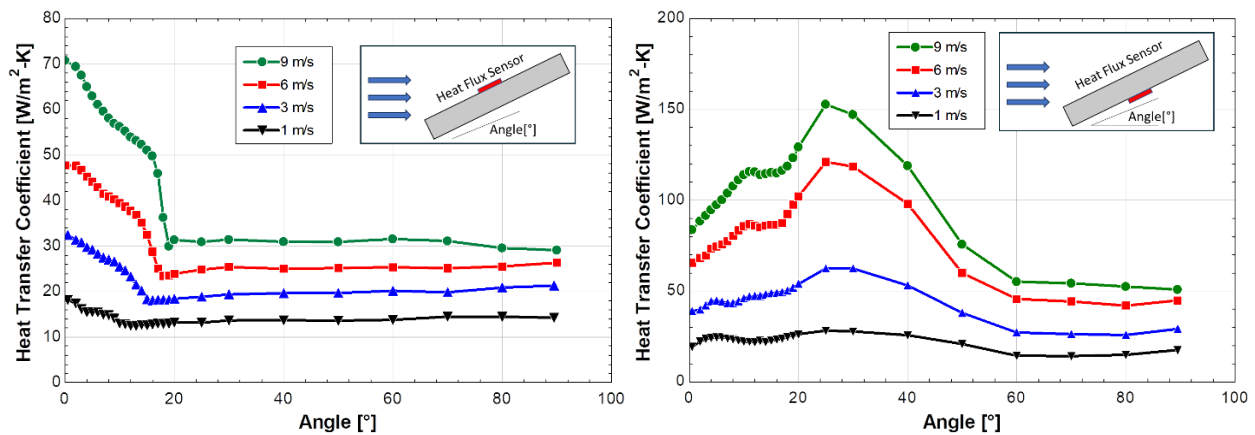


Figure 70: Center heat transfer coefficient on top of the plate (left) and bottom of the plate (right) as it is pitched into the wind source as a function of Reynolds number at various angles using just the center heat flux sensors. Note that the y axes in these graphs have different scaling from one another.

3.8.3 Nusselt Number

Using data from the center top heat flux sensor, the relationship between Re and Nu across a range of angles from 5,000 to 90,000 Re is presented in Table 9. This "heat map" highlights the significant effects of low angles of attack, particularly when combined with high Re values, on Nu . To accurately capture the rapid changes in Nusselt number at low angles, the bin size is reduced below 28° . A two-dimensional

interpolation function or piecewise curve fit, which will be shown in the Appendix, can be employed to efficiently "look up" Nusselt numbers as a function of both Reynolds number and angle for further analysis or modeling purposes.

Table 9: Measured Nusselt number as a function of Reynolds number and Angle for the center top sensor.

Nusselt #																					
Reynolds #	90000	501	466	447	425	408	394	379	361	329	221	205	204	203	208	210	207	205	204	203	203
	80000	485	452	435	406	388	384	376	355	315	218	203	201	199	204	207	203	204	203	201	205
	70000	433	407	395	364	339	344	348	329	272	206	192	190	189	193	198	204	204	202	200	213
	60000	381	358	356	337	316	315	303	284	224	183	175	174	178	182	184	187	186	186	185	205
	50000	328	310	316	303	290	278	264	239	191	167	161	161	165	166	170	174	173	178	177	190
	40000	270	261	269	255	244	235	222	186	155	145	145	146	147	148	151	154	155	156	155	164
	30000	210	213	214	202	192	184	168	137	124	124	123	124	126	128	133	136	135	137	136	160
	20000	166	172	164	151	141	130	113	102	101	102	102	104	108	112	120	124	125	128	127	137
	10000	121	129	122	110	101	94	87	84	83	84	85	87	89	90	93	94	94	93	93	101
		0	3	5	7	9	11	13	15	17	19	21	23	28	36	45	53	61	69	78	90
	Angle [°]																				

An insightful metric for evaluating heat transfer performance is the ratio of Nu at a given angle to the Nusselt number measured under a zero-angle condition. This ratio, referred to as the Nusselt number reduction ratio, or Nu_{rr} , provides a relative measure of the impact of angle on heat transfer efficiency. This is shown in Equation 74, where Nu is at a certain angle, and Nu_{0° is from the zero-angle condition:

$$Nu_{rr} = \frac{Nu}{Nu_{0^\circ}} \quad (74)$$

Table 10 presents these reduction ratios for the top center sensor, revealing that the largest deviations from the zero-angle Nusselt number occur at angles exceeding 19° , particularly at higher Re .

Table 10: The Nusselt number reduction ratio (Nu_{rr}) as a function angle and Re for the center top sensor.

		Nusselt # Reduction Ratio																			
Reynolds #	90000	1.00	0.93	0.89	0.85	0.81	0.79	0.76	0.72	0.66	0.44	0.41	0.41	0.41	0.42	0.42	0.41	0.41	0.41	0.41	
	80000	1.00	0.93	0.90	0.84	0.80	0.79	0.78	0.73	0.65	0.45	0.42	0.42	0.41	0.42	0.43	0.42	0.42	0.42	0.42	
	70000	1.00	0.94	0.91	0.84	0.78	0.79	0.80	0.76	0.63	0.48	0.44	0.44	0.44	0.45	0.46	0.47	0.47	0.47	0.46	
	60000	1.00	0.94	0.93	0.89	0.83	0.83	0.79	0.75	0.59	0.48	0.46	0.46	0.47	0.48	0.48	0.49	0.49	0.49	0.49	
	50000	1.00	0.94	0.96	0.92	0.88	0.85	0.81	0.73	0.58	0.51	0.49	0.49	0.50	0.51	0.52	0.53	0.53	0.54	0.54	
	40000	1.00	0.97	0.99	0.94	0.90	0.87	0.82	0.69	0.57	0.54	0.54	0.54	0.54	0.55	0.56	0.57	0.57	0.58	0.57	
	30000	1.00	1.01	1.02	0.96	0.91	0.88	0.80	0.65	0.59	0.59	0.58	0.59	0.60	0.61	0.63	0.64	0.64	0.65	0.65	
	20000	1.00	1.04	0.99	0.90	0.85	0.78	0.68	0.61	0.61	0.61	0.61	0.63	0.65	0.67	0.72	0.74	0.75	0.77	0.76	
	10000	1.00	1.06	1.00	0.91	0.84	0.77	0.72	0.70	0.69	0.70	0.70	0.72	0.74	0.75	0.77	0.78	0.78	0.77	0.77	
			0	3	5	7	9	11	13	15	17	19	21	23	28	36	45	53	61	69	78
		Angle [°]																			

The data for the bottom center heat flux sensor is shown in Table 11. The maximum around 28° for this backside center heat flux sensor is clearly visible.

Table 11: The Nusselt number reduction ratio as a function angle and Re for the center bottom sensor.

		Nusselt # Reduction Ratio																			
Reynolds #	90000	1.00	1.07	1.15	1.23	1.32	1.37	1.37	1.37	1.38	1.44	1.53	1.70	1.82	1.60	1.17	1.10	0.95	0.80	0.69	0.63
	80000	1.00	1.07	1.14	1.22	1.26	1.32	1.35	1.37	1.39	1.46	1.54	1.71	1.86	1.64	1.21	1.02	0.81	0.69	0.63	0.61
	70000	1.00	1.07	1.15	1.15	1.17	1.23	1.30	1.40	1.44	1.50	1.60	1.77	1.91	1.76	1.25	0.82	0.73	0.69	0.63	0.69
	60000	1.00	1.07	1.17	1.19	1.26	1.32	1.32	1.37	1.40	1.45	1.55	1.72	1.86	1.67	1.24	0.79	0.69	0.66	0.63	0.72
	50000	1.00	1.06	1.18	1.24	1.33	1.38	1.36	1.37	1.42	1.48	1.51	1.69	1.89	1.66	1.24	0.88	0.71	0.70	0.69	0.75
	40000	1.00	1.04	1.16	1.18	1.24	1.30	1.31	1.32	1.34	1.40	1.46	1.63	1.77	1.58	1.20	0.87	0.69	0.66	0.65	0.72
	30000	1.00	1.05	1.14	1.13	1.15	1.20	1.22	1.24	1.27	1.32	1.39	1.52	1.65	1.50	1.21	0.88	0.71	0.70	0.68	0.88
	20000	1.00	1.09	1.16	1.11	1.06	1.07	1.12	1.17	1.24	1.30	1.36	1.43	1.50	1.40	1.25	1.00	0.80	0.82	0.80	0.93
	10000	1.00	1.17	1.25	1.25	1.17	1.14	1.18	1.18	1.23	1.29	1.36	1.44	1.50	1.42	1.28	1.04	0.79	0.79	0.78	0.94
			0	3	5	7	9	11	13	15	17	19	21	23	28	36	45	53	61	69	78
		Angle [°]																			

3.8.4 Heat Transfer Coefficient Tables

Although specific to this experimental setup, Table 12 provides the average of all three top heat transfer coefficients as a function of angle and velocity for angles ranging from 0° to 90°. This

relationship enables the determination of the heat transfer coefficient for a given velocity and airflow angle impinging on a flat plate. Such a table offers a practical tool for estimating heat transfer coefficients using vectorized velocity data from CFD simulations, bypassing the need for solving computationally intensive energy equations within the CFD framework. This approach facilitates more efficient integration of heat transfer considerations into CFD analyses.

Table 12: Average heat transfer coefficient for all three sensors on the top (leeward) side of the plate as a function of measured velocity and angle.

		Heat Transfer Coefficient [W/m ² -K]																			
Velocity [m/s]	9.0	64.0	68.8	68.4	64.5	60.7	58.1	55.1	52.5	47.5	31.1	34.0	33.3	31.9	32.3	32.1	32.6	32.6	32.3	33.5	33.7
	8.0	57.5	59.9	60.0	56.2	53.3	50.6	48.1	45.4	36.4	28.9	29.7	29.7	29.8	29.7	29.7	29.8	29.8	29.7	30.5	30.9
	7.0	50.7	54.5	54.0	50.9	47.9	45.5	43.3	39.9	30.1	27.0	27.7	27.8	27.8	27.9	27.7	27.9	28.0	27.7	28.5	29.6
	6.0	43.8	48.8	48.6	45.5	43.2	40.7	38.5	34.2	26.4	24.5	25.0	25.3	25.8	25.8	26.1	26.4	26.2	26.1	26.5	27.8
	5.0	39.3	43.5	43.2	40.3	38.2	36.0	33.7	28.0	23.5	22.7	22.8	23.2	23.9	23.9	24.1	24.7	24.5	24.1	24.6	25.9
	4.0	35.7	38.6	38.2	35.9	34.0	31.7	28.9	23.0	21.5	21.1	21.3	21.4	21.7	22.1	22.5	22.8	22.7	22.3	23.3	24.2
	3.0	31.4	33.2	33.0	31.1	29.4	26.5	23.1	19.2	18.9	19.0	19.3	19.5	19.6	20.1	20.3	20.6	20.7	20.3	21.3	22.2
	2.0	25.1	27.4	26.8	25.4	23.8	20.0	16.9	16.2	16.5	16.6	17.4	17.3	17.4	18.0	17.8	17.7	17.7	17.9	18.6	19.1
	1.0	18.2	17.5	17.2	16.3	15.4	13.5	12.8	12.8	13.3	13.3	14.1	14.0	13.7	14.1	14.0	14.0	14.1	14.8	15.1	14.6
			0	3	5	7	9	11	13	15	17	19	21	23	28	36	45	53	61	69	78
		Angle [°]																			

Table 13 presents a reduction ratio (HTC_{rr}) in the average of three top heat transfer coefficients. In this case, HTC is at a certain angle, and HTC_{0° is at the zero-angle condition, as shown in Equation 75:

$$HTC_{rr} = \frac{HTC}{HTC_{0^\circ}} \quad (75)$$

However, these values differ slightly due to the averaging of data from multiple sensor sets used to measure and calculate heat transfer coefficients, temperatures, and thermal properties. This table retains the slight local maxima captured originally at slight angles in Figure 66.

3.8.5 Flow Separation and Edge Effects

As the blunt-faced flat plate was pitched into the wind tunnel's air stream, the average top heat transfer coefficient initially increased up to a pitch angle of 5° before sharply decreasing as the pitch angle increased further. This behavior was hypothesized to result from flow separation at the leading edge of the finite-thickness plate. Subsequent analysis using CFD, some of which is shown in Figure 71, supports this hypothesis. At slight pitch angles, the flow separation at the leading edge diminishes, leading to increased heat transfer due to a smaller separation region.

To further investigate, a simple experiment was conducted using a “D”-shaped rubber seal along the leading edge, designed to streamline the edge similar to an airfoil. When the wind tunnel test was repeated with this adjustment, the deviation in heat transfer between 0° and 5° pitch angles was significantly reduced, though this is not shown here. These findings align with classic aerodynamics literature on airfoil streamlining, such as the work by Talay (1975), further validating the role of leading-edge separation in the observed heat transfer behavior.

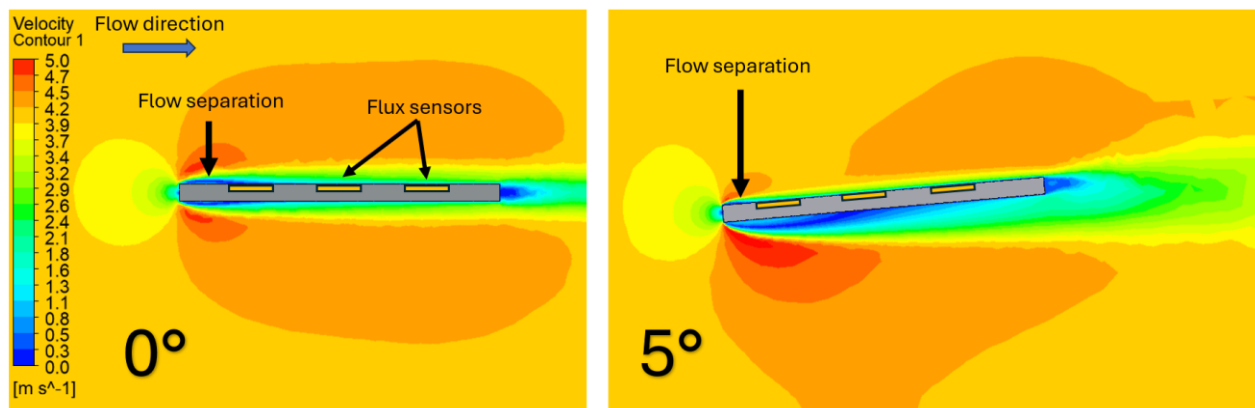


Figure 71: Flow separation reduction of a flat, blunted object as it tilts into an air stream at a mild angle.

Figure 72 shows the test apparatus in a wind tunnel using smoke (vaporized propylene glycol) and a laser light source plane parallel to the flow of air to track the flow streamlines of air over the plate. The same effect of flow separation diminishing at slight angles is observed.

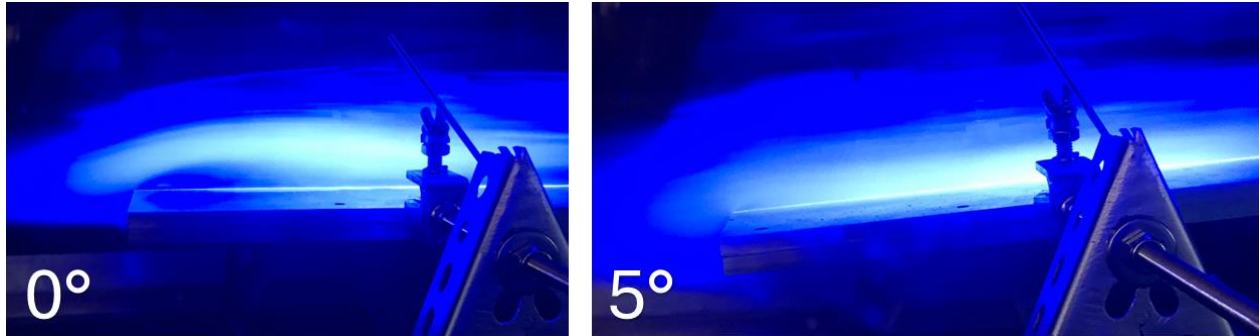


Figure 72: Flow separation reduction of a flat, blunted plate in a wind tunnel as it is pitched at a mild angle.

The sharp decrease in the top heat transfer coefficient past 5° is likely due to the flow stagnation and buildup of pressure on the front side of the plate, resulting in diminished heat transfer at angles more severe than around 12° . This is shown by a CFD model in Figure 73, where an energy equation was solved in CFD to estimate heat transfer coefficient as a plate is tilted 45° . As is shown, the heat transfer coefficient is reduced as the plate is tilted at more severe angles. The bottom surface was not investigated, but further CFD modeling would be useful here to determine reasons for the back surface experiencing significantly higher heat transfer coefficients.

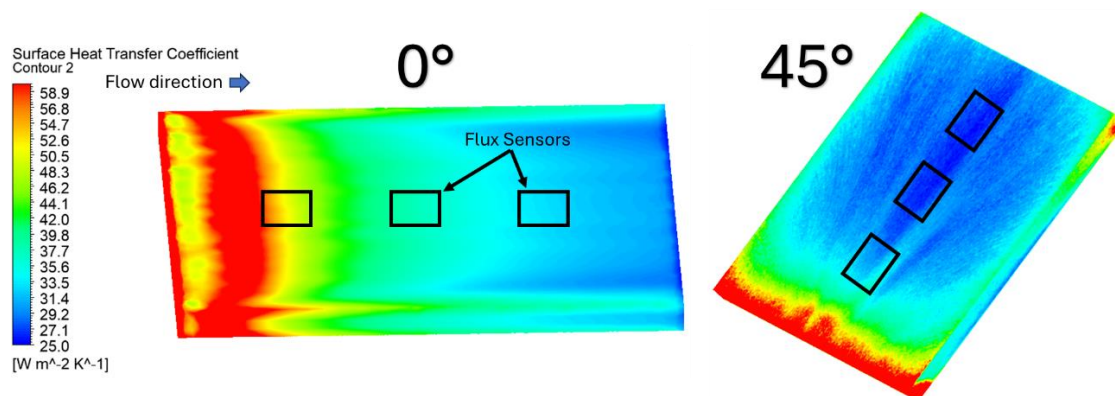


Figure 73: A flat, blunted object tilting into an air stream at a 45° angle.

3.8.6 Wind Tunnel Data Application

CFD analysis provided three-dimensional velocity vectors throughout the interior of a spiral blast freezer, enabling the calculation of both the magnitude and angle of airflow over food products as a function of position and dwell time within the freezer. This velocity data, combined with the findings presented in this work (Table 12), can be used to estimate the heat transfer coefficient as a function of product position during the freezing process. Heat transfer coefficients can be concurrently measured directly in situ using a Phantom device, outfitted with batteries, a protective enclosure, and the data monitoring system previously described in Section 2.6, and physically conveyed through a spiral freezer.

The same spiral freezer (from Plant 1) used for the in situ measurements was modeled in ANSYS Fluent to simulate airflow and heat transfer characteristics. Both the measured and CFD-simulated heat transfer coefficient data sets are compared in Figure 74. The CFD results were initially interpolated assuming horizontal airflow (no angle of impingement), followed by interpolation with the inclusion of the airflow angle, offering a more comprehensive representation of heat transfer behavior within the spiral freezer. The velocity data from the CFD was also propagated through the flat plate correlations established by Leinhard (2020) to see the comparison.

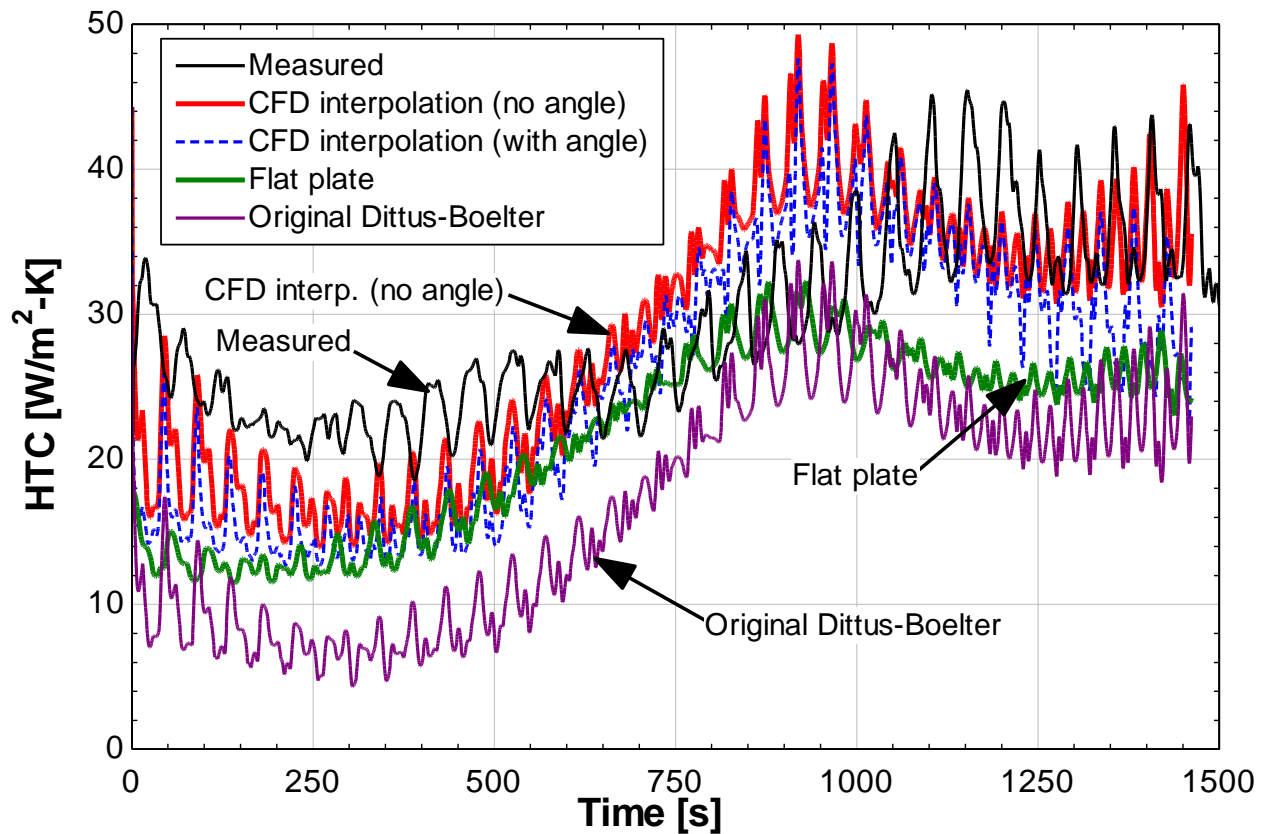


Figure 74: Measured heat transfer coefficient, and heat transfer coefficient predicted by using CFD angular velocity data to interpolate Table 12.

Figure 74 shows that when the effects of airflow angle are added, the predicted heat transfer coefficient captures more variation that exists in the measured heat transfer coefficient. Each of the cases were ran through the thermal model introduced in Chapter 2 and the results are shown in **Table 15**.

Table 15: Measured and modeled heat transfer coefficient as a function of time experienced by a product in a spiral blast freezer.

Data profile	Freezing time (s)	Belt speed (products/min)	Deviation (%)
Measured	1455	138.4	0
CFD interpolation (no angle)	1496	134.6	2.9
CFD interpolation (with angle)	1585	127.0	8.4
Flat plate	1791	112.3	19.0

Original Dittus-Boelter	2110	97.4	29.6
-------------------------	------	------	------

Table 15 highlights the discrepancies in predicting product belt speed using different methodologies. Conventional flat plate correlations resulted in a 19.0% deviation from the measured product belt speed obtained using the Phantom II. In contrast, velocity data from CFD simulations without accounting for airflow angle achieved the highest accuracy, with only a 2.9% deviation from measured values. Incorporating airflow angle into the CFD model did not enhance accuracy and instead increased the deviation to 8.4% when compared to the measured heat transfer coefficient data. One reason this might have a higher deviation is that, in reality, the attack angle of air on the product might be different than what the CFD had predicted based on the porous media used in this research versus structural tiers in an operating spiral and other geometrical considerations (including product shape). Despite this, both CFD interpolation approaches demonstrated significantly better performance than the traditional flat plate correlation, emphasizing the importance of more advanced modeling techniques.

The wind tunnel experiments and accompanying CFD analyses have provided valuable insights into the relationship between airflow dynamics and heat transfer performance over blunt-faced flat plates, with direct implications for understanding airflow within spiral blast freezers. Key findings demonstrated that pitch angle and Reynolds number significantly influence heat transfer, with optimal performance occurring at low pitch angles and higher Reynolds numbers. Beyond 20° pitch, the heat transfer coefficient became insensitive to angle, underscoring the dominance of velocity in this regime.

This work also underscores the practicality of combining experimental data from the Phantom device with CFD-generated velocity fields to estimate heat transfer coefficients throughout a freezer's operational envelope. The ability to measure and model heat transfer coefficients in situ offers a powerful tool for benchmarking and optimizing spiral freezer performance.

3.9 Phantom I Field-testing Results

This section details the field application of the Phantom I designed to directly measure the thermal performance of five operating spiral blast freezers in situ. Measurements collected by the Phantom II are supplied as boundary conditions to the established 1-D thermal model, facilitating a detailed assessment of the comparative thermal performance of the freezers. This approach validated existing CFD and thermal models and served as a novel benchmark for evaluating spiral blast freezer performance.

3.9.1 Benchmarking five Spiral Freezers

Figure 75 presents the air temperature profiles over time for five spiral blast freezers from different plants, highlighting significant variability across locations. The data has been truncated at 1500 seconds enabling a consistent time window between the different freezers for ease of comparisons across plants. Plant 2 had the coldest air, with an average temperature of approximately -38°F (-39°C), while Plant 1 recorded the warmest, averaging around -14°F (-26°C). Plants 3, 4, and 5 had air temperatures of similar magnitude, approximately -25°F (-32°C). From a performance perspective, lower air temperatures are preferable as they enable faster freezing of products. However, achieving lower air temperatures necessitates lower suction pressures within the refrigeration system, resulting in increased energy consumption. Therefore, optimal freezer performance requires a careful balance between air temperature and airflow to achieve the desired throughput efficiently.

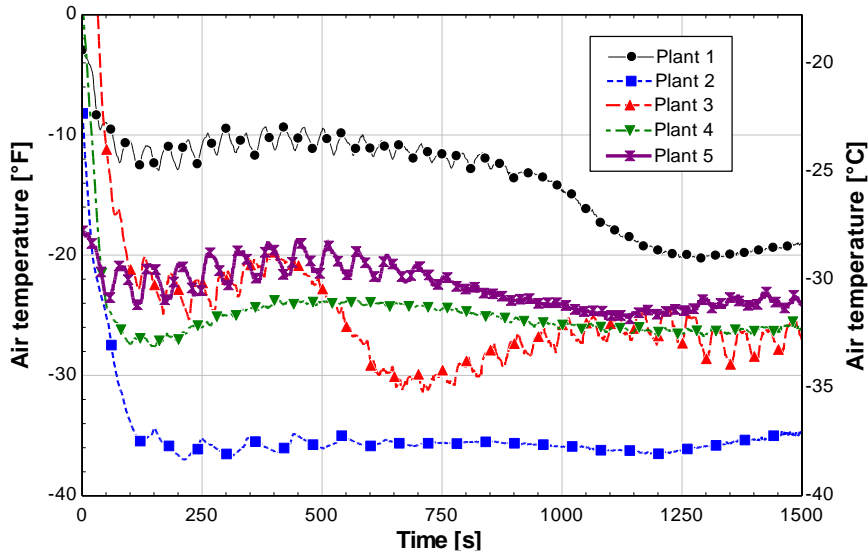


Figure 75: Air temperature as a function of dwell time from all five spiral freezers.

Figure 76 presents the measured heat transfer coefficients for all five spiral freezers, revealing distinct patterns across the plants. The data presented used an 8-point moving average to smooth out significant oscillations in the raw data, facilitating clearer visualization over the full 1500-second collection period. Plants 1 and 5 exhibited relatively high heat transfer coefficients at the start of the cooling process, which gradually tapered to moderate values by the end. As discussed in Chapter 3.4, this is considered an optimal heat transfer profile for blast freezers. Greater air velocity early in the cooling process leads to enhanced freezing efficiency.

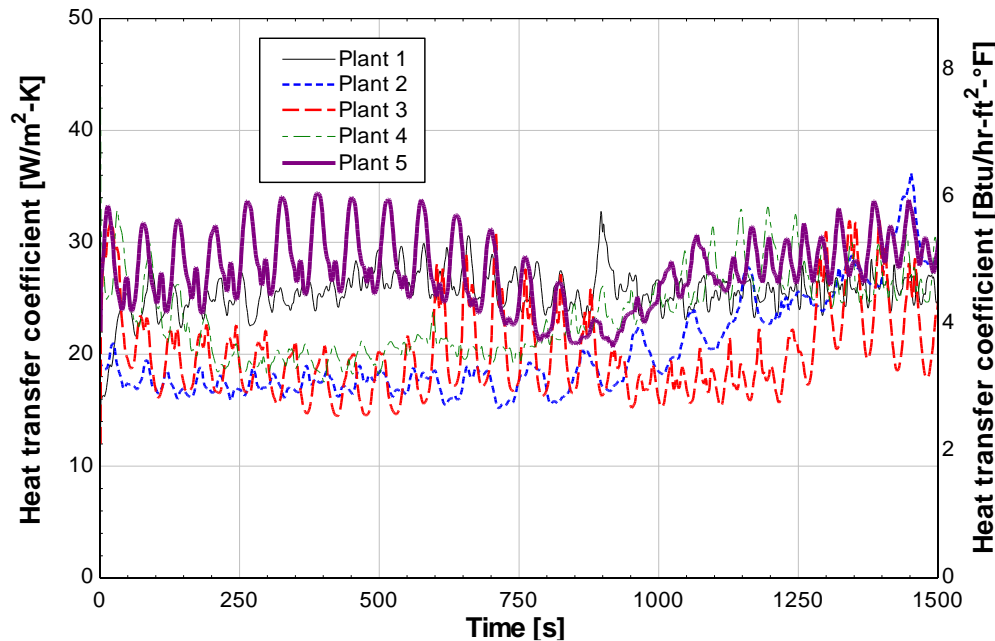


Figure 76: Heat transfer coefficient measured by the device inside five different spiral freezers.

Plants 2, 3, and 4 begin with lower heat transfer coefficients. While Plants 2 and 4 show some recovery by the end of the process, Plant 3 maintains a consistently low value of around $20 \text{ W/m}^2\text{-K}$ ($3.8 \text{ Btu/hr-ft}^2\text{-}^\circ\text{F}$), which Chapter 3.4 would identify as the least desirable profile among the five facilities. Despite Plant 2 having the coldest air temperature, it does not exhibit an ideal heat transfer profile, while Plant 5, with the most favorable velocity profile, only maintains moderate temperatures. An analysis will determine whether air temperature or airflow delivery plays a more critical role in overall freezer performance.

3.9.2 ODE Simulation

To evaluate the performance of each spiral blast freezer, the measured heat transfer coefficients and corresponding temperatures were applied as boundary conditions in a 1-D thermal model of a food product within a spiral freezer and the product temperature was allowed to come to its natural equilibrium by the end of the simulation (i.e., belt speed was not maximized). Initial analyses integrated the heat

transfer coefficient directly, but doing so missed the blast effect introduced in Section 3.2.3, and the freezer performance predictions were subsequently incorrect. Instead, the correct results of the 1-D model are presented in Figure 77, which also displays the saturation pressure of ammonia (R717) corresponding to the measured temperatures for reference. The calculated center temperature of the food product upon exiting the freezer is included in the figure.

Among the freezers, Plant 5 demonstrated the best performance, achieving optimal results with moderate temperatures and an ideal heat transfer coefficient profile. Although Plant 2 exhibited a less favorable heat transfer coefficient profile, its low air temperatures enabled it to perform nearly as well as Plant 5 by the end of the simulation. In contrast, Plant 1, despite having a promising heat transfer coefficient profile, was close to being the poorest performer due to its higher air temperatures throughout the process.

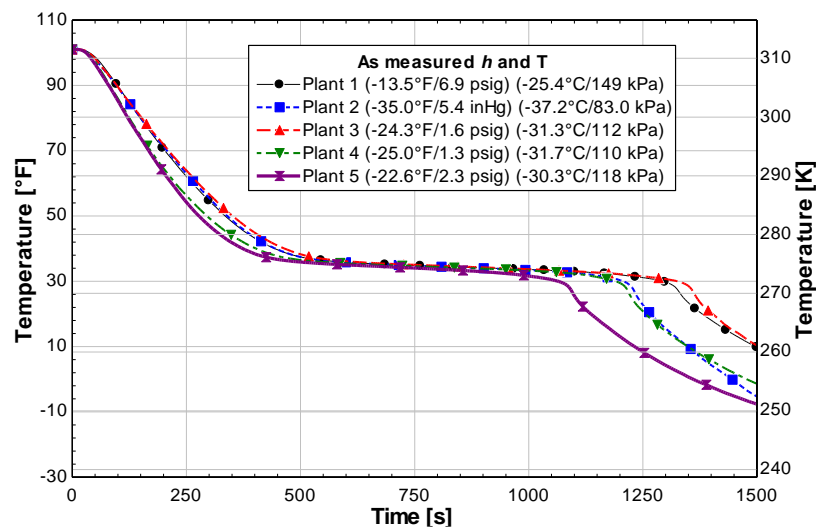


Figure 77: Simulated food center temperature as a function of time using a 1-D thermal model.

When the temperatures across all five plants are intentionally equalized, the evaluation becomes solely dependent on airflow velocity (heat transfer coefficient), as shown in Figure 78. Interestingly, with the influence of temperature removed, Plant 2, which had a less than favorable profile but a very cold

temperature originally, becomes the worst performer. As might be expected, Plant 5 remains the top-performing spiral freezer, taking full advantage of the blast effect. Notably, Plant 1 performs nearly as well as Plant 5 under these conditions, highlighting the significant impact of velocity (in turn heat transfer coefficient) magnitude and profile on freezer performance.

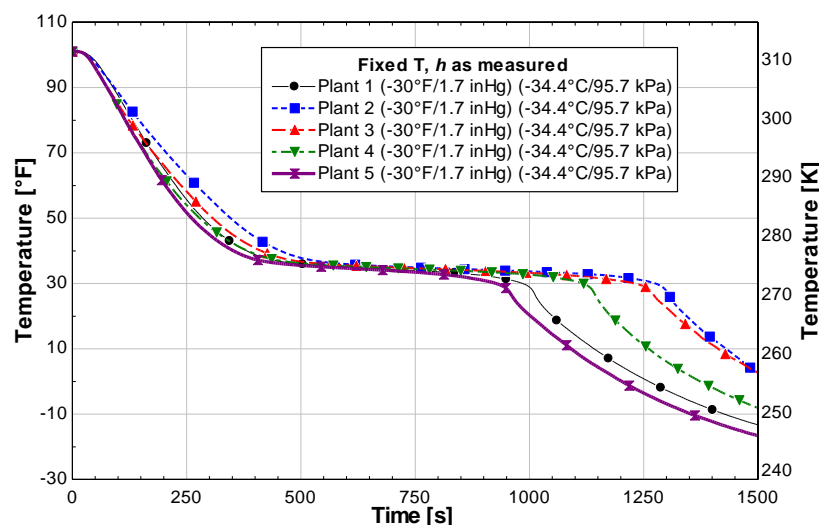


Figure 78: Simulated food center temperature as a function of time using a 1-D thermal model with temperature fixed to the same value for all five plants.

In the next analysis, the heat transfer coefficient is held constant across all five plants, allowing only the air temperature to vary based on the measured temperatures within each spiral freezer, which is shown in Figure 79. This isolates the effect of air temperature from the heat transfer coefficient. The simulations are then repeated. The performance of the spiral freezers is directly correlated with air temperature that was illustrated in Figure 75. Plant 2, which recorded the lowest air temperature, achieved the lowest food center temperature, making it the top performer. In contrast, Plant 1, with the highest air temperature, was the poorest performing spiral freezer.

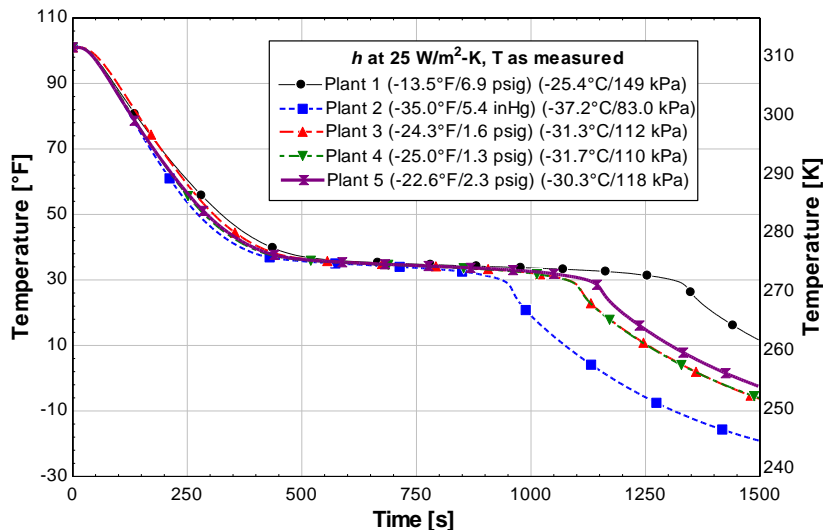


Figure 79: Simulated food center temperature as a function of time using a 1-D thermal model with heat transfer coefficient fixed to the same value for all five plants.

3.9.3 Integrated Heat Transfer Coefficient

An energy balance analysis in MATLAB can be conducted on the measured data presented in Figure 77 in the thermal model to quantify the total cooling delivered to a product as a function of its dwell time within a spiral freezer, providing a comprehensive comparison of the performance across the five plants. This is the only method that adequately captures the blast effect. The results of this analysis are depicted in Figure 80, demonstrating that the relative performance differences among the freezers align with the variations observed in Figure 77.

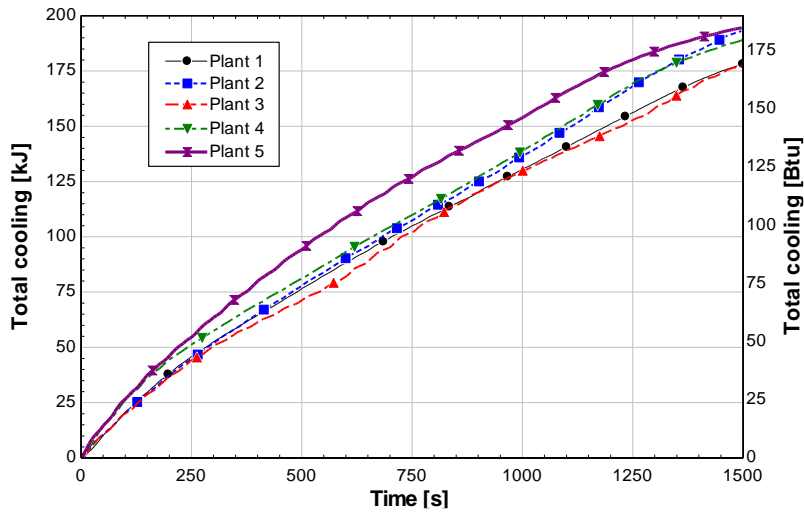


Figure 80: Integrated overall energy balance on the data for each of the five spiral freezers per product.

Alternatively, without using MATLAB, the integrated heat transfer coefficient method presented in Section 3.7.3 by Equation 72 can be used to compare the five plants. If the surface temperature of the product is kept at $T_s = 30^\circ\text{F}$ (-1.1°C), the integrated heat transfer coefficient for each plant is shown in Figure 81. The performance ranking in Figure 81 agrees with the results from Figure 80. For reference, this integrated heat transfer coefficient is on a per area basis, and the surface area of the Phantom II is approximately 0.1025 m^2 .

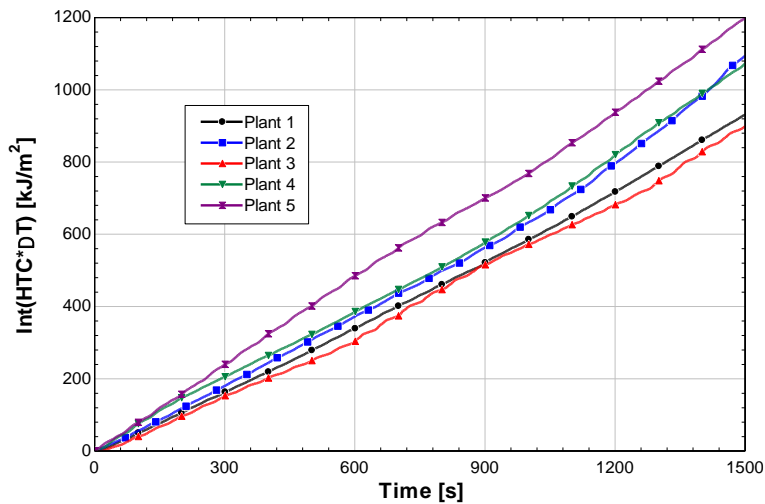


Figure 81: Integrated heat transfer coefficient multiplied by ΔT for 5 plants.

The time-averaged heat transfer coefficient and air temperature for each of the 5 plants are shown in Table 16. The integrated heat transfer coefficient metric is shown in the table as well, which predicts the total performance of a freezer. An even simpler metric shown is simply the average heat transfer coefficient, \bar{h} , multiplied by the average ΔT , which also produces the same performance ranking as the other methods in this example.

Table 16: Average heat transfer coefficient, air temperature, and integrated heat transfer coefficient metrics for all 5 plants.

	\bar{h} (W/m ² -K)	Average T _∞	int(HTC*ΔT)(kJ/m ²)	(\bar{h} *ΔT)(W/m ²)	Rank
Plant 1	25.6	-13.6°F (247.8K)	930	620	4
Plant 2	20.2	-35.0°F (235.9K)	1093	729	2
Plant 3	20.0	-24.3°F (241.9K)	898	602	5
Plant 4	23.4	-25.0°F (241.5K)	1072	715	3
Plant 5	27.5	-22.6°F (242.8K)	1198	802	1

This benchmarking study demonstrates the effectiveness of the Phantom pseudo product for evaluating the thermal performance of dynamic air blast freezers by measuring heat transfer coefficients and air temperatures in situ. The ability to gather real-time data while the device moves through the freezer alongside products allows for a comprehensive comparison of five spiral blast freezers across different facilities.

The results emphasize the importance of both airflow velocity (as indicated by the heat transfer coefficient) and air temperature in determining freezer efficiency. Freezers with higher air velocities early in the cooling process, such as Plant 5, achieved optimal performance despite moderate air temperatures. Conversely, Plant 2, with the coldest air temperature but suboptimal velocity profiles, still performed

well, highlighting that temperature alone does not guarantee superior performance. These findings demonstrate the need to balance airflow delivery and air temperature for optimal energy and thermal efficiency.

Chapter 2.6 showed the Phantom's video measuring capability as well, which was not discussed further in this section, but was valuable in evaluating the five plants shown. The inclusion of video footage when benchmarking freezers from the onboard action camera provided valuable insights into operational anomalies, such as excessive frost buildup, uneven belt transitions, and sanitation issues. This visual feed, combined with thermal data, enhances the diagnostic capabilities of the system by identifying defrost events and operational irregularities in real-time.

4 Conclusions and Recommendations

This section summarizes the research outcomes and provides recommendations for advancing the knowledgebase in areas that include air blast freezing and external forced convection heat transfer over flat plates. The conclusions portion of this chapter reviews how the originally established research goals were met through advanced thermal modeling, innovative measurement tools, and the application of optimization techniques that aimed to improve the thermal performance of low temperature air blast freezing systems. Limitations are discussed, including challenges in modeling diverse freezer configurations and the resource demands of CFD simulations, offering ideas for future refinement. Recommendations emphasize developing more generalized models, enhancing measurement technologies, exploring baffling strategies, and fostering industry collaboration to establish freezing system performance benchmarks. These efforts ensure both scientific and practical advancements in

freezing system efficiency. Recommendations intended to expand correlations for forced air convection over flat plates at varying pitch angles for both leading and trailing sides of the plate are provided.

4.1 Results and Implications

This research aimed to advance the state-of-the-art in low temperature air blast freezing systems by first understanding the thermal performance of existing freezing systems and then utilizing modern tools such as commercial CFD software and first-principles numerical modeling techniques for the food products to assess whether significant freezer performance improvements could be achieved. A dimensionally-similar instrument was created to actually measure the air-side performance of a large-scale spiral blast freezer. Measured data included surface heat flux, surface temperatures, center temperature, and local air temperature. The findings achieved strongly align with these objectives, offering significant progress in both theoretical modeling and practical applications.

The food product thermal model developed during this study incorporated temperature-dependent properties and velocity-specific heat transfer coefficients to capture the effects of varying external conditions of air velocity and air temperature on the overall freezing time of the product. A differentiator in the implementation of the 1-D food product model in the present research compared to past research is the application of varying surface heat transfer coefficients and air temperatures. Thermal conductivity and heat capacity were modeled to a level of detail that could capture the behavior of phase transitions with properties changing as the modeled water in the product froze as a function of decreasing temperature. A Gaussian-type function was used to model the product's heat capacity to reflect the expected thermal behavior during phase-change but to also maintain sufficient functional "smoothness" so the model could be rapidly solved with no significant loss in accuracy. With a robust and fast-solving product thermal model, Monte Carlo simulations were used to a significant parameter space leading to optimal results lying along a Pareto front. The overall framework developed for evaluating freezer

performance under varying operating conditions will allow other researchers to apply these techniques to improve the design of new freezing systems or existing freezing systems in operation.

The Phantom device developed during the present research provided a means to measure the in situ performance of blast freezing systems, and as a means of gathering data should modification to a freezing system be deployed with the intent of improving its thermal performance. The ability for the Phantom to gather in situ thermal measurements in an actual operating freezing system side-by-side with product was a key contribution that enabled gathering data local to the food products themselves as opposed to measurements made a fixed location within the freezer enclosure. The Phantom devices provided high-resolution data on heat transfer coefficients, temperature profiles along the same path as product experiences, and useful video footage, validating critical aspects of the thermal model and enabling direct comparisons between theoretical predictions and real-world performance. This innovation bridged a critical gap in the understanding of blast freezing systems and underscored the practical applicability of the research findings.

Optimization techniques were developed and further improved. Computational tools, including Monte Carlo simulations and iterative airflow refinements, identified strategies to improve throughput and energy efficiency. For example, optimized velocity profiles demonstrated measurable improvements in air delivery to products, reducing energy consumption while maintaining or enhancing freezing rates. Optimization was applied to a total spiral freezer thermal model to attempt to understand the interplay between belt speed, air temperature, air velocity, and overall freezing system operating (energy) cost. These insights offer a clearer pathway for industrial implementation, emphasizing the potential for targeted modifications to yield significant improvement in thermal performance.

The integration of iterative CFD analyses and confirmation using in situ measurements facilitated the establishment of predictive velocity-dependent heat transfer coefficients. These coefficients were

experimentally validated to quantify the effects of velocity magnitude and airflow angle in a wind tunnel in myriad realistic operating ranges, which were then captured in tables and functions. These correlations bridged the gap between theoretical predictions and real-world conditions, enabling more accurate modeling of airflow dynamics and the influence on freezing performance. More importantly, these techniques established a blueprint to quantify potential improvements for future designers and users of spiral freezers.

Multiple additional engineering strategies were developed to guide the design and operation of spiral blast freezers. Best practices such as enhanced airflow targeting using the blast effect, and early-stage airflow optimization were identified. Conversely, inefficiencies linked to excessive late-stage airflow were highlighted for avoidance. These strategies provide industry stakeholders with practical solutions to enhance system performance, reduce operational costs, and improve energy efficiency.

Overall, this research met and, in many cases, exceeded its initial objectives. The validated thermal modeling, innovative measurement tools, and practical optimization strategies developed in this study offer a comprehensive approach to improving spiral blast freezer performance. These outcomes contribute significantly to improving the modeling and the optimization of spiral blast freezers.

4.2 Limitations and Challenges

This research faced several limitations and challenges, many of which stemmed from the inherent complexity of industrial spiral blast freezers and the need to balance detailed analysis with practical applicability. One key limitation was the reliance on computationally intensive CFD simulations to model airflow and heat transfer dynamics. While these simulations yielded detailed velocity profiles and heat transfer coefficients, they require substantial computational resources and expertise, which may not be readily available to all facilities. The high computational cost also limits the frequency and scale at which these simulations can be employed, potentially hindering their application in small or resource-

constrained facilities. The large scale of air blast freezing systems also necessitated simplification such as the application of porous media models for complex geometric features including the spiral belt and evaporator coils. In addition, the flow and energy analysis were uncoupled. With greater computing power, the energy equation could be included along with the discretized three-dimensional Navier-Stokes equation. Coupling this solution to the food product within the CFD computational domain presents further difficulties – particularly when considering the product itself would represent a moving boundary problem to be solved.

Additionally, in a spiral freezer there is a known large chimney effect where hot, humid air rises off the product. Attempting to capture this would make an already complex modeling process even more difficult, and it is unclear whether this could be captured using CFD or with other means. In reality, the result of this chimney effect is that typically the upper coils in a spiral freezer must inherently defrost more and see a disproportionate amount of latent load. None of this was considered in this research due to the complexity it would have added, but it remains a concern.

The angular Phantom data, while new and insightful, was generated in a wind tunnel that was not originally developed for operating at low air (wind) velocities. Also, with air impinging around the entire flat plate, it is not necessarily clear why the bottom heat transfer coefficient was so high, and whether there might have been a virtual effect that could have produced this due to ΔT or heat removal anomalies. A focus was made on understanding the top heat flux sensors to focus the research bandwidth, since this surface is more directly coupled to the air velocity in practice (while the bottom surface is typically resting on a more complicated resistance network). This was the first study of its kind, and more development here is necessary. The Phantom II was a rectangular flat plate, but the embedded heater resulted in the overall thickness of the flat plate being somewhat of a “bluff body.” Further refinements

to this type of device should pursue strategies to supply heat but with a thinner “knife-edge” profile to minimize flow separation at the leading edge of the plate.

Lastly, the lack of direct industry-wide benchmarks for spiral freezer performance made it difficult to contextualize the findings against broader standards. For example, existing resources assigned extremely varying, vague, and constant heat transfer coefficients to different types of spiral blast freezer depending on the product, but these are “rules of thumb,” rather than rigidly arrived upon known factors. While this research developed a robust methodology for assessing and comparing freezer systems, the absence of universally accepted benchmarking techniques underscores the need for continued collaboration between academia and industry to establish comprehensive performance standards: *what is good?*

4.3 Future Research Ideas

Other future research in the field of spiral blast freezers could focus on addressing the above-mentioned limitations identified in this work while expanding the applicability across diverse operational settings. One priority is to develop generalized models capable of accounting for variations in product packaging, different geometries, airflow patterns, and thermal properties. This would improve the relevance of predictive models across different freezer designs and food products, enabling a wider range of facilities to adopt these advancements. For example, if there was a certain style of freezer that was known to develop certain characteristics, designers could be more confident in starting with this. By incorporating real-world data, future models could provide more accurate and actionable insights for optimizing freezing performance.

Additionally, further refinement of measurement technologies like the Phantom devices is crucial. Miniaturization, improved thermal insulation, and the integration of more versatile data logging systems such as reliable hot wire anemometers would enhance their usability in harsh freezer environments. It is difficult finding an omnidirectional anemometer small enough to fit inside of spiral freezer that can

withstand the extremely cold temperatures while reliably logging data. No solution was found in this study. These advancements would allow for more comprehensive in situ monitoring, enabling researchers to capture detailed thermal and airflow data with minimal disruption to production. Expanded field testing in a broader range of spiral freezer configurations and operational conditions would also help validate these findings and refine methodologies.

Optimizing airflow management remains a promising avenue for future work. Studies could explore various baffling designs, fan placements, and other airflow control mechanisms to achieve higher energy efficiency and throughput. Incorporating insights from the blast effect, which highlights the importance of targeted airflow during early stages of freezing, could refine strategies for managing airflow intensity and distribution. The use of new tools such as artificial intelligence in analyzing belt speed, actively monitoring exiting product temperature, airflow patterns, defrost cycles, and overall system performance offers potential for real-time optimization. These tools could identify optimal configurations for specific production scenarios and adapt to changing operational conditions, further enhancing system efficiency.

Additional research is needed to address moisture effects – particularly for unpackaged products that have high moisture content or are susceptible to the effects of moisture loss. In these cases, the effects of moisture loss from the product will have a direct impact on the reduction in saleable weight but, potentially, product quality as well. A compounding issue is the effects that moisture liberated from the product has on the refrigeration system performance. Moisture that leaves the product is deposited on surfaces within the spiral freezer’s environment but particularly on evaporator surfaces. This moisture accumulation significantly degrades evaporator performance which directly impacts product freezing capability. Strategies that can encourage “crust freezing” to minimize moisture loss has the potential to pay dividends on both the product and freezer side.

In summary, future research should aim to build upon the methodologies and findings of this study by exploring advanced modeling techniques, refining measurement technologies, and expanding field applications. These efforts will not only enhance the performance and sustainability of spiral blast freezers, but also support the broader goals of energy efficiency, environmental stewardship, and collectively shared practical knowledge in industrial food processing.

5 References

- Amarante, A., & Lanoisellé, J.-L. (2005). Heat transfer coefficients measurement in industrial freezing equipment by using heat flux sensors. *Journal of Food Engineering*, 66(3), 377–386. <https://doi.org/10.1016/j.jfoodeng.2004.04.004>
- AMCA (2019). Laboratory Methods of Testing Airflow Measurement Stations for Performance Rating. ANSI/AMCA Standard 610-19. <https://www.amca.org/publish/publications-and-standards/amca-standards/amca-standard-610-19-laboratory-methods-of-testing-airflow-measurement-stations-for-performance-rating.html>
- ASHRAE. 2014. 2014 ASHRAE Handbook – Refrigeration. Atlanta: American Society of Heating, Refrigerating and Air-Conditioning Engineers, Inc.
- ASHRAE. 2018. 2018 ASHRAE Handbook – Refrigeration. Atlanta: American Society of Heating, Refrigerating and Air-Conditioning Engineers, Inc.
- ASHRAE. (2024). *ASHRAE 34: Designation and safety classification of refrigerants*. Atlanta, GA: ASHRAE.
- ASME (2013). Test Uncertainty - Performance Test Codes. ASME PTC 19.1-2013. <https://www.asme.org/codes-standards/find-codes-standards/ptc-19-1-test-uncertainty>
- Bendsøe, M.P., & Kikuchi, N. (1988). Generating optimal topologies in structural design using a homogenization method. *Applied Mechanics and Engineering*, 71, 197-224.
- Carson, J.K., 2017. Use of simple thermal conductivity models to assess the reliability of measured thermal conductivity data. *Int. J. Refrigeration*, 74, 458–464.
- Boonsupthip, W., Heldman, D.R., 2007. Prediction of Frozen Food Properties during Freezing Using Product Composition. *J. Food Science*, 72, E254-E263.
- Carson, J.K., Wang, J., North, M.F., Cleland, D.J., 2016. Effective thermal conductivity prediction of foods using composition and temperature data. *J. Food Engineering*, 175, 65-73.

- Chen, C.C., 1985. Thermodynamic analysis of the freezing and thawing of foods: ice content and Mollier diagram. *J. Food Science*, 50, 1163-1166.
- Choi, Y., Okos, M.R., 1986. Effects of temperature and composition on the thermal properties of foods. In: Le Mageur, M., Jelen, P., *Food Engineering and Process Applications*, Elsevier Applied Science, London, 93-101.
- Cleland, D.J., Cleland, A.C., Earle, R.L., & Byrne, S.J. (1987). Prediction of freezing and thawing times for multi-dimensional shapes by numerical methods. *International Journal of Refrigeration-revue Internationale Du Froid*, 10, 32-39.
- Cleland, D.J. (2019). Prediction of food thermal properties to enable accurate design of food refrigeration processes.
- Council on Environmental Quality (CEQ). (n.d.). *Net-Zero Initiative*. Federal Sustainability Plan. Retrieved November 26, 2024, from <https://www.sustainability.gov/federalsustainabilityplan/net-zero-initiative.html>
- Dempsey, P., & Bansal, P. (2012). The Art of Air Blast Freezing: Design and efficiency considerations. *Applied Thermal Engineering*, 41, 71–83. <https://doi.org/10.1016/j.applthermaleng.2011.12.013>
- D'Errico, John (2022). `fminsearchbnd`, `fminsearchcon` (<https://www.mathworks.com/matlabcentral/fileexchange/8277-fminsearchbnd-fminsearchcon>), MATLAB Central File Exchange. Retrieved March 27, 2022.
- DOE, Manufacturing Energy Flows, Sankey Tool, DOE Office of Energy Efficiency & Renewable Energy, (2022). <https://www.energy.gov/eere/amo/dynamic-manufacturing-energy-sankey-tool-2010-units-trillion-btu-0>
- EIA, 2022 Statistics from the U.S. Energy Information Administration;
- EIA2, 2022 Electric Power Monthly, Average Price of Electricity to Ultimate Customers by End-Use Sector; https://www.eia.gov/electricity/monthly/epm_table_grapher.php?t=epmt_5_6_a
- EIA (U.S. Energy Information Administration). (2022). Total energy consumption: World. Retrieved December 19, 2024, from <https://www.eia.gov/international/data/world/total-energy/total-energy-consumption>
- European Commission. (n.d.). *The European Green Deal*. Retrieved November 26, 2024, from https://commission.europa.eu/strategy-and-policy/priorities-2019-2024/european-green-deal_en
- FAO “Energy-Smart Food for People and Climate, United Nations, Food and Agriculture Organization (FAO), (2011).
- Frick coolware. Coolware. (n.d.). Retrieved February 14, 2023, from <https://www.frickcoolware.com/>
- Guiqiang, Wang & Pinghua, Zou. (2014). Mathematical Modeling of Food Freezing in Air-Blast Freezer. *International Journal of Materials, Mechanics and Manufacturing*, 2, 278-281. 10.7763/IJMMM.2014.V2.142.
- Gulati, T., & Datta, A.K. (2013). Enabling computer-aided food process engineering: Property estimation equations for transport phenomena-based models. *Journal of Food Engineering*, 116, 483-504.
- Huan, Z., He, S., & Ma, Y. (2003). Numerical simulation and analysis for quick-frozen food processing. *Journal of Food Engineering*, 60, 267-273.

- Khenien, A., A. Benattayallah, and G. Tabor. 2019. "CFD Simulation of an Industrial Spiral Refrigeration System" *Energies* 12, no. 17: 3358. <https://doi.org/10.3390/en12173358>
- Klein, S. A. (2023). "Engineering Equation Solver (EES)," Professional V11.531. [Online]. Available: <https://fChartSoftware.com>.
- Kolbe, E., & Kramer, D. (2007). *Planning for seafood freezing*. Alaska Sea Grant College Program, University of Alaska Fairbanks.
- Leinhard, John IV & Leinhard, John V (2020). *A Heat Transfer Textbook (Version 5.10)*. Phlogiston Press.
- Leinhard V, John H. (2020). Heat Transfer in Flat-Plate Boundary Layers: A Correlation for Laminar, Transitional, and Turbulent Flow. *Journal of Heat Transfer*. 142. 10.1115/1.4046795.
- Metallica Metals. (n.d.). *Stainless steel vs. carbon steel pipes: Guide*. Retrieved November 26, 2024, from <https://www.metallicametals.com/blog/stainless-steel-vs-carbon-steel-pipes-guide>
- MG&E (2023) Residential electric rates. Madison Gas and Electric - Madison, Wisconsin. Available at: <https://www.mge.com/customer-service/for-homes/electric-rates> (Accessed: March 2, 2023).
- Miles, C.A., Mayer, Z., Morley, M.J., Houska, M. 1997. Estimating the initial freezing point of foods from composition data. *Int. J. Food Science & Technology*, 32, 389-400.
- Nellis, G., & Klein, S. A. (2009). *Heat transfer*. Cambridge University Press.
- Okita, Willian & Reno, M. & Peres, A. & Resende, Jaime. (2013). Heat transfer analyses using computational fluid dynamics in the air blast freezing of guava pulp in large containers. *Brazilian Journal of Chemical Engineering*. 30. 811-824. 10.1590/S0104-66322013000400013.
- Reindl, D., & Jekel, T. (2008). Infiltration Rate Determination for Low Temperature Freezing Systems. *ASHRAE Transactions* (Vol. 114, Issue 2)
- Sigmund, O., & Maute, K. (2013). Topology optimization approaches. *Structural and Multidisciplinary Optimization*, 48, 1031-1055.
- SciPy community, The. (2023). *Scipy.optimize.minimize*. SciPy documentation. <https://docs.scipy.org/doc/scipy/reference/generated/scipy.optimize.minimize.html>
- Suresh, Krishnan (2021). *Design Optimization using MATLAB and SOLIDWORKS (1st ed.)*. Cambridge University Press.
- United Nations Framework Convention on Climate Change (UNFCCC). (n.d.). *The Paris Agreement*. Retrieved November 26, 2024, from <https://unfccc.int/process-and-meetings/the-paris-agreement>
- Winterton, R.H.S. (February 1998). "Where did the Dittus and Boelter equation come from?" (PDF). *International Journal of Heat and Mass Transfer*. Elsevier. 41 (4–5): 809–810. doi:10.1016/S0017-9310(97)00177-4.
- Wu, Z., Ma, W., Xian, Z., Liu, Q., Hui, A., & Zhang, W. (2021). The impact of quick-freezing methods on the quality, moisture distribution and microstructure of prepared ground pork during storage duration. *Ultrasonics Sonochemistry*, 78, 105707. <https://doi.org/10.1016/j.ultsonch.2021.105707>
- Young, Tyler (2023). *Improving Performance and Energy Efficiency of Blast Freezing Systems*. Master of Science Thesis, University of Wisconsin – Madison, <https://sel.me.wisc.edu/publications/theses/young23.zip>

Acknowledgements

This project was funded by EPA Region 5 under the Pollution Prevention program Grant Number: 00E02908.

6 Appendix

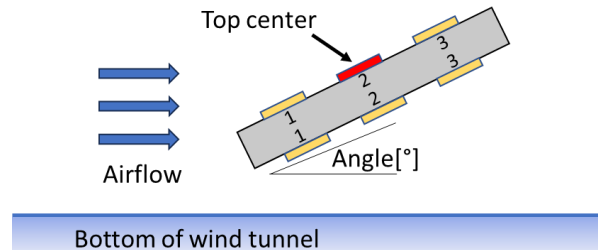


Figure 82: Top center heat flux sensor highlighted.

A correlation equation is developed from the data in Table 10, Nusselt number reduction ratio (Nu_{rr}) of the **top center** heat flux sensor shown in Figure 82. Nu_{rr} is the Nu reduction ratio as a function of the coefficients in Table 17, Re , and θ . Relative to the measured data, the $R^2 = 89.54\%$, maximum error = 29.7%, average error 8.1%, and standard deviation is 6.1%.

$$Nu_{rr} = A + B Re + C Re^2 + D Re^3 + E \theta + F \theta^2 + G \theta^3 + H Re \theta + I Re \theta^2 + J Re^2 \theta + K Re^2 \theta^2 \quad (76)$$

Table 17: Coefficients for Nu_{rr} Equation 76.

Coefficient	Value	Description
A	1.149835	Constant term
B	-6.617989E-06	Linear term for Re
C	1.509135E-10	Quadratic term for Re
D	-1.00087E-15	Cubic term for Re
E	-0.023862	Linear term for θ
F	0.0005610169	Quadratic term for θ
G	-3.566097E-06	Cubic term for θ
H	-3.513375E-07	Interaction term for Re and θ
I	3.080172E-09	Interaction term for Re and θ^2
J	2.254790E-12	Interaction term for Re^2 and θ
K	-2.321617E-14	Interaction term for Re^2 and θ^2

Table 18: Nusselt number reduction ratio equation (Equation 76) error versus experimental data.

Nu_{rr} Equation Error vs Experimental (%) Top Center

Reynolds #	90000	4.7	1.0	1.8	3.7	6.4	9.6	12.1	13.6	11.2	24.7	26.7	20.4	7.4	7.9	13.1	10.4	5.4	1.1	0.5	10.3
	80000	7.4	3.8	0.5	0.6	1.8	7.1	11.1	11.8	6.4	27.4	29.7	24.1	12.0	2.6	7.8	3.6	1.3	7.1	11.1	2.3
	70000	8.3	4.0	0.1	1.4	1.7	6.0	12.7	13.4	1.1	23.5	25.6	21.0	9.0	4.0	8.8	8.6	2.7	4.5	9.7	1.4
	60000	8.0	3.8	2.3	3.6	3.6	9.4	11.3	10.8	6.7	24.0	23.0	17.9	4.8	6.4	9.1	6.7	0.2	6.5	12.1	1.4
	50000	7.1	2.7	5.9	7.9	9.5	11.3	11.9	8.0	9.2	18.2	17.0	12.3	0.7	7.7	10.3	7.8	0.9	2.9	7.9	1.5
	40000	6.3	0.1	8.8	9.6	10.9	12.9	12.4	1.0	13.0	15.2	11.0	6.2	2.4	8.6	10.0	7.0	1.0	5.1	10.3	1.7
	30000	6.0	4.2	10.0	10.0	10.5	11.4	7.5	8.3	14.4	10.4	7.1	3.0	4.7	10.2	11.8	8.3	2.2	2.1	7.0	11.7
	20000	7.0	4.8	5.3	1.8	0.1	3.4	13.9	22.3	18.7	13.9	10.6	5.7	2.3	7.9	11.7	9.4	4.9	2.6	0.9	9.9
	10000	9.8	3.9	2.7	3.3	7.4	11.9	16.8	16.5	14.7	10.6	7.2	3.6	1.9	3.9	2.8	0.9	6.0	11.8	13.8	0.3
		0	3	5	7	9	11	13	15	17	19	21	23	28	36	45	53	61	69	78	90
	Angle [°]																				

Bottom Center

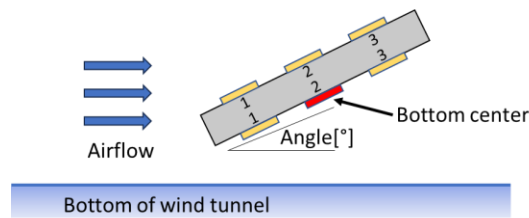


Figure 83: Bottom center heat transfer coefficient sensor.

Table 19: Bottom center Nusselt number reduction ratio.

Nusselt #																					
Reynolds #	90000	1.00	1.07	1.15	1.23	1.32	1.37	1.37	1.37	1.38	1.44	1.53	1.70	1.82	1.60	1.17	1.10	0.95	0.80	0.69	0.63
	80000	1.00	1.07	1.14	1.22	1.26	1.32	1.35	1.37	1.39	1.46	1.54	1.71	1.86	1.64	1.21	1.02	0.81	0.69	0.63	0.61
	70000	1.00	1.07	1.15	1.15	1.17	1.23	1.30	1.40	1.44	1.50	1.60	1.77	1.91	1.76	1.25	0.82	0.73	0.69	0.63	0.69
	60000	1.00	1.07	1.17	1.19	1.26	1.32	1.32	1.37	1.40	1.45	1.55	1.72	1.86	1.67	1.24	0.79	0.69	0.66	0.63	0.72
	50000	1.00	1.06	1.18	1.24	1.33	1.38	1.36	1.37	1.42	1.48	1.51	1.69	1.89	1.66	1.24	0.88	0.71	0.70	0.69	0.75
	40000	1.00	1.04	1.16	1.18	1.24	1.30	1.31	1.32	1.34	1.40	1.46	1.63	1.77	1.58	1.20	0.87	0.69	0.66	0.65	0.72
	30000	1.00	1.05	1.14	1.13	1.15	1.20	1.22	1.24	1.27	1.32	1.39	1.52	1.65	1.50	1.21	0.88	0.71	0.70	0.68	0.88
	20000	1.00	1.09	1.16	1.11	1.06	1.07	1.12	1.17	1.24	1.30	1.36	1.43	1.50	1.40	1.25	1.00	0.80	0.82	0.80	0.93
	10000	1.00	1.17	1.25	1.25	1.17	1.14	1.18	1.18	1.23	1.29	1.36	1.44	1.50	1.42	1.28	1.04	0.79	0.79	0.78	0.94
		0	3	5	7	9	11	13	15	17	19	21	23	28	36	45	53	61	69	78	90
	Angle [°]																				

$$Nu_{rr} = A + B Re + C Re^2 + D Re^3 + E \theta + F \theta^2 + G \theta^3 + H Re \theta + I Re \theta^2 + J Re^2 \theta + K Re^2 \theta^2 \tag{77}$$

Relative to the measured data, the $R^2 = 82.64\%$, maximum error = 37.2%, average error 8.2%, and standard deviation is 6.5%.

Table 20: Coefficients for Nu_{rr} Equation 77.

Coefficient	Value	Description
A	0.992776	Constant term
B	-8.849169E-06	Linear term for Re
C	2.069088E-10	Quadratic term for Re
D	-1.361317E-15	Cubic term for Re
E	4.340437E-02	Linear term for θ
F	-1.290504E-03	Quadratic term for θ
G	9.428362E-06	Cubic term for θ
H	3.373336E-07	Interaction term for Re and θ
I	-5.939648E-09	Interaction term for Re and θ^2
J	-1.695769E-12	Interaction term for Re^2 and θ
K	3.421033E-14	Interaction term for Re^2 and θ^2

Table 21: Nusselt number reduction ratio equation (Equation 77) error versus experimental data.

Nu_{rr} Equation Error vs Experimental (%) Bottom Center

Reynolds #	90000	12.0	2.4	0.6	0.5	1.5	0.7	3.3	7.0	8.6	6.3	1.2	8.4	14.5	7.9	11.8	1.2	3.4	6.2	10.5	1.7
	80000	8.8	0.5	2.6	2.8	5.2	5.4	7.0	8.6	9.5	6.4	2.0	7.8	15.3	9.1	9.3	10.1	15.3	8.5	1.6	1.0
	70000	8.0	1.1	2.0	9.3	13.7	13.1	10.8	6.3	5.6	3.2	2.4	11.4	18.1	15.7	4.6	36.5	26.3	7.7	3.3	11.1
	60000	8.7	0.5	0.3	4.9	3.9	3.7	8.0	7.3	7.1	4.7	0.9	10.2	17.5	13.4	2.8	37.2	29.7	9.9	4.2	13.9
	50000	10.3	0.4	2.9	1.8	2.9	2.7	2.4	4.7	3.1	0.5	0.9	10.7	20.8	15.4	0.3	20.2	22.0	1.6	12.7	13.9
	40000	11.7	1.1	3.8	0.8	1.7	1.1	3.5	6.0	6.7	3.4	0.2	10.1	17.8	13.4	0.6	16.8	22.7	6.4	5.3	3.1
	30000	12.3	2.6	3.4	4.0	7.3	7.0	8.7	10.0	9.5	7.0	2.3	6.0	14.2	11.7	4.1	12.9	17.8	3.0	3.8	10.7
	20000	11.2	6.1	4.7	5.6	16.0	19.1	17.1	15.5	10.7	7.0	2.9	1.9	7.8	7.0	8.2	1.0	6.2	8.1	8.5	2.3
	10000	7.6	10.2	10.4	5.0	5.6	12.5	12.1	14.2	11.7	7.6	2.5	2.9	7.9	8.5	10.1	2.3	13.3	5.0	7.2	14.9
		0	3	5	7	9	11	13	15	17	19	21	23	28	36	45	53	61	69	78	90
		Angle [°]																			

MATLAB Code:

```

% ODEsolver.m
% Creates plots Temperature vs Time given a velocity distribution,
%Temperature of the crust at various times throughout the thickness of the
%product, and then temperature of the center of the product as a function
%of vertical position inside the spiral freezer
clear;
close all;
tic
belt = 141.6247;
T_infinity =238.706; %Default air temperature value in K - by default
temperature is constant
N = 40; %number of nodes (-)
t_sim = 2*5000; %simulation time (sec) 1800 is default
% flag = 4; %default
flag = 4; %property model 6 is raw chicken wings/breasts
(sphere), 5 is aluminum, 4 is dough food symmetrical 1D, 8 is chicken package
with resistance on bottom, 9 is symmetrical chicken
hm = 1; %htc multiplier
reltol = 1e-6;
name = "spiral_midlane_existingEA.csv"; %Column 1 is time in seconds, column
2 is velocity

[time,T, dim1,xi_new_1,asdf] = dTdtEngine(N,t_sim,flag, hm, name, belt,
reltol,[],[],T_infinity);

figure
hold on;
grid on

T_f = (T-273.15)*(9/5)+32; %Converting temperature to F
tes0r = T_f(time<xi_new_1,floor(N/2)); %xi_new_1 is the time that the pizza
is in the spiral based on belt speed -
%this is selecting those times/temperatures

dist = length(time); %determining the length of the temperature matrix
if flag == 8
T_target = 26
else
T_target = 10
end
if flag == 6
T_low = T_f(length(time),1)
else
T_low = T_f(length(time),floor(N/2))
end

```

```

deltaT = abs(T_target-T_low)
dims = linspace(21,0,dist); %stretching the temperature data over 21 vertical
feet in the spiral
set(gca, 'XDir','reverse')

if flag == 6
plot(dims,T_f(:,1))
else

plot(dims,T_f(:,floor(N/2)))
end
ylabel('Temperature of product center (F)', 'FontSize',12, 'FontWeight', 'bold')
xlabel('Vertical position inside spiral
(feet)', 'FontSize',12, 'FontWeight', 'bold')

figure
hold on
grid on
Toft=readtable("tempdata2.csv");
x_temp =table2array(Toft);           %converting the table to an array
xi_T = x_temp(:,1);                 %column 1 of time
yi_T = x_temp(:,2);                 %column 2 of temperature
T_infinityK = interp1q(xi_T,yi_T,time);
T_infinityF = (T_infinityK-273.15)*(9/5)+32;
plot(time, T_infinityF)

ylabel('Temperature of the air inside the spiral
(F)', 'FontSize',12, 'FontWeight', 'bold')
xlabel('Time (s)', 'FontSize',12, 'FontWeight', 'bold')
toc

```

```

% dTdtEngine.m
%This is the dTdt function engine that calls ODE113 or ODE45

function [time,T,dim1,xi_new_1,asdf] = dTdtEngine(N,t_sim,flag, hm, name,
belt, reltol, xil, yil,T_infinity)

%User supplied temp. By Default, this is deactivated in dTdt_functionv.m
Toft=readtable("tempdata2.csv"); %Column 1 is time, column 2 is temperature
in K
x_temp =table2array(Toft);           %converting the table to an array
xi_T = x_temp(:,1);                 %column 1 of time
yi_T = x_temp(:,2);                 %column 2 of temperature
T_ini = 311.5;                       %initial temperature(K) Default - all models
if flag ==6
L = 0.03175;                         %Radius of a chicken wing (m)
elseif flag == 8

```

```

L = .0508;           %thickness of chicken package (2 inches)
elseif flag == 9
L = 0.015875;       %same thickness as pizza, but made out of chicken
else
L = 0.015875;       %dough product thickness(m)
end
rho = 533.8;        %density of pizza crust (kg/m^3)
c = 2376;           %specific heat capacity of non frozen pizza crust
(J/kg-K) NOT USED
T_m = 239;          %temperature of the plastic/nylon in K - not used by
default
Rc = .037;          %Contact resistance between the crust and the nylon
belt (K-m^2/W) - not used by default
belt_d = 140;       %default belt speed (products/min)

if name=='tempplot'
xi = xil;           %column 1 of time
yi = yil;           %column 2 of velocity
else
Voft=readtable(name);
x_vel =table2array(Voft); %converting the table to an array
xi = x_vel(:,1);    %column 1 of time
yi = x_vel(:,2);    %column 2 of velocity
end

%Scaling time based on belt speed
lng = length(xi);  %Length of the time vector that comes in
lng_n = (belt_d/belt)*xi(lng); %New xi length
xi_new = linspace(0,lng_n,lng)';
xi_new_l = xi_new(lng); %Largest value of belt-scaled time
t_sim = xi_new_l+10; %simulation time is 10 seconds longer than the pizza
is in the freezer

%Setup grid
y = zeros(1,N);
for i = 1:N
    y(i) = (i-1)*L/(N-1); %position of each node (m)
end

OPTIONS = odeset('RelTol',1e-6, 'MaxStep',1); %Max time step set to 0.01 and
tolerance lowered by 1000x"
[time,T] =
ode113(@(time,T)dTdt_functionv(time,T,L,name,rho,c,T_infinity,T_m,hm,Rc,flag,
xi, yi, belt, xi_T, yi_T),[0,t_sim],T_ini*ones(N,1),OPTIONS);

%Plotting routine (i.e., plot only 10 lines of temperature)
[rows,~] = size(T); %number of rows in temperature matrix
T_f = (T-273.15)*(9/5)+32; %Converting temperature to F
T_c = (T_f-32)/1.8; %Temperature in celsius

if name=='tempplot'
lng = length(xi); %Length of the time vector that comes in

```

```

lng_n = (belt_d/belt)*xi(lng); %New xi length
xi_new = linspace(0,lng_n,lng)';
xi_new_l = xi_new(lng); %Largest value of belt-scaled time
T_f1 = T_f(:,floor(N/2));
dim1 = time(nnz(T_f1)-nnz(T_f1<=10));
disp(append('Velocity profile: ',name));
display(append(' Freezing time (Mid temp <= 10F): ',num2str(dim1), '
seconds'));
else

plotline = 5; %number of lines to plot
rowsfloor = floor(rows/plotline); %Rounding down
figure
hold on;

if flag == 6
plot(y,T_c(1,:), 'linewidth',2);
grid on
xlabel('Position in food [m]', 'FontSize',12, 'FontWeight', 'bold')
ylabel('Temperature [C]', 'FontSize',12, 'FontWeight', 'bold')
for i = 1:(plotline-2)
plot(y,T_c(i*rowsfloor,:), 'linewidth',2)
end
plot(y,T_c(rows,:), 'linewidth',2)
legend('Time = 0', 'Time = 0.25', 'Time = 0.5', 'Time = 0.75', 'Time = 1')
else

% Find the index corresponding to y = 0.008
start_idx = find(y >= 0.008, 1);
% Extract the portion of y and T_c starting from y = 0.008
y_right = y(start_idx:end);
T_c_right = T_c(:, start_idx:end);
% Plot the first temperature profile
plot(y_right, T_c_right(1, :), 'linewidth', 2);
grid on
xlabel('Position in food [m]', 'FontSize', 12, 'FontWeight', 'bold');
ylabel('Temperature [C]', 'FontSize', 12, 'FontWeight', 'bold');

% Plot subsequent temperature profiles
hold on;
for i = 1:(plotline - 2)
    plot(y_right, T_c_right(i * rowsfloor, :), 'linewidth', 2);
end

% Plot the last temperature profile
plot(y_right, T_c_right(rows, :), 'linewidth', 2);
% Adjust x-axis limits to start at 0.008
xlim([0.008 max(y_right)]);
% Add a legend
legend('Time = 0', 'Time = 0.25', 'Time = 0.5', 'Time = 0.75', 'Time = 1');
end

```

```

figure
hold on;
grid on
plot(time,T_f(:,1))
plot(time,T_f(:,floor(N/4)))
plot(time,T_f(:,floor(N/2)))
plot(time,T_f(:,floor((3/4)*N)))
plot(time,T_f(:,N))
tim = linspace(0,xi_new_1,10000)';
yyaxis right;
plot(tim,velocity(tim, name, xi, yi,belt))

asdf = velocity(tim, name, xi, yi,belt);
if flag == 6
legend('x/R = 0 (center)', 'x/R = 0.25', 'x/R = 0.5 (mid radius)', 'x/R =
0.75', 'x/R = 1 (surface of sphere)', 'Velocity (m/s)')
else
legend('x/L = 0 (bottom)', 'x/L = 0.25', 'x/L = 0.5 (center)', 'x/L = 0.75',
'x/L = 1 (top)', 'Velocity (m/s)')
end
xlabel('Time [s]','FontSize',12,'FontWeight','bold')
yyaxis left;
ylabel('Temperature [F]','FontSize',12,'FontWeight','bold')
yyaxis right;
ylabel('Velocity [m/s]','FontSize',12,'FontWeight','bold', 'color', 'black')

T_f1 = T_f(:,floor(N/2));

dim1 = time(nnz(T_f1)-nnz(T_f1<=10));
disp(append('Velocity profile: ',name));
display(append(' Freezing time (Mid temp <= 10F): ',num2str(dim1), '
seconds')));

c_nodes = heatcap(T(length(T),:), flag);
rho_nodes = density(T(length(T),:), flag);
v_nodes = zeros(N,1);
v_nodes(2:N-1) = 1;
v_nodes(1) = 0.5;
v_nodes(N) = 0.5;
bulk_n = zeros(N,1);
bulk_d = zeros(N,1);
for i = 1:N
bulk_n(i) = c_nodes(i)*rho_nodes(i)*v_nodes(i)*T(length(T),i);
bulk_d(i) = c_nodes(i)*rho_nodes(i)*v_nodes(i);
end
bulk_numerator = sum(bulk_n,"all");
bulk_denomenator = sum(bulk_d,"all");
T_bulk = bulk_numerator/bulk_denomenator;
T_bulk_f = (T_bulk-273.15)*(9/5)+32;

display(append(' Equalized Bulk Temperature: ',num2str(T_bulk_f), ' F'));

```

```

T_c = (T_f-32)*(5/9);

figure
hold on;
grid on
if flag == 6 %Chicken
plot(time,T_c(:,N), 'color',[0, 0.5, 0], 'linewidth',2)
plot(time,T_c(:,floor(N/2)), 'linewidth',2)
plot(time,T_c(:,1), 'linewidth',2)
else %Pizza crust
plot(time,T_c(:,1), 'linewidth',2)
plot(time,T_c(:,floor(N/4)), 'linewidth',2)
plot(time,T_c(:,floor(N/2)), 'linewidth',2)
end

tim = linspace(0,xi_new_1,10000)';
yyaxis right;
ylabel('Velocity [m/s]', 'FontSize',12, 'FontWeight', 'bold', 'color', 'black')
plot(tim,velocity(tim, name, xi, yi,belt), 'color','blue')

if flag == 6
legend('x/R = 1 (surface of sphere)', 'x/R = 0.5 (mid radius)', 'x/R = 0
(center)', 'Velocity')
else
legend('x/L = 0, 1 (top, bottom)', 'x/L = 0.25, 0.75', 'x/L = 0.5 (center)',
'VeLOCITY (m/s)')
end

xlabel('Time [s]', 'FontSize',12, 'FontWeight', 'bold')
yyaxis left;
ylabel('Temperature [C]', 'FontSize',12, 'FontWeight', 'bold')

figure
plot(time,htc(time,hm,name, xi, yi, belt))
xlabel('Time [s]', 'FontSize',12, 'FontWeight', 'bold')
ylabel('Heat Transfer Coefficient [W/m^2-
K]', 'FontSize',12, 'FontWeight', 'bold')

end
end

```

```

% dTdt_functionv.m
%This is the dTdt function in cartesian and radial coordinates

function [dTdt] = dTdt_functionv(time,T,L,name,~,~,T_infinity,T_m,hm,Rc,flag,
xi, yi,belt, xi_T, yi_T)

```

```

h=htc(time,hm,name, xi, yi,belt);

%User supplied heat transfer coefficient
% h = htc_given(time);

%User supplied temperature vs time
% T_infinitytest = t_gettemp(time,xi_T,yi_T)
% T_infinity = interp1q(xi_T,yi_T,time); %1D interpolation - use this for

%Inputs
[N] = length(T);
DELTAy = L/(N-1); %distance between adjacent nodes (m)
dTdt = zeros(N,1); %initialize the dTdt vector
rho = density(T,flag)'; %Density
c=heatcap(T, flag)'; %Heat Capacity

if flag == 6
j = 1:N;
r(j) = (((j-1)*L)/(N-1));
% This is the code for chicken wings & individual breasts
dTdt(1) =
(4*pi.*(conductivity((T(1)+T(2))/2,flag)')*(r(1)+DELTAy/2)^2.*(T(2)-
T(1))/DELTAy)/(rho(1).*(c(1).*(4/3).*pi.*(DELTAy/2).^3));
dTdt(2) =
(4*pi.*(conductivity((T(1)+T(2))/2,flag)')*(r(1)+DELTAy/2)^2.*(T(1) -
T(2))/DELTAy + (T(3) -
T(2))./(1./(4.*pi.*(conductivity((T(3)+T(2))/2,flag)'))).*(1./r(2)-
1./r(3)))/(rho(2).*(c(2).*((4/3).*pi.*(r(2)+DELTAy/2).^3 - (4/3).*pi.*(r(2)
- DELTAy/2).^3));
i=3:(N-1);
dTdt(i) = (4*pi.*(conductivity((T(i-1)+T(i))/2,flag)')*(T(i-1)-
T(i))./(1./r(i-1)-1./r(i))' +
4*pi.*(conductivity((T(i+1)+T(i))/2,flag)')*(T(i+1)-T(i))./(1./r(i)-
1./r(i+1))')/(rho(i).*(c(i).*((4/3)*pi.*(r(i)'+DELTAy/2).^3-(4/3)*pi.*(r(i) '-
DELTAy/2).^3));
dTdt(N) = (4*pi.*(conductivity((T(N-1)+T(N))/2,flag)')*(T(N-1)-
T(N))./(1./r(N-1)+1./r(N)) + h*4*pi.*L.^2.*(T_infinity-
T(N)))/(rho(N).*(c(N).*((4/3)*pi.*r(N).^3 - (4/3)*pi.*(r(N-1)+DELTAy/2).^3));

elseif flag == 8
%This is for packaged chicken in polystyrene, 3 mm thick, Rpoly =
%0.1[m^2-K/w], Rtotal = 0.15[m^2-K/W] - chicken package base assumed to be
%1 m^2
R_poly=0.1;
dTdt(1) =
((2.*conductivity((T(1)+T(2))/2,flag)')/(DELTAy.^2.*(rho(1)).*(c(1)))*.(T(2)
-T(1)))+(2.*(T_infinity-T(1)))/(DELTAy.*rho(1).*(c(1).*(1/h)+R_poly));
i=2:(N-1);
dTdt(i) =
conductivity((T(i+1)+T(i))/2,flag)')/(DELTAy.^2.*(rho(i)).*(c(i)))*.(T(i+1)
-T(i)) + conductivity((T(i-
1)+T(i))/2,flag)')/(DELTAy.^2.*(rho(i)).*(c(i)))*.(T(i-1)-T(i));

```

```

dTdt(N) = ((2.*(conductivity((T(N-
1)+T(N))/2,flag)')./((DELTAy.^2.*(rho(N)).*c(N))))).*(T(N-1)-T(N)) +
(2.*h.*(T_infinity-T(N))./(DELTAy.*rho(N).*c(N)));

else
% This is the code for dough/pizza crust/chicken disk (standard algorithm -
symmetrical)
dTdt(1) =
((2.*conductivity((T(1)+T(2))/2,flag)')./((DELTAy.^2.*(rho(1)).*(c(1))))).*(T(2)
-T(1))+2.*h.*(T_infinity-T(1))./(DELTAy.*rho(1).*c(1)));
i=2:(N-1);
dTdt(i) =
conductivity((T(i+1)+T(i))/2,flag)')./((DELTAy.^2.*(rho(i)).*(c(i))))).*(T(i+1)
-T(i)) + conductivity((T(i-
1)+T(i))/2,flag)')./((DELTAy.^2.*(rho(i)).*(c(i))))).*(T(i-1)-T(i));
dTdt(N) = ((2.*(conductivity((T(N-
1)+T(N))/2,flag)')./((DELTAy.^2.*(rho(N)).*c(N))))).*(T(N-1)-T(N)) +
(2.*h.*(T_infinity-T(N))./(DELTAy.*rho(N).*c(N)));
end
end

```

```

% BeltSpeedOptimizer.m
%This determines the optimum belt speed to minimize delta T given a
%velocity distribution and a guess for belt speed
clear;
close all;
flag = 4; %property model 6 is raw chicken wings/breasts
(sphere), 5 is aluminum, 4 is dough food symmetrical 1D, 8 is chicken package
with resistance on bottom, 9 is symmetrical chicken
belt = 100; %Belt speed
T_infinity =238.706; %Eric's default value

name ="spiral_midlane_existingEA.csv";

%name ="spiral_midlane_existingEA.csv";
opts = optimset('fminsearch');
opts.TolFun = .001;
opts.TolX = .001;
[xMin, fMin, Flag, Output] =
fminsearchcon(@(belt)belt_speed_optimizer(belt,name,T_infinity,flag),belt,5,
[], [], [], [], opts);

```

```

% belt_speed_optimizer.m
%this is a function that must be called from somewhere else. Input is belt
%speed and output is delta T of the product at the exit of the freezer. It
%is used by an optimization routine like Fminsearchcon to minimize the
%delta T by varying the belt speed
function [deltaT,belt,time] = belt_speed_optimizer(belt,name,
T_infinity,flag)
N = 40;                %number of nodes (-)
t_sim = 2*5000;       %simulation time (sec)
hm =1;                %htc multiplier
reltol = 1e-6;
if flag == 8
T_target = 26;
else
T_target = 10; %Target freezing temperature
end

[time,T, dim1,xi_new_1] = dTdtEngine_noplot(N,t_sim,flag, hm, name, belt,
reltol, [],[],T_infinity);

T_f = (T-273.15)*(9/5)+32; %Converting temperature to F
if flag == 6
T_low = T_f(length(time),1);
else
T_low = T_f(length(time),floor(N/2));
end
deltaT = abs(T_target-T_low);
display(append(' Temperature delta T: ',num2str(deltaT), ' @ a belt speed of
',num2str(belt)));
close all;
end

```

```

% dTdtEngine_noplot.m
%This is just like dTdtEngine except with no plots

function [time,T,dim1,xi_new_1] = dTdtEngine_noplot(N,t_sim,flag, hm, name,
belt, reltol, xil, yil,T_infinity)
tic
T_ini = 311.5; %initial temperature(K)
if flag ==6
L = 0.03175; %Radius of a chicken wing (m)
elseif flag == 8
L = .0508; %thickness of chicken package (2 inches)

```

```

elseif flag == 9
L = 0.015875;           %same thickness as pizza, but made out of chicken
else
L = 0.015875;           %dough product thickness(m)
end

rho = 533.8;           %density of pizza crust (kg/m^3)
c = 2376;              %specific heat capacity of non frozen pizza crust
(J/kg-K) NOT USED
T_m = T_infinity;      %temperature of the plastic/nylon
Rc = .037;             %Contact resistance between the crust and the nylon
belt (K-m^2/W)
belt_d = 140;          %default belt speed

if name=='tempplot'
xi = xil;              %column 1 of time
yi = yil;              %column 2 of velocity
else

Voft=readtable(name);
x_vel =table2array(Voft);           %converting the table to an array
xi = x_vel(:,1);                    %column 1 of time
yi = x_vel(:,2);                    %column 2 of velocity
end

lng = length(xi);    %Length of the time vector that comes in

lng_n = (belt_d/belt)*xi(lng); %New xi length
xi_new = linspace(0,lng_n,lng)';
xi_new_1 = xi_new(lng);        %Largest value of belt-scaled time
t_sim = xi_new_1+10;          %simulation time is 10 seconds longer than the pizza
is in the freezer

%Setup grid
y = zeros(1,N);
for i = 1:N
    y(i) = (i-1)*L/(N-1);    %position of each node (m)
end

OPTIONS = odeset('RelTol',1e-6, 'MaxStep',10); %Max time step set to 0.01 and
tolerance lowered by 1000x"
[time,T] =
ode113(@(time,T)dTdt_functionv(time,T,L,name,rho,c,T_infinity,T_m,hm,Rc,flag,
xi, yi, belt),[0,t_sim],T_ini*ones(N,1),OPTIONS);

[rows,~] = size(T);          %number of rows in temperature matrix
T_f = (T-273.15)*(9/5)+32;   %Converting temperature to F

if name=='tempplot'
lng = length(xi);    %Length of the time vector that comes in
% lng_n = ((belt_d-belt)/belt_d)*xi(lng) + xi(lng);    %New xi length
lng_n = (belt_d/belt)*xi(lng); %New xi length

```

```

xi_new = linspace(0,lng_n,lng)';
xi_new_l = xi_new(lng); %Largest value of belt-scaled time
T_f1 = T_f(:,floor(N/2));
dim1 = time(nnz(T_f1)-nnz(T_f1<=10));
disp(append('Velocity profile: ',name));
display(append(' Freezing time (Mid temp <= 10F): ',num2str(dim1), '
seconds'));
else

T_f1 = T_f(:,floor(N/2));
dim1 = time(nnz(T_f1)-nnz(T_f1<=10));
disp(append('Velocity profile: ',name));
display(append(' Freezing time (Mid temp <= 10F): ',num2str(dim1), '
seconds'));
end
toc
end

```

```

% conductivity.m
%Food thermal conductivity calculations

function [k] = conductivity(temp,flag)
%Conductivity as a function of temperature
%This has been smoothed out over the freezing range
%The freezing point is at 271.7 (K)
%Conductivity frozen: 0.2259 (W/m-K)
%Conductivity non frozen: 0.1602 (W/m-K)
% flag = 4;
if flag == 1
lt = length(temp);
k(1:lt) = .3;
elseif flag == 2
lt = length(temp);
k(1:lt) = .2259;
k(temp>=265) = .2;
k(temp>=271.7) = .18;
k(temp>=276) = .1602;
elseif flag == 3 %flag 3 is the same as flag 2 - flag 3 is used for heat
capacity
lt = length(temp);
k(1:lt) = .2259;
k(temp>=265) = .2;
k(temp>=271.7) = .18;
k(temp>=276) = .1602;
elseif flag == 4 || flag == 7 || flag == 10 %flag 4 is from Cleland (2019)
R = 8.314; %"Gas constant"
M_w = 18.01528; %"Molecular weight of water"
L_w = 333.550; %"Latent heat of fusion of water"
x_tw = 0.346081917; %"Mass fraction of total water"

```

```

x_bw = x_tw./10;      %"Bound water - estimate is 10%"
xj = 0.625146427;    %"Solids other than water and fat"
Mj = 50000; %"Estimated molecular weight of solids"
tempc = temp-273.15;
T_if_K = 1/((1/273.15) - (R/(M_w*L_w))*log(((x_tw-x_bw)/M_w)/((x_tw-x_bw)/M_w+xj/Mj)));
T_if = T_if_K-273.15;
x_ice(tempc>T_if) = 0;
x_ice(tempc<=T_if) = (x_tw-x_bw).*(1-T_if./tempc(tempc<=T_if));
x_w = x_tw-x_ice;
x_f = 1-x_tw-xj;
Void_f = 0.5405;
kwater = 5.7109E-1 + 1.7625E-3.*tempc(:)' - 6.7036E-6.*tempc(:)'.^2;
kfat = 1.8071E-1 - 2.7604E-4.*tempc(:)' - 1.7749E-7.*tempc(:)'.^2;
kcarb = 2.0141E-1 + 1.3874E-3.*tempc(:)' - 4.3312E-6.*tempc(:)'.^2;
kair = 2.4125E-2 + 7.9976E-5.*tempc(:)'+ 3.4657E-8.*tempc(:)'.^2;
kice = 2.2196- 6.2489E-3.*tempc(:)'+ 1.0154E-4.*tempc(:)'.^2;
rho_water = 9.9718E2+3.1439E-3.*tempc(:)'+3.7574E-3.*tempc(:)'.^2;
rho_carbs = 1.5991E3-3.1046E-1.*tempc(:)';
rho_fat = 9.2559E2-4.1757E-1.*tempc(:)';
rho_ice = 9.1689E2-1.3071E-1.*tempc(:)';
x1 = 1./((x_w./rho_water)+(xj./rho_carbs)+(x_f./rho_fat)+(x_ice./rho_ice));
V_w = (x_w./rho_water).*x1;
V_c = (xj./rho_carbs).*x1;
V_fat = (x_f./rho_fat).*x1;
V_ice = (x_ice./rho_ice).*x1;
k_I = (kwater.*V_w+kfat.*V_fat+kcarb.*V_c)./(1-V_ice);
G = (kice-k_I).^2./((kice+k_I).^2 + kice.*k_I./2);
F = (2./G-1+2.*(1-V_ice)-sqrt((2./G-1+2.*(1-V_ice)).^2-8.*(1-V_ice)./G))./2;
k_II = kice.*(2.*kice+k_I-2.*(kice-k_I).*F)./(2.*kice+k_I+(kice-k_I).*F);
V_air = Void_f;
k = (3.*Void_f - 1).*kair+(3.*(1-V_air)-1).*k_II+sqrt(((3.*V_air-1).*kair+(3.*(1-V_air)-1).*k_II).^2+8.*k_II.*kair)./4;
elseif flag == 5
%Conductivity of aluminum 6061
lt = length(temp);
k(1:lt) = 167;
% k(1:lt) = 50;

elseif (flag == 6) || (flag == 8)|| (flag == 9)

%Conductivity of Chicken
%Conductivity in W/m-K
R = 8.314; %"Gas constant"
M_w = 18.01528; %"Molecular weight of water"
L_w = 333.550; %"Latent heat of fusion of water"
x_tw = 0.77 ; %"Mass fraction of total water"
x_bw = 0.7; %"Bound water - estimate is 10%"
xj = 0.1675; %"Solids other than water and fat"
Mj = 50000; %"Estimated molecular weight of solids"
tempc = temp-273.15;
T_if_K = 1/((1/273.15) - (R/(M_w*L_w))*log(((x_tw-x_bw)/M_w)/((x_tw-x_bw)/M_w+xj/Mj)));

```

```

T_if = T_if_K-273.15;
x_ice(tempc>T_if) = 0;
x_ice(tempc<=T_if) = (x_tw-x_bw).*(1-T_if./tempc(tempc<=T_if));
x_w = x_tw-x_ice;
x_f = 1-x_tw-x_j;
Void_f = 0;
kwater = 5.7109E-1 + 1.7625E-3.*tempc(:)' - 6.7036E-6.*tempc(:)'.^2;
kfat = 1.8071E-1 - 2.7604E-4.*tempc(:)' - 1.7749E-7.*tempc(:)'.^2;
kcarb = 2.0141E-1 + 1.3874E-3.*tempc(:)' - 4.3312E-6.*tempc(:)'.^2;
kair = 2.4125E-2 + 7.9976E-5.*tempc(:)'+ 3.4657E-8.*tempc(:)'.^2;
kice = 2.2196- 6.2489E-3.*tempc(:)'+ 1.0154E-4.*tempc(:)'.^2;
rho_water = 9.9718E2+3.1439E-3.*tempc(:)'+3.7574E-3.*tempc(:)'.^2;
rho_carbs = 1.5991E3-3.1046E-1.*tempc(:)';
rho_fat = 9.2559E2-4.1757E-1.*tempc(:)';
rho_ice = 9.1689E2-1.3071E-1.*tempc(:)';
x1 = 1./((x_w./rho_water)+(x_j./rho_carbs)+(x_f./rho_fat)+(x_ice./rho_ice));
V_w = (x_w./rho_water).*x1;
V_c = (x_j./rho_carbs).*x1;
V_fat = ( x_f./rho_fat).*x1;
V_ice =(x_ice./rho_ice).*x1;
k_I = (kwater.*V_w+kfat.*V_fat+kcarb.*V_c)./(1-V_ice);
G = (kice-k_I).^2./((kice+k_I).^2 + kice.*k_I./2);
F = (2./G-1+2.*(1-V_ice)-sqrt((2./G-1+2.*(1-V_ice)).^2-8.*(1-V_ice)./G))./2;
k = kice.*(2.*kice+k_I-2.*(kice-k_I).*F)./(2.*kice+k_I+(kice-k_I).*F);
else
k = .3;
end

```

```

% density.m
%Food density functions

function [rho] = density(temp,flag)
% flag = 4;
if flag ==1
rho = zeros(1,length(temp));
rho(:) = 690;
% rho = 533.8;           %density of pizza crust (kg/m^3)
elseif flag == 2
rho = zeros(1,length(temp));
rho(:) = 690;
% rho = 533.8;           %density of pizza crust (kg/m^3)
elseif flag == 3
rho = zeros(1,length(temp));
rho(:) = 690;
% rho = 533.8;           %density of pizza crust (kg/m^3)

```

```

elseif flag == 4 || (flag == 7) || (flag == 10)
rho = zeros(1,length(temp));
rho(:) = 533.8;
%Variable density:
%This density is from Cleland (2019)
% Void_f = 0.5405;
% R = 8.314;      %"Gas constant"
% M_w = 18.01528; %"Molecular weight of water"
% L_w = 333.550;  %"Latent heat of fusion of water"
% x_tw = 0.346081917; %"Mass fraction of total water"
% x_bw = x_tw/10;  %"Bound water - estimate is 10%"
% x_j = 0.625146427; %"Solids other than water and fat"
% x_f = 1-x_tw-x_j;
%
% M_j = 50000;    %"Estimated molecular weight of solids"
%
% tempc = temp-273.15;
%
% T_if_K = 1/((1/273.15) - (R/(M_w*L_w))*log(((x_tw-x_bw)/M_w)/((x_tw-
x_bw)/M_w+x_j/M_j)));
% T_if = T_if_K-273.15;
%
% x_ice = (x_tw-x_bw).*(1-T_if./tempc);
% x_w = x_tw-x_ice;
%
% rho_water = 9.9718E2+3.1439E-3.*tempc-3.7574E-3.*tempc.^2;
% rho_carbs = 1.5991E3-3.1046E-1.*tempc;
% rho_fat = 9.2559E2-4.1757E-1.*tempc;
% rho_ice = 9.1689E2-1.3071E-1.*tempc;
%
% rho(tempc<T_if) = Void_f*(1./(x_j./rho_carbs(tempc<T_if) +
x_f./rho_fat(tempc<T_if) + x_w(tempc<T_if)./rho_water(tempc<T_if) +
x_ice(tempc<T_if)./rho_ice(tempc<T_if)));
% rho(tempc>=T_if) = Void_f*(1./(x_j./rho_carbs(tempc>=T_if) +
x_f./rho_fat(tempc>=T_if) + x_tw./rho_water(tempc>=T_if)));
elseif flag == 5
%This is the density of Aluminum 6061 for testing the phantom out
rho = zeros(1,length(temp));
rho(:) = 2700; %2700 kg/m^3
elseif (flag == 6) || (flag == 8) || (flag == 9)
%This is the density of chicken breast
rho = zeros(1,length(temp));
rho(:) = 1150; %kg/m^3
end
end

```

```

% heatcap.m
%Food heat capacity functions

```

```

function [c] = heatcap(temp, flag)
%Specific heat capacity as a function of temperature
%This has been smoothed out over the freezing range
%The freezing point is at 271.7 (K)
%Heat capacity frozen: 1982 (J/kg-K)
%Heat capacity non frozen: 2376 (J/kg-K)
% flag = 4;
if flag ==1
    lt = length(temp);
    c(1:lt) = 2376;
elseif flag == 2
    lt = length(temp);
    c(1:lt) = 1982;
    c(temp>=265) = 2114;
    c(temp>=271.7) = 2245;
    c(temp>=276) = 2376;
elseif flag == 5
%Specific heat for 6061 aluminum
lt = length(temp);
c(1:lt) = 896;
elseif flag == 7 %flag 5 uses Cleland (2019) for heat capacity
% Below Code is from Cleland(2019). It works fine
tempc = temp-273.15;
R = 8.314; %"Gas constant"
M_w = 18.01528; %"Molecular weight of water"
L_w = 333.550; %"Latent heat of fusion of water"
x_tw = 0.346081917; %"Mass fraction of total water"
x_bw = x_tw/10; %"Bound water - estimate is 10%"
xj = 0.625146427; %"Solids other than water and fat"
x_f = 1-x_tw-xj;
Mj = 50000; %"Estimated molecular weight of solids"
T_if_K = 1/((1/273.15) - (R/(M_w*L_w))*log(((x_tw-x_bw)/M_w)/((x_tw-
x_bw)/M_w+xj/Mj)));
T_if = T_if_K-273.15;
x_ice = (x_tw-x_bw).*(1-T_if./tempc);
c_w = 4.1289-5.3062E-3.*tempc+9.9516E-4.*tempc.^2;
c_ice = 2.0623+6.0769E-3.*tempc;
c_fat = 1.9842 + 1.47339E-3.*tempc - 4.8008E-6.*tempc.^2;
c_carbs = 1.5488 + 1.9625E-3.*tempc-5.9399E-6.*tempc.^2;
c(tempc<T_if) =
1000*(c_carbs(tempc<T_if).*xj+x_f.*c_fat(tempc<T_if)+x_ice(tempc<T_if).*c_ice
(tempc<T_if)-(L_w+(c_w(tempc<T_if)-
c_ice(tempc<T_if)).*tempc((tempc<T_if)).*(x_tw-
x_bw).*(T_if./tempc((tempc<T_if)).^2)));
c(tempc>=T_if) =
1000*(c_carbs(tempc>=T_if).*xj+x_f.*c_fat(tempc>=T_if)+x_tw.*c_w(tempc>=T_if)
);
elseif flag == 4
%Dough
%simplified hybrid continuous function using Cleland and Gaussian
sigma = 1;
mu = 273.075;
%c = (1./(sigma.*sqrt(2.*pi)).*exp((-1/2).*((temp-
mu)./sigma).^2)).*113100+2460;

```

```

c = (1./(sigma.*sqrt(2.*pi)).*exp((-1/2).*((temp-
mu)./sigma).^2)).*101587+2097;
c = c';
elseif (flag == 6) || (flag == 8)|| (flag == 9)
%Chicken
%simplified hybrid continuous function using Cleland and Gaussian
sigma = 1;
mu = 273.075;
c = (1./(sigma.*sqrt(2.*pi)).*exp((-1/2).*((temp-
mu)./sigma).^2)).*256410+3490;
c = c';
elseif flag == 10
alpha=-10; %Skewness
mu = 273.05; %Mean
sigma = .2; %Standard deviation
PHI_1 = (1./((2.*pi).^(1./2)).*exp(-((temp-mu)./sigma).^2./2));
% temp
PHI_2 = (1./2).*(1+erf((alpha.*(temp-mu)./sigma)./(2).^(1./2)));
c = (2.*PHI_1.*PHI_2.*600000)+2000;
c = c';
else
c = 2376;
end

```

```

% htc.m
function [h] = htc(time,hm,name, xi, yi, belt)
%hm is a multiplier for heat transfer coefficient
h_ini = hm*23.85;
v_ini = 5;
vel2 = velocity(time,name,xi,yi,belt);
h = ((vel2.^8)./(v_ini.^8)).*h_ini;
end

```

```

% velocity.m

function [vel,xi_new,yi] = velocity(time,~,xi,yi,belt)
belt_d = 140; %Default belt speed - Old default
lng = length(xi); %Length of the time vector that comes in
lng_n = (belt_d/belt)*xi(lng); %New xi length
xi_new = linspace(0,lng_n,lng)';
xi_new_1 = xi_new(lng); %Largest value of belt-scaled time

```

```
%THIS OVERRIDES SIMULATION TIME
vel = interp1q(xi_new, yi, time); %1D interpolation
vel(time>xi_new_1) = 0; %times above 1696 produce velocity of 0
vel(time<0) = 0; %times below 0 have velocity of 0
end
```

```
% htc_given.m
function [h] = htc_given(time)
time = time';
hfile=readtable("htc_given.csv"); %Column 1 is time, column 2 is htc
hdata =table2array(hfile); %converting the table to an array
xi_H = hdata(:,1); %column 1 of time
yi_H = hdata(:,2); %column 2 of htc
h= interp1q(xi_H , yi_H, time); %1D interpolation
end
```

```
% t_gettemp.m
function [t_inf] = t_gettemp(time,xi,yi)
t_inf = interp1q(xi, yi, time); %1D interpolation
end
```

Python Code:

```
#Top Center Nusselt #

import numpy as np
import matplotlib.pyplot as plt
from mpl_toolkits.mplot3d import Axes3D
from matplotlib import cm
from scipy.interpolate import RegularGridInterpolator

# Hardcoded data
angles = np.array([0, 3, 5, 7, 9, 11, 13, 15, 17, 19, 21, 23, 28, 36, 45, 53, 61,
69, 78, 90])
reynolds_numbers = np.array([0, 10000, 20000, 30000, 40000, 50000, 60000, 70000,
80000, 90000])
nusselt_numbers = np.array([[76.04882096, 98.51562896, 94.05231856, 81.68445007,
71.63887862, 69.97936162, 69.17408537, 68.76791426, 67.4430397, 67.81077159,
69.9415664, 69.91426982, 69.98515959, 70.93433068, 71.08318543, 72.66406589,
72.91434499, 69.78478976, 71.16791718, 78.19220472], [121.1275764, 128.7300981,
121.531302, 109.6555114, 101.3176735, 93.67775505, 86.79533717, 84.35484345,
83.31261736, 84.35628072, 85.23359653, 86.75522709, 89.03501832, 90.48929356,
92.80792758, 94.12438671, 94.39686434, 93.15647613, 93.0760682,
100.7307953], [166.462072, 172.2888075, 164.2729303, 150.5900656, 141.1781931,
130.320458, 113.4223926, 101.5501298, 100.9336398, 101.8984435, 102.0264798,
104.1675242, 107.8106179, 111.901294, 120.1741019, 123.5694738, 124.8427092,
128.0822433, 127.078063, 136.5879143], [210.4894467, 212.8234745, 213.6980503,
201.9544497, 192.2361844, 184.2856446, 168.0356534, 137.0042556, 124.1704269,
123.7555695, 123.0588658, 124.0102125, 126.1328937, 128.4278585, 133.4261413,
135.506113, 135.4467852, 137.41926, 135.9251315, 159.7640661], [270.3085986,
261.1634321, 268.676303, 255.1110167, 243.7198439, 235.3245474, 221.6093464,
186.090905, 155.1889251, 145.4443844, 144.810108, 145.7061736, 147.0414514,
147.7057215, 151.4423757, 154.3830581, 155.1080982, 155.5397208, 154.7208989,
163.8652311], [327.7847662, 309.5207135, 316.2190078, 303.0994547, 289.6164256,
278.0460372, 263.9036842, 238.7847607, 190.5752531, 167.4748153, 161.4510229,
161.1576003, 164.5461628, 166.1473542, 170.3307348, 173.7136066, 173.0444459,
177.7705325, 177.4899193, 190.2788693], [381.0804939, 358.1696747, 355.774736,
```

```

337.4844013, 316.1519504, 315.3866048, 302.817899, 283.9640078, 224.1091986,
182.8058893, 175.1775441, 174.4810249, 178.1228135, 181.5854674, 183.9229998,
186.9437225, 186.4152951, 186.2657498, 185.0540469, 204.8951177], [433.2374606,
406.9117965, 395.2905122, 364.0123421, 339.4868418, 344.0345985, 347.8352918,
329.4010084, 271.9165935, 205.8247904, 191.9051819, 189.6545326, 189.4426237,
193.4889871, 198.0761377, 204.4939398, 204.0099147, 201.5642698, 199.7070109,
213.4987844], [484.7330233, 451.7485502, 434.9680863, 405.6714798, 388.4061164,
384.1354189, 375.6717019, 355.3976791, 315.0464291, 218.3280494, 202.9265969,
201.4546766, 199.4949225, 203.9365821, 207.0904009, 203.2201595, 203.9080046,
203.1607297, 201.4773368, 204.8943774], [500.565, 466.2845965, 447.0629314,
424.9371293, 407.6717659, 394.0720283, 378.9085752, 360.7971008, 329.3762308,
220.8485539, 205.0372779, 204.2713105, 203.4258462, 208.2874353, 209.5271759,
206.6125788, 204.5802476, 203.882994, 202.8403535, 203.0706892]])

# Create a meshgrid for the angles (X-axis) and Reynolds numbers (Y-axis)
X, Y = np.meshgrid(angles, reynolds_numbers)

# Create the interpolator
interpolator = RegularGridInterpolator((reynolds_numbers, angles),
nusselt_numbers)

# Function to interpolate Nusselt number
def interpolate_nusselt(reynolds, angle):
    point = np.array([reynolds, angle])
    return interpolator(point)

# Example: Interpolate for a specific angle and Reynolds number
example_reynolds = 90000
example_angle = 69
interpolated_value = interpolate_nusselt(example_reynolds,
example_angle).item() # Extract scalar value

print(f"Interpolated Nusselt number at Reynolds {example_reynolds} and angle
{example_angle}°: {interpolated_value:.2f}")

# Plotting the data using the specified settings
fig = plt.figure(figsize=(10, 8))
ax = fig.add_subplot(111, projection='3d')

# Plot the surface
surf = ax.plot_surface(X, Y, nusselt_numbers, cmap=cm.turbo, linewidth=0,
antialiased=False)

```

```

# Adding labels and a color bar
ax.set_xlabel('Angle (degrees)')
ax.set_ylabel('Reynolds Number')
ax.set_zlabel('Nusselt Number')
fig.colorbar(surf, shrink=0.5, aspect=10)

# Show the plot
plt.show()

```

```

#Top Center Nusselt Number Reduction Ratio

```

```

import numpy as np
import matplotlib.pyplot as plt
from mpl_toolkits.mplot3d import Axes3D
from matplotlib import cm
from scipy.interpolate import RegularGridInterpolator

# Hardcoded data
angles = np.array([0, 3, 5, 7, 9, 11, 13, 15, 17, 19, 21, 23, 28, 36, 45, 53, 61,
69, 78, 90])
reynolds_numbers = np.array([0, 10000, 20000, 30000, 40000, 50000, 60000, 70000,
80000, 90000])
nusselt_numbers = np.array([[1.0, 1.295426119, 1.236736052, 1.074105411,
0.942011693, 0.920189961, 0.909601023, 0.904260098, 0.886838729, 0.8916742,
0.919692975, 0.91933404, 0.920266201, 0.932747277, 0.934704635, 0.95549234,
0.958783372, 0.917631449, 0.935818811, 1.028184313], [1.0, 1.062764583,
1.003333061, 0.905289404, 0.836454229, 0.773380909, 0.71656133, 0.696413203,
0.687808836, 0.696425069, 0.703667976, 0.71623019, 0.735051596, 0.747057741,
0.766199823, 0.777068192, 0.779317701, 0.769077356, 0.768413527, 0.831609104],
[1.0, 1.035003382, 0.986849006, 0.904650914, 0.848110271, 0.782883791,
0.681370785, 0.610049656, 0.60634617, 0.612142107, 0.612911269, 0.625773324,
0.647658753, 0.672232975, 0.721930831, 0.742328101, 0.749976903, 0.769437997,
0.76340551, 0.820534748], [1.0, 1.011088574, 1.015243537, 0.959451663,
0.913281817, 0.875510139, 0.79830916, 0.650884202, 0.589912838, 0.58794192,
0.584631998, 0.589151686, 0.599236188, 0.610139181, 0.633885183, 0.643766778,

```

```

0.643484922, 0.652855819, 0.645757465, 0.759012238], [1.0, 0.966167682,
0.993961363, 0.94377692, 0.901635557, 0.870577365, 0.819838316, 0.688438718,
0.574117604, 0.538067916, 0.535721426, 0.539036399, 0.543976226, 0.546433677,
0.560257337, 0.571136319, 0.573818587, 0.575415365, 0.572386153, 0.606215385],
[1.0, 0.944280349, 0.964715388, 0.924690486, 0.883556698, 0.84825796,
0.805112718, 0.728480348, 0.581403631, 0.510929221, 0.492551941, 0.491656773,
0.50199454, 0.506879426, 0.51964201, 0.529962416, 0.527920952, 0.542339214,
0.541483124, 0.580499428], [1.0, 0.939879318, 0.933594717, 0.88559873,
0.829619872, 0.827611515, 0.794629754, 0.745154928, 0.588088874, 0.479704137,
0.459686462, 0.457858714, 0.467415195, 0.476501606, 0.482635566, 0.490562297,
0.489175642, 0.488783217, 0.485603566, 0.537668868], [1.0, 0.939235024,
0.912410741, 0.840214375, 0.783604542, 0.794101687, 0.802874459, 0.760324391,
0.627638693, 0.475085396, 0.442956114, 0.437761158, 0.43727203, 0.446611858,
0.457199932, 0.472013522, 0.470896294, 0.465251249, 0.460964319, 0.492798531],
[1.0, 0.93195332, 0.897335369, 0.836896725, 0.801278431, 0.792468019,
0.775007445, 0.733182313, 0.649938036, 0.450408862, 0.4186358, 0.415599241,
0.411556285, 0.42071939, 0.427225691, 0.419241417, 0.420660435, 0.419118814,
0.415645989, 0.422695314], [1.0, 0.931516579, 0.893116641, 0.848914985,
0.814423234, 0.787254459, 0.756961784, 0.72077972, 0.658008912, 0.441198553,
0.409611695, 0.408081489, 0.406392469, 0.416104672, 0.418581355, 0.41275874,
0.408698666, 0.407305733, 0.405222805, 0.405682957]])

```

```

# Create a meshgrid for the angles (X-axis) and Reynolds numbers (Y-axis)
X, Y = np.meshgrid(angles, reynolds_numbers)

```

```

# Create the interpolator
interpolator = RegularGridInterpolator((reynolds_numbers, angles),
nusselt_numbers)

```

```

# Function to interpolate Nusselt number
def interpolate_nusselt(reynolds, angle):
    point = np.array([reynolds, angle])
    return interpolator(point)

```

```

# Example: Interpolate for a specific angle and Reynolds number
example_reynolds = 90000
example_angle = 69
interpolated_value = interpolate_nusselt(example_reynolds,
example_angle).item() # Extract scalar value

```

```

print(f"Interpolated Nusselt number reduction ratio at Reynolds
{example_reynolds} and angle {example_angle}°: {interpolated_value:.2f}")

```

```

# Plotting the data using the specified settings
fig = plt.figure(figsize=(10, 8))
ax = fig.add_subplot(111, projection='3d')

# Plot the surface
surf = ax.plot_surface(X, Y, nusselt_numbers, cmap=cm.turbo, linewidth=0,
antialiased=False)

# Adding labels and a color bar
ax.set_xlabel('Angle (degrees)')
ax.set_ylabel('Reynolds Number')
ax.set_zlabel('Nusselt Number')
fig.colorbar(surf, shrink=0.5, aspect=10)

# Show the plot
plt.show()

```

```

#Bottom Center Nusselt #

import numpy as np
import matplotlib.pyplot as plt
from mpl_toolkits.mplot3d import Axes3D
from matplotlib import cm
from scipy.interpolate import RegularGridInterpolator

# Hardcoded data
angles = np.array([0, 3, 5, 7, 9, 11, 13, 15, 17, 19, 21, 23, 28, 36, 45, 53, 61,
69, 78, 90])
reynolds_numbers = np.array([0, 10000, 20000, 30000, 40000, 50000, 60000, 70000,
80000, 90000])
nusselt_numbers = np.array([[70.0079476, 98.11492728, 101.659664, 99.9335189,
97.3299138, 92.64254767, 86.10043664, 81.77822578, 81.54554468, 84.23949977,
87.22713366, 94.13774453, 99.73461816, 96.54746939, 97.02912972, 88.31021496,
72.03550415, 72.89386971, 73.34900178, 82.11062992], [114.6798613, 134.3271681,
143.9130329, 143.2701639, 134.7277826, 131.0693008, 135.3121396, 135.7181655,

```

```

140.9266772, 147.9621483, 156.231167, 165.087854, 171.785596, 162.4952857,
147.2001387, 119.1534985, 90.76882506, 90.23464208, 89.97065251, 108.3562109],
[172.1057795, 187.5479277, 198.8227287, 190.4504786, 182.0000847, 184.2755403,
193.360646, 200.7790023, 213.3199525, 223.4213537, 233.9327136, 245.8565327,
258.5364681, 240.5103083, 215.0486279, 172.7285629, 138.2053576, 141.163937,
137.3467918, 160.1649668], [229.268757, 240.0994037, 261.6432746, 258.7829544,
264.034794, 275.9104149, 280.4922993, 284.4103075,
291.3401307, 302.3254654, 318.6064625, 347.9441732, 377.285066, 343.8743523,
278.2455822, 202.5266827, 163.2218154, 159.4268487, 157.0256084, 201.0163114],
[288.3991183, 300.9587266, 335.0954417, 341.2155888, 356.8254736, 374.4292996,
378.7005824, 379.616082, 385.1194117, 402.8517492, 421.3637722, 469.9583464,
509.5132805, 454.2866048, 347.0255041, 251.6503068, 198.7084049, 190.850979,
188.5618982, 207.8316706], [341.3566812, 360.6687684, 401.3137177, 423.8044845,
452.5711121, 471.6715028, 464.1790799, 466.9402763, 484.2651731, 504.1455989,
516.5187934, 576.0497713, 644.6501254, 567.7580264, 423.4225738, 298.7453569,
242.4844753, 238.5383439, 236.2405616, 256.7399598], [391.7893497, 417.7643303,
457.2357181, 464.7267132, 495.483107, 519.0032341, 516.6564941, 534.9804687,
547.6369382, 568.9577452, 607.3507911, 674.2347123, 729.1411077, 655.3539141,
486.1819129, 309.9939991, 269.6124166, 258.7976345, 247.2025463, 283.0125439],
[440.177483, 471.5086736, 507.8596498, 506.9776511, 515.2769284, 541.9850385,
573.6424762, 615.8341022, 633.7338738, 658.886937, 704.4170374, 780.510657,
840.9442474, 772.6034266, 549.1478321, 358.959175, 319.2477816, 303.5589543,
278.7358382, 304.1786089], [486.9879961, 522.0611065, 556.5123701, 595.2634721,
615.496989, 643.1796949, 657.8834991, 667.8986396, 677.6548379, 709.0828589,
748.7462238, 833.5261198, 904.3859359, 799.0662766, 587.274101, 498.4603694,
392.222442, 338.3430593, 306.8792839, 296.5979104], [506.2878571, 542.8933656,
582.0447141, 624.6057373, 669.0426793, 695.9427346, 695.7492244, 692.8675008,
698.7683122, 727.2664642, 773.3610452, 860.535192, 920.5064143, 810.2802824,
591.2547068, 558.9963924, 483.2264012, 404.5973008, 349.9398814, 317.8056919]])
# Create a meshgrid for the angles (X-axis) and Reynolds numbers (Y-axis)
X, Y = np.meshgrid(angles, reynolds_numbers)

# Create the interpolator
interpolator = RegularGridInterpolator((reynolds_numbers, angles),
nusselt_numbers)

# Function to interpolate Nusselt number
def interpolate_nusselt(reynolds, angle):
    point = np.array([reynolds, angle])
    return interpolator(point)

# Example: Interpolate for a specific angle and Reynolds number
example_reynolds = 90000

```

```

example_angle = 69
interpolated_value = interpolate_nusselt(example_reynolds,
example_angle).item() # Extract scalar value

print(f"Interpolated Nusselt number at Reynolds {example_reynolds} and angle
{example_angle}°: {interpolated_value:.2f}")

# Plotting the data using the specified settings
fig = plt.figure(figsize=(10, 8))
ax = fig.add_subplot(111, projection='3d')

# Plot the surface
surf = ax.plot_surface(X, Y, nusselt_numbers, cmap=cm.turbo, linewidth=0,
antialiased=False)

# Adding labels and a color bar
ax.set_xlabel('Angle (degrees)')
ax.set_ylabel('Reynolds Number')
ax.set_zlabel('Nusselt Number')
fig.colorbar(surf, shrink=0.5, aspect=10)

# Show the plot
plt.show()

```

```

#Bottom Center Nusselt # Reduction Ratio

import numpy as np
import matplotlib.pyplot as plt
from mpl_toolkits.mplot3d import Axes3D
from matplotlib import cm
from scipy.interpolate import RegularGridInterpolator

# Hardcoded data

```

```

angles = np.array([0, 3, 5, 7, 9, 11, 13, 15, 17, 19, 21, 23, 28, 36, 45, 53, 61,
69, 78, 90])
reynolds_numbers = np.array([0, 10000, 20000, 30000, 40000, 50000, 60000, 70000,
80000, 90000])
nusselt_numbers = np.array([[1.0, 1.401482698, 1.452116045, 1.427459629,
1.390269493, 1.323314721, 1.229866602, 1.168127742, 1.164804104, 1.203284808,
1.245960447, 1.344672252, 1.424618512, 1.379092984, 1.385973065, 1.26143128,
1.028961805, 1.041222778, 1.047723927, 1.172875834], [1.0, 1.171323078,
1.254911118, 1.249305347, 1.174816407, 1.142914713, 1.179911957, 1.183452473,
1.228870314, 1.290219108, 1.362324346, 1.439554008, 1.497957828, 1.416947002,
1.28357444, 1.039009789, 0.791497513, 0.786839477, 0.784537507, 0.944858231],
[1.0, 1.089724751, 1.155235631, 1.106589675, 1.057489674, 1.070710936,
1.123498854, 1.166602324, 1.239470012, 1.298162992, 1.359237989, 1.42851991,
1.502195155, 1.397456314, 1.249514273, 1.003618608, 0.803025662, 0.820216133,
0.798037069, 0.930619339], [1.0, 1.047239959, 1.141207716, 1.128731877,
1.15163879, 1.203436606, 1.223421381, 1.240510531, 1.270736294, 1.318650955,
1.389663671, 1.517625767, 1.645601742, 1.499874457, 1.21362189, 0.883359274,
0.711923498, 0.695371017, 0.684897543, 0.876771497], [1.0, 1.043549399,
1.161915625, 1.183136727, 1.237262706, 1.298302511, 1.31311283, 1.316287249,
1.335369588, 1.396854996, 1.461043899, 1.629541551, 1.766695001, 1.575201088,
1.203282126, 0.872576547, 0.689004897, 0.661759925, 0.653822728, 0.720639064],
[1.0, 1.056574511, 1.175643366, 1.241529778, 1.325801243, 1.381755591,
1.359806635, 1.367895524, 1.418648586, 1.476888037, 1.513135151, 1.687530384,
1.888494238, 1.663239824, 1.240410975, 0.875170674, 0.710355147, 0.698795005,
0.692063682, 0.752116405], [1.0, 1.066298333, 1.167044787, 1.186164743,
1.264667116, 1.3246997, 1.3187099, 1.365479866, 1.397784137, 1.452203194,
1.550197298, 1.720911283, 1.861053927, 1.672720084, 1.240926823, 0.791226202,
0.688156574, 0.660553011, 0.6309578, 0.722358952], [1.0, 1.07117854, 1.153761084,
1.151757349, 1.170611738, 1.231287513, 1.303207225, 1.399058621, 1.439723517,
1.49686652, 1.600302298, 1.773172611, 1.9104663, 1.755208879, 1.247560026,
0.815487363, 0.725270587, 0.689628539, 0.633235113, 0.691036277], [1.0,
1.072020482, 1.142764041, 1.222337053, 1.26388534, 1.32073008, 1.35092344,
1.371488917, 1.391522673, 1.456058187, 1.537504476, 1.711594796, 1.857101085,
1.64083362, 1.205931369, 1.023557815, 0.805404743, 0.694766733, 0.630157799,
0.609045629], [1.0, 1.072301771, 1.149631985, 1.233696856, 1.321466968,
1.374598906, 1.374216692, 1.368524825, 1.380179877, 1.436468313, 1.527512529,
1.699695499, 1.818148315, 1.600433965, 1.167823203, 1.10410784, 0.9544449913,
0.799144785, 0.691187585, 0.627717389]])

# Create a meshgrid for the angles (X-axis) and Reynolds numbers (Y-axis)
X, Y = np.meshgrid(angles, reynolds_numbers)

# Create the interpolator

```

```
interpolator = RegularGridInterpolator((reynolds_numbers, angles),
nusselt_numbers)

# Function to interpolate Nusselt number
def interpolate_nusselt(reynolds, angle):
    point = np.array([reynolds, angle])
    return interpolator(point)

# Example: Interpolate for a specific angle and Reynolds number
example_reynolds = 90000
example_angle = 69
interpolated_value = interpolate_nusselt(example_reynolds,
example_angle).item() # Extract scalar value

print(f"Interpolated Nusselt number reduction ratio at Reynolds
{example_reynolds} and angle {example_angle}°: {interpolated_value:.2f}")

# Plotting the data using the specified settings
fig = plt.figure(figsize=(10, 8))
ax = fig.add_subplot(111, projection='3d')

# Plot the surface
surf = ax.plot_surface(X, Y, nusselt_numbers, cmap=cm.turbo, linewidth=0,
antialiased=False)

# Adding labels and a color bar
ax.set_xlabel('Angle (degrees)')
ax.set_ylabel('Reynolds Number')
ax.set_zlabel('Nusselt Number')
fig.colorbar(surf, shrink=0.5, aspect=10)

# Show the plot
plt.show()
```

EES Code:

"Phantom Calculations"

\$ifnot parametrictable

T_fluxa1 =95[F]
measured in F"

"Temperature of heat flux sensor 1-A

T_fluxa2 =95[F]
measured in F"

"Temperature of heat flux sensor 1-B

T_fluxa3 = 95 [F]
C measured in F"

"Temperature of heat flux sensor 1-

T_fluxb1 = 95 [F]
measured in F"

"Temperature of heat flux sensor 2-A

T_fluxb2 = 95 [F]
measured in F"

"Temperature of heat flux sensor 2-B

T_fluxb3 = 95 [F]
C measured in F"

"Temperature of heat flux sensor 2-

T_infinity = 72[F]

"Ambient temperature sensor"

U_inf=5[m/s]

mAa1 = 4.3

mAa2 = 4.3

mAa3 = 4.3

mAb1 = 4.3

mAb2 = 4.3

mAb3 = 4.3

voltage = 0.054

time = 1

angle = 0[degrees]

T_top_average = 80[F]

\$endif

Fluid\$ = 'Air'

S_calib_a1 = .001270[millivolt/(W/m^2)]
Sensor A-1: SN = 27410"

"Calibration sensitivity variable for

S_calib_a2 = .001270[millivolt/(W/m^2)]
Sensor A-2: SN = 27411"

"Calibration sensitivity variable for

S_calib_a3 = .001280[millivolt/(W/m^2)]
Sensor A-3: SN = 27412"

"Calibration sensitivity variable for

S_calib_b1 = .001300[millivolt/(W/m^2)]
Sensor B-1: SN = 27413"

"Calibration sensitivity variable for

$S_calib_b2 = .001250[\text{millivolt}/(\text{W}/\text{m}^2)]$ "Calibration sensitivity variable for
 Sensor B-2: SN = 27415"
 $S_calib_b3 = .001280[\text{millivolt}/(\text{W}/\text{m}^2)]$ "Calibration sensitivity variable for
 Sensor B-3: SN = 27367"
 $T_fluxtop_c = \text{ConvertTemp}(F,C,T_fluxtop)$
 "Heat Flux Sensor A - 1" "#SN = 27410"
 $V_readinga1 = ((mAa1-4)/16)*50[\text{millivolt}]$ "Converting Milliamp signal to
 millivolts (based on transmitter scaling)"
 $T_ca1 = \text{ConvertTemp}(F,C,T_fluxa1)$
 "Convert temp to C"
 $Sa1 = (.00334*1[1/C]*T_ca1+0.917)*S_calib_a1$ "Sensitivity equation"
 $\{Sa1 = (.00334*1[1/C]*T_fluxtop_c+0.917)*S_calib_a1$ "Sensitivity equation"}
 $Fluxa1 = V_readinga1/Sa1-Q_rad$ "Heat flux measured by sensor"
 $DELTA Ta1 = ((T_fluxa1-T_infinity)/1.8[F/K])$ "Delta T"
 $\{DELTA Ta1 = ((T_fluxtop-T_infinity)/1.8[F/K])$ "Delta T"}
 $htca1 = Fluxa1/DELTA Ta1$ "Heat transfer coefficient"
 "Heat Flux Sensor A - 2" "#SN = 27411"
 $V_readinga2 = ((mAa2-4)/16)*50[\text{millivolt}]$ "Converting Milliamp signal to
 millivolts (based on transmitter scaling)"
 $T_ca2 = \text{ConvertTemp}(F,C,T_fluxa2)$
 "Convert temp to C"
 $Sa2 = (.00334*1[1/C]*T_ca2+0.917)*S_calib_a2$ "Sensitivity equation"
 $\{Sa2 = (.00334*1[1/C]*T_fluxtop_c+0.917)*S_calib_a2$ "Sensitivity equation"}
 $Fluxa2 = V_readinga2/Sa2-Q_rad$ "Heat flux measured by sensor"
 $DELTA Ta2 = ((T_fluxa2-T_infinity)/1.8[F/K])$ "Delta T"
 $\{DELTA Ta2 = ((T_fluxtop-T_infinity)/1.8[F/K])$ "Delta T"}
 $htca2 = Fluxa2/DELTA Ta2$ "Heat transfer coefficient"
 "Heat Flux Sensor A - 3" "#SN = 27412"
 $V_readinga3 = ((mAa3-4)/16)*50[\text{millivolt}]$ "Converting Milliamp signal to
 millivolts (based on transmitter scaling)"
 $T_ca3 = \text{ConvertTemp}(F,C,T_fluxa3)$
 "Convert temp to C"
 $Sa3 = (.00334*1[1/C]*T_ca3+0.917)*S_calib_a3$ "Sensitivity equation"
 $\{Sa3 = (.00334*1[1/C]*T_fluxtop_c+0.917)*S_calib_a3$ "Sensitivity equation"}
 $Fluxa3 = V_readinga3/Sa3-Q_rad$ "Heat flux measured by sensor"
 $DELTA Ta3 = ((T_fluxa3-T_infinity)/1.8[F/K])$ "Delta T"
 $\{DELTA Ta3 = ((T_fluxtop-T_infinity)/1.8[F/K])$ "Delta T"}
 $htca3 = Fluxa3/DELTA Ta3$ "Heat transfer coefficient"
 "Heat Flux Sensor B - 1" "#SN = 27413"
 $V_readingb1 = ((mAb1-4)/16)*50[\text{millivolt}]$ "Converting Milliamp signal to
 millivolts (based on transmitter scaling)"
 $T_cb1 = \text{ConvertTemp}(F,C,T_fluxb1)$
 "Convert temp to C"
 $Sb1 = (.00334*1[1/C]*T_cb1+0.917)*S_calib_b1$ "Sensitivity equation"
 $Fluxb1 = V_readingb1/Sb1-Q_rad$ "Heat flux measured by sensor"

$\text{DELTA}Tb1 = ((T_fluxb1 - T_infinity) / 1.8) [F/K]$
 $htcb1 = Fluxb1 / \text{DELTA}Tb1$

"Delta T"
"Heat transfer coefficient"

"Heat Flux Sensor B - 2"

$V_readingb2 = ((mAb2 - 4) / 16) * 50$ [millivolt]
 millivolts (based on transmitter scaling)"
 $T_cb2 = \text{ConvertTemp}(F, C, T_fluxb2)$
 "Convert temp to C"
 $Sb2 = (.00334 * 1 [1/C] * T_cb2 + 0.917) * S_calib_b2$
 $Fluxb2 = V_readingb2 / Sb2 - Q_rad$
 $\text{DELTA}Tb2 = ((T_fluxb2 - T_infinity) / 1.8) [F/K]$
 $htcb2 = Fluxb2 / \text{DELTA}Tb2$

"#SN = 27415"
"Converting Milliamp signal to"
"Sensitivity equation"
"Heat flux measured by sensor"
"Delta T"
"Heat transfer coefficient"

"Heat Flux Sensor B - 3"

$V_readingb3 = ((mAb3 - 4) / 16) * 50$ [millivolt]
 millivolts (based on transmitter scaling)"
 $T_cb3 = \text{ConvertTemp}(F, C, T_fluxb3)$
 "Convert temp to C"
 $Sb3 = (.00334 * 1 [1/C] * T_cb3 + 0.917) * S_calib_b3$
 $Fluxb3 = V_readingb3 / Sb3 - Q_rad$
 $\text{DELTA}Tb3 = ((T_fluxb3 - T_infinity) / 1.8) [F/K]$
 $htcb3 = Fluxb3 / \text{DELTA}Tb3$

"#SN = 27367"
"Converting Milliamp signal to"
"Sensitivity equation"
"Heat flux measured by sensor"
"Delta T"
"Heat transfer coefficient"

"Averaging the current top and bottom sensors to get new values for all variables used below"

$T_fluxtop = (T_fluxa1 + T_fluxa2 + T_fluxa3) / 3$
 $T_fluxbot = (T_fluxb1 + T_fluxb2 + T_fluxb3) / 3$

$Fluxtop = (Fluxa1 + Fluxa2 + Fluxa3) / 3$
 $Fluxbot = (Fluxb1 + Fluxb2 + Fluxb3) / 3$

"Calculating (estimating) the radiation heat transfer"

$A_pizza = (0.31 [in] * 12 [in] * 4 + 12 [in] * 12 [in]) * \text{Convert}(in^2, m^2)$
 "upper and lower surfaces of the plate and the thickness"

$\sigma = 5.67E-8 [W/m^2-K^4]$
 $\epsilon = .1$
 $R_rad =$
 $1 / (A_pizza * \epsilon * \sigma * ((\text{ConvertTemp}(F, K, T_fluxtop))^2 + (\text{ConvertTemp}(F, K, T_infinity))^2) * ((\text{ConvertTemp}(F, K, T_fluxtop) + \text{ConvertTemp}(F, K, T_infinity))))$ "Radiation resistance"
 $Q_rad = (\text{ConvertTemp}(F, K, T_fluxtop) - \text{ConvertTemp}(F, K, T_infinity)) / R_rad / A_pizza$ "Radiation heat transfer per area on the plate"

$P = 1 [atm] * \text{Convert}(atm, Psia)$ "assuming atmospheric pressure"
 $L = 12 [in] * \text{Convert}(in, ft)$
 $\{u_inf = 5 [m/s] * \text{convert}(m/s, ft/min)$ "how are we planning to calculate air velocity"}

{"Heat transfer correlation from MATLAB Model (dittus boelter relationship)"

$hm = 1.25$
 $h_ini = hm * 22.5$
 $v_ini = 5$

```
"Just using htca1 to solve backwards for vel2, but vel2 can be sent here and htc can be solved for"
{htca1 = (vel2^0.8)/(v_ini^0.8)*h_ini}
vel2 = 685.8384615 [ft/min]
u_inf = vel2
```

```
//CALCULATED HTC
```

```
Call external_flow_plate(Fluid$, T_infinity, T_fluxa1, P, u_inf, L: tau_a1, h_forced_a1, C_f_a1,
Nusselt_forced_a1, Re_forced_a1)
```

```
Call fc_plate_horizontal1(Fluid$, T_fluxa1, T_infinity, P, L: h_nat_a1, Nusselt_nat_a1, Ra_nat_a1)
```

```
Call external_flow_plate(Fluid$, T_infinity, T_fluxa2, P, u_inf, L: tau_a2, h_forced_a2, C_f_a2,
Nusselt_forced_a2, Re_forced_a2)
```

```
Call fc_plate_horizontal1(Fluid$, T_fluxa2, T_infinity, P, L: h_nat_a2, Nusselt_nat_a2, Ra_nat_a2)
```

```
Call external_flow_plate(Fluid$, T_infinity, T_fluxa3, P, u_inf, L: tau_a3, h_forced_a3, C_f_a3,
Nusselt_forced_a3, Re_forced_a3)
```

```
Call fc_plate_horizontal1(Fluid$, T_fluxa3, T_infinity, P, L: h_nat_a3, Nusselt_nat_a3, Ra_nat_a3)
```

```
Call external_flow_plate(Fluid$, T_infinity, T_fluxb1, P, u_inf, L: tau_b1, h_forced_b1, C_f_b1,
Nusselt_forced_b1, Re_forced_b1)
```

```
Call fc_plate_horizontal1(Fluid$, T_fluxb1, T_infinity, P, L: h_nat_b1, Nusselt_nat_b1, Ra_nat_b1)
```

```
Call external_flow_plate(Fluid$, T_infinity, T_fluxb2, P, u_inf, L: tau_b2, h_forced_b2, C_f_b2,
Nusselt_forced_b2, Re_forced_b2)
```

```
Call fc_plate_horizontal1(Fluid$, T_fluxb2, T_infinity, P, L: h_nat_b2, Nusselt_nat_b2, Ra_nat_b2)
```

```
Call external_flow_plate(Fluid$, T_infinity, T_fluxb3, P, u_inf, L: tau_b3, h_forced_b3, C_f_b3,
Nusselt_forced_b3, Re_forced_b3)
```

```
Call fc_plate_horizontal1(Fluid$, T_fluxb3, T_infinity, P, L: h_nat_b3, Nusselt_nat_b3, Ra_nat_b3)
```

```
//COMBINED HTC CALCULATIONS
```

```
htc_combined_a1 = (((max(h_nat_a1, h_forced_a1)^3) +
(min(h_nat_a1, h_forced_a1)^3))^(1/3))*convert(Btu/hr-ft^2-R, W/m^2-K)
htc_combined_a2 = (((max(h_nat_a2, h_forced_a2)^3) +
(min(h_nat_a2, h_forced_a2)^3))^(1/3))*convert(Btu/hr-ft^2-R, W/m^2-K)
htc_combined_a3 = (((max(h_nat_a3, h_forced_a3)^3) +
(min(h_nat_a3, h_forced_a3)^3))^(1/3))*convert(Btu/hr-ft^2-R, W/m^2-K)
htc_combined_b1 = (((max(h_nat_b1, h_forced_b1)^3) +
(min(h_nat_b1, h_forced_b1)^3))^(1/3))*convert(Btu/hr-ft^2-R, W/m^2-K)
htc_combined_b2 = (((max(h_nat_b2, h_forced_b2)^3) +
(min(h_nat_b2, h_forced_b2)^3))^(1/3))*convert(Btu/hr-ft^2-R, W/m^2-K)
htc_combined_b3 = (((max(h_nat_b3, h_forced_b3)^3) +
(min(h_nat_b3, h_forced_b3)^3))^(1/3))*convert(Btu/hr-ft^2-R, W/m^2-K)}
```

```
"Non-Dimensional Analysis"
```

```
L_a1=12[in]/4*1*Convert(in,m)
```

```
L_a2=12[in]/4*2*Convert(in,m)
```

```
L_a3=12[in]/4*3*Convert(in,m)
```

```
L_b1=L_a1
```

```
L_b2=L_a2
```

```
L_b3=L_a3
```

```
"Film Temperatures"
```

$T_{\text{film_a1}} = \text{ConvertTemp}(F, K, (T_{\text{fluxa1}} + T_{\text{infinity}}) / 2)$
 $T_{\text{film_a2}} = \text{ConvertTemp}(F, K, (T_{\text{fluxa2}} + T_{\text{infinity}}) / 2)$
 $T_{\text{film_a3}} = \text{ConvertTemp}(F, K, (T_{\text{fluxa3}} + T_{\text{infinity}}) / 2)$
 $T_{\text{film_b1}} = \text{ConvertTemp}(F, K, (T_{\text{fluxb1}} + T_{\text{infinity}}) / 2)$
 $T_{\text{film_b2}} = \text{ConvertTemp}(F, K, (T_{\text{fluxb2}} + T_{\text{infinity}}) / 2)$
 $T_{\text{film_b3}} = \text{ConvertTemp}(F, K, (T_{\text{fluxb3}} + T_{\text{infinity}}) / 2)$

"Film Densities"

$\rho_{\text{a1}} = \text{density}(\text{'air'}, T = T_{\text{film_a1}}, P = P_{\text{o\#}})$
 $\rho_{\text{a2}} = \text{density}(\text{'air'}, T = T_{\text{film_a2}}, P = P_{\text{o\#}})$
 $\rho_{\text{a3}} = \text{density}(\text{'air'}, T = T_{\text{film_a3}}, P = P_{\text{o\#}})$
 $\rho_{\text{b1}} = \text{density}(\text{'air'}, T = T_{\text{film_b1}}, P = P_{\text{o\#}})$
 $\rho_{\text{b2}} = \text{density}(\text{'air'}, T = T_{\text{film_b2}}, P = P_{\text{o\#}})$
 $\rho_{\text{b3}} = \text{density}(\text{'air'}, T = T_{\text{film_b3}}, P = P_{\text{o\#}})$

"Film Viscosities"

$\mu_{\text{a1}} = \text{viscosity}(\text{'air'}, T = T_{\text{film_a1}})$
 $\mu_{\text{a2}} = \text{viscosity}(\text{'air'}, T = T_{\text{film_a2}})$
 $\mu_{\text{a3}} = \text{viscosity}(\text{'air'}, T = T_{\text{film_a3}})$
 $\mu_{\text{b1}} = \text{viscosity}(\text{'air'}, T = T_{\text{film_b1}})$
 $\mu_{\text{b2}} = \text{viscosity}(\text{'air'}, T = T_{\text{film_b2}})$
 $\mu_{\text{b3}} = \text{viscosity}(\text{'air'}, T = T_{\text{film_b3}})$

"Film Conductivities"

$k_{\text{a1}} = \text{conductivity}(\text{'air'}, T = T_{\text{film_a1}})$
 $k_{\text{a2}} = \text{conductivity}(\text{'air'}, T = T_{\text{film_a2}})$
 $k_{\text{a3}} = \text{conductivity}(\text{'air'}, T = T_{\text{film_a3}})$
 $k_{\text{b1}} = \text{conductivity}(\text{'air'}, T = T_{\text{film_b1}})$
 $k_{\text{b2}} = \text{conductivity}(\text{'air'}, T = T_{\text{film_b2}})$
 $k_{\text{b3}} = \text{conductivity}(\text{'air'}, T = T_{\text{film_b3}})$

"Reynold's Numbers"

$Re_{\text{a1}} = U_{\text{inf}} * L_{\text{a1}} * \rho_{\text{a1}} / \mu_{\text{a1}}$
 $Re_{\text{a2}} = U_{\text{inf}} * L_{\text{a2}} * \rho_{\text{a2}} / \mu_{\text{a2}}$
 $Re_{\text{a3}} = U_{\text{inf}} * L_{\text{a3}} * \rho_{\text{a3}} / \mu_{\text{a3}}$
 $Re_{\text{b1}} = U_{\text{inf}} * L_{\text{b1}} * \rho_{\text{b1}} / \mu_{\text{b1}}$
 $Re_{\text{b2}} = U_{\text{inf}} * L_{\text{b2}} * \rho_{\text{b2}} / \mu_{\text{b2}}$
 $Re_{\text{b3}} = U_{\text{inf}} * L_{\text{b3}} * \rho_{\text{b3}} / \mu_{\text{b3}}$

$Nus_{\text{a1}} = htca1 * L_{\text{a1}} / k_{\text{a1}}$
 $Nus_{\text{a2}} = htca2 * L_{\text{a2}} / k_{\text{a2}}$
 $Nus_{\text{a3}} = htca3 * L_{\text{a3}} / k_{\text{a3}}$
 $Nus_{\text{b1}} = htcb1 * L_{\text{b1}} / k_{\text{b1}}$
 $Nus_{\text{b2}} = htcb2 * L_{\text{b2}} / k_{\text{b2}}$
 $Nus_{\text{b3}} = htcb3 * L_{\text{b3}} / k_{\text{b3}}$

$Nus_{\text{a_avg}} = (Nus_{\text{a1}} + Nus_{\text{a2}} + Nus_{\text{a3}}) / 3$
 $Re_{\text{a_avg}} = (Re_{\text{a1}} + Re_{\text{a2}} + Re_{\text{a3}}) / 3$

$Nus_{\text{b_avg}} = (Nus_{\text{b1}} + Nus_{\text{b2}} + Nus_{\text{b3}}) / 3$

"Correction calculations"

{V_anem = 1.277[m/s] "Velocity measured from anemometer"}

V_anem = U_inf+.001[m/s] "Velocity measured from anemometer"

T_fluxa1_k = **ConvertTemp**(F,K, T_fluxa1)

T_infinity_K = **ConvertTemp**(F,K, T_infinity)

P_kpa = p***Convert**(psi,kPa)

L_m = L***Convert**(ft,m)

T_fluxtop_K = **ConvertTemp**(F,K,T_fluxtop)

CALL External_Flow_Plate(Fluid\$, T_infinity_K, T_fluxtop_K, P_kpa, V_anem, L_m: tau_a1, h_forced_top, C_f_a1, Nusselt_forced_a1, Re_forced_a1)

CALL FC_Plate_Horizontal1(Fluid\$, T_fluxtop_K, T_infinity_K, P_kpa, L_m: h_nat_top, Nusselt_nat_a1, Ra_nat_a1)

htc_combined_top = (((**Max**(h_nat_top, h_forced_top)^3) + (**Min**(h_nat_top,h_forced_top)^3))^(1/3))

h_top_average = (htca1+htca2+htca3)/3

h_bot_average = (htcb1+htcb2+htcb3)/3

"Dough thermal properties"

FUNCTION heatcap(T)

mf_w = 0.3461[-]

"Mass fraction of water"

{mf_w = 1[-]}

"Mass fraction of water"}

R = 8.314

"Gas constant"

M_w = 18.01528

"Molecular weight of water"

L_w = 333.550

"Latent heat of fusion of water"

x_tw = 0.346081917

"Mass fraction of total water"

x_bw = x_tw/10

"Bound water - estimate is 10%"

xj = 0.625146427

"Solids other than water and fat"

x_f = 1-x_tw-xj

Mj = 50000

"Estimated molecular weight of solids"

T_if_K = 1/((1/273.15) - (R/(M_w*L_w))***Ln**((x_tw-x_bw)/M_w)/((x_tw-x_bw)/M_w+xj/Mj)))

T_if = T_if_K-273.15

x_ice = (x_tw-x_bw)*(1-T_if/T)

x_w = x_tw-x_ice

```

c_w = 4.1289-5.3062E-3*T+9.9516E-4*T^2
c_ice = 2.0623+6.0769E-3*T
c_fat = 1.9842 + 1.47339E-3*T - 4.8008E-6*T^2
c_air = 1.0051+8.64629E-7*T+4.87E-7*T^2 + 8.0004E-9*T^3 + 5.4E-11*T^4
c_carbs = 1.5488 + 1.9625E-3*T-5.9399E-6*T^2

c_e = c_carbs*xj+x_f*c_fat+x_ice*c_ice-(L_w+(c_w-c_ice)*T)*(x_tw-x_bw)*(T_if/T^2)

IF (T<T_if) THEN
heatcap := c_carbs*xj+x_f*c_fat+x_ice*c_ice-(L_w+(c_w-c_ice)*T)*(x_tw-x_bw)*(T_if/T^2)

ENDIF
IF (T>=T_if) THEN
heatcap := c_carbs*xj+x_f*c_fat+x_tw*c_w

ENDIF

END

FUNCTION densityp(T)

Void_f = 0.5405
R = 8.314 "Gas constant"
M_w = 18.01528 "Molecular weight of water"
L_w = 333.550 "Latent heat of fusion of water"
x_tw = 0.346081917 "Mass fraction of total water"
x_bw = x_tw/10 "Bound water - estimate is 10%"
xj = 0.625146427 "Solids other than water and fat"
x_f = 1-x_tw-xj

Mj = 50000 "Estimated molecular weight of solids"

T_if_K = 1/((1/273.15) - (R/(M_w*L_w))*Ln(((x_tw-x_bw)/M_w)/((x_tw-x_bw)/M_w+xj/Mj)))
T_if = T_if_K-273.15

x_ice = (x_tw-x_bw)*(1-T_if/T)
x_w = x_tw-x_ice

rho_water = 9.9718E2+3.1439E-3*T-3.7574E-3*T^2
rho_carbs = 1.5991E3-3.1046E-1*T
rho_fat = 9.2559E2-4.1757E-1*T
rho_air = 1.3180-4.8312E-3*T-1.1237E-5*T^2-3.428E-7*T^3
rho_ice = 9.1689E2-1.3071E-1*T

rho_solid = 1/(xj/rho_carbs + x_f/rho_fat + x_w/rho_water + x_ice/rho_ice)
densityp = rho_solid*Void_f

IF (T<T_if) THEN

```

```
rho_solid:= 1/(xj/rho_carbs + x_f/rho_fat + x_w/rho_water + x_ice/rho_ice)
densityp := rho_solid*Void_f
```

```
ENDIF
```

```
IF (T>=T_if) THEN
```

```
rho_solid:= 1/(xj/rho_carbs + x_f/rho_fat + x_tw/rho_water )
```

```
densityp := rho_solid*Void_f
```

```
ENDIF
```

```
END
```

```
FUNCTION kwater(T)
```

```
kwater := 5.7109E-1 + 1.7625E-3*T - 6.7036E-6*T^2
```

```
END
```

```
FUNCTION kfat(T)
```

```
kfat:= 1.8071E-1 - 2.7604E-4*T - 1.7749E-7*T^2
```

```
END
```

```
FUNCTION kcarb(T)
```

```
kcarb:= 2.0141E-1 + 1.3874E-3*T - 4.3312E-6*T^2
```

```
END
```

```
FUNCTION icefract(T_if,T,x_tw, x_bw)
```

```
IF T > T_if THEN
```

```
icefract := 0
```

```
ENDIF
```

```
IF T <= T_if THEN
```

```
icefract := (x_tw-x_bw)*(1-T_if/T)
```

```
ENDIF
```

```
END
```

```
FUNCTION kice(T)
```

```
kice = 2.2196- 6.2489E-3*T+ 1.0154E-4*T^2
```

```
END
```

```
FUNCTION kair(T)
```

```
kair = 2.4125E-2 + 7.9976E-5*T- 3.4657E-8*T^2
```

```
END
```

```
R = 8.314[J/mol-K]
```

```
M_w = 18.01528[g/mol]
```

```
L_w = 333.550[J/g]
```

```
x_tw = 0.346081917
```

```
x_bw = x_tw/10
```

```
xj = 0.625146427
```

```
Mj = 50000[g/mol]
```

```
"Gas constant"
```

```
"Molecular weight of water"
```

```
"Latent heat of fusion of water"
```

```
"Mass fraction of total water"
```

```
"Bound water - estimate is 10%"
```

```
"Solids other than water and fat"
```

```
"Estimated molecular weight of solids"
```

```
1/(T_if_K) = (1/273.15[K]) - (R/(M_w*L_w))*Ln(((x_tw-x_bw)/M_w)/((x_tw-x_bw)/M_w+xj/Mj))
T_if = ConvertTemp(K,C,T_if_K)
```

```
x_ice = icefract(T_if, T, x_tw, x_bw)
$ifnot parametrictable
T = -20[C]
$endif
T_kelvin = ConvertTemp(C,K,T)
T_F = ConvertTemp(C,F,T)
```

```
{x_ice = (1.105*x_tw)/(1+.7318/ln(T_if-T+1[C]))}
{x_ice = (x_tw-x_bw)*(1-T_if/T)}
x_w = x_tw-x_ice
```

```
rho_water = 9.9718E2+3.1439E-3*T-3.7574E-3*T^2
rho_carbs = 1.5991E3-3.1046E-1*T
rho_fat = 9.2559E2-4.1757E-1*T
rho_air = 1.3180-4.8312E-3*T-1.1237E-5*T^2-3.428E-7*T^3
rho_ice = 9.1689E2-1.3071E-1*T
```

```
x_f = 1-x_tw-xj
Void_f = 0.5405
```

```
1/rho_solid = xj/rho_carbs + x_f/rho_fat + x_w/rho_water + x_ice/rho_ice
rho_e = rho_solid*Void_f
```

```
{1/rho_solid = xj2/rho_carbs + x_f2/rho_fat + x_w2/rho_water + x_ice2/rho_ice+Void_f/rho_air}
```

```
c_w = 4.1289-5.3062E-3*T+9.9516E-4*T^2
c_ice = 2.0623+6.0769E-3*T
c_fat = 1.9842 + 1.47339E-3*T - 4.8008E-6*T^2
c_air = 1.0051+8.64629E-7*T+4.87E-7*T^2 + 8.0004E-9*T^3 + 5.4E-11*T^4
c_carbs = 1.5488 + 1.9625E-3*T-5.9399E-6*T^2
```

```
c_e = c_carbs*xj+x_f*c_fat+x_ice*c_ice-(L_w+(c_w-c_ice)*T)*(x_tw-x_bw)*(T_if/T^2)
c_unfrozen = c_carbs*xj+x_f*c_fat+x_w*c_w
```

```
{c_e2 = c_carbs*xj+x_f*c_fat+x_ice*c_ice-(L_w+(c_w-c_ice)*T1)*(x_tw-x_bw)*(T_if/T1^2)}
```

```
{h = integral(c_e,T,-5,-0.07466)}
T2 = -1
h = heatcap(T2)
rhop = densityp(T2)
```

```
k_w = kwater(T)
k_f = kfat(T)
k_c = kcarb(T)
k_air = kair(T)
```

$$(x_w/\rho_{water}) * x1 + (x_j/\rho_{carbs}) * x1 + (x_f/\rho_{fat}) * x1 + (x_{ice}/\rho_{ice}) * x1 = 1$$

$$V_w = (x_w/\rho_{water}) * x1$$

$$V_c = (x_j/\rho_{carbs}) * x1$$

$$V_{fat} = (x_f/\rho_{fat}) * x1$$

$$V_{ice} = (x_{ice}/\rho_{ice}) * x1$$

$$k_I = (k_w * V_w + k_f * V_{fat} + k_c * V_c) / ((1 - V_{ice}))$$

$$check = x_w + x_f + x_j + x_{ice}$$

$$k_{ice} = k_{ice}(T)$$

$$G = (K_{ice} - k_I)^2 / ((k_{ice} + k_I)^2 + k_{ice} * k_I / 2)$$

$$F = (2/G - 1 + 2 * (1 - V_{ice}) - \text{Sqrt}((2/G - 1 + 2 * (1 - V_{ice}))^2 - 8 * (1 - V_{ice})/G)) / 2$$

$$k_{II} = k_{ice} * (2 * k_{ice} + k_I - 2 * (k_{ice} - k_I) * F) / (2 * k_{ice} + k_I + (k_{ice} - k_I) * F)$$

$$V_{air} = \text{Void}_f$$

$$k_{IV} = (3 * \text{Void}_f - 1) * k_{air} + (3 * (1 - V_{air}) - 1) * k_{II} + \text{Sqrt}(((3 * V_{air} - 1) * k_{air} + (3 * (1 - V_{air}) - 1) * k_{II})^2 + 8 * k_{II} * k_{air}) / 4$$

$$\text{Dia}_{pizza} = 11.5 * \text{Convert}(\text{in}, \text{m})$$

$$\text{Area}_p = \pi * (\text{dia}_{pizza} / 2)^2$$

$$\text{th}_{pizza} = (5/8) * \text{Convert}(\text{in}, \text{m})$$

$$\text{Vol} = \text{Area}_p * \text{th}_{pizza}$$

$$\rho_{pp} = 533.8 \text{ [kg/m}^3\text{]}$$

$$\text{mass} = \text{Vol} * \rho_{PP}$$

$$\text{mass2} = 19 * \text{Convert}(\text{oz}, \text{kg})$$

$$\text{vol2} = (\pi * (11.2/2)^2 * (5/8)) * \text{Convert}(\text{in}^3, \text{m}^3)$$

$$\rho_{o2} = \text{mass2} / \text{vol2}$$

"Chicken properties"

FUNCTION icefract(T_if, T, x_tw, x_bw)

IF T > T_if **THEN**

icefract := 0

ENDIF

IF T <= T_if **THEN**

```
icefract := (x_tw-x_bw)*(1-T_if/T)
ENDIF
END
```

```
FUNCTION kwater(T)
kwater := 5.7109E-1 + 1.7625E-3*T - 6.7036E-6*T^2
END
```

```
FUNCTION kfat(T)
kfat:= 1.8071E-1 - 2.7604E-4*T - 1.7749E-7*T^2
END
```

```
FUNCTION kcarb(T)
kcarb:= 2.0141E-1 + 1.3874E-3*T - 4.3312E-6*T^2
END
```

```
FUNCTION kice(T)
kice = 2.2196- 6.2489E-3*T+ 1.0154E-4*T^2
END
```

```
FUNCTION kair(T)
kair = 2.4125E-2 + 7.9976E-5*T- 3.4657E-8*T^2
END
```

```
R = 8.314[J/mol-K]           "Gas constant"
M_w = 18.01528[g/mol]       "Molecular weight of water"
L_w = 333.550[J/g]          "Latent heat of fusion of water"
x_tw = mf_w                 "Mass fraction of total water"
x_bw = 0.7                  "Bound water - estimate is 70%"
xj = S                      "Solids other than water and fat"
Mj = 50000[g/mol]          "Estimated molecular weight of solids"
```

```
$ifnot parametrictable
```

```
T = -40[C]
```

```
$endif
```

```
mf_w = 0.77                 "Mass fraction of water chicken breast"
```

```
W = mf_w
```

```
Fat = 6.2
```

```
Protein = 53.4
```

```
water = (Fat+Protein)/(1-W)
```

```
F = Fat/(protein+water+Fat)
```

```
S = protein/(protein+water+fat)
```

```
T_f = (-1.8 + W)           "Initial freezing temperature"
```

$I = (W - 0.25 * S) * (1 - (T_f / (-20)))$ "Ice mass fraction when fully frozen"

$\rho = 1 / (W / 1000 + S / 1300 + F / 850)$ "Density in kg/m³, no void fraction"

$k = \rho * (W / 1695 + S / 5306 + F / 4722)$ "Thermal conductivity W/m-K of unfrozen material, no void fraction"

$v_p = ((W - I) / 1000 + S / 1300 + F / 850) / (I / 920 + (W - I) / 1000 + S / 1300 + F / 850)$

$k_p = ((W - I) / 1695 + S / 5306 + F / 4722) / ((W - I) / 1000 + S / 1300 + F / 850)$

$G = (2.4 - k_p)^2 / ((2.4 + k_p)^2 + 1.2 * k_p)$

$C = ((2 / G) - 1 + 2 * v_p - \text{Sqrt}(((2 / G) - 1 + 2 * v_p)^2 - 8 * v_p / G)) / 2$

$k_s = 2.4 * ((4.8 + k_p - 2 * (2.4 - k_p) * C) / (4.8 + k_p + (2.4 - k_p) * C))$ "Thermal conductivity of frozen pizza crust W/m-K"

$c_l = 4180 * W + 1400 * S + 1900 * F$ "Specific heat capacity of unfrozen material J/kg-K, no void fraction"

$c_s = 4180 * (W - I) + 1940 * I + 1400 * S + 1900 * F$ "Specific heat capacity of frozen material J/kg-K"

$\rho_{eff} = 1.15 [g/cm^3] * \text{Convert}(g/cm^3, kg/m^3)$ "Density of chicken from the internet"

$V = PI * (11.2 [in] / 2)^2 * (5/8) [in]$
 $W_{pizza} = 19 * \text{Convert}(oz, kg)$

$\rho_{kg} = \rho * 1 [kg/m^3]$
 $V_m = V * \text{Convert}(in^3, m^3)$

$V_{m1} = W_{pizza} / \rho_{kg}$

$\text{Void_fraction} = ((V_m - V_{m1}) / V_m)$

$\epsilon = 1 - W_{pizza} / (V_m * \rho_{kg})$

$\{\rho_{eff} = \rho * (1 - \epsilon)\}$ "Effective density kg/m³ with Void fraction"

$k_{eff} = k * ((2 * k + 0.03 - 2 * \epsilon * (k - 0.03)) / (2 * k + 0.03 + \epsilon * (k - 0.03)))$ "Effective thermal conductivity W/m-K of unfrozen material w/Void fraction"

$k_{eff_s} = k_s * ((2 * k_s + 0.03 - 2 * \epsilon * (k_s - 0.03)) / (2 * k_s + 0.03 + \epsilon * (k_s - 0.03)))$ "Effective thermal conductivity W/m-K of frozen material w/Void fraction"

$k_w = k_{water}(T)$
 $k_f = k_{fat}(T)$
 $k_c = k_{carb}(T)$
 $k_{air} = k_{air}(T)$

```
rho_water = 9.9718E2+3.1439E-3*T-3.7574E-3*T^2
rho_carbs = 1.5991E3-3.1046E-1*T
rho_fat = 9.2559E2-4.1757E-1*T
rho_air = 1.3180-4.8312E-3*T-1.1237E-5*T^2-3.428E-7*T^3
rho_ice = 9.1689E2-1.3071E-1*T
```

```
1/(T_if_K) = (1/273.15[K]) - (R/(M_w*L_w))*Ln(((x_tw-x_bw)/M_w)/((x_tw-x_bw)/M_w+xj/Mj))
T_if = ConvertTemp(K,C,T_if_K)
```

```
x_ice = icefract(T_if, T, x_tw, x_bw)
```

```
T_kelvin = ConvertTemp(C,K,T)
```

```
{x_ice = (1.105*x_tw)/(1+.7318/ln(T_if-T+1[C]))}
```

```
{x_ice = (x_tw-x_bw)*(1-T_if/T)}
```

```
x_w = x_tw-x_ice
```

```
x_f = 1-x_tw-xj
```

```
Void_f = 0
```

```
1/rho_solid = xj/rho_carbs + x_f/rho_fat + x_w/rho_water + x_ice/rho_ice
rho_e = rho_solid*Void_f
```

```
(x_w/rho_water)*x1+(xj/rho_carbs)*x1+( x_f/rho_fat)*x1+(x_ice/rho_ice)*x1 = 1
```

```
V_w = (x_w/rho_water)*x1
```

```
V_c = (xj/rho_carbs)*x1
```

```
V_fat = ( x_f/rho_fat)*x1
```

```
V_ice =(x_ice/rho_ice)*x1
```

```
k_I = (k_w*V_w+k_f*V_fat+k_c*V_c)/((1-V_ice))
```

```
k_ice = kice(T)
```

```
G1 = (K_ice-K_I)^2/((k_ice+k_I)^2 + k_ice*k_I/2)
```

```
F1 = (2/G-1+2*(1-V_ice)-Sqrt((2/G-1+2*(1-V_ice))^2-8*(1-V_ice)/G))/2
```

```
k_II = k_ice*(2*k_ice+k_I-2*(k_ice-k_I)*F1)/(2*k_ice+k_I+(k_ice-k_I)*F1)
```

```
V_air = Void_f
```

```
k_IV = (3*Void_f - 1)*k_air+(3*(1-V_air)-1)*k_II+Sqrt(((3*V_air-1)*k_air+(3*(1-V_air)-1)*k_II)^2+8*k_II*k_air)/4
```